Design Study of an Underreamer for Casing While Drilling Operations

Development, design analysis and concept selection

P.A. Kamp

Delft University of Technology

TU Delft Delft University of Technology

Challenge the future

Cover image source: http://marcelkooiman.com/wp-content/uploads/2013/04/portfolio-2013-13941-1024x682.jpg by Marcel Kooiman.

DELFT UNIVERSITY OF TECHNOLOGY

Faculty of Mechanical, Maritime and Materials Engineering

Department of Offshore and Dredging Engineering

Design Study of an Underreamer for Casing While Drilling Operations

Development, design analysis and concept selection

BY

PHILIP ALBERT KAMP

A thesis submitted in partial fulfilment of the requirements for the degree of

MASTER OF SCIENCE
in
OFFSHORE AND DREDGING ENGINEERING

Delft, the Netherlands
August 30, 2018

Information

About the thesis

This report represents the master thesis of Philip Kamp for the multidisciplinary Master of Science (MSc) program of the department of Offshore and Dredging Engineering (ODE). The department results from interfaculty collaboration between the Faculty of Civil Engineering and Geosciences (CEG) and the Faculty of Mechanical, Maritime and Materials Engineering (3ME) at the Delft University of Technology (TU Delft).

A design study is carried out at Huisman Well Technology B.V. (HWT) in Schiedam, The Netherlands, at the Research and Development (R&D) Department. Huisman Well Technology is a joint venture between Well Engineering Partners B.V. (WEP) and Huisman Equipment B.V.

Author

Philip A. Kamp, BSc
4285522

Thesis committee

The thesis committee is comprised of:

Dr. Ir. Sape A. Miedema (Principal Tutor)	:	Associate Professor of Dredging Engineering and Mechatronics at TU Delft, 3ME
Ir. Xiuhan Chen	:	PHD Candidate of Offshore and Dredging Engineering at TU Delft, 3ME
Ir. Roel van de Pas	:	Lecturer and coordinator at TU Delft, Faculty of Architecture
Ir. Thijs Max (Company Supervisor)	:	R&D Engineer at Huisman Well Technology B.V.

Confidential

This document is made available subject to the condition that the recipient will neither use nor disclose the contents except as agreed in writing with the copyright owner. Copyright is vested in Huisman Well Technology B.V., Schiedam, The Netherlands.

© Huisman Well Technology B.V., 2018. All rights reserved.

Neither the whole nor any part of this document may be reproduced or distributed in any form or by any means (electronic, mechanical, reprographic, recording or otherwise) without the prior consent of the copyright owner.

An electronic version of this thesis is available at http://repository.tudelft.nl/.

Acknowledgements

This thesis was written over the course of nine months, from November 2017 until August 2018. During this period, different parts of the report have been revised and improved many times. The author recognizes that this would not be possible without the help of several individuals from Delft University of Technology and Huisman Equipment. Therefore, the author would like to humbly express his greatest appreciation and deepest gratitude to these people.

The author would like to thank Thijs Max for his major engagement and mindful attitude during the project. During the many talks, fruitful ideas have been exchanged and the feedback provided encouraged to author to rethink about the design decisions that were made.

Furthermore, the author wants to thank Sape Miedema for his friendly and insightful assistance as TU Delft supervisor. The progress meetings were very pleasant and the author will keep good memories of the conversations, both project and non-project related.

The author is also highly indebted to Pieter van Duivendijk. His guidance and comments on the design helped the author to make founded choices. As a team leader, he gave the author the possibility to conduct spring tests and permission to produce several 3D conceptual design models.

In addition, the author wants to thank Idtz Wieling for providing the author with some of the basic information on the subject. His support and openness to questions were greatly appreciated and the author expresses his admiration for his helpful and unselfish attitude.

Numerous people have given their opinion during the span of the thesis project. The author would like to give an honourable mention to Xiuhan Chen and Roel van de Pas, for joining the committee, Martin Legué, for sharing his knowledge on manufacturing techniques, Leo-Jan Pronk, for helping with the 3D-printer, Goran and Tom, for their assistance in the laboratory and colleagues and graduates from both the office and testing laboratory for contributing to a nice working environment.

Philip Kamp

Delft, The Netherlands
August 30, 2018

Abstract

For present-day drilling operations in deep and challenging well sections, a technology called casing while drilling can be used. It involves isolating and 'casing' a formation while drilling, where the casing itself is used as the drill pipe, which is cemented in after a certain depth is reached. By doing this, the need for separate casing runs will be eliminated and well stability is improved. The concept has become increasingly popular since the beginning of the 21st century, due to an increase in technical possibilities and use of this technique, which makes it more profitable.

To enlarge a wellbore past its original drilled size, to enable lowering of the casing, an underreamer is used. Under reaming can be performed in a reaming while drilling (RWD) configuration. To perform these operations, the bottom-hole assembly (BHA) containing the underreamer is lowered in the casing string to a depth just below the casing shoe. Afterwards, drilling fluids are used to fill the casing and pumps will be engaged to drive a hydraulic piston in the underreamer assembly that opens the cutter blades. Hydraulic pressure is used to fold the blades outward and prohibits closure of the tool.

The width of the reamed borehole is not only determined by the outer diameter of the casing couplings that have to fit thru, but there also has to be a clearance for the drilling mud**.** The annular space between the borehole and casing is relatively small which causes relatively high friction losses during current operation. Because of this, the dynamic pressure loss of the drilling fluid along the outside of the casing becomes too high. To lower the pressure, the borehole needs to be enlarged further than possible with underreamers currently available. There are also limitations on the length of the underreamer. From tests carried out by Huisman, it is found that an increase in length has adverse effects on the steering behaviour of the BHA. Therefore, the length of the reamer should be kept at a minimum.

The *DRILLSTAR Z600H* design that is currently being used does not allow for a diameter enlargement. New concepts must be devised to enable this. A solution to this problem can provide Huisman Well Technology (HWT) with the opportunity to perform the drilling of more and deeper wells.

A solution to the problem was found by splitting the piston and spring internally. This enabled the spring to be placed in the top part of the underreamer while the piston remains in the lower part. The blocks are located in the middle and fold out eccentrically to reach a hole diameter of 228.6 mm (9 inch). The angle under which the blocks fold out has been reduced from 60 degrees to 45 degrees to allow the underreamer to be shorter by 66 mm.

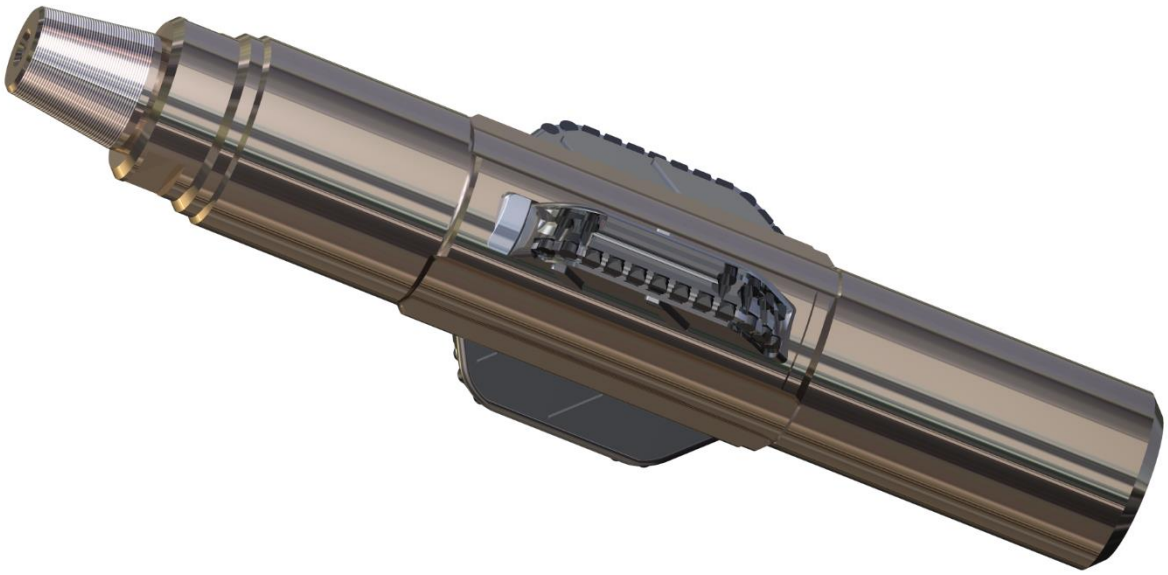

Table of contents

INFORMATION ..... **V**

ACKNOWLEDGEMENTS ..... **VII**

ABSTRACT ..... **IX**

1. INTRODUCTION **1**

1.1. BACKGROUND 1
1.2. PROBLEM STATEMENT 2
1.3. THESIS ASSIGNMENT 2
1.4. REPORT OUTLINE 2

2. THEORY AND PROCEDURES **3**

2.1. CASING WHILE DRILLING 3
2.1.1. Levels of casing while drilling 3
2.1.2. Enhanced Casing Installation 4
2.2. FUNCTIONS OF DRILLING MUD 5
2.2.1. Transportation 5
2.2.2. Stability and well-control 5
2.3. WELLBORE PRESSURE MANAGEMENT 5
2.4. BOTTOM HOLE ASSEMBLY 7

3. CONCEPT DESIGN AND SELECTION **10**

3.1. HOW DOES IT WORK: THE UNDERREAMER 10
3.2. REQUIREMENTS AND CURRENT SPECIFICATIONS 11
3.3. TELESCOPIC BLOCKS 12
3.4. VERTICAL SLIDING BLOCKS 13
3.5. DIAPHRAGM MECHANISM 14
3.6. ECCENTRIC BLADE CONFIGURATION 15
3.7. MULTI-DISK BLADES 16
3.8. BLOCKS WITH FINGER JOINTS 17
3.9. ARROW SHAPED SLIDING GROOVES 18
3.10. MULTIMEMBER EXTENDABLE ARMS 19
3.11. CONCEPT SELECTION 20

4. BASIC CONCEPT ANALYSIS **22**

4.1. REFERENCE FRAMEWORK 22
4.2. TELESCOPIC BLOCKS 24
4.2.1. Overview 24
4.2.2. Basic design 24
4.2.3. Challenges 26
4.3. DIAPHRAGM MECHANISM 27
4.3.1. Overview 27
4.3.2. Extension mechanism 29
4.3.3. Torsional stick-slip 30
4.3.4. Challenges 30
4.4. ECCENTRIC BLADE CONFIGURATION 31
4.4.1. Overview 31
4.4.2. Internal reaction forces 32
4.4.3. Normal stress analysis 33
4.4.4. Block deformation analysis 36
4.4.5. Core assembly deformation analysis 39
4.5. BLOCKS WITH FINGER JOINTS 41
4.5.1. Overview 41
4.5.2. Technical drawings and calculations 42
4.5.3. Prototype and shaping 44
4.5.4. Challenges 45
4.6. FINAL CONCEPT SELECTION 47

5. DETAILED DESIGN **49**

5.1. INTRODUCTION 49

5.2. ACTUATOR 49
5.3. EXPANSION MECHANISM 50
5.3.1. Extension length 52
5.3.2. Determination of spring characteristics 53
5.3.3. Buckling analysis 55
5.3.4. Verification of spring characteristics 57
5.4. CUTTER BLOCK MODELLING 64
5.4.1. Introduction 64
5.4.2. Cutter block - force analysis 66
5.5. UR COMPONENTS 72
5.5.1. Introduction 72
5.5.2. Upper-core 72
5.5.3. Bottom-core 73
5.5.4. Block 79
5.5.5. Armstopper 83
5.5.6. Coupling rod 84
5.5.7. Piston 88
5.5.8. Grease cap 90
5.5.9. Mud channel 91
5.5.10. Sleeve channel 92
5.5.11. Plug 95
5.6. ASSEMBLY 96
5.6.1. Introduction 96
5.6.2. Procedure 96
5.7. MANUFACTURING 100
5.7.1. Introduction 100
5.7.2. Hardfacing 100
5.7.3. Brazing 100
5.7.4. Milling 101
5.7.5. Boring 101
5.7.6. Sintering 102
5.7.7. Honing 102
5.7.8. Broaching 103
5.8. FEA USING ANSYS WORKBENCH 104
5.8.1. General introduction 104
5.8.2. General procedure 104
5.8.3. ANSYS element types 105
5.8.4. Support and boundary conditions 106
5.9. DETAILED CONCEPT ANALYSIS 107
5.9.1. Introduction 107
5.9.2. Link-piston analysis 109
5.9.3. UR – borehole analysis 119
5.9.4. Armstopper part analysis 137
5.9.5. Sleeve channel analysis 142

6. EVALUATION AND RECOMMENDATIONS 147

6.1. PROCESS EVALUATION 147
6.2. PROTOTYPE EVALUATION 148
6.2.1. Printer 148
6.2.2. Model adaption 150
6.2.3. Conclusions 151
6.3. DESIGN EVALUATION 152
6.3.1. UR specifications and operating parameters 152
6.3.2. Annulus pressure loss – calculation 153
6.3.3. Steerability – calculation 156
6.4. RECOMMENDATIONS 160

7. CONCLUSION 163

BIBLIOGRAPHY 164

LIST OF ABBREVIATIONS 171

METRIC AND U.S. MEASUREMENT EQUIVALENCES 172

LIST OF FIGURES 173

LIST OF TABLES **177**

APPENDIX A **178**

A.1: TECHNICAL DRAWING Z600H 178
A.2: Z-REAMER INFORMATION 179

APPENDIX B: AISI 4145 MODIFIED PROPERTIES **181**

APPENDIX C: API CASING SPECIFICATIONS **183**

APPENDIX D: REACTION FORCE ANALYSIS **184**

APPENDIX E: WEIGHT ON BIT APPROXIMATION **186**

APPENDIX F: ECI: SPECIFICATIONS, FEATURES AND APPLICATIONS **187**

APPENDIX G: ASSEMBLY OVERVIEW **189**

APPENDIX H **190**

H.1: NOMINAL TORQUE, PEAK WOB 190
H.2: MAXIMUM TORQUE, PEAK WOB 191
H.3: LIMITING LOAD CASE 192

APPENDIX I: ARMSTOPPER LIMITING LOAD CASE **193**

APPENDIX J: SPECIFIC ENERGY, CUTTING POWER AND SOIL TYPE DERIVATION **194**

1. Introduction

The first section of this introductory chapter is concerned with providing background information. Subsequently, the problem statement, thesis assignment and research goal are mentioned in the following sections. The last part provides a succinct summary of the project outline, which serves as a reading guide.

1.1. Background

Huisman Well Technology B.V. (HWT), a joint venture between Well Engineering Partners B.V. (WEP) and Huisman Equipment B.V., develops downhole tools for Casing while Drilling (CwD). Within HWT, this is referred to as Enhanced Casing Installation (ECI). ECI is classified as a level 3 casing drilling technique, which means that the casing is used as a drill pipe, through which a so-called Bottom Hole Assembly (BHA) can be retrieved up to the drill floor when a certain depth is reached. To allow for this method of drilling, an underreamer (UR) is used.

Since CwD requires the drill head to be lowered inside the casing, its size is limited by the drift diameter of the casing, a reamer must be deployed to enlarge the borehole, while casing is being run simultaneously. The width of the reamed borehole is not only determined by the outer diameter of the casing couplings that have to fit thru but there also has to be a clearance for the drilling fluid that flows between the outside of the casing and the borehole.

Currently, HWT is drilling with a reamer from the firm DRILLSTAR Industries. Standard dimensions for the type used are shown in table 1.1. This block-type Z-reamer is capable of enlarging the pilot hole by up to 50%. Additionally, its simple and compact design makes it suitable for directional reaming-while-drilling operations, because of its short length and the ability to be placed directly above the bit, in a so-called point-the-bit rotary steerable system (RSS) configuration, or in combination with a more conventional mud motor. In figure 1.1, a model (Z1225H), which is only different in scale to the Z600H, is shown.

Table 1.1: Standard dimensions.

Type	Pilot Bit size	Max Body OD	Max enlarged hole size	Max flow (GPM)	Standard connection
Z600H	5 7/8" – 6"	5 3/4"	8 1/2"	450	3 1/2" REG

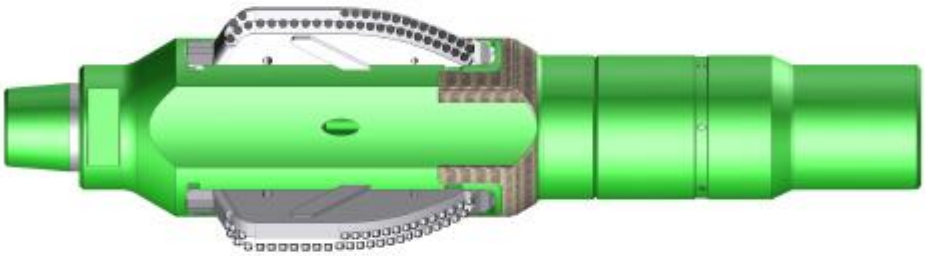

Figure 1.1: DRILLSTAR Z1225H type underreamer.[1]

1.2. Problem statement

The annular space between the borehole and casing is relatively small which causes relatively high friction losses during current operation. Because of this, the dynamic pressure loss of the drilling fluid along the outside of the casing becomes too high. To lower the pressure, the borehole needs to be enlarged further than possible with underreamers currently available. There are also limitations on the length of the underreamer. By means of testing, it is found that an increase in length will have adverse effects on the steering behaviour of the BHA. Therefore, the length of the reamer should be kept at a minimum.

1.3. Thesis assignment

To address the problems mentioned in the previous sections, a new concept has to meet requirements that are more stringent. In consultation with Huisman, the following research objective is proposed:

"Design an underreamer with a drill diameter of 9 inch (228.6 mm) or more and a body diameter of 5 7/8 inch (149.225 mm). The length of the underreamer should be as short as possible and be no longer than 750 mm.

The current design of DRILLSTAR will serve as a base-case and the specifications of the base-case determine the minimal requirements for the new concept design. The reamer blades have to move outwards under the influence of mud pressure and have to retract by using one or more springs."

The DRILLSTAR design does not allow for a diameter enlargement. New concepts must be devised to enable this. A solution to this problem can provide HWT with the opportunity to perform the drilling of more and deeper wells. In the next chapter, the terms discussed here will be explained and further elaborated on. A technical drawing of the base-case and some additional information about the Z-reamer can be found in appendices A.1 and A.2.

1.4. Report outline

A schematic outline of the remainder of the thesis, starting from chapter 2, is shown below.

Chapter 2	**Theory and procedures**: includes a description of the casing while drilling method, downhole conditions and equipment used in the bottom hole assembly.
Chapter 3	**Concept design and selection**: the working principles of the UR are explained. It also contains information about the design process and the development of concept ideas. Describes how four out of nine concepts are chosen based on a selection method (MCA). These will be treated in chapter 4.
Chapter 4	**Basic design and selection**: the remaining concept ideas are analysed by doing calculations and making drawings. Whenever possible a comparison is made to existing designs. From the four concepts, one concept is selected for detailing, which is described in chapter 5.
Chapter 5	**Detailed design**: this chapter describes in detail the working principles of the designed underreamer, its components and the production methods used. Finite element simulations are performed to prove it fulfils the operation requirements.
Chapter 6	**Evaluation and recommendations**: evaluates the design process, prototype and conceptual design. Some recommendations on the design are given.
Chapter 7	**Conclusion:** in this chapter, it is checked whether the two main research objectives of the thesis assignment are met.

2. Theory and procedures

This part of the report discusses the basics of casing while drilling operations, the DRILLSTAR Z600H design and the relation of downhole fluid properties and pressures to the working principles of the underreamer. The last section briefly mentions tools that run in conjunction with the underreamer in the Bottom Hole Assembly (BHA).

2.1. Casing while drilling

For present-day drilling operations, a technology called casing while drilling (CwD) can be used. It involves isolating and casing a formation while drilling, where the casing itself is used as the drill pipe, which is cemented in after a certain depth is reached. By doing this, the need for separate casing runs is eliminated and well stability is improved. Although the concept itself is known for a long time (United States Patent number 443,070 issued Dec. 16, 1890), it has become increasingly popular since the beginning of the 21st century, due to an increase in technical possibilities and use of this technique, which makes it more profitable.[2]

2.1.1. Levels of casing while drilling

Casing while Drilling is usually categorized into different levels. These levels indicate the configuration and operation of the drill and the complexity of the well architecture. In general, the main types of CwD are classified as: non-retrievable CwD, retrievable BHA CwD and drilling with liner systems. The levels and their capabilities will be discussed below. An overview of the levels 1, 2, 3 and 4 compared to the conventional drilling method, is presented in figure 2.1.[3]

Level 1

At this level, the wellbore has been drilled before with a traditional drill pipe. When lowering, the casing is rotated to smoothen the process. The casing can be run by using a top drive and Casing Running Tool (CRT), which provides extended control over the drill string. The casing string can also be rotated for cementing jobs or casing reaming for shale gas wells or ERD wells. Although the casing is rotated and some reaming operations or wiper trips are performed, this might not yet be considered as a true case of CwD, since the reamer has a fixed diameter, and the actual hole is drilled with a (conventional) drillpipe.

Level 2

The most basic form of casing while drilling uses a power swivel machine connected to a drive system in combination with Oil Country Tubular Goods (OCTG) piping used for the drilling. The term OCTG indicates the casing pipes are manufactured according to API specifications and are commonly utilized in the petroleum industry. The casing is used as a drill to transmit torque to a disposable or drillable bit, located at the bottom end or drill shoe of the casing string. The target depth is often reached in a single run and the deployment of logging or directional tools is not permitted. The system is therefore limited to drilling straight holes. Some tools however can be used in the casing string for centralization and vibration limiting purposes.[4]

Level 3

The method used in level 3 also involves the use of a top drive system or downhole motor and standard casing. The BHA, which is connected to the bottom of the casing string, drills a pilot hole. Some methods used to enlarge this pilot hole are: a reaming casing shoe, a near casing shoe underreamer and a near bit underreamer. After or during drilling the BHA can be retrieved through the casing string, before the cementing starts. Retrieval can be done by using a wireline or a drillpipe, depending on the angle and weight of the BHA. The casing is rotated more slowly and a motor inside the retrievable BHA enables the use of MWD (Measurement While Drilling), LWD (Logging While Drilling) and RSS (Rotary Steerable System) devices.

Level 4

In addition to the equipment used for level 3 drilling, level 4 makes use of liners. Liners are pieces of casing string that are not extended back to the wellhead but are connected to a liner hanger. The liner hanger is attached to the inside of the previous casing string and thus serves as a transition point. In contrast to the level 2 and 3 CwD methods, this configuration does not involve a casing drive system. By not running the liner all the way to the top of the well, metal costs and cementing costs can be reduced. This is what distinguishes it from a regular casing column.

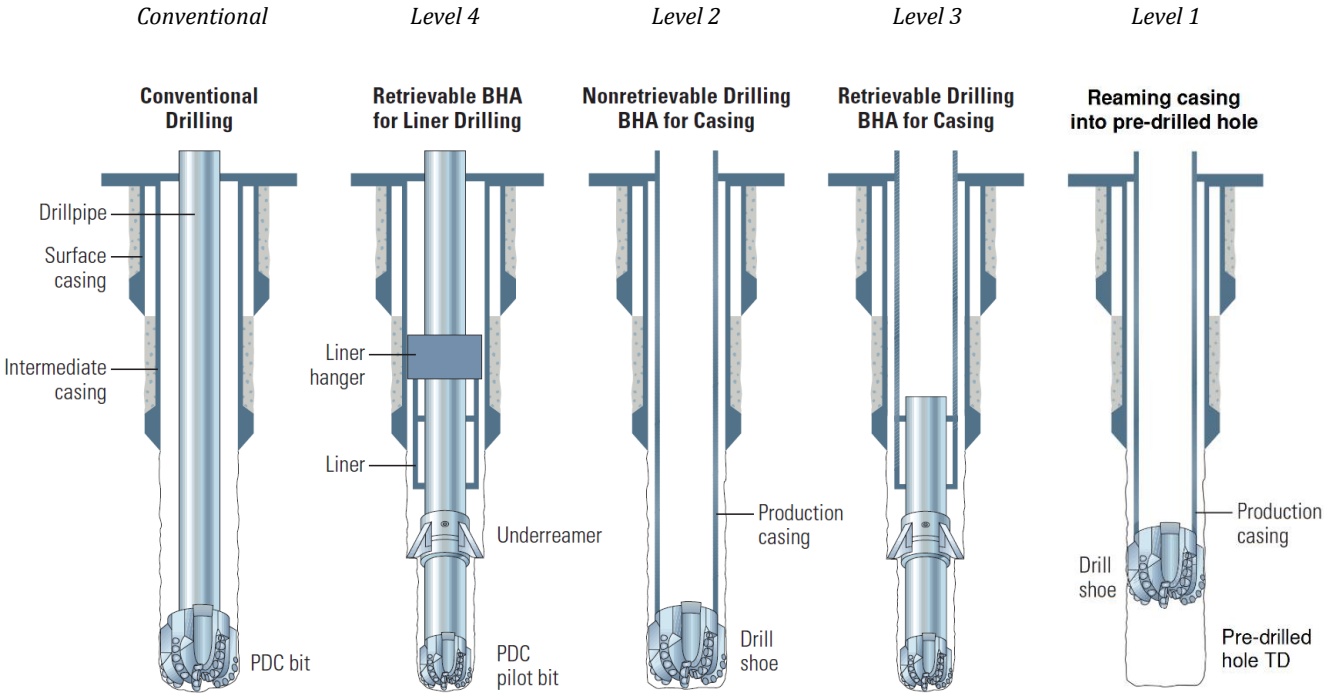

Figure 2.1: Overview of a conventional drilling method and the main types of CwD methods.[47, 48]

2.1.2. Enhanced Casing Installation

Within HWT, CwD is referred to as enhanced casing installation (ECI). The installation system comprises an innovative retrievable casing installation system that allows BHA components to be brought back to the surface by using a cable or by reverse circulation. The components of the BHA can be changed mid-section if required or at TD.

The ECI system is designed to be used in the Huisman LOC400 land drilling rig. However, the design is generally applicable meaning it can be used in a wide range of drilling situations with various types of BHA equipment (logging tools, bits, and mud motors).

Another unique feature of the ECI system involves the use of a see-through shoetrack section. Logging tools (MWD and LWD) can remain inside the casing while being in operation. This reduces the stick-out below the casing shoe and reduces the reamer to bit distance, which improves the stability of the BHA.

More specifications, features and applications of the ECI system can be found in appendix F.

2.2. Functions of drilling mud

Drilling fluids have several functions that can influence drilling characteristics. These include the transport of cuttings, preservation of the wellbore stability, cooling, lubrication, well control, providence of information and minimization of the risks associated with material failure, equipment handling by personnel and the environment.

Managing the fluid and utilizing it in a proper way can contribute to a higher penetration rate and increase performance of the drill bit. The drilling fluid flow rate has to be high enough so that sufficient cleaning of the system can be achieved for a certain combination of rotary speed and weight on bit (WOB), while the pressure losses have to stay as low as possible. This will amount to enough hydraulic horsepower for the bit to ensure an acceptable ROP while premature erosion can be avoided to provide a long service life.[5]

2.2.1. Transportation

After successful cutting of the formation rock, the cuttings need to be transported to the surface, to remove them from the hole. The solids present in the fluid need to be suspended and are carried upwards with a certain fluid velocity, such to prevent any further fragmentation of the solids. This makes it easier to remove the particles once they arrive at the surface. By cleaning the hole, problems related to clogging and formation sloughing can be avoided. In CwD applications, the annular velocity is relatively high, causing an increase in borehole cleaning efficiency.

2.2.2. Stability and well-control

The wellbore stability is dependent on the consistency of the drilling fluid. The borehole might tend to collapse due to a misbalance in mechanical stresses and chemical processes between the drilling fluid and the formation rock, affecting its composition. By controlling the downhole pressure, the inflow and outflow of formation fluids and drilling fluid can be managed.

On top of this, the well stability may also be affected by the deposition of filtrates along the wellbore surface. These can form a thick layer called a filter cake, which can cause problems in case the filtrate is not compatible with the formation. When using the CwD method, the annular space is in general smaller than with conventional drilling methods. A thick filter cake may further narrow the hole, impeding the passage of the pipe or result in bad quality cementing. On top of that, it can cause the dynamic pressure losses of the drilling fluid to become too high.

2.3. Wellbore pressure management

During drilling operations, the pressures that exist in a well need to be handled appropriately. By adjusting the circulation pressure in the annulus around the casing string, there can either be an inflow (kick) or outflow of formation fluids or drilling fluids (lost circulation), respectively. For a long time the industry was confronted with problems related to fluid loss. This issue was eventually addressed by using the (conventional) method of underbalanced drilling (UBD).

However, when the industry advanced further and improved its ability drill excessively long wells, problems related to well control and bore instability became more important. This resulted in the development of managed pressure drilling (MPD), which is aimed at preventing flow across the borehole surface. MPD systems manage the downhole pressure by supplying backpressure from the surface. This way, downhole pressures can be altered faster in comparison with the conventional method that relies on changing mud weights. By applying the MPD method, drilling efficiencies can be improved and safety can be enhanced.[6]

An important parameter in managing the downhole pressures is the equivalent mud weight (EMW). The EMW indicates the total amount of pressure that is being exerted on the formation and may not fall below the pore pressure or exceed the fracture pressure of the formation for reasons mentioned above. In imperial units, a relation for the EMW can be expressed as (eq. 2.1):

$$EMW\ at\ depth\ D\ (ppg) = (Annulus\ Pressure\ Loss\ Imposed\ Pressures\ (psi) + HSP\ (psi)) / (0.052 \cdot TVD\ (ft)) \quad [2.1]$$

The hydrostatic pressure (HSP) can be calculated according to (eq. 2.2):

$$HSP\ (psi) = 0.052 \cdot Mud\ Weight\ (ppg) \cdot TVD\ (ft) \quad [2.2]$$

Here TVD stands for the true vertical depth. The 'Annulus Pressure Loss Imposed Pressures' term does not only include the pressure that pumps need to deliver to circulate the flow but it does also include the surge and swab pressures, which are associated with pipe lowering and tool extraction operations, respectively. However, since the latter two are not easily determined, direct downhole measurements are preferred for the most accurate analysis of the pressure.

If the EMW goes outside of the pressure window between the pore and fracture pressure, the drilling operator has to set the current casing and start drilling a new, smaller sized one. This is shown in figure 2.2.

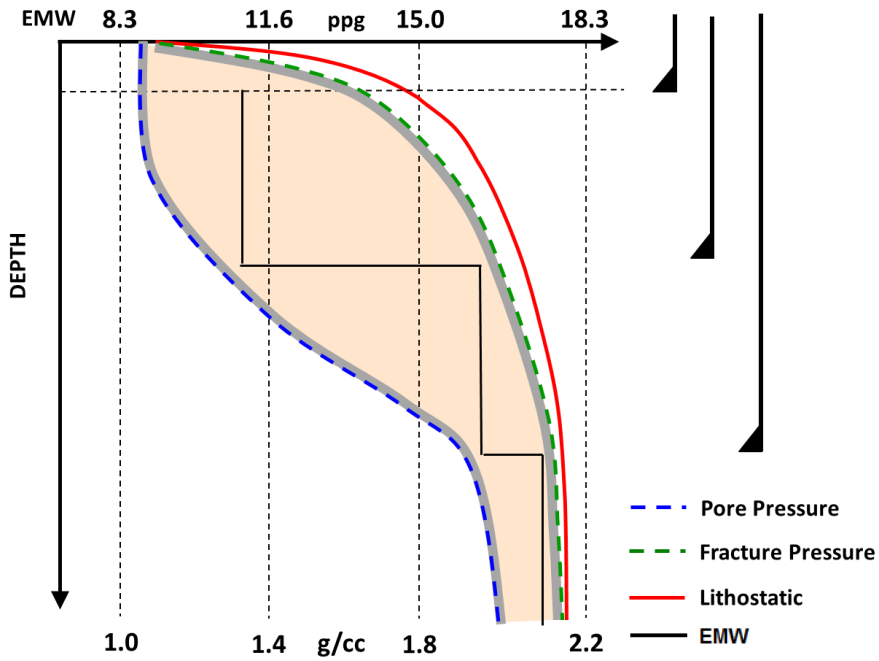

Figure 2.2: Depth vs pressure gradient plot.[7]

As for the underreamer, making the borehole bigger can reduce the fluid circulating friction pressure drop, which may lower the EMW for the casing size used, so that is does not exceed the fracture line. In that case, an even smaller casing size may be used to drill even deeper wells. This is particularly important in wells with a small margin between the pore and fracture pressure.

2.4. Bottom hole assembly

For level 3 CwD operations, a retrievable (directional) BHA is used. The BHA forms the lowest part of the drill string and can be retrieved by using a braided wireline cable, a drillstring or by applying pressure. The ability to retrieve the BHA is essential because expensive modules need to be recovered and equipment that fails before TD is reached needs to be repaired. It can also be convenient for a cost-effective and quick data assessment. The modules of which a generic BHA is comprised are elaborated on below. The UR is not mentioned here as it was treated earlier.

Drill Lock Assembly (DLA)

It is connected to the inside of the casing string by means of a Drill Lock Assembly (DLA). The DLA consists of seal components and mechanical components that can lock the BHA into place; axially by securing it to a profile nipple on the casing and torsionally by expandable grooved pads, see figure 2.3.

Figure 2.3: Axial (left) and torsional (right) sections.

Downhole measurement techniques

Measurement tools that are often used are Measurement While Drilling (MWD) and Logging while drilling (LWD). MWD equipment is used in deviation control to determine the top-bottom inclination angle and left-right azimuth angle of the steering assembly. Together with a measured depth and magnetic direction evaluation, trigonometry can be used to plot the trajectory of the well in 3D. LWD tools on the other hand gather information about the geological properties of the formation rock by measuring characteristics such as resistivity, porosity, density, formation pressure and magnetic resonance.[8]

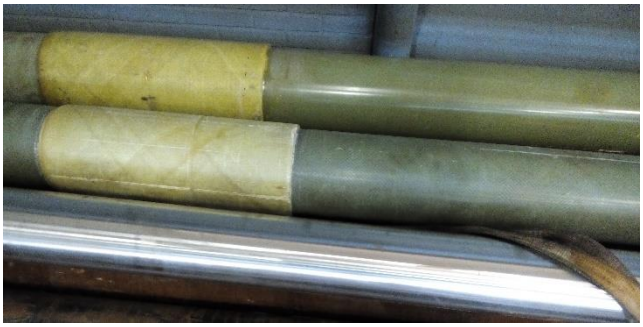

Figure 2.4: Composite (top and middle) and stainless steel (bottom) casing joints.

To prevent magnetic disturbances, the MWD and LWD tools need to be isolated from other steel components downhole. Akiet B.V. together with HWT recently developed the Enhanced Composite Casing Installation (ECCI) system[9], which offers the possibility to position the measurement tools inside a composite shoetrack section, see figure 2.4. This reduces both the bit-underreamer distance and stick-out distance, which improves the stabilization of the BHA. The information that is collected with the tools can be transmitted to the surface by means of mud-pulse telemetry. Pressure fluctuations caused by sequentially opening and closing valves can be measured and converted at the surface.

Polycrystalline Diamond Compact (PDC) bit with fish tail design

The PDC drill bit is located at the bottom of the BHA. These drill bits have a fish tail design. The body is composed of tungsten carbide grains, and a cobalt binder fused together by sintering (matrix-body type). The cutters themselves consist of diamond tables that are bond to tungsten carbide materials. These tungsten carbide materials are then brazed to the body, see figure 2.5.

Figure 2.5: The matrix body structure (left) and the PDC cutting elements (right).

Drilling stabilizer

Drilling stabilizers (figure 2.6) act as a standoff between the pilot-hole and drillpipe (e.g. near-bit stabilizer) or drillpipe and casing (string stabilizers) and are used to prevent or reduce pipe sticking, vibrations and side-tracking.

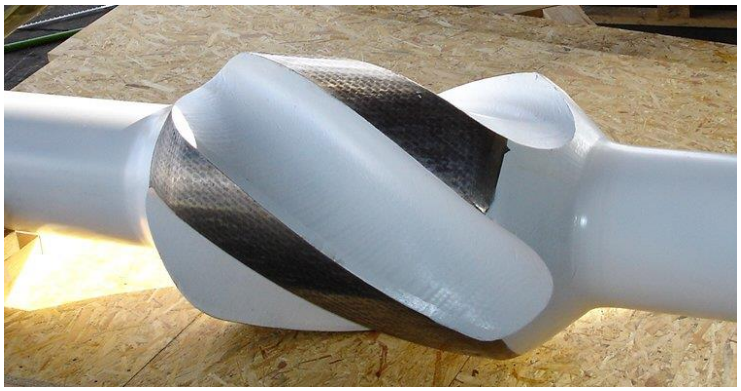

Figure 2.6: Drilling stabilizer.

Float substitutes

Float subs prevent the back flow of drilling fluids. This prohibits cuttings from entering the drill collars and mud motor above. It may also help to avoid clogging of the drill bit. A plunger-type float valve is shown in figure 2.7.

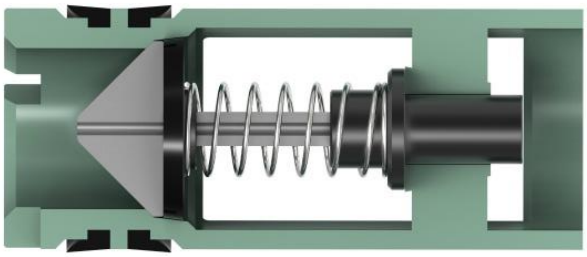

Figure 2.7: Drill pipe float valve.

Mud motors

Mud motors are used to power rotary steerable assemblies or to rotate the drill bit relative to the casing. These motors are classified as Progressive Cavity Positive Displacement (PCPD) pumps in which an eccentric motion in the power section of the motor is transferred via a transmission section to convert power to the drill bit. The power section consists of a rotor, made of a metallic material, and a stator, made of an elastomer. Mud motors are often used in slide drilling. Figure 2.8 shows the basic layout of a mud motor.

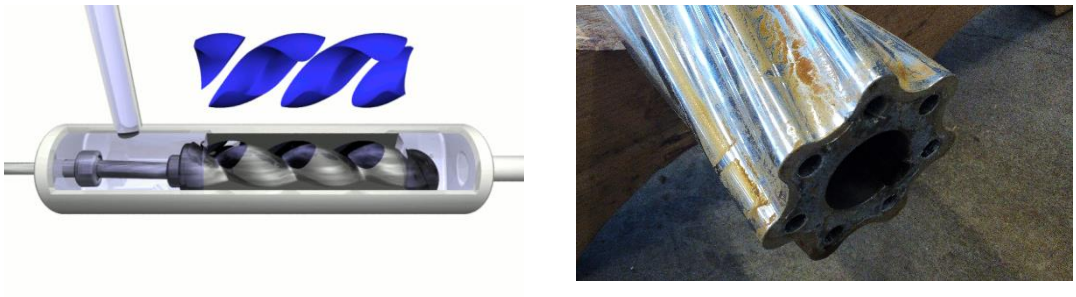

Figure 2.8: Mud motor principle (left) and rotor (right).

Rotary Steerable Systems (RSS)

Instead of using a bent-housing in combination with a mud motor, a RSS can be used for directional drilling by driving the bit with the top drive. RSS systems allow for a continuous drillstring rotation, which enables the drilling of deeper wells. This is due to a lower friction when compared to slide drilling.

Two RSS methods are commonly used: push-the-bit and point-the-bit. Push-the-bit systems apply a side force on the drillstring, by sequentially actuating pads from within the RSS assembly[10]. Point-the-bit systems use a deflection mechanism that resembles a bent-housing mechanism, so that the bit can be tilted during rotation of the RSS steering section. Now, by varying the rotational speed of the casing, the eccentricity of the drill bit can be controlled. Both systems are shown in figure 2.9.

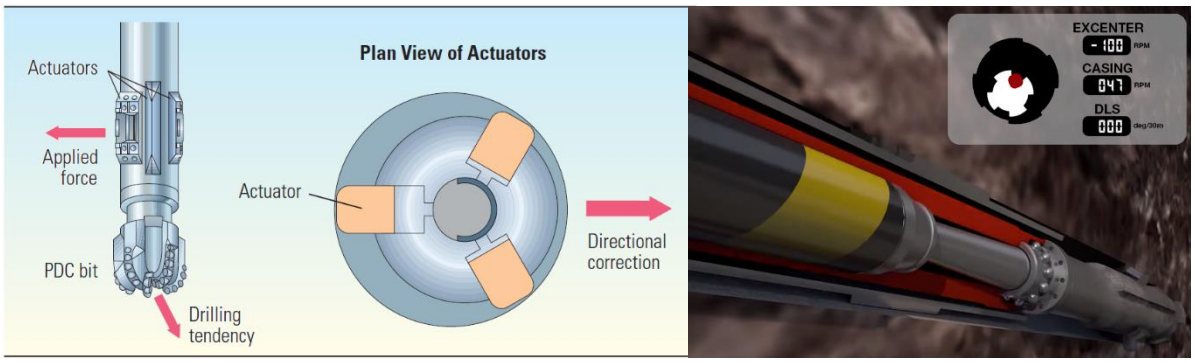

Figure 2.9: Push-the-bit (left) and point-the-bit (right).

3. Concept design and selection

This chapter is concerned with introducing the current base-case design and the initial phases of the design process. The first design phase involves coming up with new and innovative concept ideas for the extension mechanism. Restrictions on the concepts are not imposed yet, since this will allow for the most diverse set of concept possibilities. Each of the concepts will be discussed succinctly. Together with a MCA, this will result in a recommendation on how to proceed to the next stage with some of the provisional concepts.

3.1. How does it work: the underreamer

To enlarge a wellbore past its original drilled size an underreamer is used. Under reaming can be performed in a reaming while drilling (RWD) configuration. To perform these operations, the BHA containing the underreamer is lowered in the casing string to a depth just below the casing shoe. Afterwards, drilling fluids are used to fill the casing and pumps will be engaged to drive a hydraulic piston in the underreamer assembly that opens the cutter blades. Hydraulic pressure is used to fold the blades outward and prohibits closure of the tool. During normal reaming operations a pressure difference of at least 10 bar is required between the inside of the drillstring and the borehole.

The tool considered in this report (DRILLSTAR Z600H), shown in figure 3.1, makes use of expandable hydraulic tools (blocks) to remove formation. These blocks (1) slide along the main body (2) by means of a tongue-groove fitting. In the figure, only one tongue (3) is depicted. Another tongue is located on the other side of the block. In total, three blocks are present which are fitted in a concentric manner around the inner drilling fluid flow tube (4). The blocks are moved upward with a piston assembly (piston (5) & upper stem (11)) that is connected to the blades though coupling rods (6) which are connected to both components by means of roll pins (7). When the tool is activated and the piston reaches its maximum position, the blades are locked into place by arm stops (8) that where installed during the assembly of the tool. These prohibit the blades from further moving outward. Shear pins (9) can additionally be installed to delay activation.

While the blades remain in their extended position, a return spring (10) inside the piston assembly (5 & 11) is compressed. When the tool is deactivated by stopping the pumps, this spring helps with retracting the blades by pushing the piston assembly down until it contacts the bottom sub (12). Due to the holdup of debris, a spring alone might sometimes not provide a high enough pulling force to fully retract the blades. When the tool is pulled out of the hole (POOH), it might bounce of the borehole wall. These lateral forces can help the blocks to fully retract. So for a better reliability and redundancy, the grooves mentioned earlier are orientated under an angle, which improves the blade retraction and keeps the tool from jamming while pulling it up. In some cases, back reaming is required to smoothen the borehole. In this case, a larger pressure difference between the inside of the drillstring and the borehole is required (20 bar). The amount of force used to pull the pipe to the surface (overpull) may not exceed two tonnes in this case.[11]

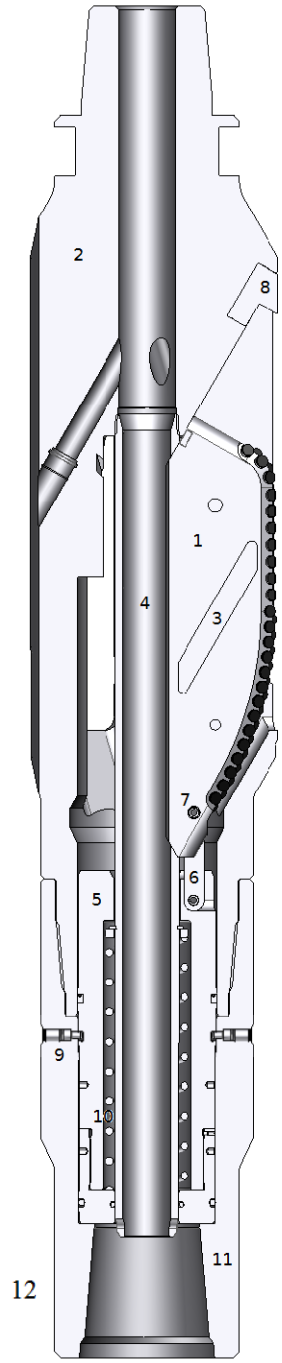

Figure 3.1: DRILLSTAR Z600H layout in section view.

3.2. Requirements and current specifications

To the design of the UR has to fulfil certain requirements to function properly down hole. These requirements need to be translated to engineering specifications for guiding the conceptual design process. The following design requirements are determined:

- *The UR must have a drill diameter of 9 inch (228.6 mm) or more.*
- *The UR can have a maximum body diameter of 5 7/8 inch (149.225 mm).*
- *The length of the underreamer should be as short as possible and be no longer than 750 mm.*
- *The current design of DRILLSTAR will serve as a base-case and the specifications of the base-case determine the minimal requirements for the new concept design.*
- *The reamer blades have to move outwards under the influence of mud pressure.*
- *The reamer blades have to retract by using one or more springs.*

It is desired that the new design out performs the current base-case design. To compare these designs, the characteristics of the base case design must be known. The most important specifications and parameters of the base case design are summarized in table 3.1.

Table 3.1: Product Data Sheet Hydraulic Reamer 600.[12]

Specification		
Max. body OD (hardfaced)	5 ¾“	146 mm
Shoulder to shoulder length (A)	32“	813 mm
Bit to blade length (B)	20,7”	525 mm
Blade length (C)	7,7”	195 mm
Approx. Weight	170 lbs	77 kg
Top thread	3 ½” API REG Pin	-
Top shank OD	4 ¾”	121 mm
Bottom thread	3 ½” API REG Box	-
Rec. m/u torque 3 ½” REG	Min 10.000 ft-lbs Max 11.500 ft-lbs	13.558 N·m 15.592 N·m
Rec. m/u torque 4 ¼” XHTDI	13.500 ft-lbs	18.300 N·m
Min. ID (operating)	1.1”	28 mm
Operating Parameters		
Min. pilot hole size	5 7/8”	149 mm
Opening range	6 ¼” – 8 ½”	159-216 mm
Collapsed diameter	5 ¾”	146 mm
Max flow rate	450 GPM	1.700 lpm
Min. operating pressure	150 psi	10 bar
Max. operating pressure	725 1) psi	50 1) bar
Max. WOB	14.300 2) lbs	6.5 2) mt
Max. torque	7000 3) lbs·ft	9.490 3) N·m
Max. operating temp (std. seals)	392 °F	300 °C
Base material	AISI 4145 H	-
Seal material	Viton 80 Shores	-
Shear value (for 1 shear pin)	101 – 116 psi	7 – 8 bars

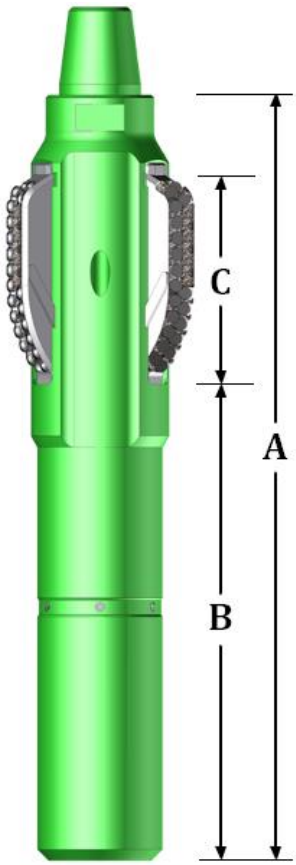

1) Recommended. Max. pressure can be increased if required. It is estimated that the piston seal system can take 150 bars before it starts leaking.
2) Based on full opening (8 ½”), blades provided with standard 13 mm cutters. Max. WOB will depend on the blade type: cutter size, cutter type, number of cutters etc.
3) Based on 8 ½” opening.

3.3. Telescopic blocks

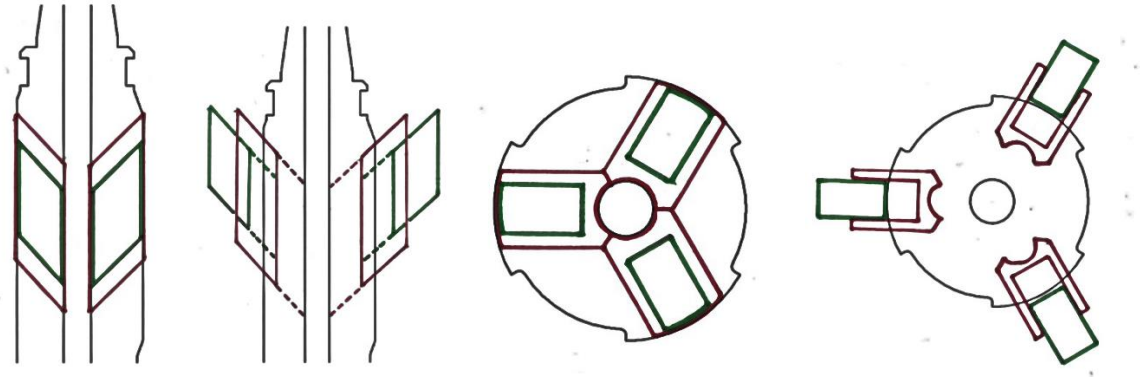

Figure 3.2: Telescopic blocks consisting of a shell (red) and inner block (green).

The first concept, shown in figures 3.2 and 3.3, involves a block-type underreamer consisting of three blocks, similar to the base-case design. A single channel to allow for the passing of mud is located in centre of the underreamer structure. The blades are concentric with respect to the centre of this flow channel. They will move upwards when sliding out. Each individual blade consist of two parts:

- The outer shell that can move partially out of the underreamer structure.
- The inner block that will move partially out of the shell.

This design allows for an extended reach of the blades without the need for extra storage space. Besides, the underreamer is in this way also capable to ream on more than one diameter. The shell could be extended from the underreamer structure with the inner blade still in place, which is useful for drilling out concrete at transition sections between the casings.

However, designs that involve a sliding mechanism are prone to clogging, as is known from practice. Extending the sliding range will therefore have adverse effects on the reliability of the device. The design expert at Huisman is also concerned about the presence of a large couple moment at the block-shell interface. This will not only require high strength requirements of the materials used but also gives problems when retracting the block and shell back into the main structure.

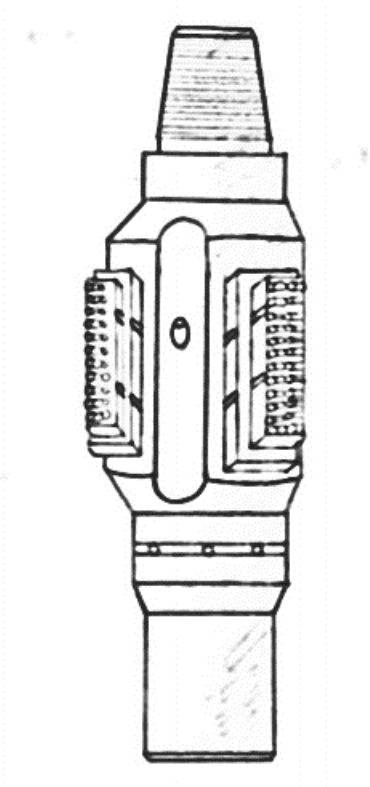

Figure 3.3: Side-view with blocks extended.

3.4. Vertical sliding blocks

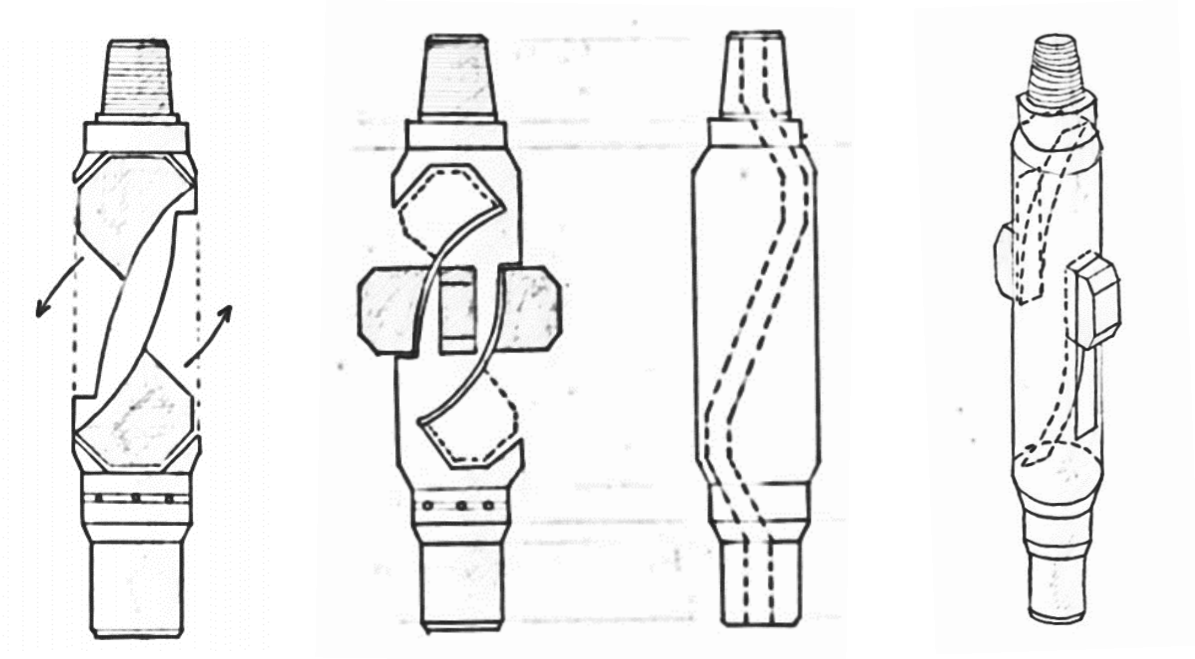

Figure 3.4: Vertical sliding blocks.

The second concept (figure 3.4) provides a potential solution in which the blocks are 'stored' not horizontally, but vertically inside the underreamer column. The sketch shows the case for which two blades almost fully occupy the space above and under the third blade, which slides out horizontally, as can be seen in the sketch (2nd left).

Storing the blades in this way might significantly increase the diameter that can be reached. There will also be enough room for the third blade pass the centre of the underreamer column, as there are no other blades obstructing its path. The mudflow will in this case enter the underreamer to the right of the upper blade and exit it via a channel that passes the lower blade on the left (2nd right sketch).

As these sketches are not very detailed yet, many questions remain. Due to the vertical storage of the blades, the height of the underreamer will increase. This is not desirable when looking at steer-ability of the drill. Because the underreamer opens by sliding the two vertically stored blades all the way to their drilling position, large slots are required in the main structure of the underreamer. This will reduce the ability to transmit a certain amount of torque to the bit. The large opening might also be susceptible to clogging.

Since the upper blade in the sketch in the left opens by sliding downwards in the drilling direction, retracting it might also become more difficult, while it is not pushed back into the reamer by the lower side of the casing while retracting the UR. By only relying on a spring only, the reliability of the design is severely affected. The underreamer might become stuck in the borehole since the blade will remain in the open position.

3.5. Diaphragm mechanism

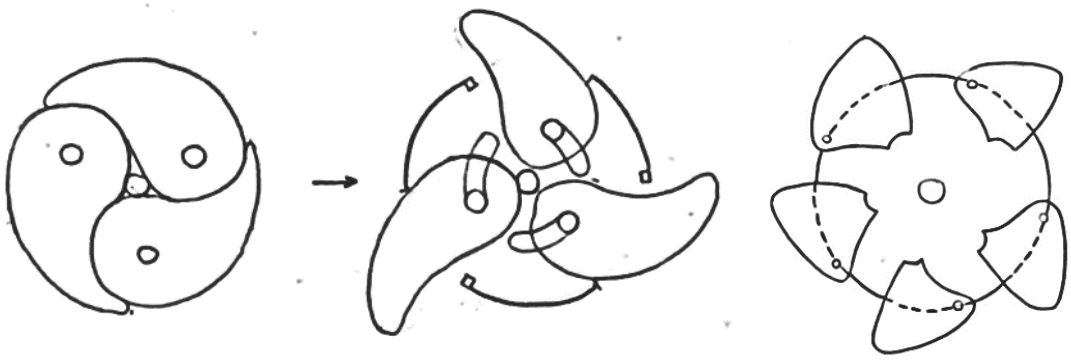

Figure 3.5: Diaphragm mechanism. Left and middle: three-bladed design. Right: five-bladed design.

This concept involves the use of blades that are 'folded' together around the centre of the underreamer. When deployed, the blades turn outward and slide sideward by the use of a slot. Whether the pins are connected to the blades or a disk beneath the blades is not determined at this stage. It is clear that the mechanism allows for both a (small) translation and rotation of the blades.

The concept (figure 3.5) shows a holding pin to guide the vanes or lobes outward and keep them into place. Instead, the blades might also be hold into place by parts of the core structure at the broad side of the lobes, once they are in the extended position. The sketch to the left shows however that there is little room for holding pins as well as for the remaining part of the core structure of the underreamer. The passage of mud might also be difficult as the blades occupy a large part of the internal cross-sectional area. In the sketch, the only possible route would be through the centre of the underreamer.

The right most sketch shows the use of multiple blades. This could be beneficial in terms of vibrations. The blade length for the individual blades will however decrease and more components are present, which means more maintenance and a higher probability of failure of the underreamer as a whole. These smaller blades are now also subject to a relatively high load, which could deform the blades or push them out of the slots.

The combined translational and rotational motion might be problematic in practice. A rotational spring would have to be used to fully retract the lobes into the main underreamer structure. The concept, as is presented here, is as far as currently known not used in an actual underreamer. Either the rotation motion or translational motion needs to be eliminated in order to make the design more feasible.

3.6. Eccentric blade configuration

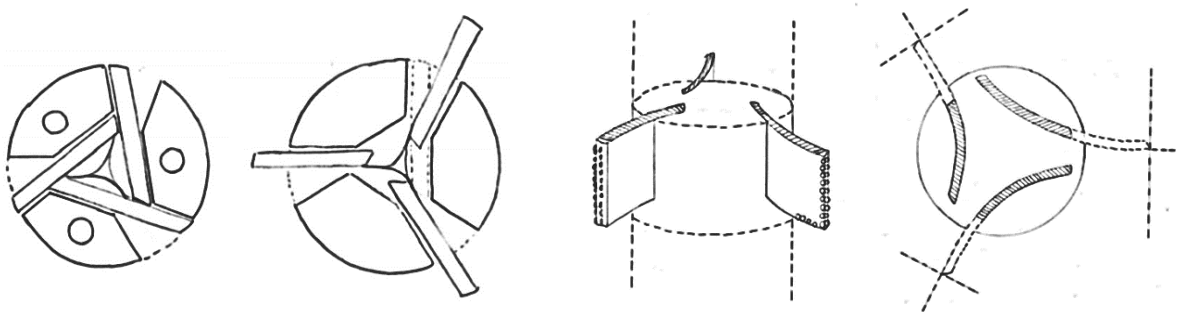

Figure 3.6: Eccentric blade interfaces. Left: straight blocks. Right: curved blocks.

This concept (figure 3.6) exhibits the idea of shifting the blade slots internally. The cross sections show a rotational symmetric concept where the sketches appears to be the same when rotated by one third of a full rotation. The blades do not 'meet' in the centre but they are directed slightly sideways, in order to increase the blade length. The left sketch shows a moderate solution in which the blades are shifted from the middle to about a half of the radius (where one blade end meets the other blade halfway). Going to the full radius would result in a full triangular arrangement.

The left sketch also shows that there might not be enough room for a centralized mud channel. In this case, the mud flow is split in three channels, which pass the underreamer along the sides of the blades. The combined cross-sectional area of the mud channels will be bigger than the cross-sectional area of a single channel because of the Bingham plastic material properties of the bentonite suspension that has to flow thru it.

The right sketch shows that the blades might be extended from the underreamer by sliding them around the centre. This could be a way to position the blades perpendicular to the underreamer wall. Whether a perpendicular interaction is necessary depends upon the (instantaneous) turning direction. The blades might be more shock resistant in certain orientations. Since this design also involves a simultaneous rotation and translation, eliminating one of these motions can improve the feasibility of this concept.

Because a blade rotation requires a bigger slot in the side of the underreamer, the option to rotate could be disabled. The couple moment that has to counter-act the moment from drilling has to be compensated. It can be seen that the blades cannot be properly locked into place, if a gap is still present. One solution could be the use of curved blades (right and 2nd right). These are however difficult and expensive to machine and might not slide very smooth.

3.7. Multi-disk blades

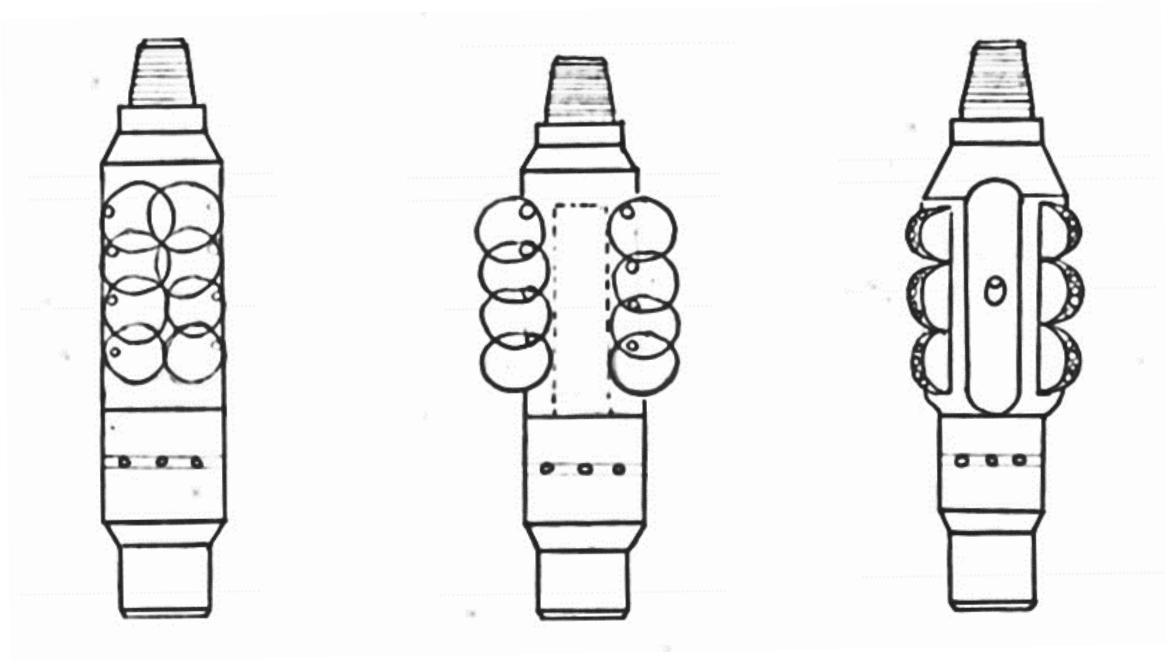

Figure 3.7: Multi-disk blades.

Instead of using a single blade on each side, one may also use multiple blades (figure 3.7). Circular disk are vertically stacked under and above each other. The disks do overlap internally, so they can slide over each other. To push the disks outward, a single cylinder within the core of the underreamer could be used. It may be a cylinder, which is pushed down all the way, but it can also involve a notched cylinder. At this stage, the extension mechanism itself is not considered in detail but it might be difficult to use a central rod anyway when there is not enough space in the centre of the underreamer.

The sketch to the right gives the idea that three columns of disk are present, but that is not the case. No solution has been found at this moment to make more than two columns of cylinders overlap in the middle. One of the biggest concerns with this concept however, is that the amount of moveable parts is relatively large. The disks might also be unable to handle peak loads since they are in no way connected with each other. The connection of the disks to the main underreamer structure is also a topic of discussion, since the pins might become too small to handle the large loads. The disks could deform or even break off.

3.8. Blocks with finger joints

As a variation on the concept in chapter 3.6, another concept has been conceived to serve as a potential solution to the intersection problem. Instead of using off-centred blades, it is also possible to slide the parts together by using finger or box joints (figure 3.8). Since the blade is still in one piece, in contrast to concept 4, its capability to handle large loads will be better. The blade might be just long enough to reach a few millimetres further, which is beneficial in terms of the reduction of the dynamic pressure. The concept could also be adjusted a bit to allow the finger joints to extend beyond the centre, resulting in even longer blades.

In this early stage, the exact location of the mud channel has not been determined yet, because it is closely related to the location of the opening mechanism. A bottom piston or cylinder can be used in case the finger joints slide over each other smoothly.

In the sketch, the blades are assumed to move horizontally. However, the use of blades that slide upwards is preferred, because when the underreamer repeatedly bumps onto the wall of the well, the blades can be forced to close during retrieval of the BHA.

Upward moving blades can make the concept more complicated. At least two guiding rails need to be along the blocks to ensure a smooth motion and prevent oblique angles between the blades. This should prevent the 'fingers' and blades from getting stuck.

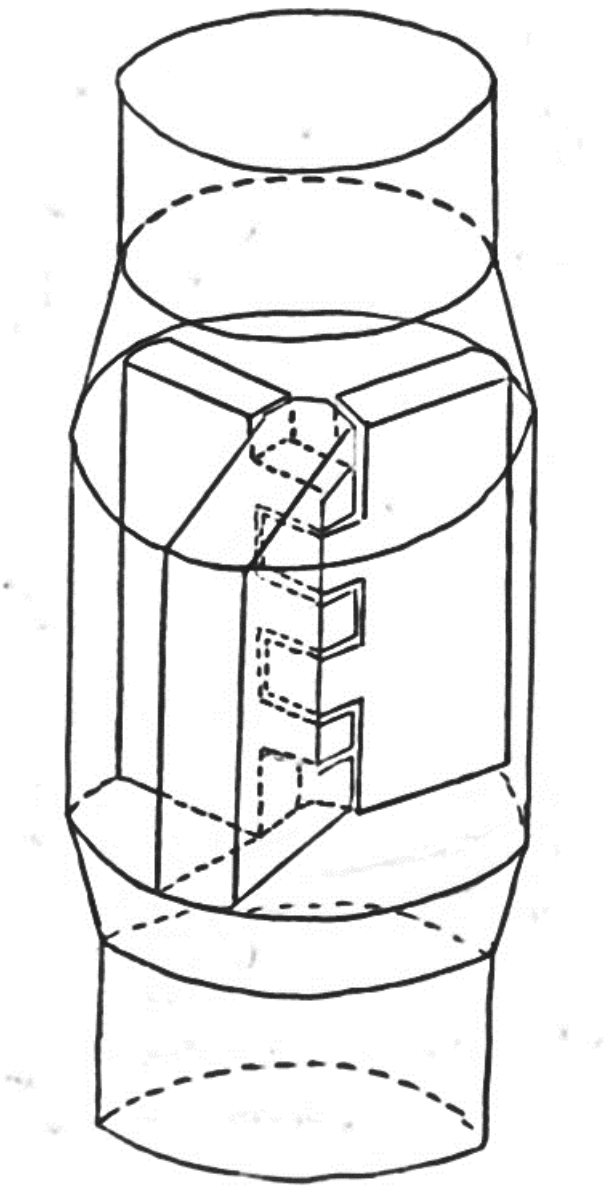

Figure 3.8: Blocks with finger joints.

3.9. Arrow shaped sliding grooves

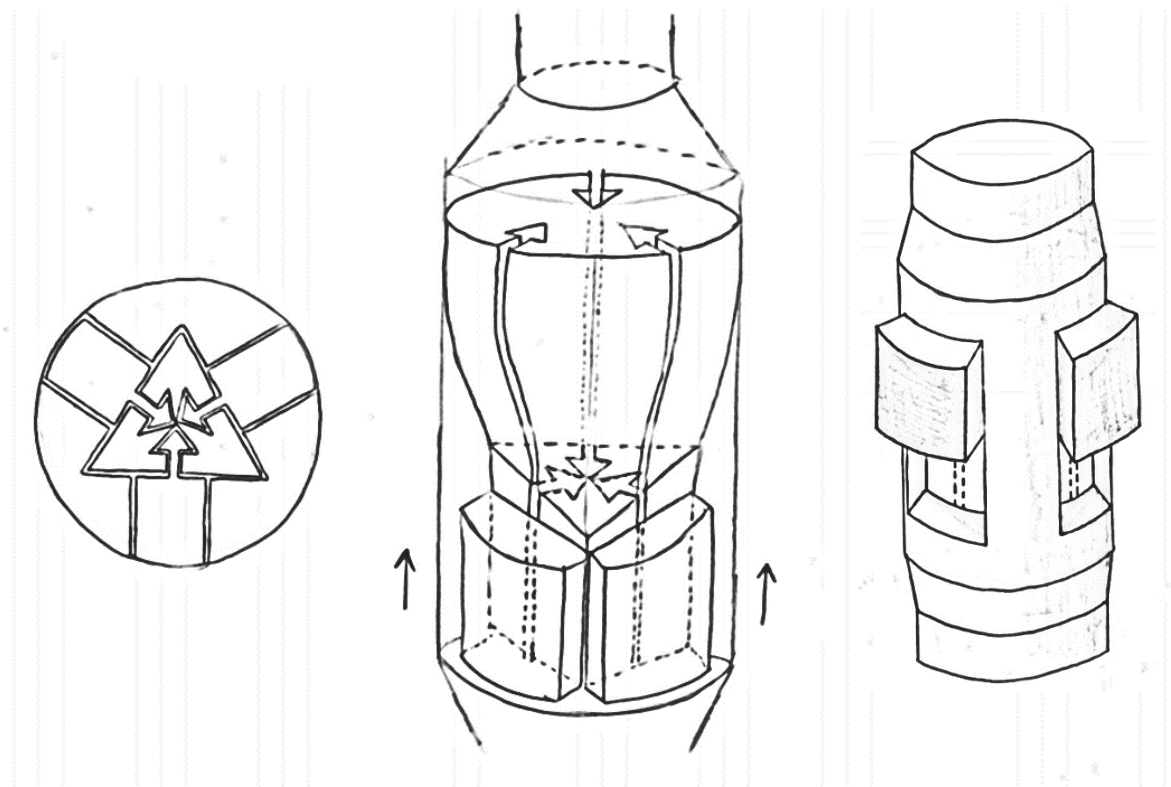

Figure 3.9: Arrow shaped sliding grooves.

The seventh concept, again, uses a slot as a rail for the blocks to move along. Three or more blocks can be inside of the underreamer along its circumference (figure 3.9). By means of a dovetail connection, the blocks are connected to the core structure of the underreamer. This core structure expands outwards to the wall for increasing height. The triangle will become a circle that is somewhat smaller than the outer diameter of the underreamer. The blocks will be in contact with the surface behind it at all times.

From practice, it is known that a similar experimental design that has already been build, does not work properly. The combination of sliding and moving outward simultaneously is the most probable cause for this. The rail must be quite steep to reduce the length of the underreamer as much as possible. Besides, the empty space left by the blocks, as can be seen in the right sketch, can be clogged preventing the blades from sliding back to their original position.

3.10. Multimember extendable arms

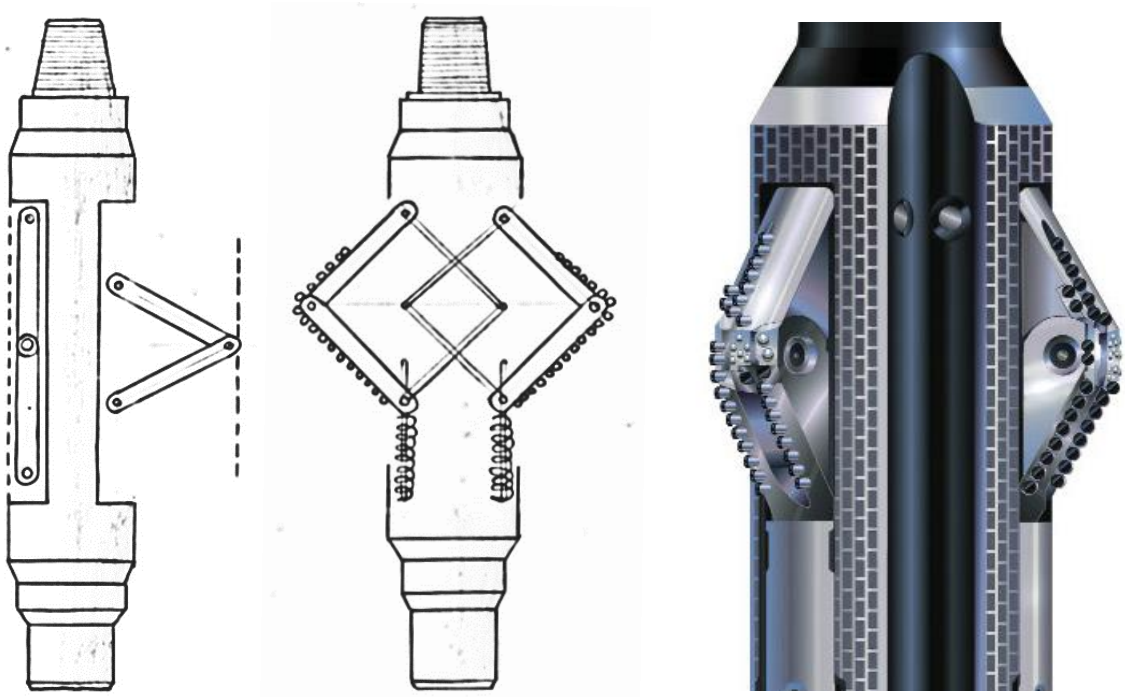

Figure 3.10: Multimember extendable arms (XR™ Reamer Hole Enlargement Tool – Halliburton, 2016).

This concept resembles the concept of an x-type underreamer, where the blades fold out like arms (figure 3.10). However, instead of using one single member at each side, two members are connected to each other to increase the cutting surface area. The concept as drawn here consists of two sets of arms.

To move the arms outwards, a scissor like mechanism can be used to pull the arms together. This mechanism will however contain a lot of joints and moving parts, which is not preferred. Instead of using this mechanism, one could also devise a concept in which upper and lower joints of the arms are pushed towards each other by means of a disk connected to them. This can make it possible to add more arms.

This concept seems to have nice capabilities but the arms are relatively fragile and might not be capable to handle large lateral loads. To reduce the lateral loads, a large stabilizing structure will have to be included into the design. The arms are drawn very thin, but for a sufficient strong design, they would need to be much thicker. Storing these along the length of the underreamer could also be problematic because of the long slots that are needed for storing the arms in their retracted position.

3.11. Concept selection

Based on the working principles of the concepts in the previous sections, factors that determine the overall functionality of the design have been identified. These factors will be used as boundary conditions in an MCA the order the concepts according to their expected functionality. The boundary conditions are mentioned in table 3.2, along with a description.

Table 3.2: Boundary conditions.

Boundary condition	Description
Clogging and jamming	Clogging is caused by drill cuttings that accumulate in cavities of the underreamer. Deposits of these materials on the cutters will negatively influence the underreamer performance. Debris can cause the blocks to get stuck when they need to retracted. Jamming occurs when the motion of parts is inhibited due to excessive deformations.
Moving parts	The number of moving parts and the joints needed to connect them can have influence on the reliability of the underreamer. Chances of premature failure downhole will be higher and this will result in an increase of non-productive time (NPT).
Internal space	The blocks have be designed such that there is enough room available for the extension mechanism and the mud channel. Blocks that take up too much space at a particular horizontal cross-section will locally reduce the structural integrity of the core assembly.
Vibration/shock resistance	The number of cutter blades can have influence on the vibration resistance of the underreamer structure. The blades need to be tightly secured into place to prevent the blades from impacting on the along the contact surface with the core structure. A higher number of blades can reduce vibrations and increases the stability of the underreamer.
Wear resistance	The wear resistance in this context is related to the interaction surface between the blocks and borehole wall. Small contact areas of the cutter-blocks with the borehole wall increases the wear rate. High wear rates can cause the reamed hole to become slightly conical. This will impair the fluid flow along the annulus.
Hole enlargement	The increase in hole-enlargement is related to the maximum distance the blades can slide outwards. Some concepts have been devised in a way the extension distance is maximized, while other factor were not considered.
Complexity and cost	A complex or difficult to grasp concept can be difficult to explain and challenging to work with. Manufacturing parts that are curved or helical can be problematic and costly. Complex mechanisms might also be prone to jamming.
Range of applications	Some types of underreamers are more suitable for drilling in certain orientations (horizontal or vertical) or for drilling and under reaming simultaneously.

The boundary conditions are given a weighing factor. These weighing factors are determined by normalizing the factors to sum 1. Each factor is therefore divided by the sum of the factors. Each concept is also given a score, ranging between -2 and 2, for each boundary condition, to indicate to what extent the concept satisfies this condition relative to the base-case. The weighing factors and the scores for the boundary conditions are then multiplied and summed up for each concept, which results in a total score.

A high (positive) score means that the design has favourable characteristics. A low or negative score means the design is not suitable under certain conditions or is not able to perform an under reaming job at all. The most promising designs will be selected for further analysis. Weighing factors are given in table 3.3.

Table 3.3: Weighing factors.

	Clogging and jamming	Moving parts	Internal space	Vibration/shock resistance	Wear resistance	Hole enlargement	Complexity and cost	Range of applications	SUM	Weight factor
Clogging and jamming	-	1	1	1	1	0	1	1	6	0.21
Moving parts	0	-	1	0	0	0	0	1	2	0.07
Internal space	0	0	-	0	0	0	0	1	1	0.04
Vibration/shock resistance	0	1	1	-	0	0	1	1	4	0.14
Wear resistance	0	1	1	1	-	0	1	1	5	0.18
Hole enlargement	1	1	1	1	1	-	1	1	7	0.25
Complexity and cost	0	1	1	0	0	0	-	1	3	0.11
Range of applications	0	0	0	0	0	0	0	-	0	0

Since 'Range of applications' is at the bottom of the ranking (weighing factor 0), it is left out of the MCA. The MCA outcome is presented in table 3.4.

Table 3.4: MCA.

	Clogging and jamming	Moving parts	Internal space	Vibration/shock resistance	Wear resistance	Hole enlargement	Complexity and cost	Total score
Telescopic blocks	-1	-1	2	-1	-1	2	-1	**-0,13**
Vertical sliding blocks	-2	-1	-2	-1	1	1	0	-0,28
Diaphragm mechanism	-1	-1	-1	-2	0	2	-1	**-0,21**
Eccentric blade configuration	1	0	0	0	0	1	0	***0,46***
Multi-disk blades	-1	-2	-1	-2	-2	0	-1	-1,14
Blocks with finger joints	0	0	-1	0	0	1	-1	***0,1***
Arrow shaped sliding grooves	-2	-1	-2	-1	1	0	-2	-0,75
Multimember extendable arms	-2	-2	-2	-2	-2	2	-1	-0,89

From the MCA, it can be seen that two designs have a positive or favourable outcome. The two concept with a slightly negative outcome might still work for certain applications or under certain operating conditions. This is why the four best concepts will be considered in the next phase. Drawings to scale and basic hand calculations are being made to check their feasibility further. Later on, one of these four concepts will then be selected for the detailed design phase.

4. Basic concept analysis

This chapter is concerned with the second phase of the design process. The second design phase involves analysing the remaining concept ideas by doing calculations and making drawings. Whenever possible they are compared to existing designs.

4.1. Reference framework

To describe the selected concepts in more detail, a reference framework will be developed that allows for an accurate comparison of the concepts. A drawing of the base-case is used to scale diameters from their dimension in the drawing to their real full sized dimension. The drawing is shown in figure 4.1. The scaled dimensions are presented in table 4.1.

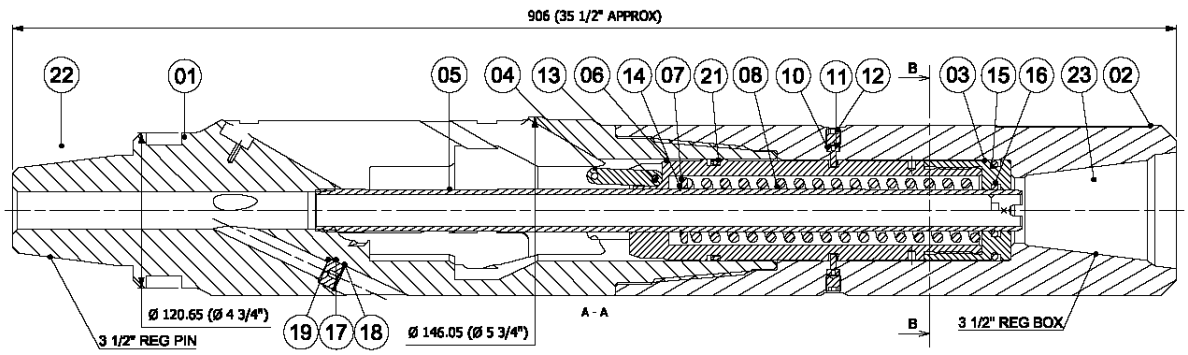

Figure 4.1: Section view of the base-case including dimensions.[13]

Table 4.1: Base – case dimensions.

Element	Actual size (mm)	Actual size (in.)
Main body collar diameter	120.65 mm	4 3/4"
Mud channel ID (main body)	29.1 mm	1.15 in.
Mud channel ID (tubular section)	23.28 mm	0.92 in.
Mud channel OD (tubular section)	34.92 mm	1.37 in.
'Marquage' depth	5.82 mm	0.23 in.
Diameter spring housing	78.57 mm	3.093 in.

After the base-case dimensions are determined, a simplified drawing (figure 4.2) of the well architecture is constructed that contains the external diameters of some components that could be relevant for the assessment of the concepts. The sizes are mentioned in table 4.2.

Table 4.2: Important reference dimensions.

Element	Size (mm)	Size (in)	Weight (lbs/ft)
Outer diameter previous casing (A)	244.5	9 5/8	47.00
Inner diameter previous casing (B)	220.5	8.681	
Casing coupling diameter (C)	203.2	8	-
Casing outer diameter (D)	177.8	7	35.00
Casing inner diameter (E)	152.5	6.004	
BHA component diameter (F)	120.7-139.7	4 ¾ - 5.5	-
UR DRILLSTAR ream diameter (G)	215.9	8.5	-
Drill bit diameter (H)	149.2	5 7/8	-

A table with characteristics of standard API casing joints can be found in appendix C.

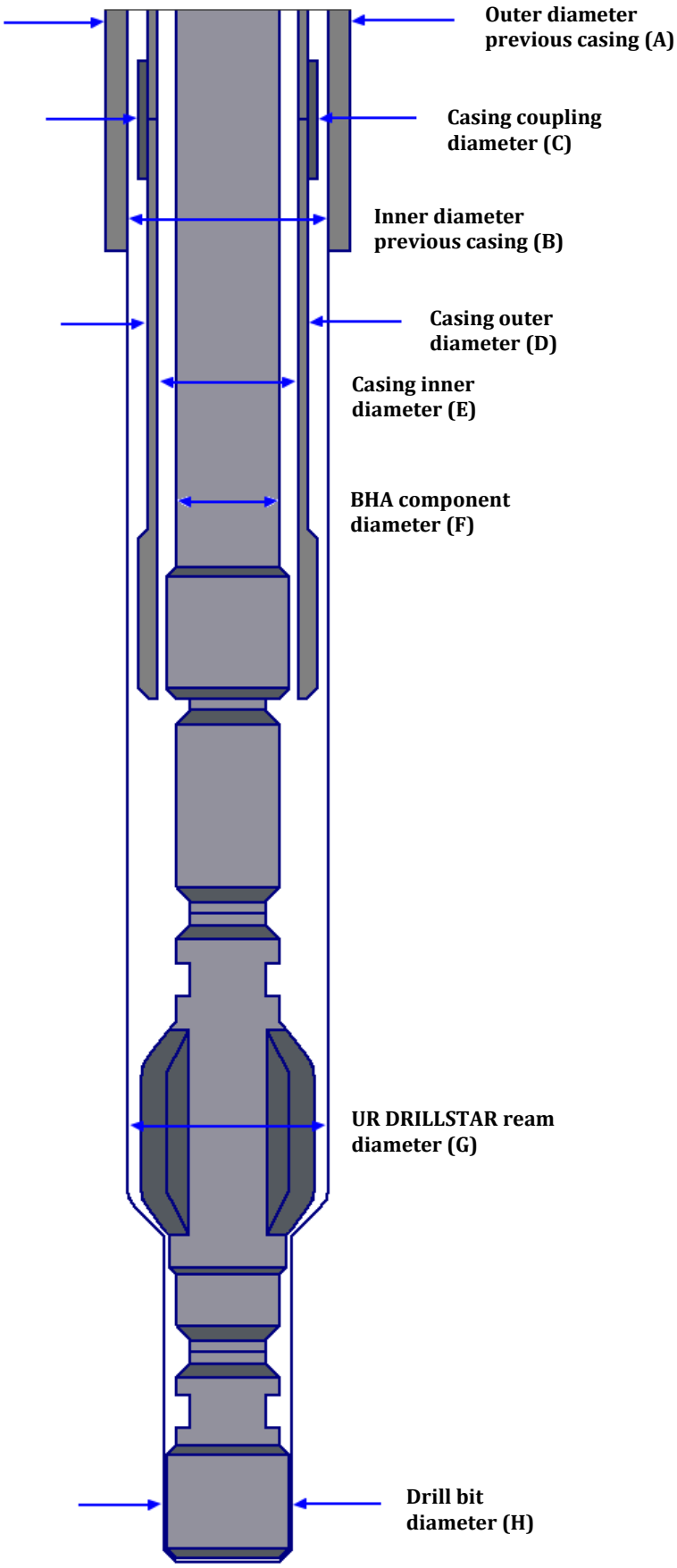

Figure 4.2: Diameters of string elements.

4.2. Telescopic blocks

In this section, the concept idea as discussed in section 3.3 will be worked out in more detail.

4.2.1. Overview

As discussed previously, the concept resembles the base case where the blades are concentric with respect to the centre of the flow channel, and will move upwards when sliding out. Each individual blade consist of two parts:

- The outer shell that can move partially out of the underreamer structure.
- The inner block that will move partially out of the shell.

Some parts that have to be redesigned are involved with the way the blocks are stopped inside the underreamer and the shell. On top, a tongue-groove fitting has to be implemented in between the shell and inner block to ensure smooth sliding and prevent the mechanism from jamming. Lastly, the pin(s) that extend(s) the blocks have to be fitted, as both of the blocks need to be pulled back by a spring mechanism.

4.2.2. Basic design

A mechanism is drawn in *Inventor* that shows how both blocks could be extended with one coupling rod. The rod has three pins. The middle pin connects to the shell while the top pin can be fitted in the inner block. A model of the block is shown in figure 4.3.

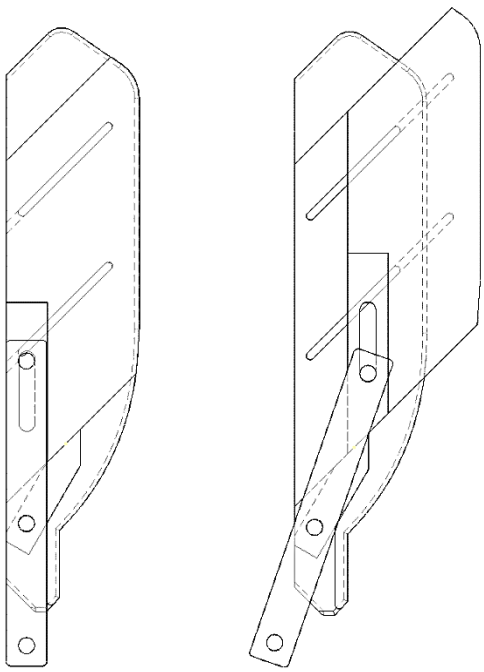

Figure 4.3: Coupling rod that connects to the inner and outer block with pins.

It can be seen that the coupling rod now has to make a stroke that reaches inside the outer blade. Some material has to be removed for this reason, which results in a fragile outer block. On top, the coupling rod can not reach a horizontal oriëntation because this would mean it would stick through the shell completely. This means that the outer block will not be able to reach as far outward as the blocks in the base-case.

Because the inner block can only move in one direction, a pure pin connection will not work, since the pin does not make a semi-circular motion. Therefore slots have to be added to the inner block (or coupling rod) to make it possible for the inner block to slide out.

Subsequently the tongue-groove sliding connections between the blades have to be designed. During extension and retraction of the blades, they should prevent or reduce the effect of tilting. Determining the location and the number of grooves on each side of each blade may be difficult since adding the grooves or tongues will cause a local stress increase during operation. If the grooves are not positioned right, they may also interfere with the sliding pin mechanism, which makes the design even more fragile. An example of such a design flaw is shown in figure 4.4.

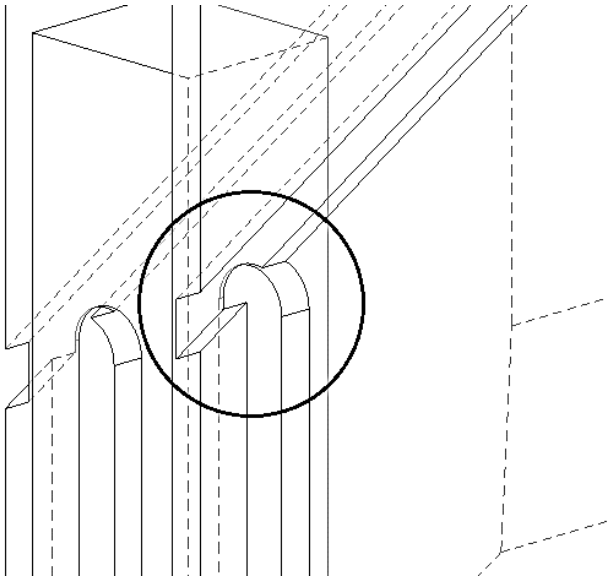

Figure 4.4: Groove overlap with slot.

Positioning the slots at the proper location, such that the blocks move out steadily requires watchmaker precision. A slight misfit will therefore cause stiff movement and possibly even jamming of the mechanism. Some views of the basic design are presented in figure 4.5.

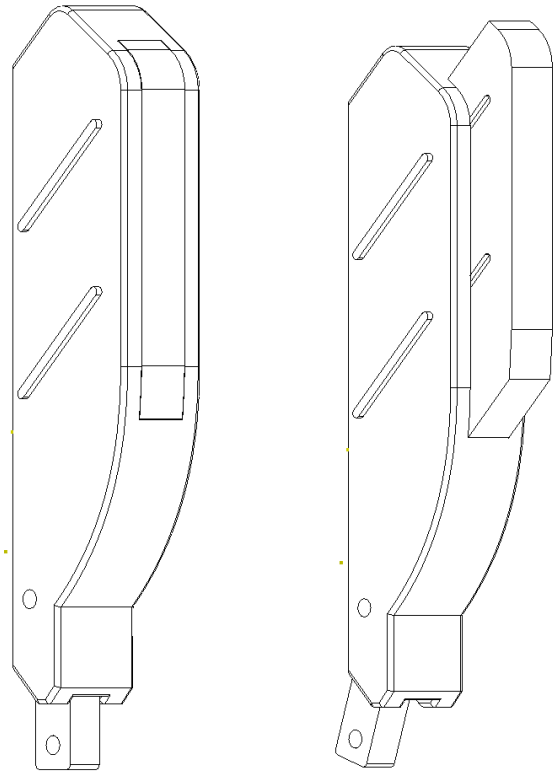

Figure 4.5: Views of the preliminary basic concept.

The blocks are put in a model of the underreamer, shown in figure 4.6. A top view of the assembly reveals that 228.6 mm or 9 inch should be easy to reach. The outermost circle indicates the maximum drill diameter, which is about equal to 280 mm or about 11 inch.

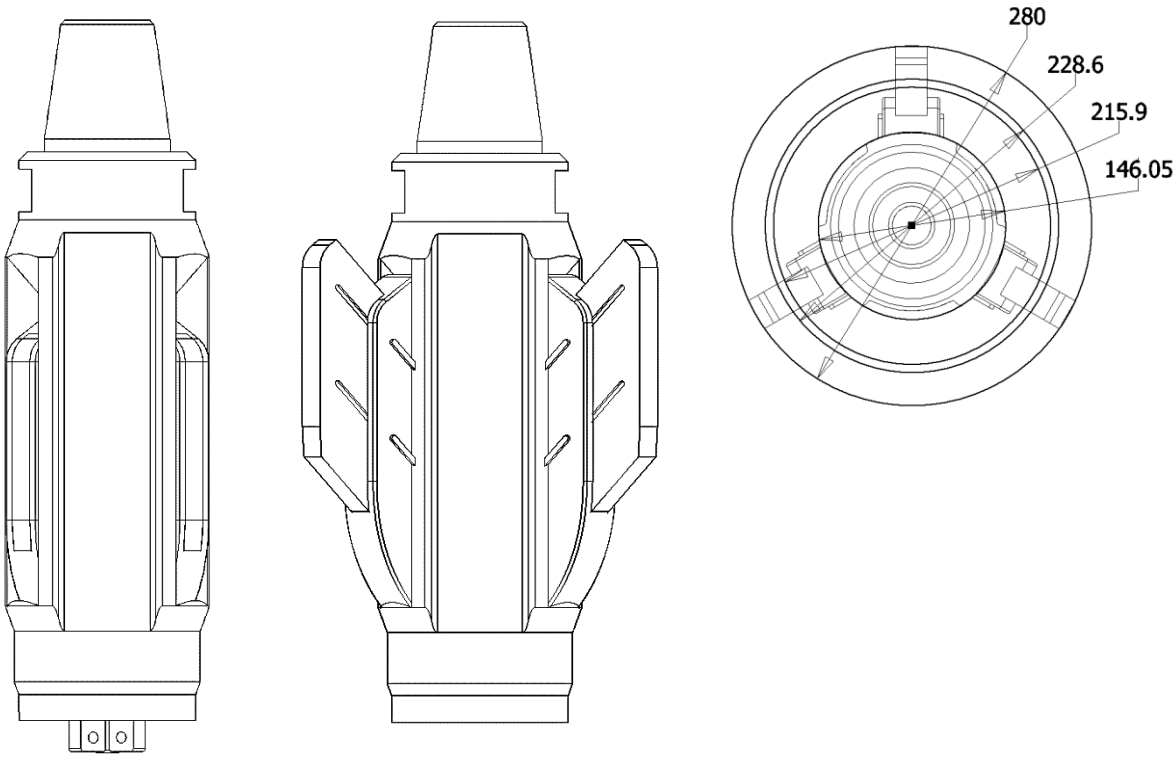

Figure 4.6: Telescopic concept with extended blocks including dimensions in mm.

4.2.3. Challenges

The basic design of this concept shows that there are some serious challenges. Since the design consists of various parts that are all less robust than their base-case counterparts are, the reliability of the design is severely affected. The presence of more cavities and slots also means that the design is more prone to clogging.

It is also likely that the design is more susceptible to the phenomenon of stick-slip while in operation. Since both inner and outer block have a certain tolerance on them for sliding, there will be more places where high accelerations occur and this results in more wear. The tolerances may also give difficulties with sliding out due to excessive deformations. Although the design appears favourable in terms of hole-enlargement, it seems that the advantages do not outweigh the disadvantages.

4.3. Diaphragm mechanism

In this section, the concept idea as discussed in section 3.5 will be worked out in more detail.

4.3.1. Overview

It was mentioned earlier that this concept involves the use of vanes or lobes that are 'folded' together around the centre of the underreamer. Instead of sliding outward, these vanes have to rotate around a vertical rod to extend them. They will be kept in place by either the rod or the core structure. A first sketch is made with the last idea in mind. A top view of an initial sketch is shown in figure 4.7.

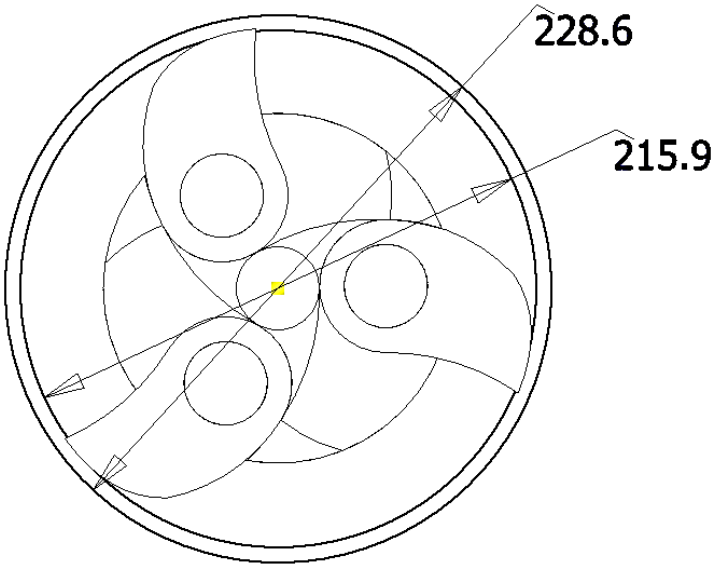

Figure 4.7: Diaphragm concept drawn in reference framework.

In the sketch, it can be seen that the vanes cannot reach the required 228.6 mm or 9-inch with their current shape, as they are too short. The vane extension length can be enlarged in three ways.

One way is the make the vanes rotate further so that the tip just reaches the 228.6 mm circle. Consequently, some core material has to be cut-out, which weakens the underreamer structure and leaves little room for the internal contact surface that needs to push against the blade to resist the external moment.

A second way is to make the vanes longer which will also have the negative effect of cutting away too much of the core material.

The third way to increase the drill diameter is by moving the vertical cylinder about which the vane rotates further outward. To do this, the width of the vanes must be decreased. The diameter of the vertical cylinder also has to be decreased so that the vane does not become too thin around the cylinder. An example of the first adaption in combination with the third adaption is shown in figure 4.8.

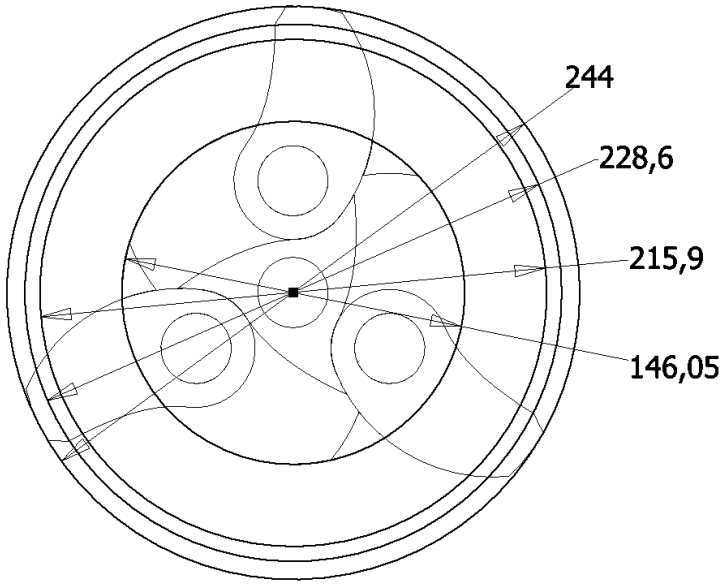

Figure 4.8: Vanes adjusted rotation angle and rotation axis (bottom view).

It can be seen from figure 4.8 that the vanes now reach and exceed the 9-inch target diameter. The core material left is however minimal but the external moment can be compensated in other ways. In figure 4.9, it can be seen that the vertical cylinders can be equipped with grooves. Ridges on the vanes enables them move around the vertical cylinder inside the groove.

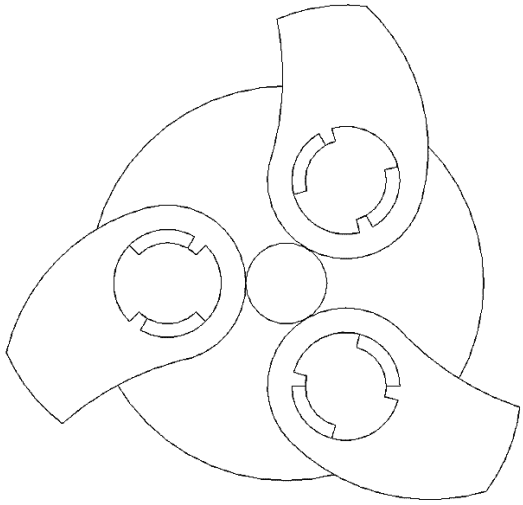

Figure 4.9: Groove-ridge connection (bottom view).

However, because the rotation is almost 180 degrees, the grooves run along most of the circumference of the vertical cylinders and the ridges on the vanes and cylinder become too small to transfer the torque.

4.3.2. Extension mechanism

At this moment, the opening mechanism is not yet considered. Opening blocks via a rotational motion requires another mechanism than for blocks that open by sliding in a straight line. A US company called the Harvest Tool Company, LLC, manufactured a reamer that works according to the same principle (Patent US 20100065264). It was designed to ream to diameters that are slightly larger than the original hole diameter. A picture of the device and its working principle is shown in figure 4.10.

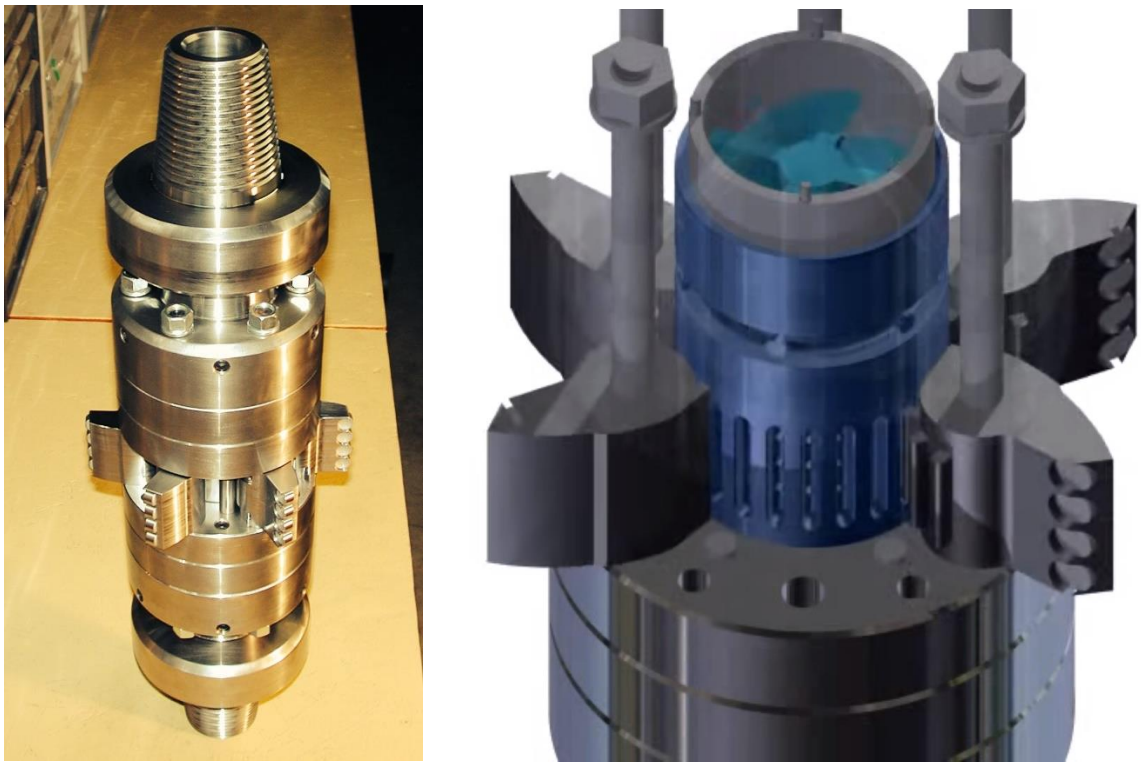

Figure 4.10: Rotor underreamer of the Harvest Tool Company, LLC.[14]

The design consists of multiple blades for better hole tracking and centralization. The blocks open by means of a rotor, located in the mud channel. The rotor is connected to a hollow cylinder with grooves on the outside. This cylinder hooks together with teeth on the blocks so that they can be opened when fluid flow through a central rotor assembly. The blades can return to their closed position by tension springs and wirelines attached from the blades to the rotor.

According to the patent description, debris holdup in the area where the blades need to retract to close is minimized by putting 'gap cylinder pins' close to the rotor. The pins are also used to make sure the vanes are not squeezed by the cylindrical plates from which the device consists of. It can be questioned however if using springs only as a way to retract the blades is sufficiently reliable. The rotor assembly also seems quite large, leaving little room for larger vanes.

4.3.3. Torsional stick-slip

Another phenomenon that plays a significant role is stick-slip, see figure 4.11. Like for the telescopic concept, the blades might be vulnerable to the varying load conditions. At some moment in time, the blocks become stationary with respect to the borehole. Depending on the length of the 'stuck period', a certain amount of energy accumulates, which is released when the blocks break free. This causes rotational accelerations to occur, resulting in a high momentary RPM of the drillstring. These frequent fluctuations also cause more fatigue and damage to the blocks.

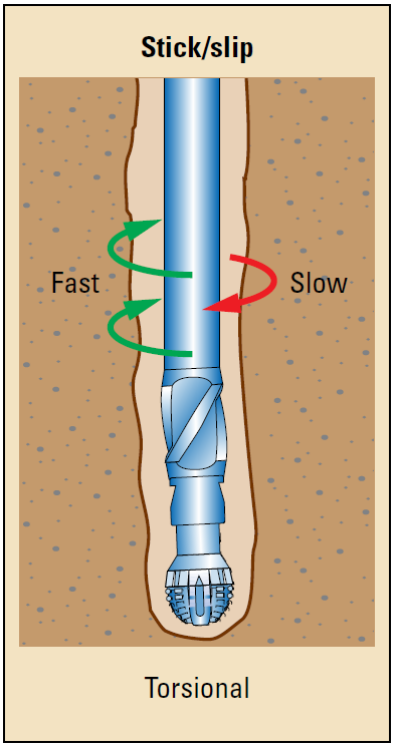

Figure 4.11: Stick-slip phenomenon.[15]

A design that is more susceptible to stick-slip might also have lower ROP, due to the energy that is consumed by additional wall friction. The stick-slip phenomenon is fairly common and does not depend on blade geometry alone. It may be reduced by the use of a mud motor, if the bit is the main origin of the excitation, but it is not entirely prevented. Another factor that influences the severity of stick-slip is well orientation. The torsional vibration mode is often observed in deep and high angle wells. Other aspects that are known to initiate stick-slip include the use of PDC bits with a high WOB, often in combination with hard formation rock.

Since the design idea that is proposed above it likely to have a low torsional stiffness, the vibration dampening might be less than that of the base-case. If the vibrations are not dampened enough, the torsional vibration mode can be clearly distinguished at the surface as large torque variations can be measured. In conclusion, it can be said that concentric rotational design, which involves blades that are not fully constraint in a slot of some sort, is likely to fail downhole due to stick-slip.

4.3.4. Challenges

At first glance, the arrangement of the components inside the underreamer looks quite 'exotic' and may be difficult and costly to manufacture. The underreamer blades will also suffer from severe (torsional) vibration problems, since the vanes are not constraint at one side in the extended position. This poses strict limits on the use of this concept.

4.4. Eccentric blade configuration

In this section, the concept idea as discussed in section 3.6 will be worked out in more detail.

4.4.1. Overview

This concept exhibits the idea of moving the location the blade slots internally. The cross sectional views, presented in figure 4.12 A, B and C, show a rotational symmetric concept where the drawings appears to be the same when rotated by one third of a full rotation. The blades do not 'meet' in the centre and they are directed (slightly) sideways, in order to increase the blade length. Figure 4.12 B shows a moderate solution in which the blades are slightly shifted from the middle, so that the end of the blade partially surrounds the mud channel and partially contacts a neighbouring block. By keeping in mind the need for an opening mechanism and the presence of the mud channel, this concept seems to be the most feasible. Several calculations will be done to show how the concept performs.

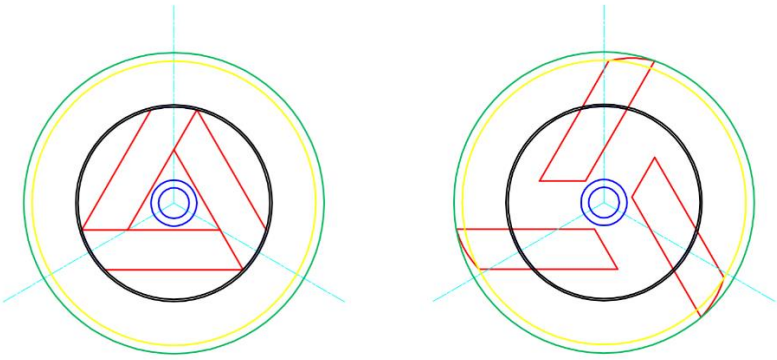

Figure 4.12 A: Full eccentric (triangular) configuration.

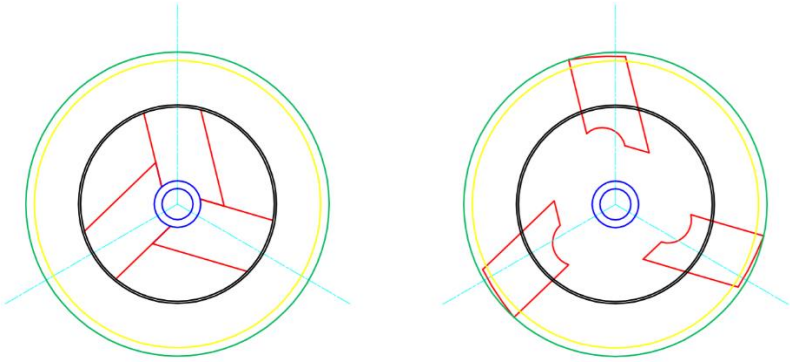

Figure 4.12 B: Partial circumjacent configuration.

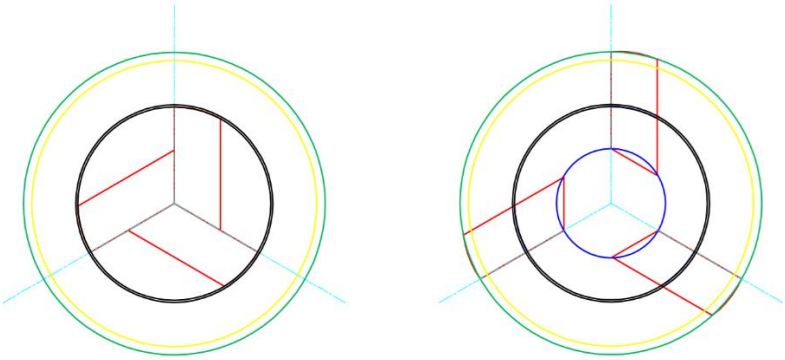

Figure 4.12 C: Full adjacent configuration.

4.4.2. Internal reaction forces

The torque that is applied to the drillstring by the top drive is counteracted by a reaction torque. This reaction torque is the result of cutting forces at the bit and UR and friction forces along the remaining part of the drillstring. Due to stick-slip, a distinction is made between the nominal and maximum torque load. There might also be some clearance between some of the blades of the UR and the borehole at certain moments in time. The torque can only be transmitted through the blocks that are in contact with the formation rock.

For the analysis, a reference framework will be created for proper analysis of the geometry that is shown in figure 4.12 B. A drawing of the parametric model is shown in figure 4.13.

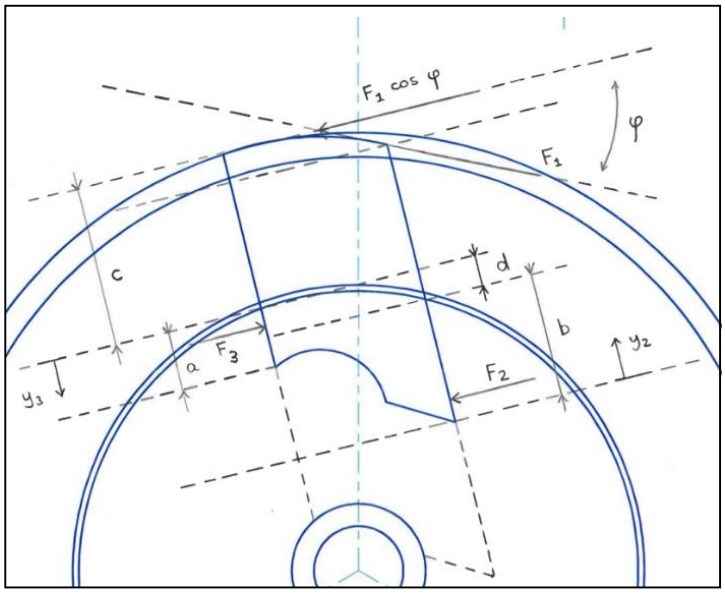

Figure 4.13: Parametric model.

The forces $\mathbf{F_1}$, $\mathbf{F_2}$ and $\mathbf{F_3}$ have to be in horizontal and moment equilibrium when doing a static equilibrium analysis. The location the forces along the sides of the blade with length **a** and **b** can be determined by choosing two variables $\mathbf{y_2}$ and $\mathbf{y_3}$. For these variables holds that $0 < \boldsymbol{y_2} < b$ and $0 < \boldsymbol{y_3} < a$. They are used to determine the location of the forces $\mathbf{F_2}$ and $\mathbf{F_3}$ and represent the line of contact between the block and the core of the UR. Angle $\boldsymbol{\varphi}$ is used to indicate the angle between the force that is applied on the line of action and a corresponding force that is directed perpendicular to the rotation direction of the block. For the torque equilibrium, the following equation holds:

$$M = n \cdot F_1 \cdot r \qquad [4.1]$$

Here **M** [kNm] represents the torque, F_1 [kN] represents the force that acts on the blade, **r** [m] indicates the radial distance and **n** is a parameter to indicate how many blades are in contact with the formation (n=1,2,3). For horizontal equilibrium, the next equation applies:

$$F_1 \cdot \cos\varphi + F_2 = F_3 \qquad [4.2]$$

$$\sigma_{\text{yield}} = \frac{F_2}{A_2} = \frac{F_2}{h \cdot y_2} = \frac{F_3}{A_3} = \frac{F_3}{h \cdot y_3} \qquad [4.3]$$

$$\rightarrow F_1 \cdot \cos\varphi + \sigma_{\text{yield}} \cdot h \cdot y_2 = \sigma_{\text{yield}} \cdot h \cdot y_3 \qquad [4.4]$$

Here **h** represents the height of the block. The only unknowns in this equation are y_2 and y_3, which will be determined to calculate the forces F_2 and F_3.

Taking the moment equilibrium around the point at which force F_1 is applied results in:

$$F_3 \cdot \left(c + \frac{1}{2}y_3\right) - F_2 \cdot \left(c + d + b + \frac{1}{2}y_2\right) = 0 \qquad [4.5]$$

$$\rightarrow \sigma_{\text{yield}} \cdot h \cdot y_3 \cdot \left(c + \frac{1}{2}y_3\right) - \sigma_{\text{yield}} \cdot h \cdot y_2 \cdot \left(c + d + b + \frac{1}{2}y_2\right) = 0 \qquad [4.6]$$

Equation 4.5 and 4.6 can now be solved as a system of linear equations. A table with the input and output for a numerical current model is shown in table 4.3:

Table 4.3: Input and output values for the current design.

Parameter	Input value	Unit
a	15.774	mm
b	33.126	mm
c	41.275	mm
d	7.84	mm
M	8	kN
$F_1 \cos \boldsymbol{\varphi}$	70	kN
h	0.25	m
$\boldsymbol{\sigma}_{\text{yield}}$	600	MPa
n	1	-
r	114.3	mm

Parameter	Output value	Unit
y_2	0.47	mm
y_3	0.94	mm
F_2	71	kN
F_3	141	kN

The results show that the length of the contact line (for the chosen yield strength) is small compared to the extension length of the block. It is from now on assumed that this contact length can be neglected and the forces F_2 and F_3 are assumed to work as point loads with their point of action at $y_2 = 0$ and $y_3 = 0$.

4.4.3. Normal stress analysis

To find the stresses due to bending of the blocks, the shear and moment lines are determined first. This is done by using a simple beam model by assuming a 'loose' fitting and high yield strength. The beam model as proposed in figure 4.14 is used for a basic analysis. The model presented here can be seen as a standalone model with its own parameters.

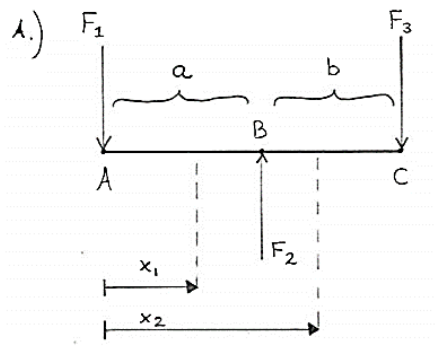

Figure 4.14: Beam model of the block.

The coordinates x_1 and x_2 are used to determine the shear and moment diagram. They are positive in the right direction and range between:

$$0 \leq x_1 \leq a \qquad [4.7]$$

$$a \leq x_2 \leq a + b \qquad [4.8]$$

These coordinates divide the length into segments that can be considered separately (figure 4.14 B, C). For the first segment $0 \leq x_1 \leq a$, the equilibrium in y-direction and the moment equilibrium are given by:

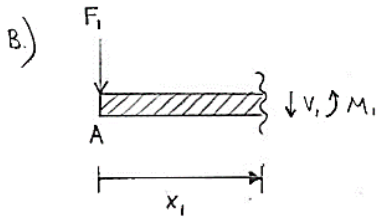

$$+\uparrow \Sigma Fy=0; \qquad [4.9]$$

$$-F_1 - V_1 = 0 \qquad [4.10]$$

$$\rightarrow V_1 = -F_1 \qquad [4.11]$$

$$+\circlearrowleft \Sigma M = 0; \qquad [4.12]$$

$$F_1 x_1 + M_1 = 0 \qquad [4.13]$$

$$\rightarrow M_1 = -F_1 x_1 \qquad [4.14]$$

For the second segment $a \leq x_2 \leq a + b$, the equilibrium in y-direction and the moment equilibrium are given by:

$$+\uparrow \Sigma F_y = 0; \qquad [4.15]$$

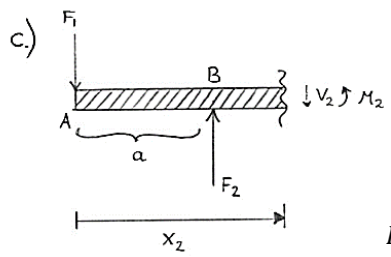

$$-F_1 + F_2 - V_2 = 0 \qquad [4.16]$$

$$\rightarrow V_2 = -F_1 + F_2 \; (= F_3) \qquad [4.17]$$

$$+\circlearrowleft \Sigma M = 0; \qquad [4.18]$$

$$F_1 x_2 - F_2(x_2 - a) + M_2 = 0 \qquad [4.19]$$

$$\rightarrow M_2 = -F_1 x_2 + F_2(x_2 - a) \qquad [4.20]$$

Subsequently the corresponding shear and moment diagrams can be drawn schematically (figure 4.15).

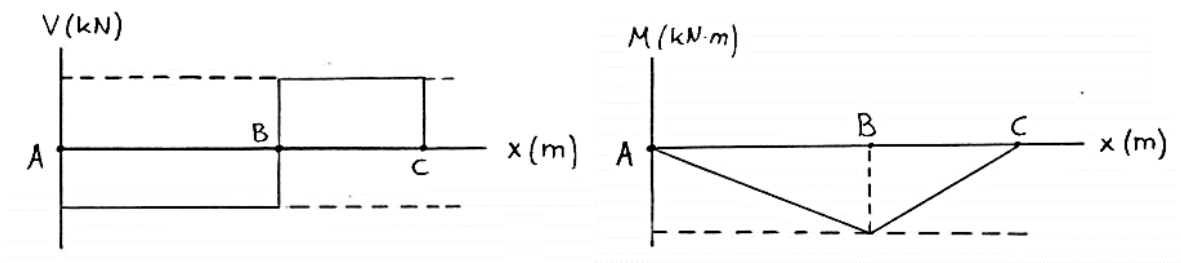

Figure 4.15: Shear (left) and moment (right) diagram.

From the diagrams, the maximum internal shear force and moment can be determined. For the shear force, $V_{max} = F_3$, and for the moment, $M_{max} = -F_1 a$.

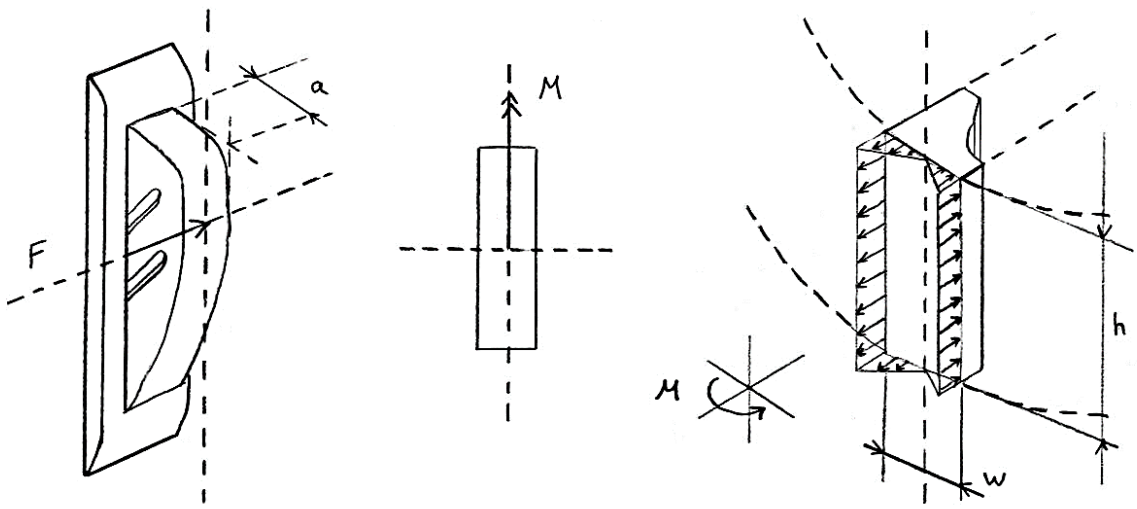

Figure 4.16: Bending stress at section B.

With the result from the previous analysis, the absolute maximum bending stress can now be determined. Some assumptions are required to simplify the model. The block is assumed to be homogeneous, symmetric, prismatic and the internal moment is directed in vertical direction (figure 4.16).

The maximum internal moment for the cross-section at point B was determined earlier to be:

$$M_{max} = -F \cdot a \qquad [4.21]$$

The moment of inertia of the cross-sectional section area about the vertical axis can be determined from:

$$I = \frac{1}{12} \cdot h \cdot w^3 \qquad [4.22]$$

The maximum normal stress in the block, which occurs at a point **c** on the cross-sectional area farthest away from the vertical axis, can be determined with the flexure formula:

$$\sigma = \frac{\mathrm{M} \cdot \mathrm{y}}{\mathrm{I}} \qquad [4.23]$$

Where, for the maximum normal stress, σ becomes σ_{max} if y = c.

By filling in the formulas for the internal moment and second moment of inertia, an equation for σ at cross section B can be written as:

$$\sigma_{abs,max} = \frac{F \cdot a}{\frac{1}{6} \cdot h \cdot w^2} \qquad [4.24]$$

By filling in the corresponding numerical values mentioned in first example and by assuming w = 45 mm, the absolute maximum normal stress becomes $\sigma_{abs,max} = \mathbf{34.24\ MPa}$. From the datasheet (appendix B), the yield strength for AISI 4145 steel is equal to 758 MPa (110 ksi). If a safety factor of '3' would be applied, then it is evident that the normal stress (34.24 MPa) caused by the bending moment around the vertical axis is much lower than allowed (253 MPa), so that the material only deforms elastically.

4.4.4. Block deformation analysis

To see if the contact points of the blocks will shift within the core structure, the elastic curve will be established. This curve represents the deflection of the longitudinal axis of the block that passes through the centroid of each of its cross-sections. For the problem that is discussed next, the flexural rigidity (EI) is assumed constant. A sketch of the model is shown in figure 4.17.

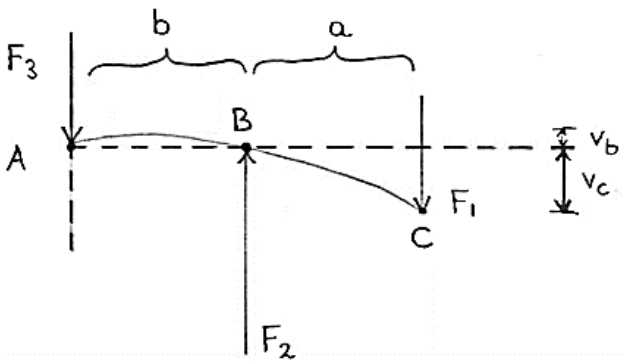

Figure 4.17: Schematic representation of the elastic curve.

If the deflection inside the UR would be too large, the contact points may move closer to each other. This has a negative effect on the magnitude of the forces. In the extreme case, it could be visualised as prying open the core structure. This is shown in figure 4.18.

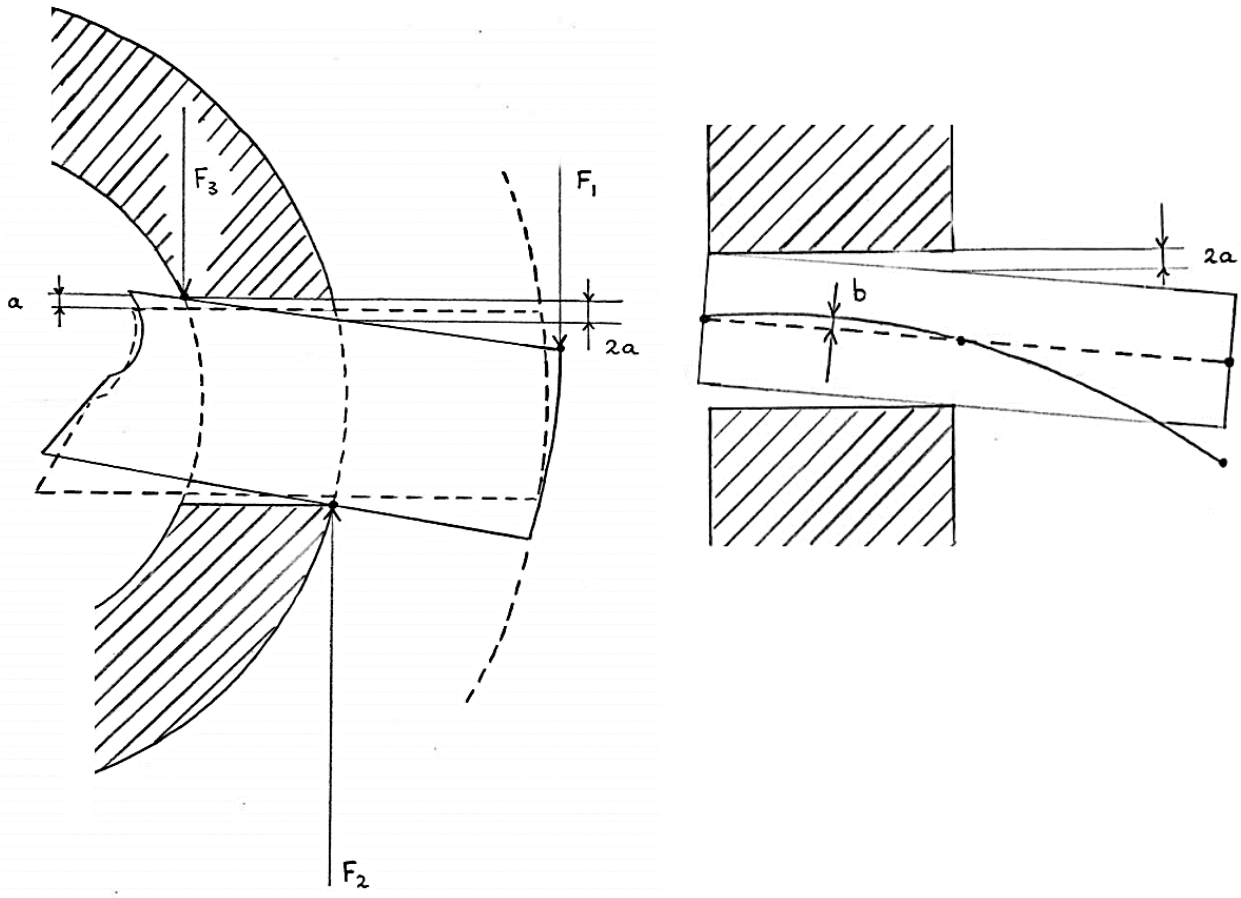

Figure 4.18: Tilting and clearance of the block in the UR core structure.

To determine the displacement **b** inside the core structure, the elastic curve has to be determined. This can be done by considering the free-body diagrams that are shown in figure 4.19.

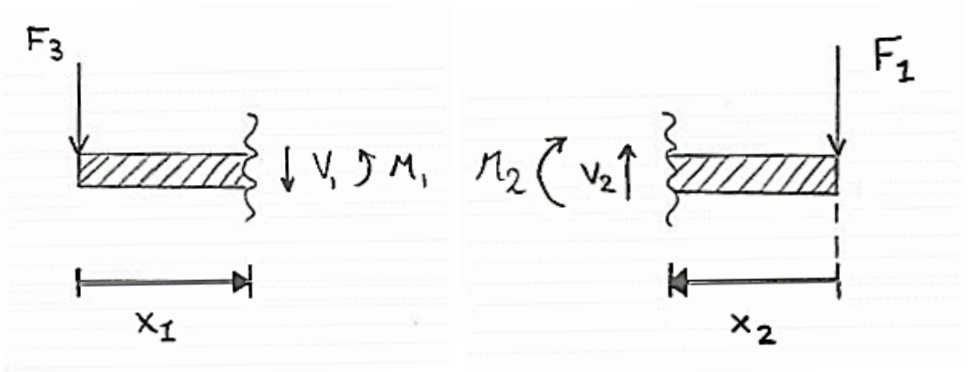

Figure 4.19: Free-body diagrams of the segments of the block.

By applying moment equilibrium, the moment function are determined:

$$M_1 = -F_3 x_1 \qquad [4.25]$$

$$M_2 = -F_1 x_2 \qquad [4.26]$$

To find the equations for the elastic curve, which is expressed mathematically as $v = f(x)$, the moment functions are equated to $EI = \frac{d^2v}{dx^2}$ .This simplification is valid because the assumption is made that deflections and therefore the slope of the elastic curve will be very small. This results in the following second order differential equations for both segments:

$$EI\frac{d^2v_1}{dx_1^2} = -F_3 x_1 \qquad [4.27]$$

$$EI\frac{d^2v_2}{dx_2^2} = -F_1 x_2 \qquad [4.28]$$

To acquire the solution in terms of v to these equations, successive integrations are required, which also result in four constants of integration that have to be determined. By assuming that the block is constrained by a pin connection at point A and a roller support at point B, the following boundary conditions and continuity condition can be used:

$$v_1 = 0 \; at \; x_1 = 0 \qquad [4.29]$$

$$v_1 = 0 \; at \; x_1 = b \qquad [4.30]$$

$$v_2 = 0 \; at \; x_2 = a \qquad [4.31]$$

$$\frac{dv_1}{dx_1} = -\frac{dv_2}{dx_2} \; at \; x_1 = b, x_2 = a \qquad [4.32]$$

By solving the above equations, the following constants are obtained:

$$C_1 = \frac{F_3}{6} b^3 \qquad [4.33]$$

$$C_2 = 0 \qquad [4.34]$$

$$C_3 = -\frac{F_3}{2} b^2 + \frac{F_3}{6} b^2 + \frac{F_1}{2} a^2 \qquad [4.35]$$

$$C_4 = \frac{F_1}{6} a^3 - C_3 a \qquad [4.36]$$

Constants C_1 and C_2 can filled in the equation of v_1 (obtained by the integration of the first differential equation). This results in:

$$v_1 = -\frac{F_3}{6EI} x^3 + \frac{C_1}{EI} x_1 + \frac{C_2}{EI} \qquad [4.37]$$

$$\rightarrow v_1 = -\frac{F_3}{6EI} x^3 + \frac{F_3}{6EI} b^2 x_1 \qquad [4.38]$$

$$\rightarrow v_1 = \frac{F_3 x_1}{6EI} (-x_1^2 + b^2) \qquad [4.39]$$

By solving $\frac{dv_1}{dx_1} = 0$, the location of the maximum deflection between can be found:

$$x_1 = b/\sqrt{3} \qquad [4.40]$$

Filling in this result in the equation (with E = 209 GPa) for v_1 results in a deflection of **0.03 mm**, which is negligible in comparison to the clearance (≈ 0.5 mm) at this location along the block. Jamming due to excessive deformations is therefore improbable to occur.

4.4.5. Core assembly deformation analysis

To assess whether stress in the core assembly would initiate yielding, a static structural analysis will be performed in Ansys Workbench. Because the UR is subjected to combined loadings, a finite element analysis is performed to see if the equivalent von Mises stress does not exceed to the yield stress of the material and to see if the core structure deformation will not the obstruction of moving parts inside the core. The blocks are located inside slots that typically have a clearance of 1 mm, so larger deformations are not desired at those locations.

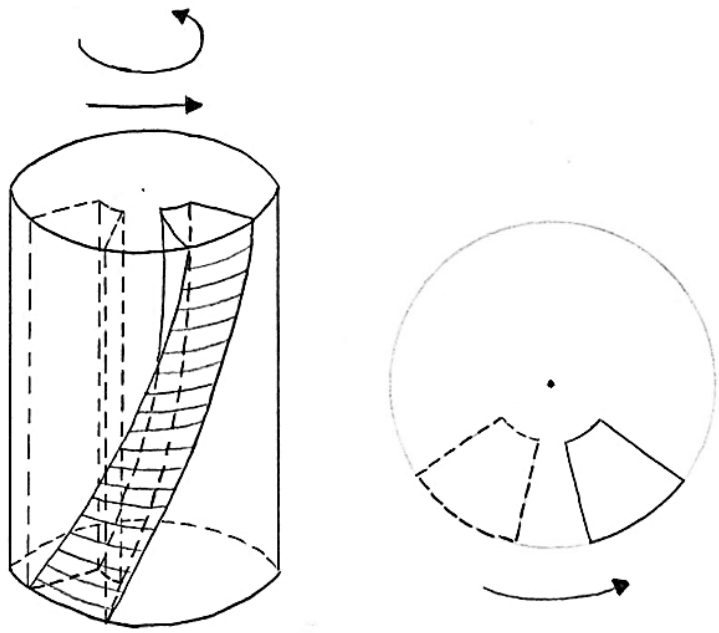

Figure 4.20: Exaggerated representation of the column deformation.

Because the blades inside the slots are free to move, the remaining columns have to transmit the torque. The top and bottom of each column are constraint by their connected with the rest of the core, applying torque does result in both bending and torsion. This is schematically shown in figure 4.20.

A load case in which the UR has to operate at nominal torque and WOB is considered. Values measured from measurement done with the Z600H from DRILLSTAR are mentioned in table 4.4. By assuming that the blocks are momentarily not in contact with the borehole, the counteracting torque is presumed to be generated completely by the contact of the bit with the formation below. In the Workbench model, this is implemented as a fixed constraint. Since the UR does not generate a counteracting moment, the blades can be left out of the model.

Table 4.4: Measurements of torque and WOB.

Parameter	Value	Units
WOB - nominal	5000	[kg]
WOB - peak	10000	[kg]
Torque - nominal	8000	[Nm]
Torque - maximum	20000	[Nm]

The outcome of the finite element analysis is presented in figure 4.21 for the equivalent stress and total deformation for combined loading.

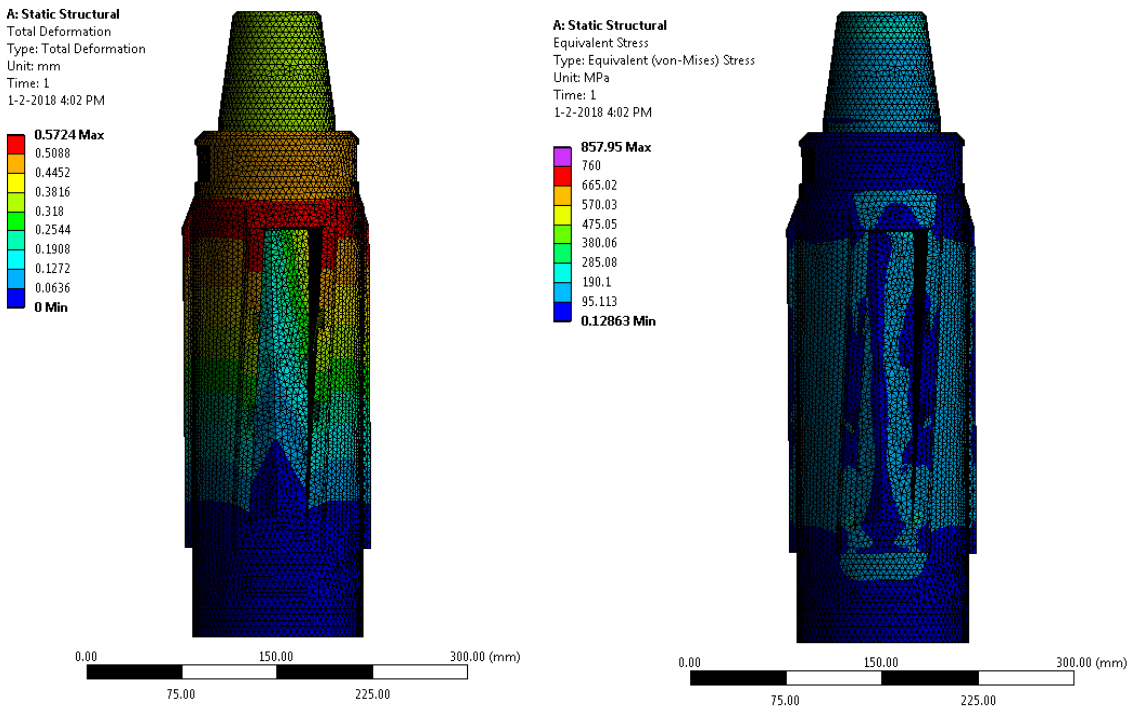

Figure 4.21: Finite element analysis of the UR core structure.

A scale factor of 23 has been applied to make the deformation visible. The total deformation analysis (figure 4.21) shows that a maximum deformation of 0.57 mm can be expected at the top of the slots. Since this value does not exceed the value of the clearance, no problems should occur. The equivalent stress analysis displays the distribution of the shear stress. Although the equivalent stress seems sufficiently low, a local maximum of about 858 MPa can be expected at the bottom corner. A close up is shown in figure 4.22. The rounding (fillet) around the edge could be increased to distribute the stress more evenly to avoid crack formation.

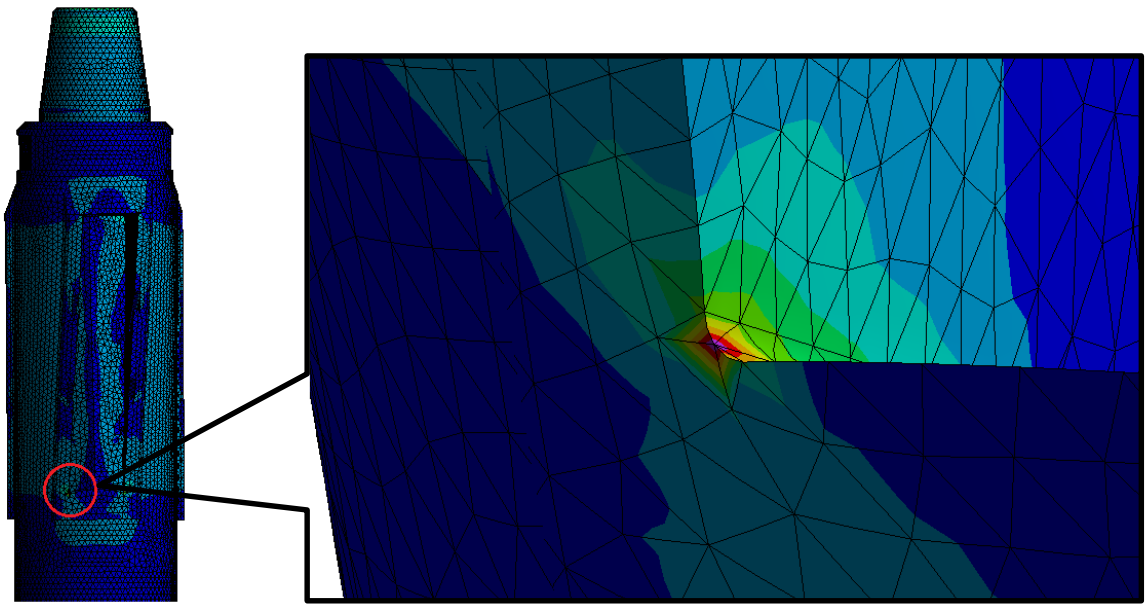

Figure 4.22: Local stress maximum.

4.5. Blocks with finger joints

In this section, the concept idea as discussed in section 3.8 will be worked out in more detail.

4.5.1. Overview

This concept involves the use of conventional blades, which meet in the centre of the underreamer by means of finger joints. A few leaps in the design process have to be made to make the blocks so that the way of extending the blades resembles that of the base case. These leaps are shown in sequential diagrams in figure 4.23.

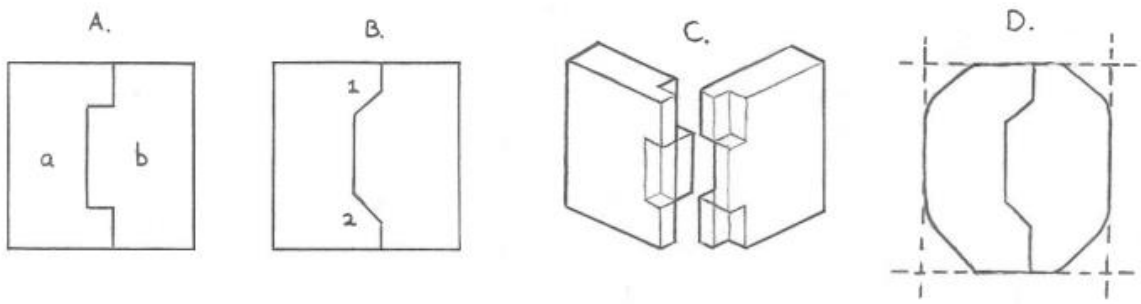

Figure 4.23: stages in designing the block joints and shapes.

It is rather easy for two blocks to extend horizontally and independently from each other (figure 4.23 **A**.). When two blocks have to meet under an angle, the meeting interface or surface cannot have straight joints. Instead, the right angles have to be chamfered to allow the blocks to move upwards (figure 4.23 **B**.). Since both the top and bottom side of the protruding part of block **b** are chamfered, the blocks can move upwards (and theoretically also downwards) independently from each other.

For three blocks, the situation becomes more complex. If all blocks have to slide in one another, then each block will at least need two rows of 'teeth' to slide in cut-outs of the other blocks (figure 4.23 **C**.). Since the space in the underreamer is limited (the blocks may not exceed a certain length), the amount of cut-outs must be limited to assure the block has enough strength to withstand the external moment caused by underreaming. For this reason, pulling a vertical line through the blocks may only run through two blocks. A top view of the meeting interface is shown in figure 4.24.

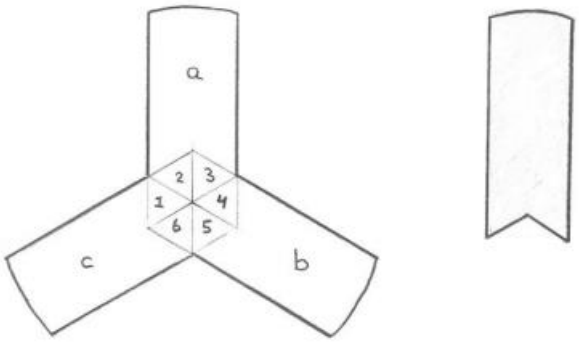

Figure 4.24: Top view of the meeting interface between three cutter blocks.

In figure 4.24 on the left side, the blocks, indicated **a**, **b** and **c**, are drawn in their fully retracted position. Around the centre of the sketch, the hexagon **1**, **2**, **3**, **4**, **5**, **6** is constructed. Block **a** takes up the space that is indicated by the surfaces **a**, **1**, **2**, **3** and **4**. Drawing this shape separately results in the sketch that is shown on the right. For block **b**, its space consists of **b**, **3**, **4**, **5** and **6**. The shape of block **c** is found in the same way (**c**, **5**, **6**, **1** and **2**).

From figure 4.24 and the sequences described above, it can be seen that all areas are taken up by no more than two blocks e.g. block **b** and block **c** both 'share' surface **5** while block **a** does not. Once the shape and the angles of the internal surfaces on the block are determined, a block shape that is suitable for reaming must be designed (figure 4.23 **D**.)

4.5.2. Technical drawings and calculations

To draw the shape of the blocks as described in section 4.5.1 more accurately, Inventor Professional 3D CAD software was used to model the blocks. If the blocks would slide out horizontally, its shape can again be easily modelled. The result is shown in figure 4.25.

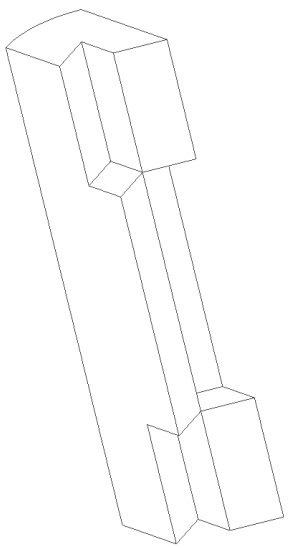

Figure 4.25: Block with finger joints.

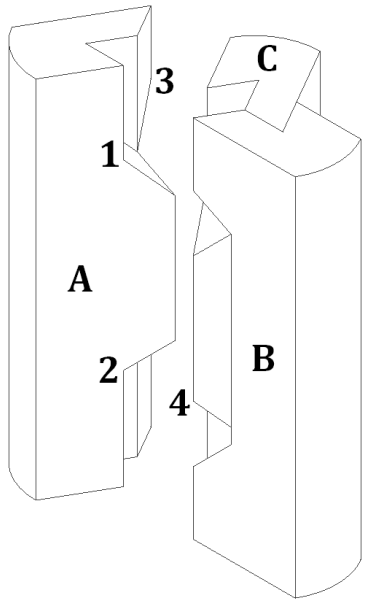

Figure 4.26: Block slide-out position.

It can be seen in figure 4.25 that the block has three 'teeth', one in the middle and two more, located at the top and bottom. The teeth are sized in such a way that both the left and right side of the block have the same abutment area inside the underreamer.

To determine the angle of the kite shaped surfaces, some boundary conditions have to be established. It can be seen from figure 4.25 that there are four kite shaped surfaces present at the interface. These have to be orientated at a certain angle to allow for the upward motion. This is shown in figure 4.26. The angles have already been modelled here.

When block **A** in figure 4.26 moves upward with respect to block **B** (assumed fixed), initially only the surfaces **1** and **2** remain in contact with block **B** and block **C** respectively. Relative to **A**, block **B** and **C** can slide out along surfaces **3** and **4**.

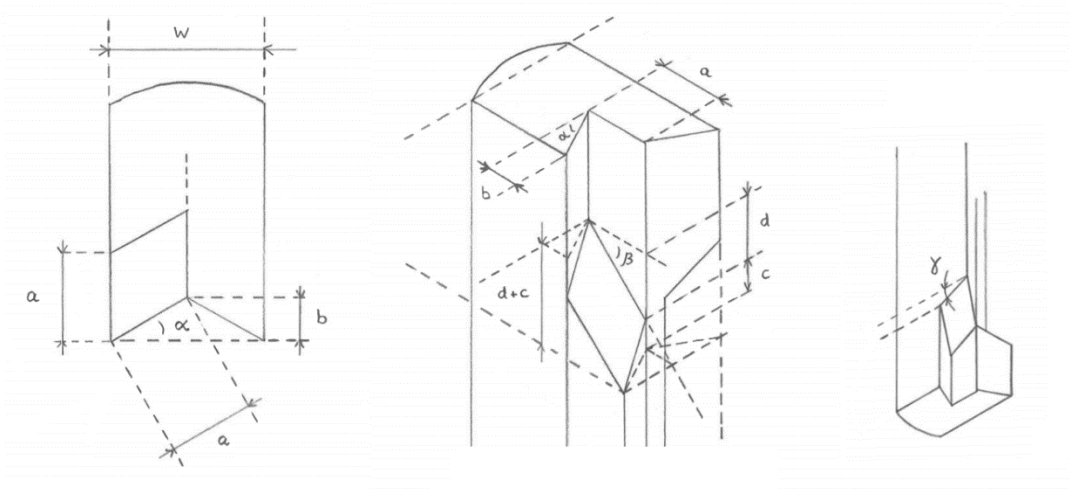

Figure 4.27: Block geometry.

A geometrical model (figure 4.27) can be used to determine the dimensions of the block meeting-interface, where Latin symbols indicate lengths [m] and Greek symbols indicate angles [deg]. Distance '**d** + **c**' in the sketch indicates the 'total height' of the kite. At the position of the kites, there is no surface on both sides, which can support the block inside the core structure of the underreamer. For structural reasons this kite height should stay as low as possible. However, for an increase in the departure angle **β**, the kite height will increase. Ideally, the kites should be located such that the teeth on both sides of the block make up half of the area. Therefore, the height of the middle teeth needs to be as height as the total height of the two teeth on the other side combined.

From the geometry presented in figure 4.27, the total kite height can be determined as follows:

$$a = \frac{w}{2 \cdot \cos\alpha} \qquad [4.41]$$

$$b = \frac{1}{2} \cdot w \cdot \tan\alpha \qquad [4.42]$$

$$c = b \cdot \tan\beta \qquad [4.43]$$

$$d = a \cdot \tan\beta \qquad [4.44]$$

$$\rightarrow d + c = (\sec\alpha + \tan\alpha) \cdot \frac{1}{2} \cdot \mathrm{w} \cdot \tan\beta \qquad [4.45]$$

The angle **γ** can be determined from symmetry and is given by:

$$\tan\gamma = \frac{c}{a} = b \cdot \tan\beta \cdot \left(\frac{2 \cdot \cos\alpha}{w}\right) \qquad [4.46]$$

$$\rightarrow \gamma = \arctan\left(b \cdot \tan\beta \cdot \left(\frac{2 \cdot \cos\alpha}{w}\right)\right) \qquad [4.47]$$

$$\rightarrow \gamma = \arctan\left(\frac{1}{2} \cdot w \cdot \tan\alpha \cdot \tan\beta \cdot \frac{2 \cdot \cos\alpha}{w}\right) \qquad [4.48]$$

$$\rightarrow \gamma = \arctan(\tan\alpha \cdot \tan\beta \cdot \cos\alpha) \qquad [4.49]$$

From the geometry, it is easy to determine the lengths and angles of the remaining two kites, because the blocks are in this case symmetric (by mirroring in the vertical and horizontal mid-planes of the block).

4.5.3. Prototype and shaping

To make the blocks suitable for underreaming, their shape needs to be adjusted and some details have to be added in order for the blocks to slide out under a certain angle. Some difficulties arise when moulding the block into a shape that is actually used in practice (figure 4.28).

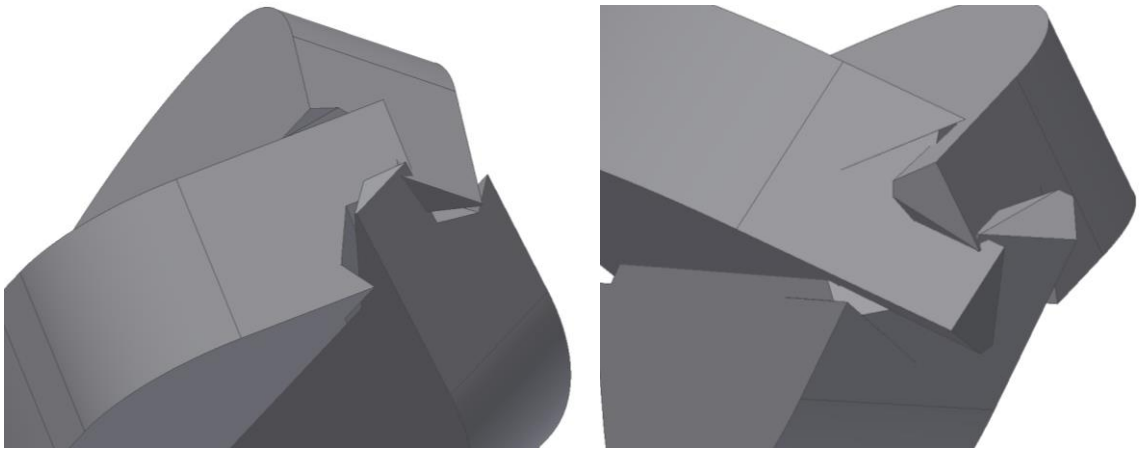

Figure 4.28: Block edges around the top (left) and bottom (right) corners.

In figure 4.28, the blocks are shown after reshaping. The protrusions that can be seen weaken the structure and provide no support for the stop blocks at the top. One way to deal with this problem is to simply cut-off these top and bottom parts.

Because of flattening the block on the top side, the stop block that holds the reaming block in its maximum extended position will also have to be redesigned compared to the one used in the base-case. After guide rails were added to the blocks, two prototypes were made for testing. The second prototype is shown in figure 4.29.

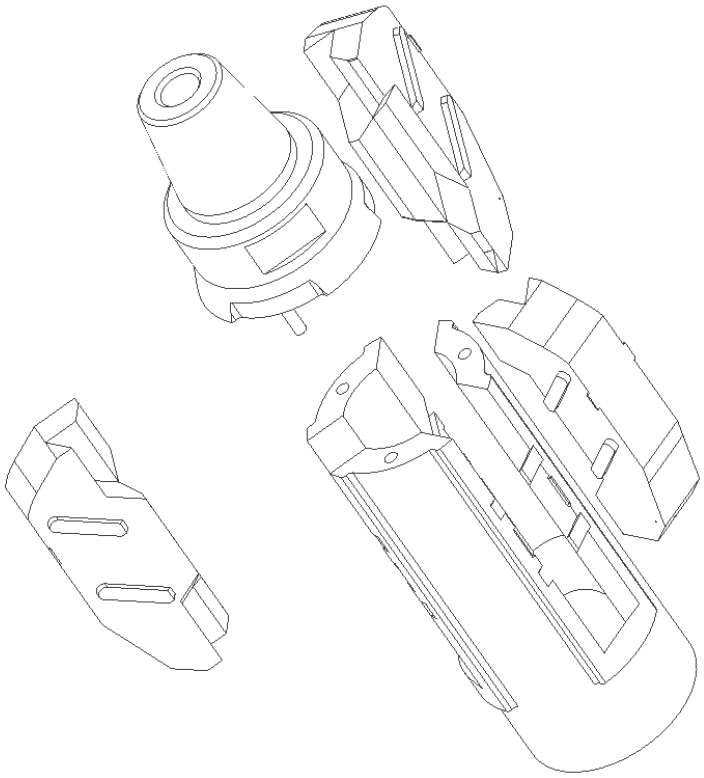

Figure 4.29: Exploded view of the second prototype of the finger joint concept.

4.5.4. Challenges

This innovative concept has the potential ream holes further than the 9 inch described in the assignment. The assumption is made that the block might slide out until the internal groove section becomes exposed. Reasons for this decision are the prevention of clogging by not exposing cavities of the blocks, preventing the block from running of its rails that ends at the start of the teeth-shaped internal structure and the need to counteract the external moment by leaving enough contact area between the core structure and the block. The rails cannot extend along the full length of the block because the rails also run into each other internally (figure 4.30 A.)

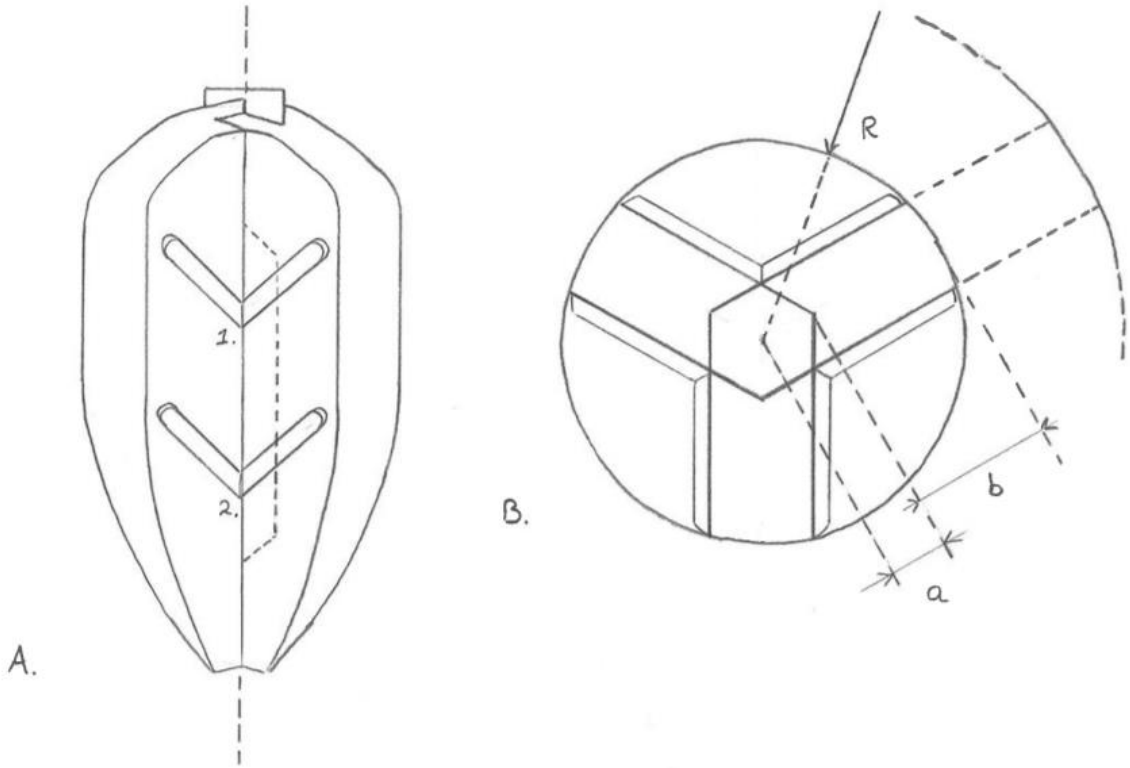

Figure 4.30 A: Tongue-groove fittings 1 and 2 meeting along the edge of the blocks.
Figure 4.30 B: Graphical representation of drill diameter calculation.

The enlarged hole diameter can be calculated by using the dimensions used in figure 4.30 and the following formula:

$$D = 2R + 2(R - a) \qquad [4.50]$$

$$a = \frac{w}{2 \cdot \cos \alpha} \qquad [4.51]$$

This results in a diameter of 240 mm or 9.45 inch.

Although the blocks can easily extend to the desired diameter, this concept proves to be difficult to realise when looking at some of the other parts and mechanisms inside the underreamer. A centralized mud channel would only be feasible in case the width of the blocks **w** is larger than the diameter of the mud channel $\mathbf{D_m}$. Instinctively, aside from the reduced structural integrity (torsion resistance), larger blocks seem to solve the problem. However, making the blocks wider also results in a bigger teeth structure, reducing the extension length of the blade ($\mathbf{x_1 < x_2}$). This is shown in figure 4.31.

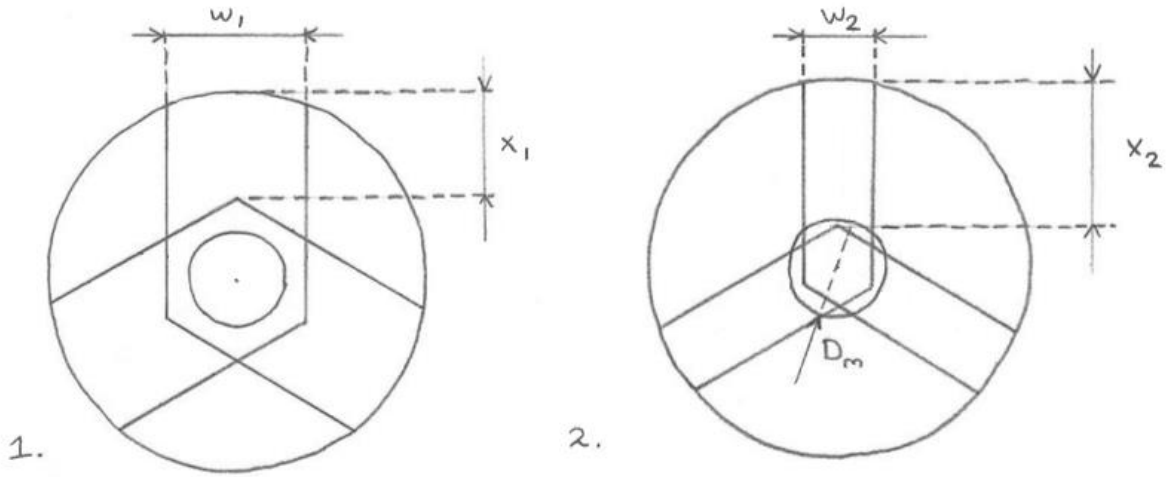

Figure 4.31: Relation between block width and stick-out length.

Another challenge is about the coupling rod connection. If the coupling connection would located around the centre of the underreamer, space needs to be cut out of the blocks to make room for the coupling rod. By removing this material, the edges of the blades are cut-off, which shortens their length. This can be seen in the 2nd right sketch of figure 4.32, where the shaded area indicates the new block shape.

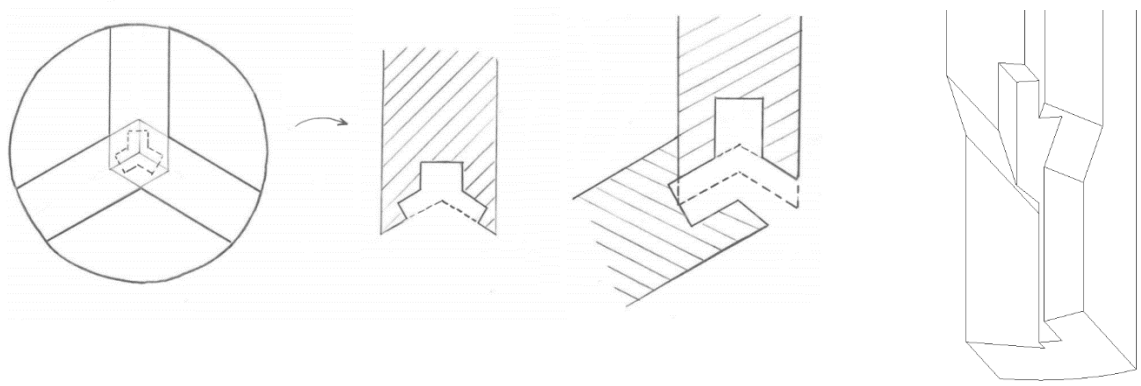

Figure 4.32: Impact of including the coupling rod into the design.

A weird shape could also result by cutting until a certain depth is reached (2nd left). On top of that, it is difficult to connect the rod on both sides to the block, since the 'teeth' do not overlap when looked at from the side of the block. This can be seen in the inventor model to the right (figure 4.32).

4.6. Final concept selection

Based on the elaboration of the concepts in the previous sections, factors that determine the overall feasibility of these designs have again been identified. These factors will be used as boundary conditions in an MCA to order the concepts according to their expected functionality. The boundary conditions are mentioned in table 4.5, along with a description.

Table 4.5: Boundary conditions.

Boundary condition	Description
Proven technology	Similar concepts have already been patented or built. The conceptual design will be compared to the existing design. The circumstances and purposes under which these similar concepts are used are being considered.
Technical feasibility	This includes the ease of fabrication and required production techniques.
Reliability and durability	The blocks need to expand and collapse downhole. Partially extended blocks can result in an under gauged hole. If the blocks cannot be retracted, a lot of time could be wasted in retrieving the tool. The durability of the parts could be an important factor in determining the reliability of the UR.
Maintenance	This parameter determines how easily parts can be exchanged among each other. The number of unique parts determines the complexity of the operation. For easy maintenance debris must be removed fast (for cleaning), and if needed lubrication needs to be applied.
Ease of assembly	Includes ease of handling, time required to put all parts together, the type of connections that are involves, the order of installation and if the parts can be connected by hands or machines. The number of parts also affects the ease of assembly.
Design flexibility	How versatile is the design? Can the design easily be adjusted of detailing? How flexible is the development path?
Expected cutting performance	How much formation rock can be removed per unit of time? Are there any design restrictions on the use of the device that could affect the cutting performance?

The boundary conditions are given a weighing factor. These weighing factors are determined by normalizing the factors to sum 1. Each factor is therefore divided by the sum of the factors. Each concept is also given a score, ranging between -2 and 2, for each boundary condition, to indicate to what extent the concept satisfies this condition relative to the base-case. The weighing factors and the scores for the boundary conditions are then multiplied and summed up for each concept, which results in a total score.

A high (positive) score means that the design has favourable characteristics. A low or negative score means the design is not suitable under certain conditions or is not able to perform an underreaming job at all. Weighing factors are given in table 4.6.

Table 4.6: Weighing factors.

	Proven technology	Technical feasibility	Reliability and durability	Maintenance	Ease of assembly	Design flexibility	Expected cutting performance	SUM	Weight factor
Proven technology	-	1	1	1	1	1	1	6	0.29
Technical feasibility	0	-	1	1	1	1	1	5	0.24
Reliability and durability	0	0	-	1	1	1	1	4	0.19
Maintenance	0	0	0	-	1	1	0	2	0.10
Ease of assembly	0	0	0	0	-	1	0	1	0.05
Design flexibility	0	0	0	0	0	-	0	0	0
Expected cutting performance	0	0	0	1	1	1	-	3	0.14

Since 'Design flexibility' is at the bottom of the ranking (weighing factor 0), it is left out of the MCA. The MCA outcome is presented in table 4.7.

Table 4.7: MCA.

	Proven technology	Technical feasibility	Reliability and durability	Maintenance	Ease of assembly	Expected cutting performance	Total score
Telescopic blocks	-2	-2	-1	-1	-1	1	-1,26
Diaphragm mechanism	1	-1	-1	-2	0	-1	-0,48
Eccentric blade configuration	-1	2	0	0	0	1	**0,33**
Blocks with finger joints	-1	-2	0	-1	0	1	-0,73

From the MCA, it can be seen that one design has a positive or favourable outcome. This concept will be considered in the next detailed phase. Detailed models will be developed and FEM calculations will be made to check if the design could actually withstand downhole conditions. In chapter 6, recommendations will be given on how to further improve and test the conceptual design.

5. Detailed design

This chapter describes in detail the working principles of the conceptual underreamer, its components and the production methods that are used. Simulations are performed to prove it fulfils the requirements that are described by the thesis assignment.

5.1. Introduction

Now that the general conceptual design with respect to the internal placement of the blades is determined, the conceptual design has to be developed in more detail. This involves the development of the parts that make up the UR. Solutions have to be found so that the different subsystems can work together without compromising their individual performance. By analysing the previous discussed reamer concepts, the some key points of attention have been identified. These will be discussed in the upcoming chapters.

5.2. Actuator

To activate the UR for reaming, blocks have to be extended to start the hole-enlargement operation. This can be done by rotary or linear actuators. For flip-arm expansion mechanisms, a rack and pinion actuator is used where a linear piston-cylinder mechanism produces a rotation by a gearing (figure 5.1). To drive such an actuator both pneumatic and hydraulic power may be used. The blocks could also be activated by a solenoid valve that is connected to an electromagnetic activation system.

For block type underreamers however, linear actuators are most often used. A hydraulic actuator in the form of a piston encased in a cylindrical housing can be activated by a pressure differential. This type of actuator is often used in combination with a mechanical actuator in the form of a spring, see figure 5.2. This spring is set under pretension that causes the blades to open only when a certain fluid pressure is reached. Another possible mechanism that is already being used includes the rotor assembly mentioned earlier.

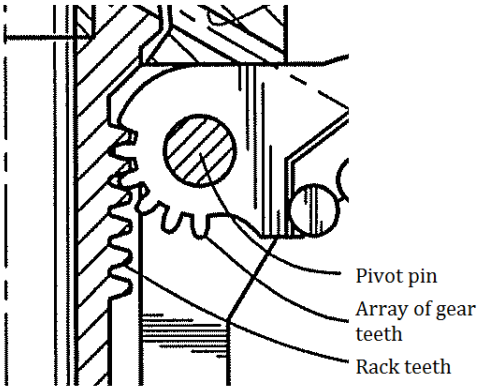

Figure 5.1: Rack and pinion actuator.[16]

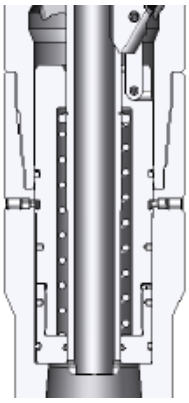

Figure 5.2: Spring with piston.

There might of course be different ways in which these actuators can fit in the UR. There are also many types of springs, which can be connected in either a serial or a parallel configuration. To determine what kind of spring is favourable the mechanism itself has to be designed. Parameters that are of paramount importance include the stroke of the spring and the pretension that will be necessary to keep the blocks in the closed position at low circulation pressures.

Technology that involves the use of Radio-Frequency-Identification (RFID) type activation systems or solenoid valves are not considered in this report. Although RFID gains popularity, there are several disadvantages, which include its complex design, the use of non-reusable tags, the need for batteries to power the receiver downhole and the robustness of the tags and (electronic) components themselves.

5.3. Expansion mechanism

Before the type of spring or any of its characteristics are determined, the principle according to which the extension mechanism works will be developed. Four conceptual designs are proposed in figure 5.3 A. Their working principle will be discussed below.

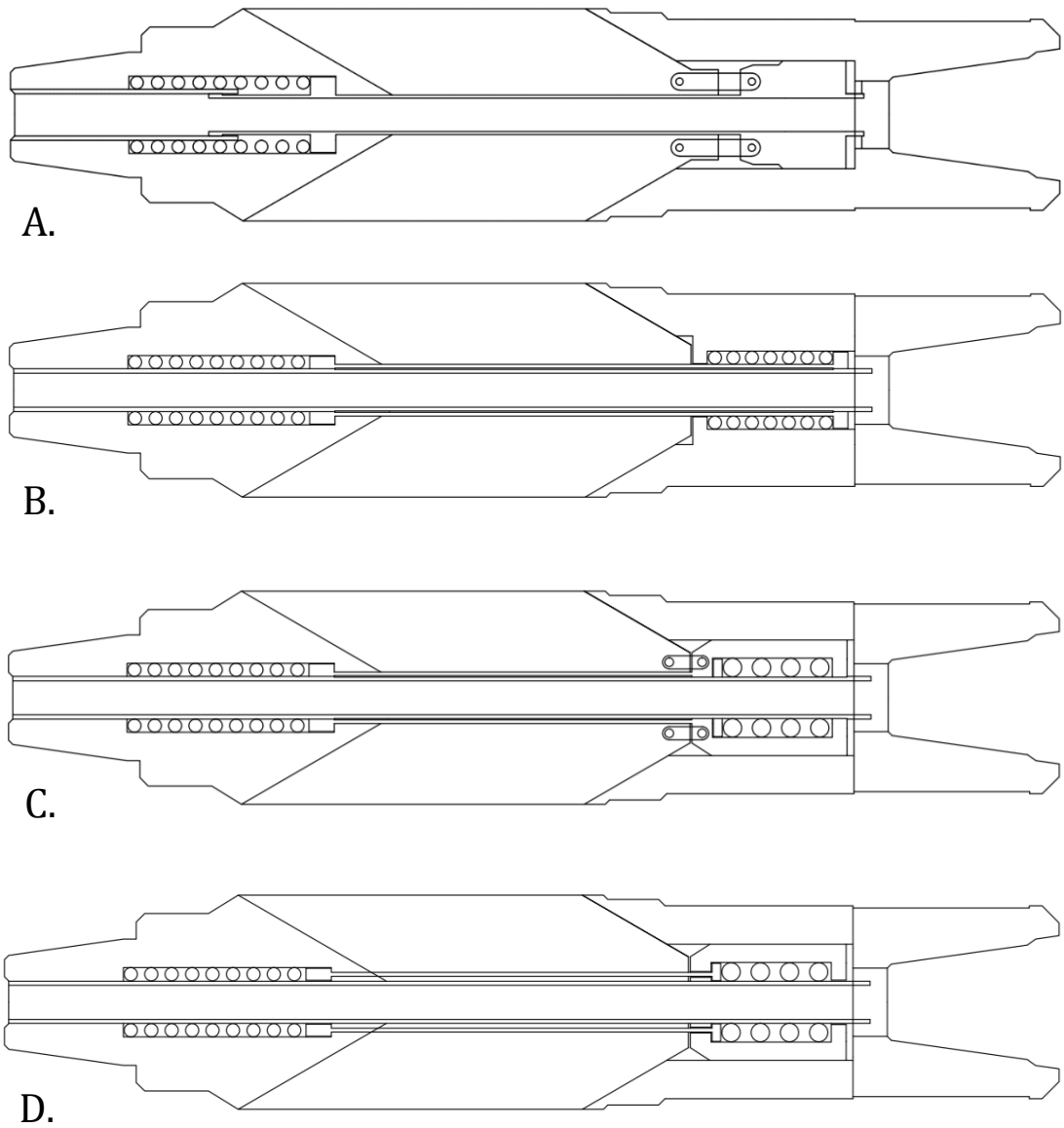

Figure 5.3: Conceptual designs for the expansion mechanism.

Conceptual design ***A*** shows that the spring is moved from the right to the left. The moving cylinder around the spring that is present in the base-case is absent here. A hollow tube that compresses the spring surrounds the inner wall of the mud channel at the location of the spring. Coupling rods are attached to the bottom of this tube and the blocks, so that they are pushed out when the spring is compressed.

By moving the spring to the top, the empty space above the blocks can be filled in a useful way. It becomes however difficult to fit the nozzle at this location so these will have to be relocated if not left out. It can also be seen that the diameter of the flow channel along the entire length of the UR varies in diameter. Since a narrow channel will increase the flow velocity, the entrance channel could be widened. This will slightly reduce the length up to which the spring can stick into the pin connection, because the wall becomes thinner.

Another point of discussion involves the sliding connection of the tubes. Since the flow direction is from left to right in the drawing, drilling fluids might pour in between the connection or wear down the sides, because of the flow contraction. If this inhibits the working of the mechanism, the connection should be inverted. A similar problem with turbulence can be found at the other end. When the hollow tube moves to the left, an empty space appears in which vortices can be present. For this reason, it is preferred that the flow tube should extend to both ends via a single channel. It could be that the hollow flow tube takes up to much space around the UR, such that the length increase of the blades by putting them in an eccentric configuration, is cancelled out. Therefore, it could be necessary to replace the hollow tube that run along the sides or inside of the blocks.

The last point of discussion has to do with the assembly of the parts. In drawing *A* the tube is supported to the right of the spring, where it pushes the tube against the core structure, because it is under pretension. The location of the contact area could however be reconsidered in this case because the disk that is attached to the tube might not fit through the constriction. In that case, the point of contact should be at the piston on the right side of the drawing.

In conceptual design ***B***, the flow channel consists of one part. The spring has been split so that it can be fit partially above and under the blocks. In this concept, the hollow tube surrounds the flow channel on the outside and over its entire length. Both ends feature rings, which are in contact with the springs. When the hollow tube is pressed to the left due to a pressure differential, the springs will be compressed. Because both springs are connected to the core structure and the hollow tube, their displacement will be the same (parallel configuration).

A disadvantage of this concept is that the coupling rods have to be fitted to the hollow tube. This might cause deformations that cause it to jam around the flow tube. The diameters of the tubing also need to be determined together with the wall thickness.

Another concept that involves the use of two springs is shown in figure 5.3 ***C.*** Here the existing piston-spring assembly has been modified such that it extends upwards, towards a second spring. These springs are also configured parallel as there are both connected to the core and their displacement is directly linked. Compared to conceptual design *B*, it seems that there is more room to fit the coupling rods to the piston-spring assembly.

Conceptual design ***D*** involves the use of two springs that are configured in series. A hollow tube or rods have to reach the spring within the piston-spring assembly. One might wonder if the possibility of having parts move relatively of each other is desirable. In the end, it is the position of the piston that matters.

Because a certain stroke needs to be made for the coupling rods to position the blocks for the 9-inch extension, only concepts *A* and *D* prove to be suitable.

To determine any spring characteristics, the stroke length for the extension of the blocks needs to be determined first.

5.3.1. Extension length

The extension length can be determined with the help of a trigonometric model, as depicted in figure 5.4.

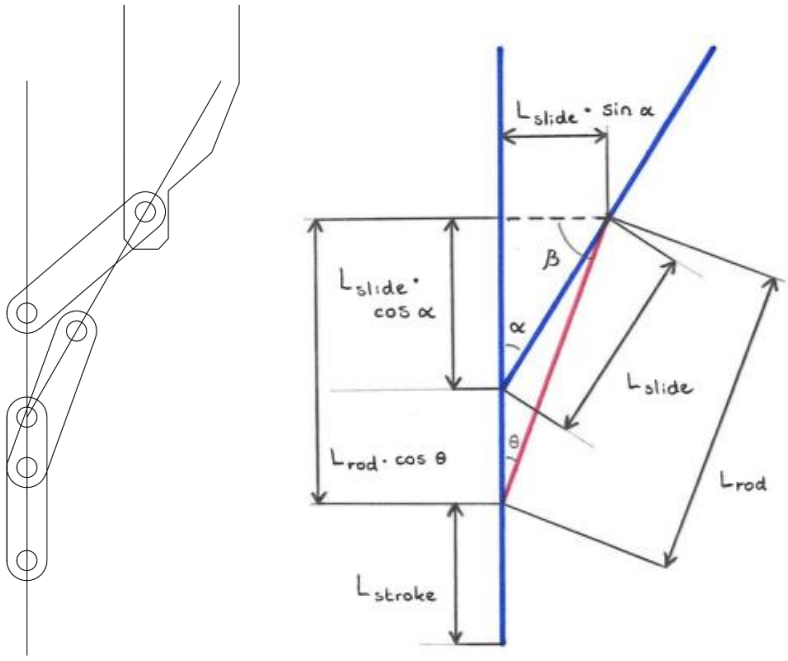

Figure 5.4: Model to determine the required stroke length.

Three different positions of the coupling rod are shown on the left of figure 5.4. The blue lines (fig. 5.4 right) indicate the paths along which the rod (red) slides. The parameters shown in figure 5.4 are related in the following way:

$$L_{extension} = L_{slide} \cdot \sin\alpha \qquad [5.1]$$

$$\rightarrow L_{slide} = \frac{L_{extension}}{\sin\alpha} \qquad [5.2]$$

$$L_{slide} \cdot \cos\alpha = L_{extension} \cdot \frac{\cos\alpha}{\sin\alpha} \qquad [5.3]$$

$$\sin\theta = \frac{L_{slide} \cdot \sin\alpha}{L_{rod}} \qquad [5.4]$$

$$\rightarrow \theta = \arcsin\frac{L_{slide} \cdot \sin\alpha}{L_{rod}} \qquad [5.5]$$

$$L_{rod} \cdot \cos\theta = L_{rod} \cdot \cos\left(\arcsin\frac{L_{slide} \cdot \sin\alpha}{L_{rod}}\right) \qquad [5.6]$$

$$\rightarrow L_{stroke} = L_{rod} + L_{slide} \cdot \cos\alpha - L_{rod} \cdot \cos\left(\arcsin\frac{L_{slide} \cdot \sin\alpha}{L_{rod}}\right) \qquad [5.7]$$

$$\beta = 90 - \theta \qquad [5.8]$$

For a 215.9 mm (8.5 in.) reamed hole, which is the base-case, a stroke length was determined of 76.26 mm. For a 228.6 mm (9 in.) hole however, the stroke length increases to 96.50 mm. For both calculations, the coupling rod length of the base-case was used (46.56 mm) and α was taken 30°. It can also be shown that the angle β decreases for an increased extension length. This may give problems in case the blocks need to collapse into the core.

5.3.2. Determination of spring characteristics

Shape
Since the stroke length and block shape is determined, the spring characteristics can be determined. The choice has been made to use helical coil springs because the spring rate is approximately constant. Non-linear coil or barrel springs are not used. Their characteristics may be difficult to determine and they may not fit in between the piston and the mud channel. Compact disk springs are also not considered because of wear related problems. They are generally used in applications where high forces only cause minor displacements, which is unsuitable for extending the blocks. Manufacturability also plays a role. Although coil springs with a rectangular wire can bear up to 30% more load compared to round wire springs for the same amount of deflection, they will likely have to be custom made, which could be very expensive.[17]

Operating parameters
Since the conceptual design resembles the base-case, it is assumed that a pressure difference Δp of approximately 7.5 bar is required to completely extend the blocks. The force that acts on the spring can be calculated by determining the piston area (eq. 5.9):

$$A = \frac{\pi}{4}(D_{outer}^2 - D_{inner}^2) \approx 4.3 \cdot 10^{-3}\ m^2 \qquad [5.9]$$

$$F = \Delta p \cdot A = 3225\ N \qquad [5.10]$$

Since it is assumed that the blocks are preloaded with an equivalent pressure of 3.5 bar, the spring needs to cover a distance that equals extension of the rods while the pressure is increased by 4 bar. The stroke length can be determined with the equation on pg. 71. This amounts to 58.37 mm. Now the spring stiffness can be determined with the following equation (eq. 5.11):

$$k = \frac{F}{L_{stroke}} \qquad [5.11]$$

This results in a spring stiffness of 29 kN/m. The spring has to fit around the mud channel drilled in the core of the UR, which has an outer diameter of 35 mm. A wire diameter d of 10 mm is chosen for the spring. With this information, the maximum shear stress in the spring can be determined. The maximum shear stress occurs in the outer fibre of the wire and is equal to (eq. 5.12)[18]:

$$\tau = \frac{Tr}{J} + \frac{F}{A} = \frac{8FD}{\pi d^3} + \frac{4F}{\pi d^2} \qquad [5.12]$$

Here r denotes the distance to the outer fibre and T denotes the internal torque acting at the cross section, which is equal to the product of the spring force F and the mean radius $R = \frac{D}{2}$ of the coil. The mean diameter is indicates by D. It can be deduced from the equation above that the polar moment of inertia equals (eq. 5.13):

$$J = \frac{\pi}{2}\left(\frac{d}{2}\right)^4 = \frac{\pi}{32}d^4 \qquad [5.13]$$

From this formula, the internal shear stress is determined to be 578 MPa. The yield strength of the material is related to the maximum allowable shear stress through the von Mises maximum distortion energy criterion in the following way (eq. 5.14):

$$\tau = 0.58\sigma_{yield} \qquad [5.14]$$

This means that a material with a yield strength of at least 997 MPa will be required. Since the required deflection was determined earlier, the number of active coils that is required can now be determined with the following equation (eq. 5.15):

$$n = \frac{f d^4 G}{64 R^3 F} = 14.3\ [-] \qquad [5.15]$$

This means that approximately 14 active coils are required for the desired deflection. Now that the number of coils is known, the closed spring length can also be determined (eq. 5.16):

$$L_{closed} = nd \qquad [5.16]$$

A closed length of 143.5 mm was found. By adding up the closed length and deflection length, a free spring length of approximately 253 mm is found. Since it is not desired that the spring collapses entirely and takes any additional load, a length of 260 mm is considered safe to work with. Once the maximum extension of the blocks is reached, the arm stoppers will prevent the blocks from moving and take any additional load.

Selection

The range for the value of most of the spring parameters is already determined implicitly by the design of the core body. Since custom springs are very expensive and spring suppliers only work with rounded numbers, a spring has to be selected that matches the above determined parameters the closest. A spring with matching characteristics was found at *Tevema*. Spring properties are presented in table 5.1. The material properties are presented in table 5.2. Processes that have been applied to alter the properties of the steel are not specified.

Table 5.1: Spring characteristics of item D24610.[19]

Description	Variable	Value	Units
Wire diameter	d	10.00	mm
Mean coil diameter	D_m	63.00	mm
Number of active coils	N_w	12.50	[-]
Total number of coils	N_t	14.50	[-]
Spring stiffness	C	27.99	N/mm
Maximum deflection	S_n	119.3	mm
Solid height	L_n	165.67	mm
Maximum force	F	3340.70	N
Minimum bore diameter	$D_{bore,min}$	75.00	mm
Maximum drill diameter	$D_{drill,max}$	51.00	mm
Coil outer diameter	D_{out}	73.00	mm
Free spring length	L_0	285.00	mm

Table 5.2: Chemical composition of werkstoffnummer 1.4310/AISI 302 (percentage by mass).

Steel grade		C	Si max.	Mn max.	P max.	S max.	Cr	Mo	Ni	Others
Name	Number	0.05 to 0.15	2.00	2.00	0.045	0.015	16.00-19.00	≤0.80	6.00 - 9.50	N: ≤0.11
X10CrNi 18-8	1.4310									

Initially a total clearance between the coils of 10 mm was assumed sufficient as a safety precaution. Calculations indicate that this spring will open at 3.36 bar while full cutter block extension is reached at 7.22 bar.

5.3.3. Buckling analysis

The conceptual design makes use of an expansion mechanism where a spring is coupled to a piston, such that the UR does not open below a certain pressure difference. The spring is located in the upper core of the UR while the piston only moves within the bottom core of the UR. Since the piston must be able to compress the spring, a connection has to be made between these parts. One way to do this is by using three columns that can be connected to the spring retainer. The piston is not able to rotate because of its connection to the coupling rods that are connected to the cutter blocks. The ring at the top however is able to rotate sideways. This means that for a small rotation, the column is free to move sideways at the top. This buckling shape can be described by the simplified model shown in figure 5.5.

The buckled shape of the column is shown by a dashed line.		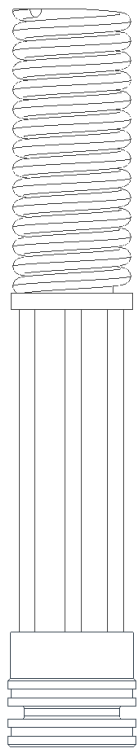
Theoretical K value.	1.0	
Recommended design value when ideal conditions are approximated.	1.2	
End condition.	Rotation fixed, translation free.	

Figure 5.5: Buckling shape.[20]

The buckling load can now be determined by using the omega-method. The critical stress will be determined by taking into account the slenderness factor of rods. The material and geometric properties of the rod are shown in table 5.3.

Table 5.3: Parameters.

Parameter	Value
E	210 GPa
I	$4.91 \cdot 10^{-10}$ m^4
A	$7.85 \cdot 10^{-5}$ m^2
$l_{buckling}$	280 mm

The slenderness can be determined with the following equation:

$$\lambda = \frac{l_{buckling}}{\sqrt{\frac{I}{A}}} \qquad [5.17]$$

For the slenderness of the rod, a value of 112 is found. The buckling stress can now be determined with:

$$\sigma_{buckling} = \frac{\pi^2 \cdot E}{1.67 \cdot \lambda^2} \qquad [5.18]$$

Here, the value 1.67 (5/3) represents a safety factor for the allowable buckling stress. By filling in the equation, a value of 94.23 MPa for the allowable buckling stress. This corresponds with a rod-force of about 7400 N. It is know that the spring that is going to be used can generate a maximum force of 3340.70 N. Therefore, the force for each rod will not exceed 1114 N, which is well below the calculated value of 7400 N.

However, due to the design of the cutter blocks, and the space they require inside the core in their retracted position, there is no space for the rods. The blocks would need to be relatively small or the piston should be enlarged. Both of these measures are not preferred and therefore the design with rods is rejected.

5.3.4. Verification of spring characteristics

Introduction
The conceptual design contains a spring that is used as an actuator and safeguard, to pull the cutter blocks back into the core of the UR and to prevent the blocks from sliding out at low pump pressures. The spring length directly contributes to the total length of the UR. The allotted space determines the limits of the spring in terms of the solid height and free length. The initial deflection of the spring is a consequence of the preload. The total deflection however is also determined by the required stroke of the piston rods, to expand the cutter blocks.

Although the manufacturer has specified all relevant parameters, it became clear from previous applications of helical springs in tools by Huisman that the spring tends to shorten up after going through a few compression cycles. This is undesirable since, in this case, the cutter blocks would not expand to the specified reaming diameter. To investigate whether the manufacturer has accounted for this phenomenon, tests will be conducted to verify the specifications.

Physical background
The stresses in a spring are governed by its loading condition. When the stress exceeds the elastic limit of the steel, the spring will get a permanent deformation. The spring will therefore not return to its original height. This plastic deformation of the spring is called 'setting' of a spring. The spring will take (most of) its set immediately after the first compression. Normally the set is accounted for and can be 'removed' by either the user or the manufacturer by performing pre-stressing operations. In some cases the set will not be removed, in which case a maximum allowable spring deflection should be specified.

Since the spring will be compressed for a longer period, cyclic fatigue does not play an important role. The spring will also be compressed sufficiently slow, such that the effects of vibration, resonance and compression waves can be neglected. Creep however might become more important, when a spring is subjected to a relative high stress and temperatures for a longer period. These plastic deformations over time are not investigated here. Lastly, the effects of buckling are not considered here because lateral movement of the spring is limited by the core bore.[18]

Material
A variety of steel types can be used in springs. Often manufacturers of springs discriminate between 'spring steel wire' and stainless steel wire. Spring steel wire (DIN 17223 C-Wire) has a high carbon content and consequently a high yield strength. Its maximum service temperature is limited to +80°C. Stainless steel (DIN 17224) on the other hand has a high chromium content and it can be applied up to a temperature of +250°C.[21]

Stainless steel is preferred over spring steel wire because it has a better resistance to hydrogen embrittlement, which is one of the most common failure mechanisms in the considered application. Down hole, the presence of hydrogen sulfide (H_2S) could cause atomic hydrogen and metal sulfides to form at the surface of unprotected metals. The hydrogen atoms diffuse into the metal and bond together to form molecular hydrogen. The hydrogen gas will accumulate in lattice voids and exert pressure on the surrounding structure. This phenomenon is referred to as 'sulphide stress cracking'. High temperatures and high hydrogen partial pressures can lead to similar cracking mechanisms.[22]

Research question and hypothesis

The following hypothesis and research question are established:

Research question: Does the spring shorten due to 'setting' and if yes, by what amount and why?

Sub-question: How does the diameter of the spring change during the cycle compression and is this change permanent?

Hypothesis:

Spring setting
The spring will set after an initial compression. It is predicted that the spring is going to deform, because it is expected that the yield strength of the material will be lower than the stresses that are experienced by the spring. The spring surpasses its elastic limit and plastic deformations cause the spring to reduce in length. The maximum shear strength can be calculated with (eq. 5.19):

$$\tau = \frac{8FD}{\pi d^3} + \frac{4F}{\pi d^2} \qquad [5.19]$$

This results in a maximum shear stress of 578 MPa. The stainless steel type used in the spring wire has an elastic limit of 515 MPa. The magnitude of the elastic limit depends on the production processes used. With equation 5.20, the corresponding force can be calculated:

$$F = \frac{\tau}{\frac{8D}{\pi d^3} + \frac{4}{\pi d^2}} \qquad [5.20]$$

This results in a force of 2974 N. By applying Hooke's law, a corresponding deformation is found of 106 mm. This means that the spring will start to deform plastically after it becomes shorter than 178 mm, which is 13 mm above the solid height.

Diameter change
The diameter of the spring will increase with increasing compression of the spring. This will in turn reduce the spring rate. For helical springs, the following relation holds (eq. 5.21):

$$\sqrt{(\pi \cdot D_m \cdot N_t)^2 + (L_0)^2} = L_{thread} \qquad [5.21]$$

$$\rightarrow OD_{expansion} = \frac{\sqrt{L_{thread}^2 - L_n^2} - \sqrt{L_{thread}^2 - L_0^2}}{\pi N_f} \qquad [5.22]$$

With the free length of the spring decreasing during compression, the mean diameter should become larger in case the total number of coils is kept fixed. This is a valid assumption since the spring will also be prevented from unwinding in the UR. The thread length of the spring is a constant. By filling in the values from the specifications, the outer diameter (OD) of the spring should increase by 0.20 mm.

Test plan

Project description
The five springs that have been ordered at *Tevema* (figure 5.6) will be compressed and expended until the difference between the free lengths after two consecutive compression cycles becomes less than 1 mm. The goal of the experiment is to determine the length reduction and diameter expansion.

Figure 5.6: Springs that will be tested.

Test objectives
For the test, three springs will be compressed until the solid height is reached, which is the worst case the spring could experience. Two springs will be compressed so that a total play of 10 mm remains. During each compression cycle, the averaged spring diameter will be determined in the open state, the pre-tensioned state and the compressed state. The top and bottom diameter are used to determine the average diameter. After each compression cycle, the free length is measured to determine the reduction in length of the spring.

Setup
The spring will be tested by clamping it in between two disks, both containing a circular cutout equal to the minimum hole diameter specified by the manufacturer. A threaded rod will protrude vertically through the disks. A hollow cylinder around the thread along the inside diameter of the spring prevents the spring from buckling. The top disk is connected to a rod to prevent the disk from rotating and applying torsion to the spring. The setup is shown in figure 5.7.

Figure 5.7: Experiment setup and schematic setup drawing.

Measurement instruments
To measure the diameter and length of the spring, a digital caliper is used. The display is accurate to ± 0.01 mm, which is essential for measuring the predicted diameter expansion. The application of the device is shown in figure 5.8.

Figure 5.8: Measurement method.

Safety
Because of the high loads on the spring, the nut needs to be lubricated properly. If the nut seizes, it should be unscrewed and thread repair operations should be performed (figure 5.9). In case the nut slips from the thread, it is prevented from shooting of the rod by a second nut at the top of the thread. In case the thread displaces too much laterally, the test should be stopped, since the measurements for the diameter will be affected by this. Engineering squares are used as a tool to check aligns to the thread and spring. During the entire experiment a helmet, glasses and gloves must be worn. The tester who leads the test will also have a contact person nearby, in case something goes wrong.

Figure 5.9: Tapping tool to repair the damaged thread.

Procedure
From the five springs that will be tested, three springs are compressed up to the solid height. The two remaining springs will be compressed to 1 cm above the solid height. For each spring, the initial length is measured first. Then the spring is compressed and relaxed with the setup described above. Afterwards, the spring length is measured again. The diameters on the other hand are measured during the compression itself. The diameter will be measured at the top and bottom of the spring in three different positions. The results from the test that was carried out according to this procedure are presented below.

Results

The values that have been measured are presented in the overview tables 5.4 and 5.5 below. All values have units of millimeters.

Table 5.4: Spring free length values.

		Free spring length			
Spring		Initial length	Compression 1	Compression 2	Compression 3
Compressed length 166 mm	1.	289	279	278	278
	2.	288	278	277	277
	3.	289	280	278	278
Compressed length 176 mm	4.	288	285	285	-
	5.	289	286	286	-

Table 5.5: Diameter values.

		Compression 1					
		Diameter uncompressed		Diameter at pretension*		Diameter compressed	
Compressed length 166 mm	Spring	Top	Bottom	Top	Bottom	Top	Bottom
	1.	72.83	72.22	72.63	73.00	72.94	73.05
	2.	72.47	72.91	72.67	72.77	72.93	72.98
	3.	72.41	72.98	72.70	72.98	72.91	72.98
Compressed length 176 mm	4.	72.36	72.95	72.76	73.01	72.94	73.03
	5.	72.88	72.53	72.87	72.78	72.92	73.04

		Compression 2					
		Diameter uncompressed		Diameter at pretension*		Diameter compressed	
Compressed length 166 mm	Spring	Top	Bottom	Top	Bottom	Top	Bottom
	1.	72.91	72.41	72.90	72.56	72.96	72.74
	2.	72.82	72.45	72.92	72.59	72.96	72.92
	3.	72.84	72.61	72.98	72.77	73.11	72.86
Compressed length 176 mm	4.	72.97	72.46	72.97	72.72	73.01	72.79
	5.	72.87	72.59	72.85	72.67	72.96	72.86

		Compression 3					
		Diameter uncompressed		Diameter at pretension*		Diameter compressed	
Compressed length 166 mm	Spring	Top	Bottom	Top	Bottom	Top	Bottom
	1.	72.35	72.81	72.72	72.78	73.04	72.78
	2.	72.54	72.39	72.84	72.52	72.97	72.72
	3.	72.80	72.47	72.93	72.52	73.02	72.92
Compressed length 176 mm	4.	-	-	-	-	-	-
	5.	-	-	-	-	-	-

* The spring length is 234 mm in its pretension state.

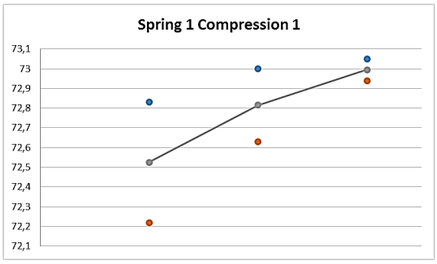
Spring 1 Compression 1
73,1
73
72,9
72,8
72,7
72,6
72,5
72,4
72,3
72,2
72,1

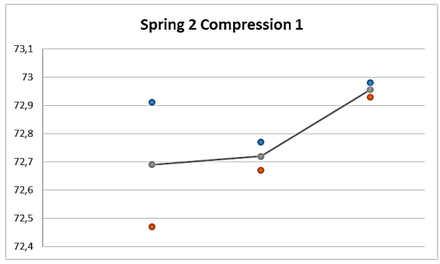
Spring 2 Compression 1
73,1
73
72,9
72,8
72,7
72,6
72,5
72,4

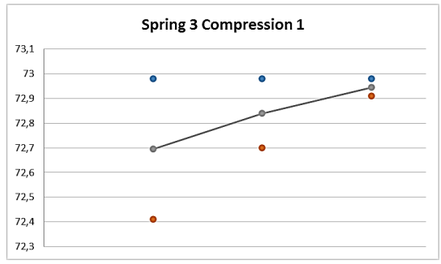
Spring 3 Compression 1
73,1
73
72,9
72,8
72,7
72,6
72,5
72,4
72,3

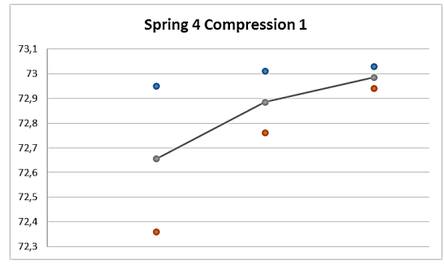
Spring 4 Compression 1
73,1
73
72,9
72,8
72,7
72,6
72,5
72,4
72,3

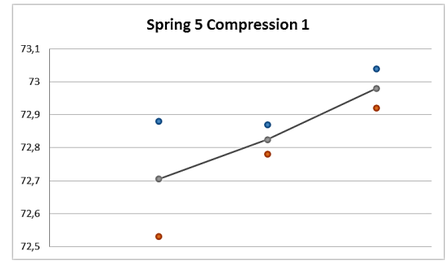
Spring 5 Compression 1
73,1
73
72,9
72,8
72,7
72,6
72,5

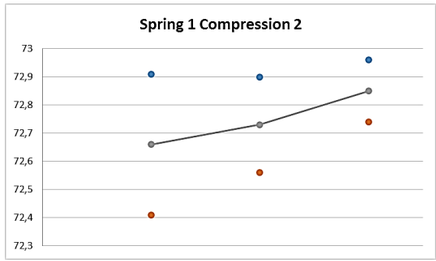
Spring 1 Compression 2
73
72,9
72,8
72,7
72,6
72,5
72,4
72,3

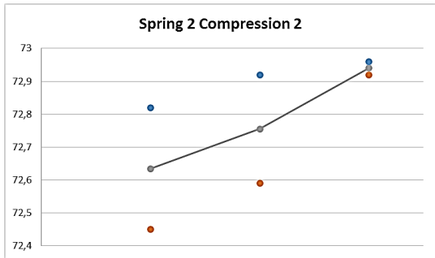
Spring 2 Compression 2
73
72,9
72,8
72,7
72,6
72,5
72,4

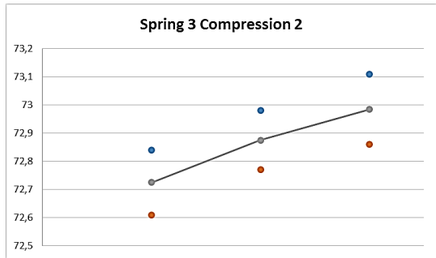
Spring 3 Compression 2
73,2
73,1
73
72,9
72,8
72,7
72,6
72,5

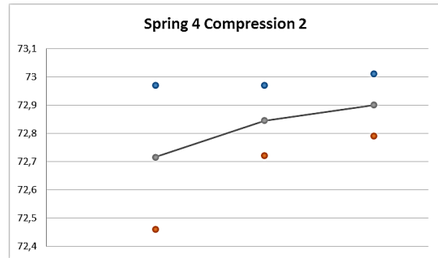
Spring 4 Compression 2
73,1
73
72,9
72,8
72,7
72,6
72,5
72,4

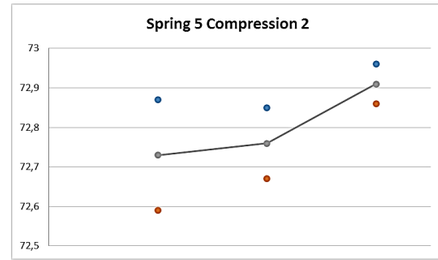
Spring 5 Compression 2
73
72,9
72,8
72,7
72,6
72,5

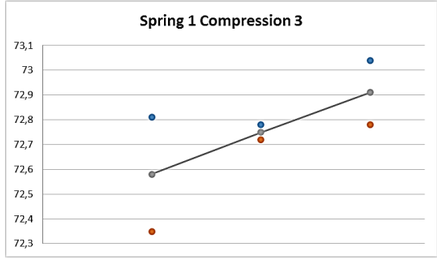
Spring 1 Compression 3
73,1
73
72,9
72,8
72,7
72,6
72,5
72,4
72,3

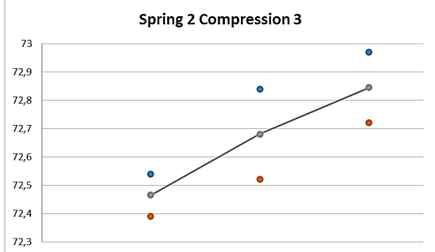
Spring 2 Compression 3
73
72,9
72,8
72,7
72,6
72,5
72,4
72,3

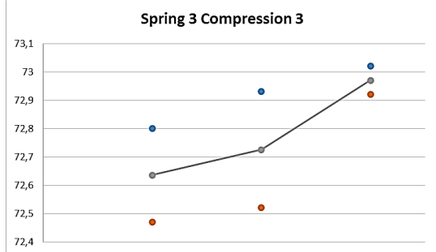
Spring 3 Compression 3
73,1
73
72,9
72,8
72,7
72,6
72,5
72,4

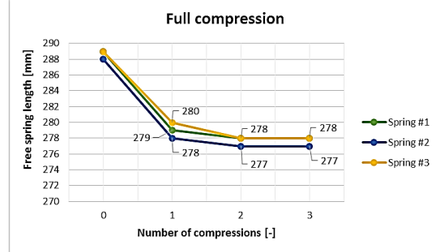
Full compression
Free spring length [mm]
290
288
286
284
282
280
278
276
274
272
270
280
279
278
278
277
278
277
0
1
2
3
Number of compressions [-]
Spring #1
Spring #2
Spring #3

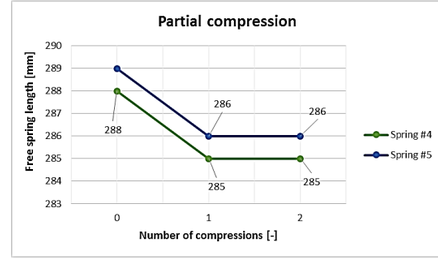
Partial compression
Free spring length [mm]
290
289
288
287
286
285
284
283
288
286
286
285
285
0
1
2
Number of compressions [-]
Spring #4
Spring #5

Conclusion

Now the research questions can be answered. They are restated below for convenience.

Research question: Does the spring shorten due to 'setting' and if yes, by what amount and why?

Sub-question: How does the diameter of the spring change during the cycle compression and is this change permanent?

Conclusion:

Spring setting
Spring gets shorter and the reduction in length is permanent. If the spring is set, by compressing it to the solid height + 10 mm, its length ranges between 285 and 286 mm according to the results. This is ideal since this is currently implemented in the design. If the compression stroke stays the same, the spring maintains its length. This can be deduced from the measurements for spring 4 and 5 when looking at the difference between compression 1 and 2. In this case, the length reduces 3 to 4 mm, while for the full compression, the length reduction ranges from 11 to 12 mm. This means that based on these results, the spring sets an additional 8 mm for the last 10 mm of the full compression stroke. Although the point at which yielding starts is still unknown, the predicted value of 13 mm above the solid height for plastic deformation seems very plausible. A picture taken at the experiment is shown in figure 5.10.

Figure 5.10: Spring end closed completely after compression and relaxation.
Left: uncompressed, Right: compressed and relaxed.

Diameter change
The grey lines in the graphs that indicate the averages of the diameter measurements shows that the diameter gets larger. The expansion is not permanent as the diameters measured at consecutive compressions does not increase but sometimes even seems to decrease, as is the case for spring 2. The overall increase in the averaged diameter is equal to 0.28 mm. This is somewhat higher than the predicted 0.20 mm, but still positive as predicted in the hypothesis. However, due to the difference in order of magnitude between the ranges of top and bottom measurements and the ranges of the increased spring diameter, this result is deemed inconclusive. Lastly, it can be seen in the graphs that the spring width still fits in the hole of 75 mm when compressed.

5.4. Cutter block modelling

5.4.1. Introduction

Before the cutter blocks are modelled, research needs to be done on the ideal angle of extension, the design of the gliding grooves and the geometry of the blocks themselves.

To begin with, the extension length is determined by the extension that is needed to reach a reaming diameter of at least 228.6 mm (9 inch). This determines the 'depth' of the block inside the core. The block also has to be wide enough to fit around the mud channel while the thickness of the lobes that fold around the channel may not be too small. Since the blades are configured back to side inside the reamer, the grooves will interfere with the neighbouring blocks. Therefore, the tongue-groove fitting could be reversed, such that the blocks are grooved and the core contains the tongues. However, for reasons of manufacturing, notches will be made on the backside of the blocks.

Each side of the UR block also has a specific function. The backside is straight, so that it is adjacent to the mud channel. The top sides of the block lie at an angle relative to the backside and each other. The side adjacent to the backside inclines under an angle, which determines the angle under which the UR extends. The top side that sticks out of the UR will have an angle that encourages the block to retract when the casing hits it during retrieval of the UR.

For a steep retrieval angle, the top angle can be relatively shallow, which eventually allows for an increased gage length along the outer side of the block. For a gentle retrieval angle, the angle of the top side may be steeper leaving less space for the side cutters or stabilizing gage structure. The steepness of the bottom side of the UR determines how many cutters can be fitted for drilling downwards. The same amount of formation rock is removed for each meter the UR descents, but the configuration of the cutters may determine whether the cutter gage pads are considered active or passive.

To examine the shape of the block further in terms of forces, a geometric model is established. This model is shown in figure 5.11. It shows how the block slides inward under the influence of a force that is exerted by the casing. This model represents a worst-case scenario, because the spring force that normally helps to retract the block is not present here.

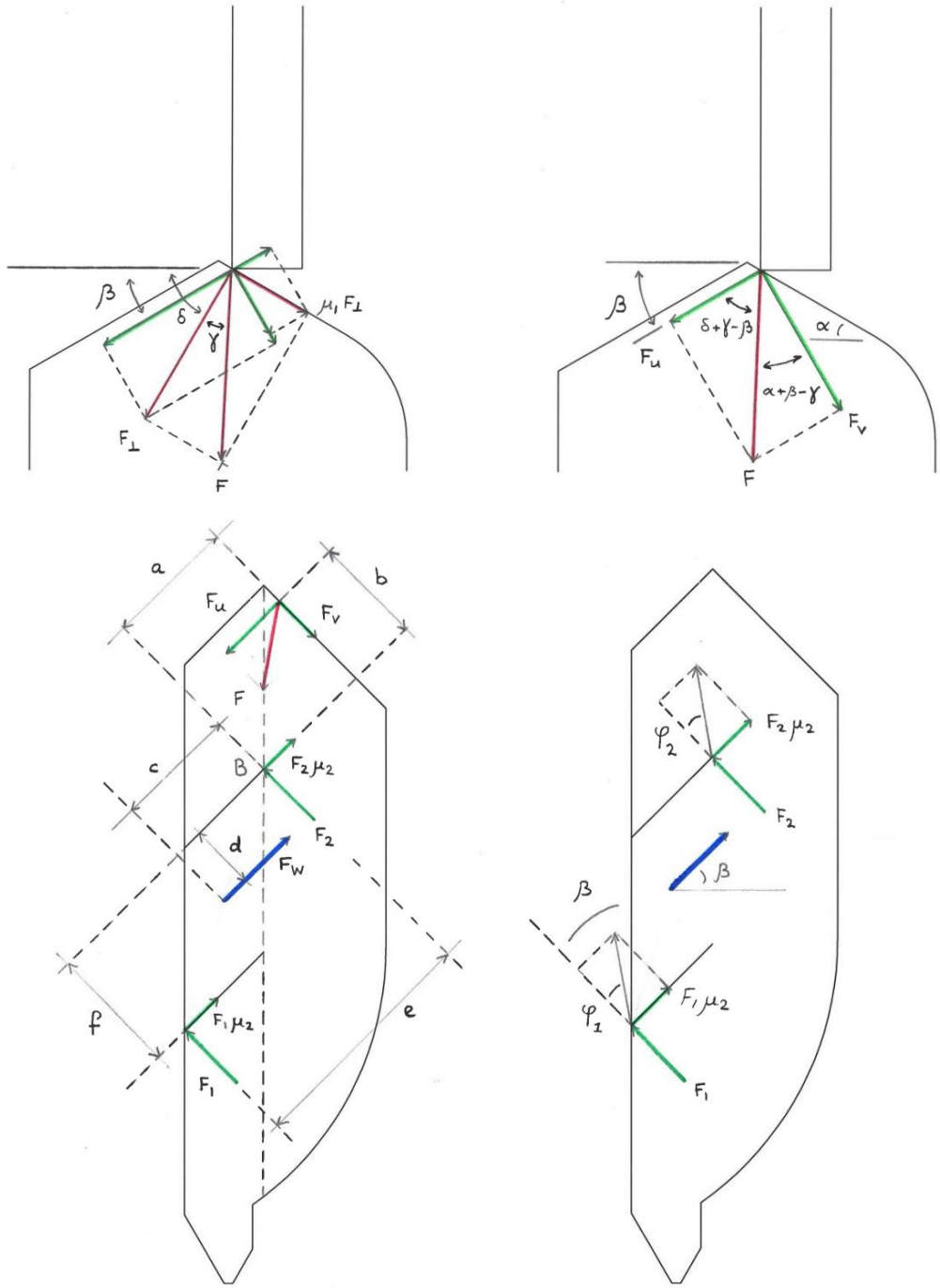

Figure 5.11: Geometric model of a block with two tongue groove fittings.

The angle γ can be determined if the friction coefficient μ_1 between the casing and the block is known. The angles α and β can be chosen freely and determine the desired block shape. The equilibrium of forces and moments can be used to determine the relation between the pulling force at the top of the UR and the friction and groove forces. It is assumed that both groove friction forces are calculated by using the same coefficient of friction $\mu_2 = 0.2$, because it is assumed that the internal surfaces are relatively smooth. The friction force along the block-casing interface is calculated by using a coefficient of 0.5, because it is assumed to be rough.

5.4.2. Cutter block - force analysis

Let us first analyse the contact point between the block and the casing. For this, the model in figure 5.11 is used. The model represents the moment just before the block starts moving. At this moment, the friction forces reach their maximum values. α is the angle between the top of the block and the horizontal. β is the angle between the slots/sliders and the horizontal, see figure 5.11.
For reason of convenience, the angle δ is introduced, see drawing. The relation between α and δ is:

$$\delta = 90° - \alpha \qquad [5.23]$$

Let us assume a force $F_\perp$ working normal to the top sliding face of the block, see figure.

Due to friction, a friction force works on top sliding face of the block in the plane of the sliding face and therefore normal to the force $F_\perp$. The magnitude of the friction force is $\mu_1 . F_\perp$, where μ_1 is the coefficient of friction between the casing and the top face of the block.

The total force on the top face of the block, called F, see figure, is the result of the normal force $F_\perp$ and the friction force $\mu_1 . F_\perp$. The angle between F and $F_\perp$is indicated as γ. The angle γ can be determined by the equation:

$$\gamma = \tan^{-1}\left(\frac{\mu_1 \cdot F_\perp}{F_\perp}\right) = \tan^{-1}\mu_1 \qquad [5.24]$$

The resultant force F can be decomposed in the forces F_u and F_v, where F_u works in the direction of the slots and F_v works perpendicular to the direction of the slots. With the help of the figure, the equations for the forces $F_u$and F_v can be determined as follows:

$$F_u = F\cos(\delta + \gamma - \beta) = F\cos(90° - \alpha - \beta + \gamma) = F\sin(\alpha + \beta - \gamma) \qquad [5.25]$$

$$F_v = F\sin(\delta + \gamma - \beta) = F\sin(90° - \alpha - \beta + \gamma) = F\cos(\alpha + \beta - \gamma) \qquad [5.26]$$

Let us now analyse the block as a so called “free body”. On the top of the block, the casing force F applies. Due to pollution between the block and the core, a friction force between the block and the core can be build up. Just before the block just starts moving, a maximum friction force F_w applies in the direction opposite to direction of motion. The point of application of the force F_w is assumed to coincide with the centre of gravity of the volume of the block that is in the core. The maximum friction force F_w is assumed to be independent of the other forces in the model.

In the slots/sliders, (reaction) forces will be build up. The points of application of the forces, and therefore their magnitudes can be dependant of several phenomena’s like the pollution between the slots and the sliders and manufacturing tolerances of the slots and the sliders. When the unknown influence of these kind of phenomena’s is ignored, the most likely points of application of the forces and the slots/slides are the points 1 and 2 as indicated in the model. The distance between these points is the largest. Therefore, due to setting, any play between slots and the sliders is assumed to be eliminated first at these points.

In the first approach, the normal (to the slots/sliders) forces $F_1$and F_2, (working on the block) are assumed to be positive in the direction as indicated in the model. The friction forces at the points 1 and 2 are always positive in the direction as indicated in the model. (This causes the model to be non-linear).

Depending on the geometry of the block, these forces also determine whether the block tends to rotate (clockwise or counter clockwise) or not.

Based on the equilibria of forces in direction of the slots/sliders ("u" direction) and in the direction perpendicular to that ("v" direction) and based on the equilibrium of moments about the point 2, the following equations can be derived:

$$F_u = F_w + \mu_2|F_1| + \mu_2|F_2| \qquad [5.27]$$

$$F_v = F_1 + F_2 \qquad [5.28]$$

$$F_v \cdot a + F_1 \cdot e = F_u \cdot b + F_w \cdot d + \mu_2 \cdot |F_1| \cdot f \qquad [5.29]$$

If, as said before, in the first approach, the forces $F_1$and F_2 are assumed to be positive in the direction as indicated, the equations above can be simplified and linearized. Afterwards, the assumption $F_1 > 0$ and $F_2 > 0$ have to be verified to conclude if this assumption, and therefore the analysis, is valid.

The equilibrium equations will be used in an Excel file to calculate values of F_1, F_2 and F_w for a certain value of F to determine in which orientation the highest amount of friction can be compensated. For both β and α, three different angles will be considered such that nine cases are threated. Depending on the sign of the value of F_1 and F_2, an appropriate set of equations is selected. In the end, one block shape is selected for the final design.

The process of going thru the nine scenarios is not straightforward. When the top side and groove angles change, the values of the internal distances (a, b, c, d and e) do also change and may even become negative. Although these values may can be determined with complicated trigonometric functions, it has been decided that these values are directly measured from Inventor drawings. The values for a certain combination of the angles β and α are presented in table 5.6.

Table 5.6: Block top angles and the corresponding block geometry.

		α					
		30°		45°		60°	
β	30°	a	35,5 mm	a	33,9 mm	a	32,7 mm
		b	54,5 mm	b	52,3 mm	b	50,3 mm
		c	31,8 mm	c	31,8 mm	c	31,8 mm
		d	28,3 mm	d	28,3 mm	d	28,3 mm
		e	63,6 mm	e	63,6 mm	e	63,6 mm
		f	56,7 mm	f	56,7 mm	f	56,7 mm
	45°	a	44,6 mm	a	43,6 mm	a	42,0 mm
		b	40,1 mm	b	39,1 mm	b	37,5 mm
		c	40,7 mm	c	40,7 mm	c	40,7 mm
		d	21,8 mm	d	21,8 mm	d	21,8 mm
		e	81,4 mm	e	81,4 mm	e	81,4 mm
		f	43,6 mm	f	43,6 mm	f	43,6 mm
	60°	a	47,8 mm	a	46,6 mm	a	44,6 mm
		b	23,9 mm	b	23,2 mm	b	22,1 mm
		c	50,6 mm	c	50,6 mm	c	50,6 mm
		d	13,8 mm	d	13,8 mm	d	13,8 mm
		e	101,2 mm	e	101,2 mm	e	101,2 mm
		f	27,6 mm	f	27,6 mm	f	27,6 mm

Case 1: $F_1 > 0$ and $F_2 > 0$

With the assumptions $F_1 > 0$ and $F_2 > 0$, the equations 5.27, 5.28 and 5.29 become:

$$F_u = F_w + \mu_2(F_1 + F_2) \qquad [5.30]$$

$$F_v = F_1 + F_2 \qquad [5.31]$$

$$F_v \cdot a + F_1 \cdot e = F_u \cdot b + F_w \cdot d + \mu_2 \cdot F_1 \cdot f \qquad [5.32]$$

From equation 5.30 and 5.31 follows:

$$F_w = F_u - \mu_2 \cdot F_v \qquad [5.33]$$

Knowing F_w as a function of F_u and F_v, the forces $F_1$and F_2 can also be determined as a function of F_u and F_v (and eventually F_w):

From equation 5.32 and 5.31 follows:

$$F_1 = \frac{F_u \cdot b + F_w \cdot d - F_v \cdot a}{e - \mu_2 \cdot f} = \frac{F_u(b + d) - F_v(a + \mu_2 \cdot d)}{e - \mu_2 \cdot f} \quad \text{(to be checked > 0)} \qquad [5.34]$$

$$F_2 = F_v - \frac{F_u \cdot b + F_w \cdot d - F_v \cdot a}{e - \mu_2 \cdot f} = F_v - \frac{F_u(b + d) - F_v(a + \mu_2 \cdot d)}{e - \mu_2 \cdot f} \quad \text{(to be checked > 0)} \qquad [5.35]$$

(Note that the forces F_u and F_v are known as a function of the casing force F)

Case 2: $F_1 < 0$ and $F_2 > 0$

In case $F_1 < 0$ and $F_2 > 0$, the equations 5.27, 5.28 and 5.29 become:

$$F_u = F_w + \mu_2(F_2 - F_1) \qquad [5.36]$$

$$F_v = F_1 + F_2 \qquad [5.37]$$

$$F_v \cdot a + F_1 \cdot e = F_u \cdot b + F_w \cdot d - \mu_2 \cdot F_1 \cdot f \qquad [5.38]$$

From equation 5.38 follows:

$$F_1 = \frac{F_u \cdot b + F_w \cdot d - F_v \cdot a}{e + \mu_2 \cdot f} \qquad [5.39]$$

Equation 5.37 can also be written as:

$$F_v = (F_2 - F_1) + 2F_1 \qquad [5.40]$$

Therefore:

$$(F_2 - F_1) = F_v - 2F_1 = F_v - 2 \cdot \frac{F_u \cdot b + F_w \cdot d - F_v \cdot a}{e + \mu_2 \cdot f} \qquad [5.41]$$

Substituting the last expression for $(F_2 - F_1)$ in equation 5.36 leads to the equation:

$$F_u = F_w + \mu_2 \left(F_v - 2 \cdot \frac{F_u \cdot b + F_w \cdot d - F_v \cdot a}{e + \mu_2 \cdot f}\right) \qquad [5.42]$$

From this equation (5.42), F_w can be solved as a function of F_u and F_v:

$$F_w = \left(F_u - \mu_2 \left(F_v - 2 \cdot \frac{F_u \cdot b - F_v \cdot a}{e + \mu_2 \cdot f}\right)\right) \cdot \frac{1}{1 - \frac{2.\mu_2 \cdot d}{e + \mu_2 \cdot f}} \qquad [5.43]$$

Knowing F_w, F_1 can be solved using equation 5.39. After that, F_2 can be solved using equation 5.37.
It has to be checked that $F_1 < 0$ and $F_2 > 0$. If these conditions are not met, the analysis is not valid.

Case 3: $F_1 > 0$ and $F_2 < 0$

In case $F_1 > 0$ and $F_2 < 0$, the equations 5.27, 5.28 and 5.29 become:

$$F_u = F_w - \mu_2(F_2 - F_1) \qquad [5.44]$$

$$F_v = F_1 + F_2 \qquad [5.45]$$

$$F_v \cdot a + F_1 \cdot e = F_u \cdot b + F_w \cdot d + \mu_2 \cdot F_1 \cdot f \qquad [5.46]$$

From equation 5.46 follows:

$$F_1 = \frac{F_u \cdot b + F_w \cdot d - F_v \cdot a}{e - \mu_2 \cdot f} \qquad [5.47]$$

Substituting this expression in the equations 5.44 and 5.45, in a similar way as done for the case $F_1 < 0$ and $F_2 > 0$, F_w can be solved as a function of F_u and F_v:

$$F_w = \left(F_u + \mu_2\left(F_v - 2 \cdot \frac{F_u \cdot b - F_v \cdot a}{e - \mu_2 \cdot f}\right)\right) \cdot \frac{1}{1 + \frac{2 \cdot \mu_2 \cdot d}{e - \mu_2 \cdot f}} \qquad [5.48]$$

Knowing F_w, F_1can be solved using equation 5.47. After that, F_2can be solved using equation 5.45.

It has to be checked that $F_1 > 0$ and $F_2 < 0$. If these conditions are not met, the analysis is not valid.

Additional lifting force

In order to optimize the shape of the block, we like to know the relation between the additional lifting force on the core and the maximum friction force (F_w) that can be overcome. In this case, additional lifting force means the force additional to the force needed to overcome gravity and friction of the pipe in the bore hole et cetera.

An additional lifting force, in order to retract the blocks in the core, of $^1/_3\, F_{lift}$ for each block is assumed. Bases on equilibrium of the vertical forces the relation between casing force F and the additional lifting force $^1/_3\, F_{lift}$ (both per block) can be derived:

$$F = \frac{^1/_3\, F_{lift}}{\sin(\gamma + \delta)} \qquad [5.49]$$

In the calculations, a fixed value for the addition lifting force per block ($^1/_3\, F_{lift}$) is assumed. From this, the casing force F can be calculated using equation 5.49. Thereafter, the forces F_u and F_v can be calculated using the equations 2 and 3. Using the appropriate equation (check validity via the conditions for F_1 and F_2), the maximum friction force F_w that can be overcome with the assumed additional lifting force per block can be determined.

The maximum friction force that can be overcome equals (in magnitude) the retraction force caused by the additional lifting force. So the higher the maximum friction force calculated for a certain additional lifting force, the higher the retraction force. From the point of view of retraction, a block shape causing a high retraction force ($= -\overrightarrow{F_w}$) at a certain additional lifting force, is advantageous.

Conclusion

With the parameters that are presented above, the friction force and the groove forces can be determined. A total pulling force of 3000 N was used. The results of the calculations are shown in table 5.7.

The results have been verified with a solver in excel. For case 1, the results are shown in blue. When F_1 or F_2 has a negative value, the adapted equations are used. The sign of the value of F_1 or F_2 should automatically be negative in case one of these forces points in the direction opposite of the direction indicated in the drawing. For example, F_2 and $F_2\mu_2$ are related but since F_2 may change direction while $F_2\mu_2$ may not, a correction factor (-1) needs to be added in the equation in front of $F_2\mu_2$ such that $F_2\mu_2$ is always directed opposite to the direction of movement. When using an algorithm that assumes F_1 or F_2 is negative, it needs to be checked in the end that this is indeed the case.

Table 5.7: Calculation results.

		α					
		30°		45°		60°	
β	30°	Friction	384,7 N	Friction	648,8 N	Friction	739,8 N
		F1	231,5 N	F1	688,2 N	F1	1097,8 N
		F2	604,5 N	F2	11,1 N	F2	561,9 N
	45°	Friction	616,6 N	Friction	845,7 N	Friction	924,3 N
		F1	190,6 N	F1	478,5 N	F1	744,4 N
		F2	474,0 N	F2	7,1 N	F2	504,1 N
	60°	Friction	806,4 N	Friction	960,4 N	Friction	1000,4 N
		F1	116,5 N	F1	286,3 N	F1	453,5 N
		F2	331,5 N	F2	75,0 N	F2	525,3 N

Now that the forces have been computed, the most promising option to proceed with has to be determined. Nine cases have been considered where both top angles range between 30 and 60 degrees. It can be seen that the case in which F_1 is negative does not occur for any of these sets. The cases in which F_2 becomes negative are shown in yellow.

The angle α can be related to length of the gage structure on the side of the block. Since the block height is assumed constant, having a high α may result in a decreased gage length, which causes the reamer to become unstable in the hole. When β becomes high, the slot length of the block increases, which in the end increases the length of the UR. Therefore, combinations involving angles of 60 degrees are left out of consideration. Low angles may however be undesirable when looking at the force component of the spring that has retract the block. Higher angles of β will result in a larger force component capable of pushing the block.

Stability is considered more important than friction because the amount of friction and the location of the friction force cannot be determined accurately. Since the spring that helps with retracting the blocks will be present in the actual reamer to counteract the friction force, an angle α of 30 degrees is preferred. Thus, a combination of **β = 45°** and **α = 30°** is chosen for the final design.

5.5. UR components

5.5.1. Introduction

In this sub-chapter, the most important conceptual design considerations are discussed. The objective is to find the most favourable combination of design options. The function of each individual part plays a key role in the decision making process. In many cases, design changes succeed each other. The design decisions will be justified by logical reasoning and calculations.

5.5.2. Upper-core

The upper core is one of the main parts of the UR assembly, see figure 5.12. It is separated from the rest of the core body so that it can be removed during assembly and maintenance. The part is located at the top, since the body diameter and wall thickness there is larger than at the bottom. Since there are no restrictions on the hole diameter at the top, all internal parts can be inserted from here. Another important reason follows from the decision of the placement of the piston. Since the piston is designed to be in the lower part, it is desired that no transitions between parts are present along the gliding surface of the piston.

The upper-core consists of a pin connection and clamping surfaces for the c-plate, to connect the UR to other parts of the BHA. On the inside, a threaded hole for the connection of the mud channel is present. An outside API thread connection is present to connect the upper part to the bottom part, by means of a double-shouldered connection. This type of connection enhances the distribution of the load across the thread and increases the torsional capacity when compared to standard API RSC connections.

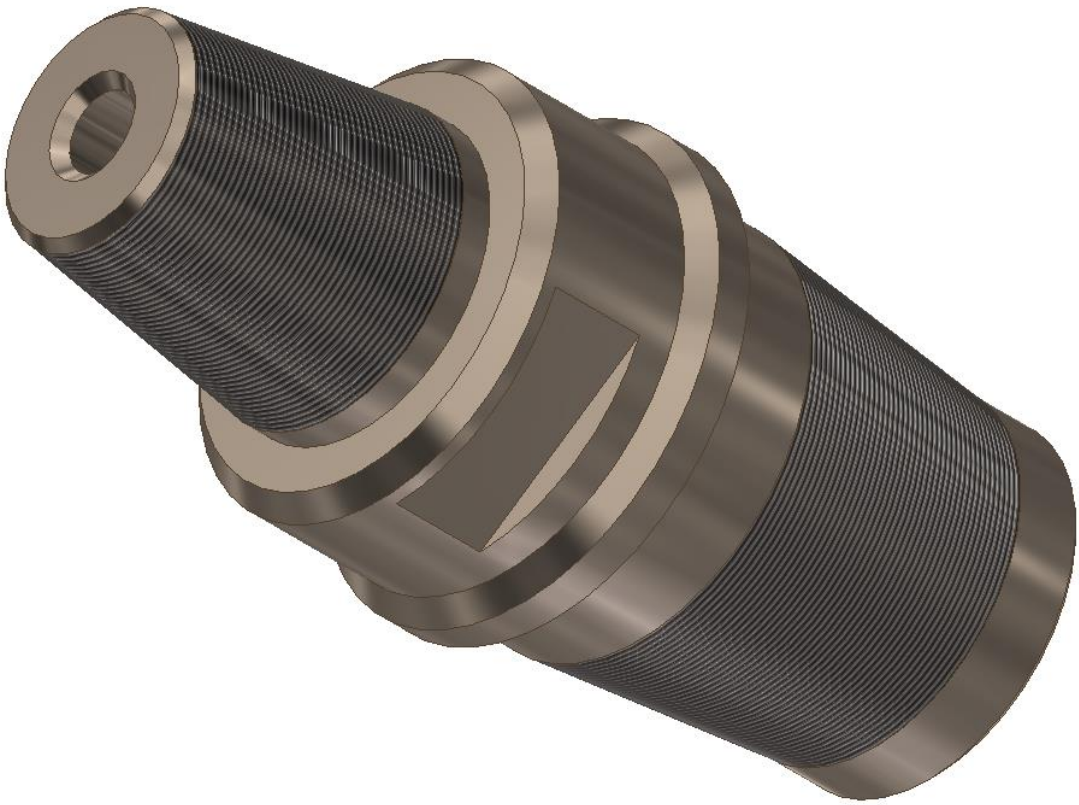

Figure 5.12: Upper-core.

5.5.3. Bottom-core

The main part of the reamer is comprised of the bottom-core. The bottom-core also houses the complete extension mechanism. This includes the spring, the piston, the links and the cutter blocks. The bottom-core has been developed from scratch. During first stage of the conceptual design, the outer contour had to be determined. The second stage was mainly concerned with the space required for the internal parts. Because the shape and the location of these objects changed many times, the bottom-core was continuously in development. The third stage was about fine-tuning the conceptual design. This meant slight adjustments had to be made for all the parts to fit properly.

At first, the idea was to move the blocks up as far as possible. At this point, it was already decided that some parts needed to be inserted through either the top or bottom of the core assembly. Since there was no room for a cap at the top, the bottom of the core was designed such that it could be disconnected. This is shown in figure 5.13.

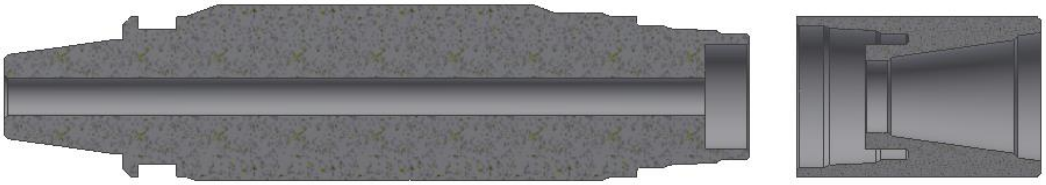

Figure 5.13: Core assembly consisting of top and bottom sub.

Because the piston-spring assembly was still assumed to be at the bottom at this stage, a large portion of the top segment remained unused. For this reason, the spring was disconnected from the piston and moved to the top. Due to the length of the spring however, it had to be placed all the way into the pin connection of the top sub. Otherwise, the UR would not get shorter. Another consequence of this decision is that the blocks had to be moved down. This is shown in figure 5.14.

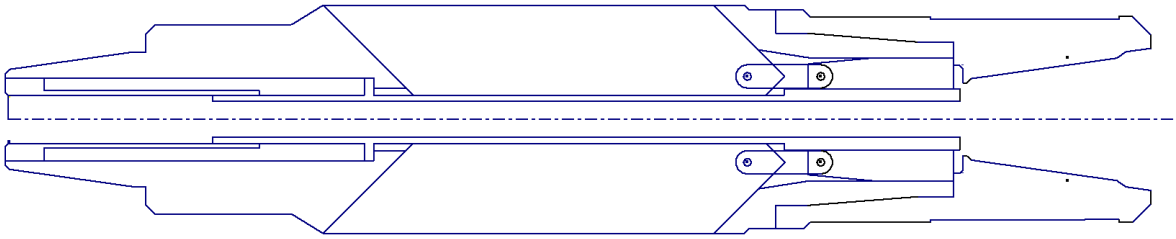

Figure 5.14: Spring moved to the top of the UR.

It can be seen that the piston and spring have to be connected in some sort of way to transfer the spring force to the piston. While keeping in mind the space the cutters would take up, it was decided that part of the mud channel should become part of the piston assembly. A collar around the top of the top would function as a resting position for the spring. This longer tube would have to slide along a shorter tube of large outside diameter. The short tube can be screwed on to the top. In that way the longer tube may also be inserted from the top. This will be important for assembly at a later stage.

Upon closer inspection, it became clear that the pin connection would be weakened too much by putting parts all the way into the top of the core. This meant that the hole had to be lowered, and that the UR would become longer. The sketch in figure 5.15 shows how the conceptual design was modified.

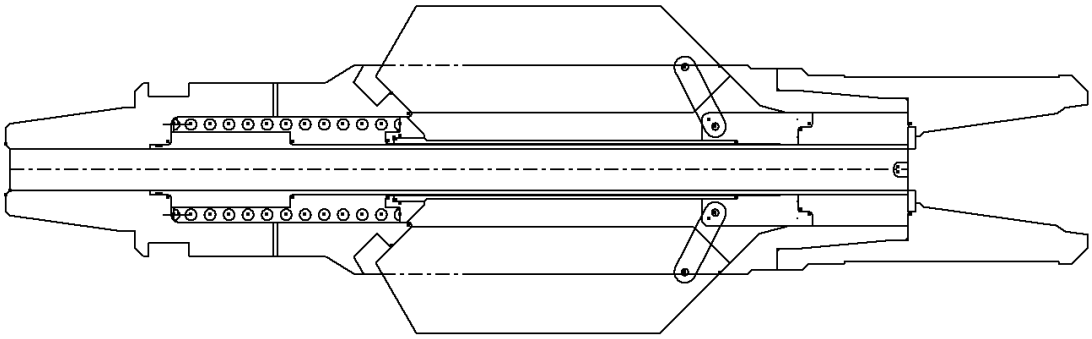

Figure 5.15: Spring moved down.

It can also be seen that channels have been drilled to the spring chamber. This was done to prevent a build-up of pressure inside the chamber. The collar around the mud channel has now been made detachable so that all parts could be fitted in from the bottom of the UR. The bottom is now also fitted with a ring, such that the mud channel is constraint in the vertical direction. The nozzle that was present in the base-case design is not considered from now on. There are three reasons for this. From tests, it is known that there is too much power loss. The pressure drop over the bit will decrease. In clay soils, the poor hydraulics could eventually lead to bit balling. This causes an increase in torque and decrease in ROP. Secondly, the nozzle stream only stirs up the cuttings around the UR, since the nozzles are originally directed downwards. This is not advantageous for the transportation of the cuttings. The third reason has to do with space requirements, since the nozzles leave the mud channel under a shallow angle. No reasonable path was found for the nozzles to fit through.

Next, the influence of the links was investigated. Links of different lengths were attached to the piston, to get an idea of the extension angle and the path of movement. This is shown in figure 5.16. In the end, it was decided that the extended angle should not be larger than 45 degrees for reasons of retractability and overloading. This meant the coupling rod would need to be 58.37 mm long.

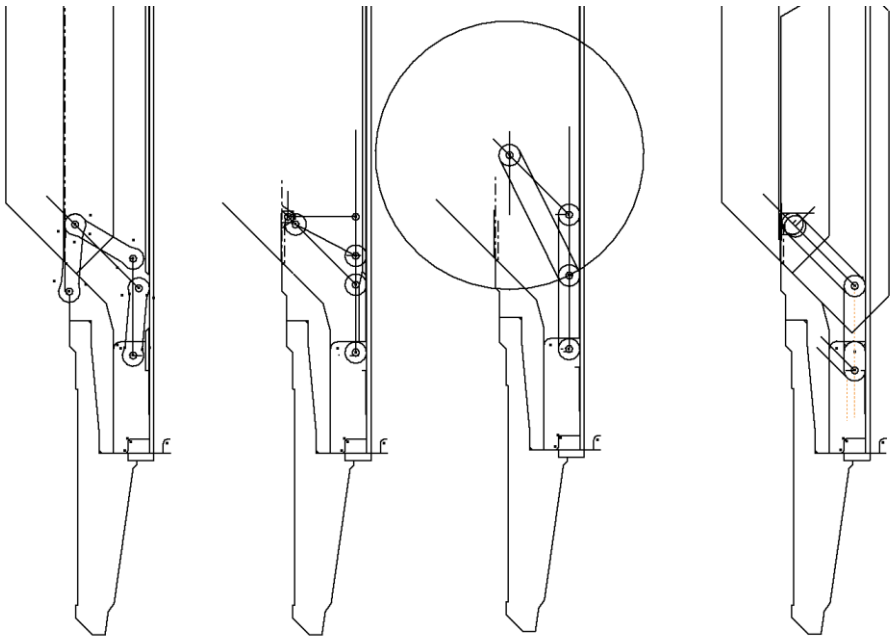

Figure 5.16: Sizing of the links.

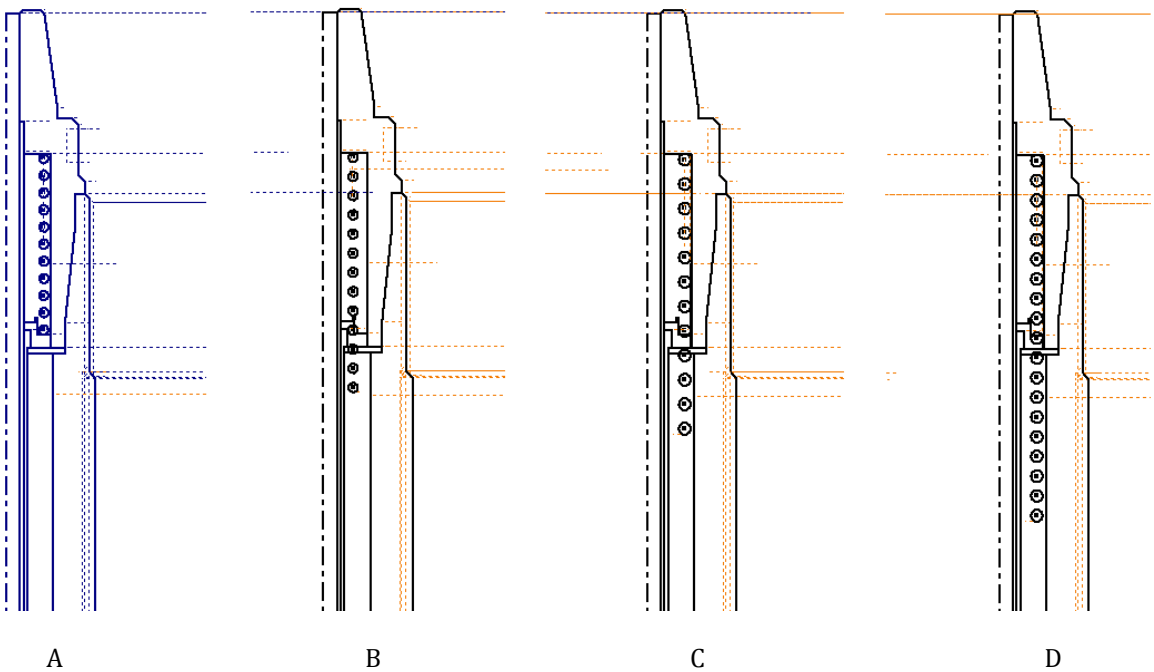

Figure 5.17: Sizing of the spring.

With choosing the links, a choice was also made for the spring. The springs were drawn in sketches according to the specifications of the manufacturer. Setting was not taken into account for the reference spring (figure 5.17 A). Since the length of the coupling rod was already selected, based on the sketches and the derivation in chapter 5.3.1, the springs could be drawn in their pretension state.

Table 5.8: Spring selection parameters.

Spring in conjunction with a 58.37 mm coupling rod							
Manufacturer	Product number	Wire diameter [mm]	Mean spring diameter [mm]	Solid length [mm]	Set accounted for [mm]	Pretension length [mm]	Material
Alcomex	D7120	8	63	91.10	0	149.47	VST
Tevema	D24360	8	50	132.37	10	200.74	RVS
Tevema	**D24610**	**10**	**63**	**165.67**	**10**	**234.04**	**RVS**
Tevema	D24620	10	63	235.54	10	303.91	RVS

Based on the sketches and pressure requirements, the spring of Tevema with product number D24610 was chosen to work with.

Now that the dimensions for the internal parts have been determined, the bottom-core contour can be drawn and revolved in Inventor, resulting in its first rough shape. From this solid, parts need to be cut-extruded to make room for the cutter blocks, the arm stoppers and the piston assembly.

Since the diameter of the bottom-core varies along the length, pockets have to be made between the blocks to allow for the upward fluid flow. Before any of the other components are fitted in the bottom-core, the depth of these grooves needs to be determined.

Annulus flow area

The outer diameter of the conceptual UR design plays a critical role, as the pressure drop would increase for a smaller annulus. At some points, the bottom-core will be thicker to house the cutter blocks. This means that for other segments along the perimeter, the diameter needs to be smaller for compensation. The effects of the blocks sliding out is neglected as for now. The intention is to prevent high surge or swab pressures. As a rule of thumb, the flow area around the UR should be equivalent to the case of a drill string with an outer diameter of 5.5 in, suspended in a 6-inch pilot hole. The flow area is given by:

$$A_{flow} = \frac{\pi}{4}\left(D_{pilot\ hole}^2 - D_{drill\ string}^2\right) = 2.914 \cdot 10^{-3}\ m^2 \qquad [5.50]$$

It follows that an annulus area of at least 2914 mm² is required. Drawings of the most critical cross-section of the UR core part are made. It is assumed that the cross-section can be divided in six equal sectors, three of which will be larger in diameter because of the cutter-block slide out at these locations. The three remaining sectors will have a smaller diameter to compensate for this. Cross-sections for different UR outer diameters are shown in figure 5.18. The hatched area indicates the annulus flow area, which is approximately equal in all three cases.

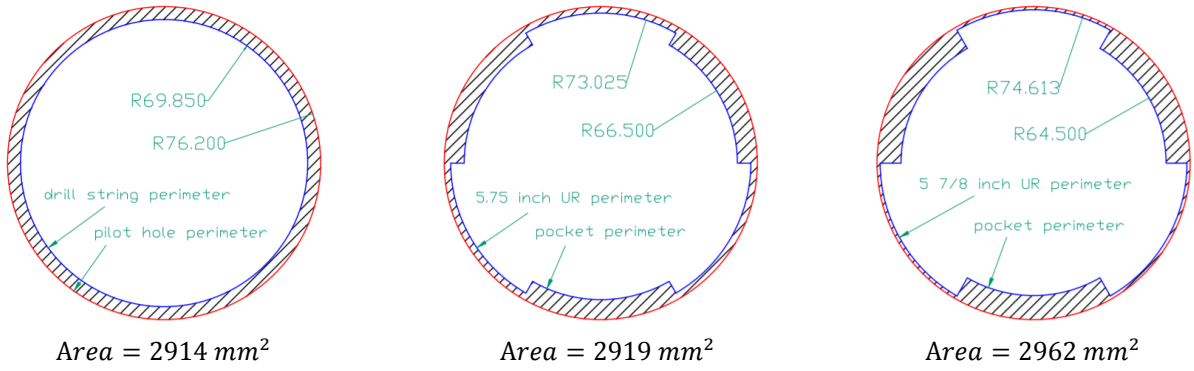

$Area = 2914\ mm^2$ $\qquad$ $Area = 2919\ mm^2$ $\qquad$ $Area = 2962\ mm^2$

Figure 5.18: Cross-sections with flow area (hatched) bounded by the pilot hole contour (red) and UR contour (blue).

The smallest diameter, the pocket diameter, can now be determined. In case the outer diameter of the UR equals 5 ¾ in, this means that the following equation should hold:

$$A_{flow} = \frac{\frac{\pi}{4}\left((D_{UR})^2 - (D_{pocket})^2\right)}{2} + \frac{\pi}{4}\left((D_{pilot\ hole})^2 - (D_{UR})^2\right) \qquad [5.51]$$

$$\rightarrow D_{pocket} = \sqrt{-\frac{8}{\pi}\left(\frac{\pi}{4}\left((D_{pilot\ hole})^2 - (D_{drill\ string})^2\right) - \frac{\pi}{4}\left((D_{pilot\ hole})^2 - (D_{UR})^2\right)\right) + (D_{UR})^2} \qquad [5.52]$$

In case the outer diameter of the UR equals 5.75 in, a pocket diameter D_{pocket} of 133 mm is found. In case the outer diameter of the UR is enlarged to 5 $^7/_8$ in, the pocket diameter becomes 129 mm. Working with these numbers, the annulus flow area for the 5.75 in UR becomes 2919 mm² while the flow area for the 5 $^7/_8$ in UR becomes 2962 mm², which meets the requirement mentioned above. This has also been indicated in figure 5.18.

Now that the depth of the pockets has been determined, the cut-extrusions for the blocks and armstoppers can be made. This results in the model shown in figure 5.19.

Figure 5.19: Conceptual design of the bottom-core.

Now that the second stage has been completed, the model can be fine-tuned. For purposes of manufacturing and assembly, several small changes were made. These are shown in figures 5.20, 5.21 and 5.22.

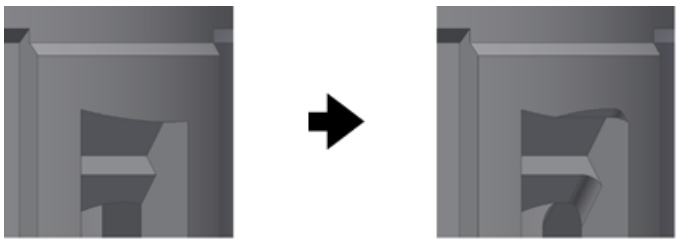

Figure 5.20: Fillets added to the slots.

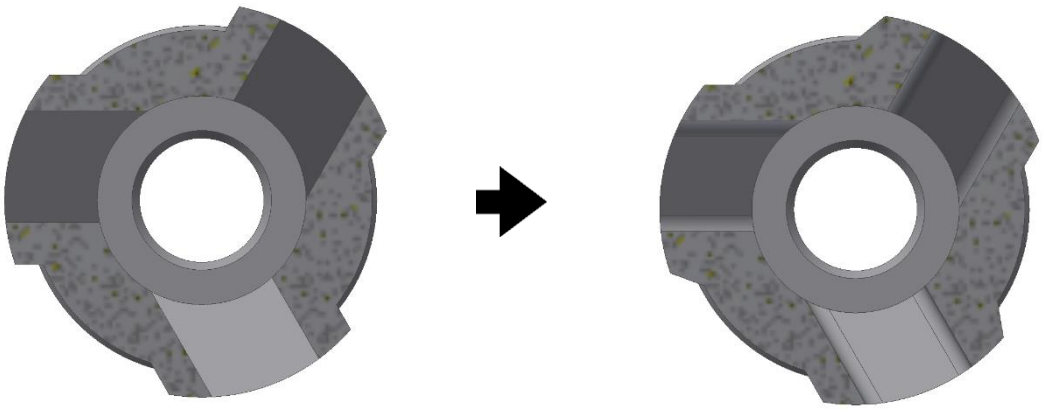

Figure 5.21: UR contour adjusted for manufacturing.

Figure 5.20 shows how fillets are added at the edges along which the block slides. These fillets were also added inside the pockets in a later stage. Figure 5.21 shows how the outer contour has been adapted for ease of manufacturing.

Because the blocks are sliding through the bottom-core by means of a tongue-groove sliding connection, extrusions also have to be made along the sides of the block slots. This is shown in figure 5.22.

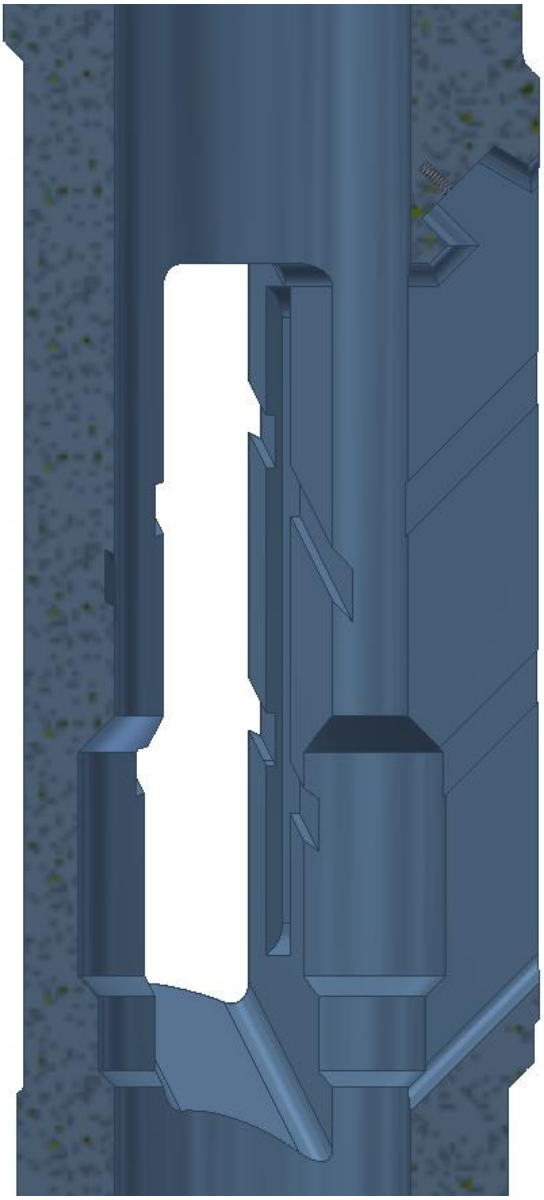

Figure 5.22: Section view of the internal grooves. The pin connection is located at the top of this picture.

Along with these grooves, the bore was widened locally to accommodate for folding out the coupling rods. This can be done by using a technique called boring. For the installation of the blocks, it is necessary for them to move a little bit inside the slot. For this to happen, additional grooves where made that run from the top to the bottom. These grooves will intersect with the sliding grooves for the rails of the blocks.

This is not a problem because in the extended position of the blocks, the ridge on the backside will rest on the side of the groove.

5.5.4. Block

The cutter blocks contain the PDC cutters that are used to cut the formation rock. In passive mode, the blocks remain retracted inside the core assembly. Once the pressure on the piston reaches about 7.2 bar, the links will push the blocks outward along a tongue-groove fitting. These fittings are located on the sides of the block. The shape of the block depends amongst others on the angle under which the block slides out and the angle for which the casing can push down the block back into the reamer body. Since the blocks are activated by links, there needs to be a pocket and a connection point. The blocks also fold around channels internally, meaning that a semi-circular cut out is needed at the back of the block.

The analysis of the block start with sketching different shapes of the contour of the block. The sketches are presented in figure 5.23. The blocks are drawn for their fully extended position. The bottom angles of the blocks have not been changed in the figure below.

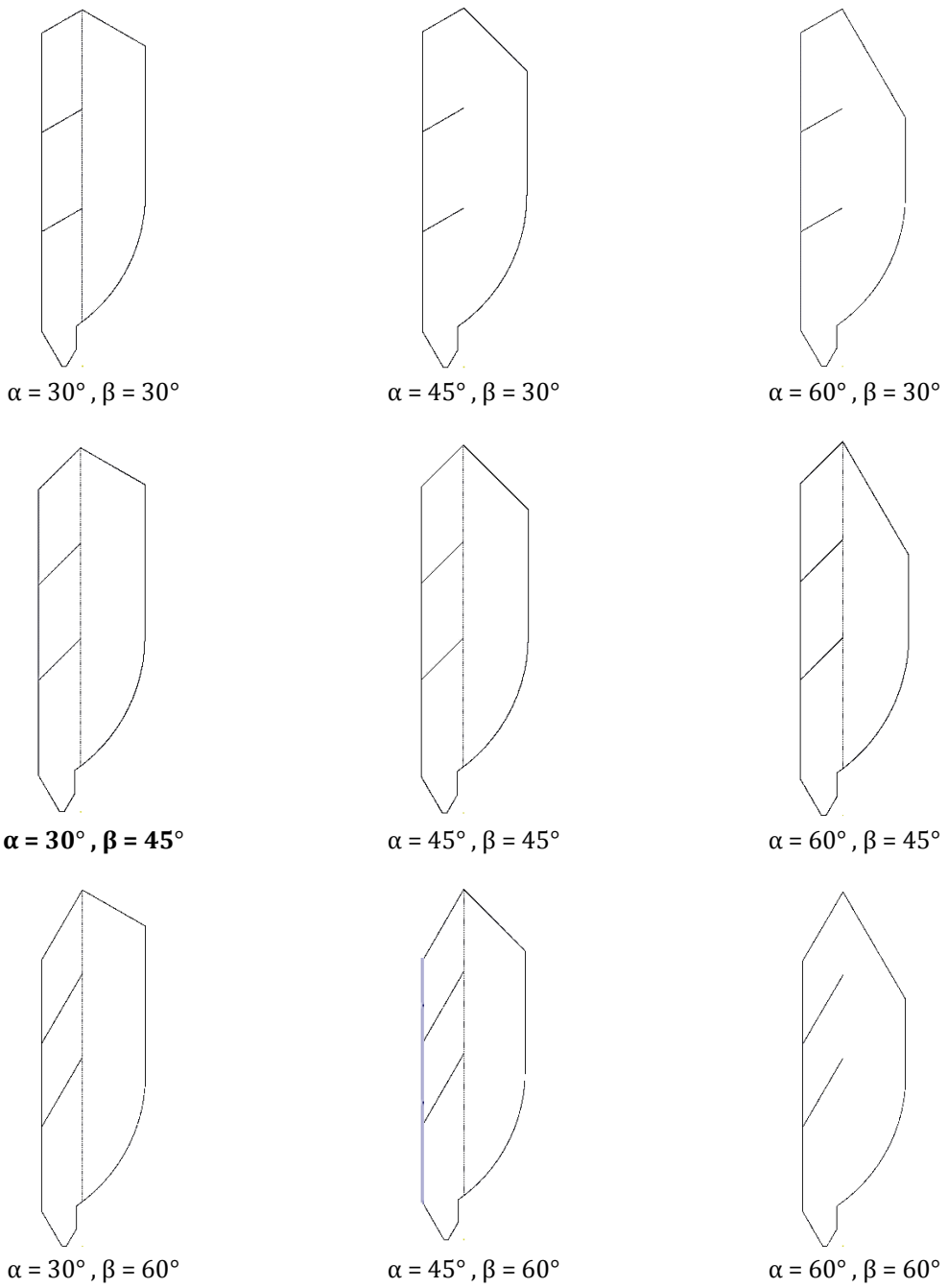

Figure 5.23: Sketches of the block shapes with varying top angles.

From the analysis in chapter 5.4.2. it was decided that a block with top angles of α = 30° , β = 45° is the most favourable shape. This resulted in a first rough 3D model of the block, see figure 5.24.

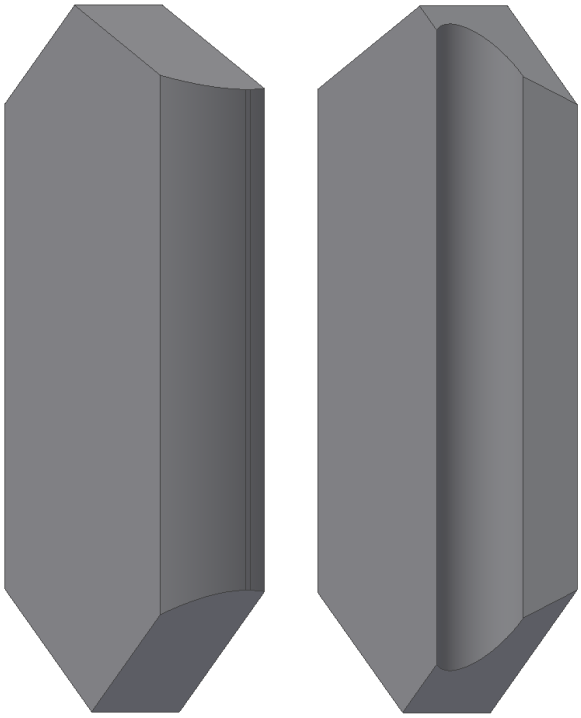

Figure 5.24: Rough 3D model of the cutter block.

For the connection of the links, a pocket needs to be cut out. Since the sleeve channel was supported by legs at this stage, at long groove over a large portion of the block is present. This is shown in figure 5.25.

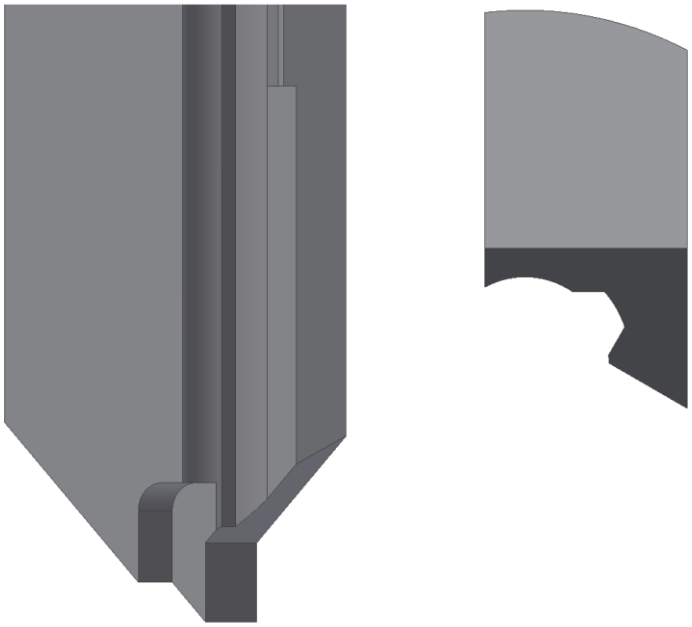

Figure 5.25: Block with room for the link connection (left) and cut out for the support legs (right).

Next, a hole for the pin connection was made, see figure 5.25. This hole is continuous and causes an opening on the side of the block that is exposed to the harsh environment outside of the core. Because this hole lies close to the location of the cutters, this could be a problem since the cutters are brazed on to the block. As high temperatures may cause this hole to deform it is not suitable for high precision holes. With this in mind, the idea of the hole was rejected. Instead, only a small groove was cut out from the block. Because a short pin at the end of the link would cause high bending stresses, the pin was changed into a semi-circular protrusion. This is shown in figure 5.26. To accommodate for the broad base of the link, an extra extrusion had to be made at the bottom of the block.

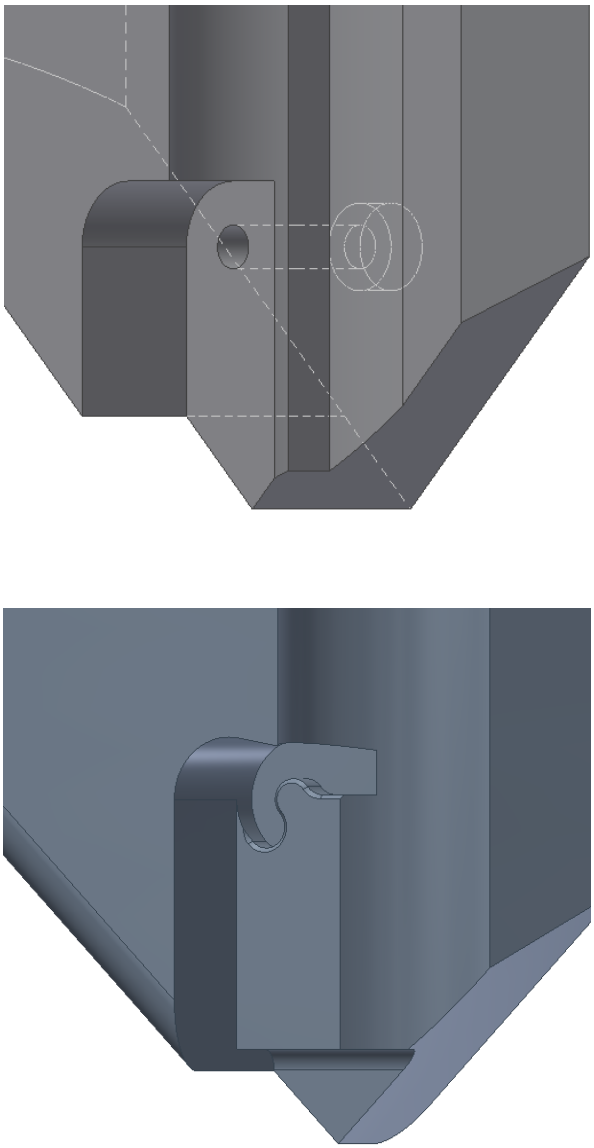

Figure 5.26: Connection for the coupling rod.

Now that the connection for the coupling rods has been made, the outside surface could be looked at. By applying a fillet to the outside surface, a double curved shape is obtained. At this stage, the tongue-groove connection rails can also be attached to the sides of the block. Later on, more cut-outs were made for the blocks to slide along each other and a groove on the side was made for purposes of assembly. The PDC cutters were finally added for aesthetic purposes. The rough block and detailed block are shown in figure 5.27. The picture on the right side shows a dual row block with a single active gauge row. Depending on the purpose of the blocks, the layout of the cutters may be changed.

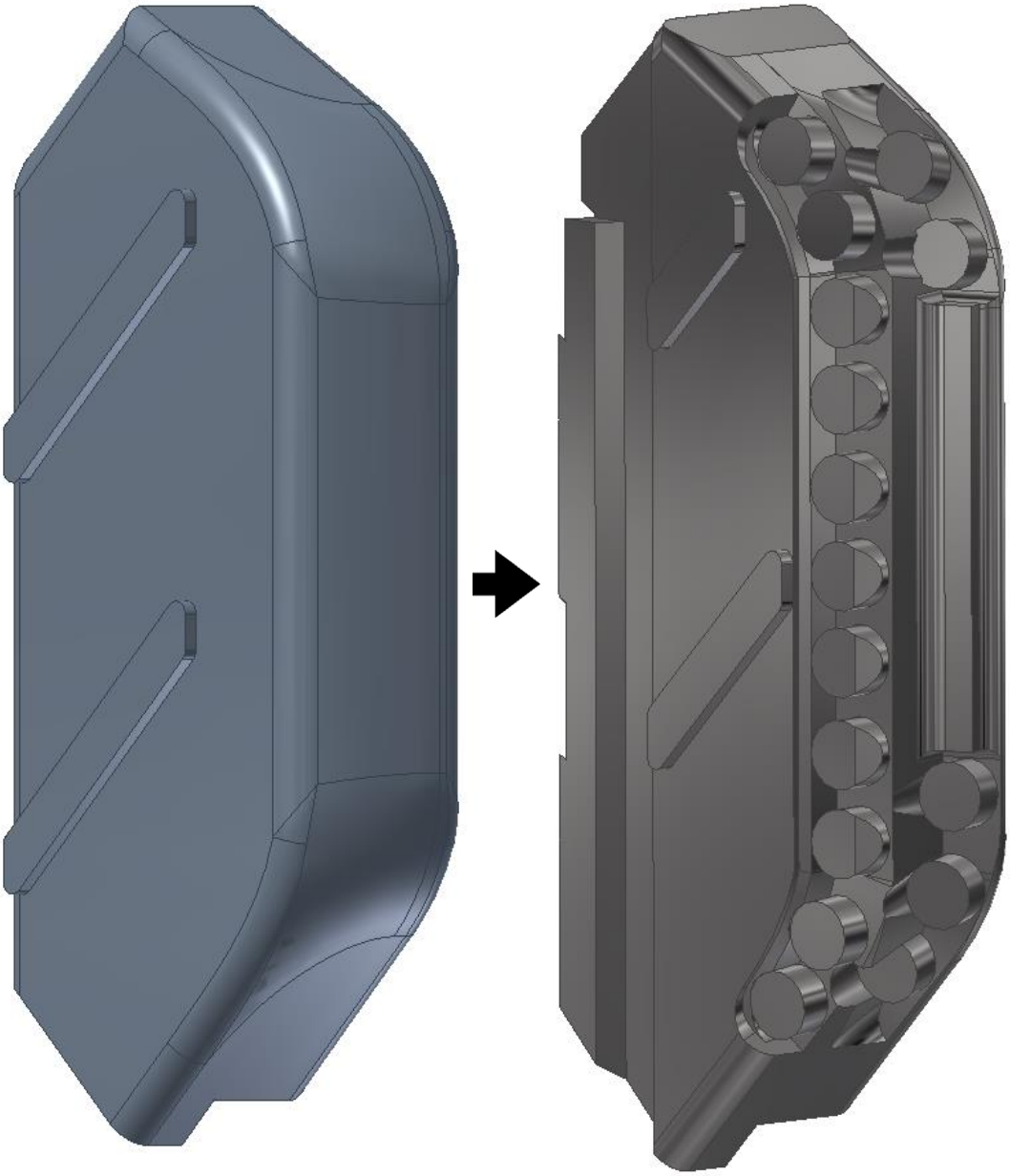

Figure 5.27: Rough shape (left) and detailed shape (right) of the cutter block.

5.5.5. Armstopper

The arm stoppers are located above the blocks inside a pocket in the core-assembly. Their main purpose is to prevent the cutter blocks from sliding out of the core body. The arm stopper is connected to the core body by means of bolts. This is because the armstoppers need to be detachable for maintenance purposes. The blocks can only be inserted when the armstoppers are taken out. Some concept sketches are shown in figure 5.28.

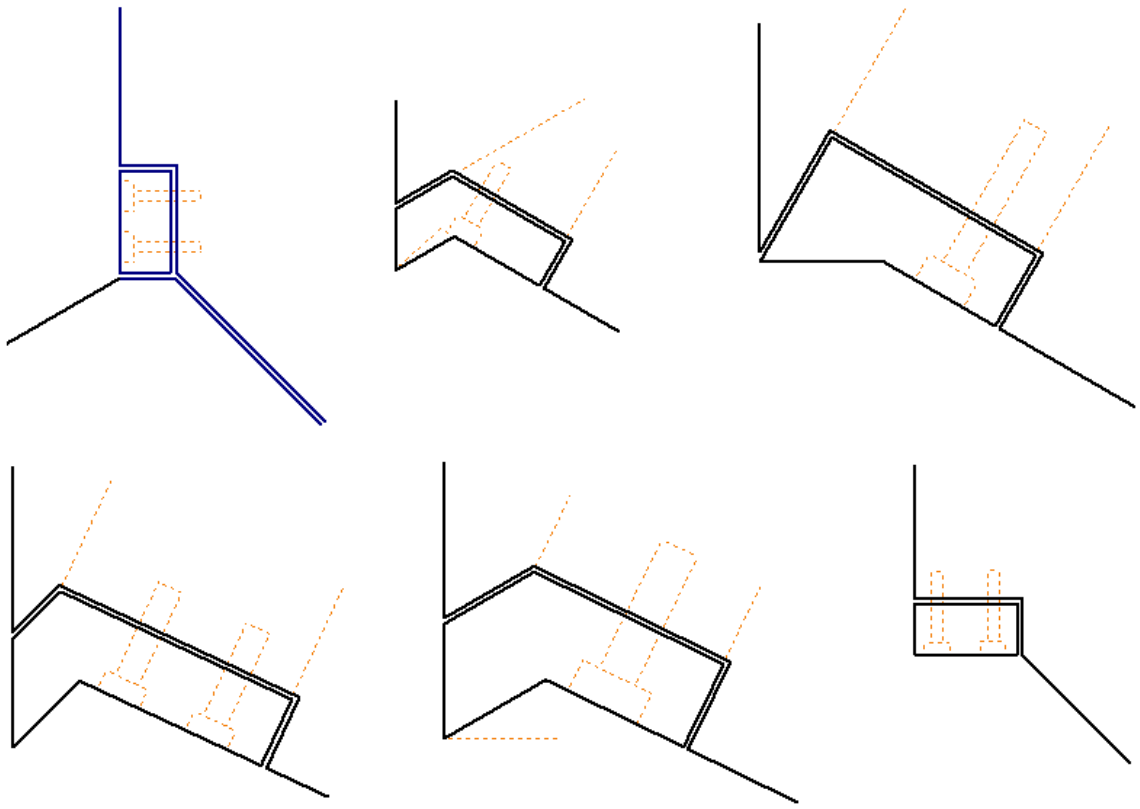

Figure 5.28: Arm stopper concepts.

It can be seen that different parameters can be changed that alter the shape of the arm stopper. The top left concept shows how two bolts are used to connect a rectangular shaped arm stopper. Friction between the arm stopper and cutter block causes the bolts to become loaded in tension. The top middle concept has been derived from the base-case design. Two bolts placed behind each other are used to fasten the arm stopper. In this concept, the top angle and bottom angle are not parallel and the head socket is partially cut out of the supporting surface. The top right design shows how the top left plane and bottom plane are parallel. The supporting surface has also been made horizontal. The force on the arm stopper will be higher, but is also directed more towards the core body of the UR, which will lower the load on the protrusion on the outside. The lower left concept has a longer bottom section. Bolts can be placed further away from the rotation point, which is assumed to be at the top corner of the arm stopper. The bottom middle concept shows how a large single bolt is used in the middle of the arm stopper. Lastly, the bottom right concept illustrates how the stopper from the top left figure could be rotated by 90 degrees. In this case, the bolts are predominantly loaded in shear.

Because the bore inside the core has a large diameter, the bolts need to be placed as high as possible on the arm stopper. For manufacturing, the bottom surface needs to be orientated perpendicular to the pocket surface while the top angle may have a slight angle to direct the force inwards. The support surface and top plane have been designed parallel, such that the arm stopper has a constant thickness. Therefore, the top middle design has been chosen.

5.5.6. Coupling rod

The coupling rods or links are used to convert the vertical upward motion of the piston to the lateral movement of the cutter blocks. Each link is connected to one block and the piston. This means that three links are connected to the piston. The links have to convey the pressure that acts on the piston to the blocks during drilling. When the mud circulation pumps are switched off, the links have to convey the spring force, used to retract the blocks. The spring force is transferred to the links by a central sleeve. When the blocks are completely retracted, the links rest against this sleeve.

Since the blocks are orientated eccentric around the centre line of the bottom-core, the links need to be located at the sides of the blocks so that no torque around the piston will be created. This poses a limit to the maximum width of the links, which is 16.8 mm. The thickness of the links, which is 15 mm, is also limited. When the links fold out, they could reach outside of the bottom-core perimeter. This is problematic since the UR is prone to clogging when openings are present. The contour around the blocks should be completely closed.

A bone-like design was developed to prevent the need for an opening, see figure 5.29a. However, due to its shape and the location of the hole, the convex surface of the link and the concave surface of the block did not have the same radius, which is not beneficial in terms of contact pressures. In reaction to these findings, a new shape was developed that consisted of two concave surfaces figure 5.29b.

The top and bottom rings through which the connection pins fit are however not located in the same curved plane. If the tolerance around the pin is not correctly determined, the piston load could be transmitted through the pin instead of the contact surfaces. For high loads, this would destroy the pins. This means that the top surface should be convex as a whole, while the bottom surface remains concave. If the bottom surface would also be convex, the surface on the piston would be concave. This means that the piston force would have to pass through less material right next to the sleeve pipe. Any deformations of the sleeve pipe could make it seize around the mud channel.

Next, it was noted that the link could be broader at the bottom. This is because the bottom part would not slide along the groove in which the block is located. Different concepts were developed for a link with the broad base. This included varying the number of pin fittings, the sizes of the pinholes and the penetration depth of the pinhole inside the top of the link. This resulted in the preliminary concept shown in figure 5.29c, d and e. The decision was made to choose for the concept with the least amount of pin fittings (figure 5.29e), for the clear reason of manufacturing.

Another step involved determining the pinhole depth inside the link (or block) and the ways the shape has to be adapted to the curvature of the sleeve pipe. The full penetration depth was reduced to half and a semi-circular cut out was made in the link to account for the sleeve pipe. The cut out was made on both sides, so the link would remain symmetric in its vertical planes (figure 5.29f). This discourages bending of the link. From simulations, it became clear that the supporting legs could be lowered. The cut out was also changed to leave more material on the link (figure 5.29g).

Simulations also made clear that peak stresses would occur in the inside of the hole. A closed link head is therefore preferred. Because a normal pin fitted on the link would be too thin, a concept was developed that involves a protrusion that sticks out from the link and revolves inside a cut out on the block. This became the basis final conceptual design for the link (figure 5.29h). New cut-outs were made that only required minor modifications to the sleeve pipe. The lower pinhole ring was also reduced in width and diameter to leave more surface for the supports. This resulted in the final design, presented in figure 5.29i.

To verify whether the link could sustain the high contact loads, a contact stress analysis is carried out.

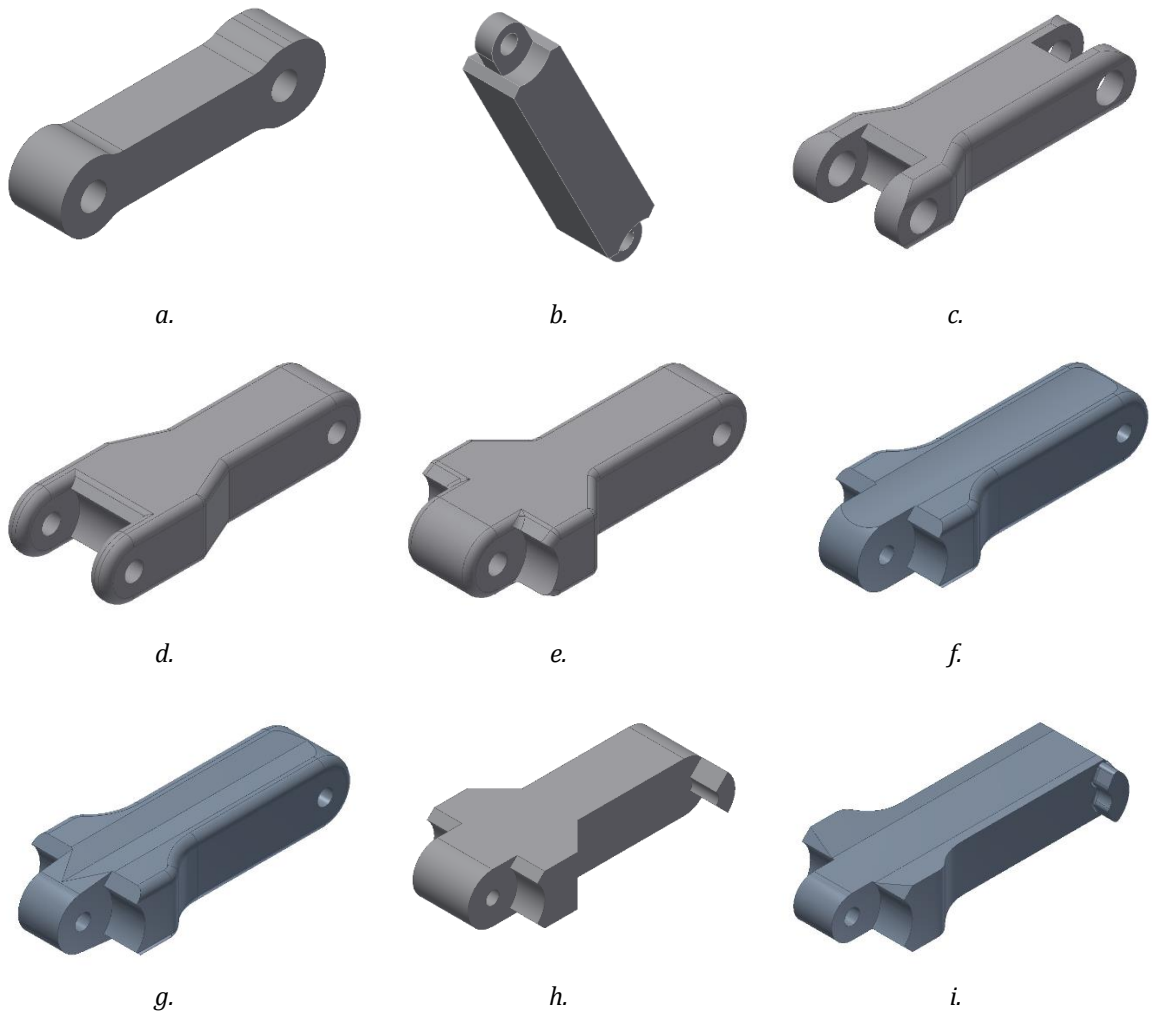

Figure 5.29: Link development.

Contact stress analysis

Introduction
When the UR starts to operate, the piston pushes the coupling rods outwards together with the cutter blocks. Due to the high forces, the coupling rods have been designed such that the interfaces are formed by convex and concave surfaces. Too high contact pressures may lead to unacceptable deformations of the rod and high stresses. For this reason, the contacts are examined in more detail.

Assumptions
In some cases, lubricant can be present in between the contact surfaces. Although mud is present down hole that can act as a lubricant, no film layer is formed because the velocity of the parts relative to each other is assumed to be negligible. Dynamic effects are not considered.

In case friction between the surfaces of the joint are also neglected, it can be assumed that the contact forces are directed normal to the contact surface. The contact is also assumed non-adhesive; meaning separation of the surfaces is not resisted.

Lastly, the tip of the rod is assumed single curved as for now. This means a line contact will be present in between the surfaces. The elastic bodies are assumed to have some clearance between the convex and concave surfaces.

Calculations
The contact stresses will be approximated with Hertz' Theory. Although this theory was originally developed for convex surfaces in contact with other convex surfaces or planes, an approximation is used where the counter-surface of the UR block is assumed to have a radius that is large compared to the rod surface radius. Because the contact surface will become smaller in this approximation, the calculated pressure will higher than the actual pressure. The approximation is however not conservative since the allowable stress will be calculated as much higher.

Method 1
A relative diameter and equivalent Young's modulus have to be determined. The relative diameter represents the case of a cylinder contacting a plane. In fact, the relative diameter represents a summation of the curvatures of the geometries. Similarly, the equivalent modulus of elasticity represent springs in a series configuration that represent the elastic properties of the bodies. The relative diameter and equivalent modulus of elasticity are defined as follows:

$$\frac{1}{D_{rel}} = \frac{1}{D_1} - \frac{1}{D_2} \qquad [5.53]$$

$$\rightarrow D_{rel} = \frac{D_1 \cdot D_2}{D_2 - D_1} \qquad [5.54]$$

$$\frac{1}{E_{eq}} = \frac{1 - \nu_1^2}{E_1} + \frac{1 - \nu_2^2}{E_2} \qquad [5.55]$$

$$\rightarrow E_{eq} = \frac{E_1 \cdot E_2}{(1 - \nu_1^2) \cdot E_2 + (1 - \nu_2^2) \cdot E_1} \qquad [5.56]$$

The diameters are filled in both as positive values. For steel, a Poisson ratio of 0.3 is assumed for the steel being used. It is also assumed that both parts have the same Young's modulus. The maximum pressure is given by:

$$p_{max} = \sqrt{\frac{2 \cdot F \cdot E_{eq}}{\pi \cdot b \cdot D_{rel}}} \qquad [5.57]$$

$$\rightarrow p_{max} = 0.591 \sqrt{\frac{F \cdot E}{b \cdot D_{rel}}} \qquad [5.58]$$

In this case, a line contact length of 16.8 mm is being considered. The diameter of the rod tip equals 15 mm while the counter surface is assumed to have a diameter of 16 mm. This results in a contact stress of 1834 MPa. The average stress in the cross-section of the rod equals 789 MPa, so the calculated value seems reasonable.

The contact stress will become lower when the surfaces diameters become increasingly conform. This will also result in a larger ellipsoidal contact surface. The rod is however not supported along the entire tip due to its design. From here, it is assumed that the width of the contact area may stretch between a 90-degree angle, centred on the middle of the tip. The contact surface is now transformed into a contact rectangle.

From the Huisman-Itrec calculation manual, the upper limit for the stress can be determined with the following equation:

$$\sigma_H \leq k_h \cdot 10 \cdot BH \qquad [5.59]$$

$$k_h = \max(0.812 - 0.07 \log_{10}(n), 0.27) \qquad [5.60]$$

Variable n indicates the number of rotations inside the slot. Since the calculated value is an extreme load case and the normal load case is much lower, n will be equal to 1. This results in a value for the Stribeck value k_h of 0.812. For structural steel 690, which is often used in these applications, the Brinell-hardness equals 235 HB. This results in an allowable stress of 1908 MPa.

Method 2
For elastic bodies having some clearance, the maximum pressure can be determined with the following equation:

$$p_{max} = \frac{4 \cdot F}{b \cdot D} \frac{1 - \cos\theta}{2\theta - \sin 2\theta} \qquad [5.61]$$

In this equation, θ indicates half of the total angle, and has units of radians. If the force in the rod equals 131 kN, due to a pressure difference of 300 bar over the piston, a maximum pressure of 1080 MPa is determined. This value seems to be a good approximation since it lies in between the limits that were determined before.

5.5.7. Piston

The piston functions as an actuator, encased within the bottom-core. The piston itself surrounds the mud channel. At the bottom of piston, the mud channel opens up. Due to the pressure differential over the piston, it is forced upwards. The links connected to it push the blocks outward. The piston reaches its highest position when the blocks hit the arm stoppers. When the pumps are disengaged, the piston is pushed back to its original position at the bottom, where it stops by hitting a shoulder support surface. Seals and scrapers are fitted on both inside and outside grooves, to prevent fluid loss and pollution of the gliding surface.

The first model only captured the anchor point of one of the coupling rods shown previously (figure 5.30a). Subsequently, the complete piston structure was formed around this model (figure 5.30b). The model showed that it would be difficult to manufacture the curved planes without removing some of the material on the sides. A new model was made where the sides were completely removed (figure 5.30c). The remaining material on top of the piston is shaped like a triangle. Some wall sections however are very thin and the edges are very sharp. This could make the part difficult to handle.

In the next model, all but the brackets were completely removed. At this stage, it became clear that several seal and wear rings are needed for smooth gliding and removing dirt between the piston and bottom-core. The cross-section of the sleeve channel that would eventually has to fit in the piston was also changed, so that it only fits in one orientation. This is shown in figure 5.30d. In consultation with a specialist in the field of manufacturability, it was decided not to proceed with this design. The brackets are relatively poor supported and milling the hole would be very difficult.

With this in mind, supports were added on the sides of the brackets. Holes are drilled through the side, so the coupling rods could later be installed with bolts or roll pins. The hole was again made circular and the number of grooves was reduced. A pocket was also made at the bottom to increase the surface area at the bottom. This is shown in figure 5.30e and 5.30f. Because the shape was still not suitable for manufacturing, a new basic shape was again considered (figure 5.30g).

However, due to the changing pin design, this model containing only grooves and no convex or concave surfaces was not suitable anymore. With the capabilities of a 4-axis milling machine in mind, the piston finally took on the shape that could more easily be made. The milling machine would start cutting in a solid piston (figure 5.30h) until a shape like presented in figure 5.30i would result. After some changes in the model related to the coupling-rod extension angle, the piston itself took its most recent shape (figure 5.30j). Lastly, figure 5.30k shows the appearance of the piston when seal and wear rings are added.

Piston seals

The piston will need wear and seal rings to function properly. The following rings have been selected from the *Trelleborg* online catalogue:

1. Piston seal ring — Turcon® Glyd Ring® T - PT0400800-T46V
2. Piston wear ring — Turcite® and Zurcon® Slydring® for Piston - GP6500800-T47
3. Shaft seal ring — Turcon® Roto Glyd Ring®, with O-Ring (as Set) - TG3100280-T10V
4. Shaft wear ring — Turcon® Excluder® 2 with O-Ring (as set) - WE3100280-M12V

These seals have been selected mainly based on their temperature resistance, chemical resistance and maximum pressure gradient. All technical details can be found on the product webpage.

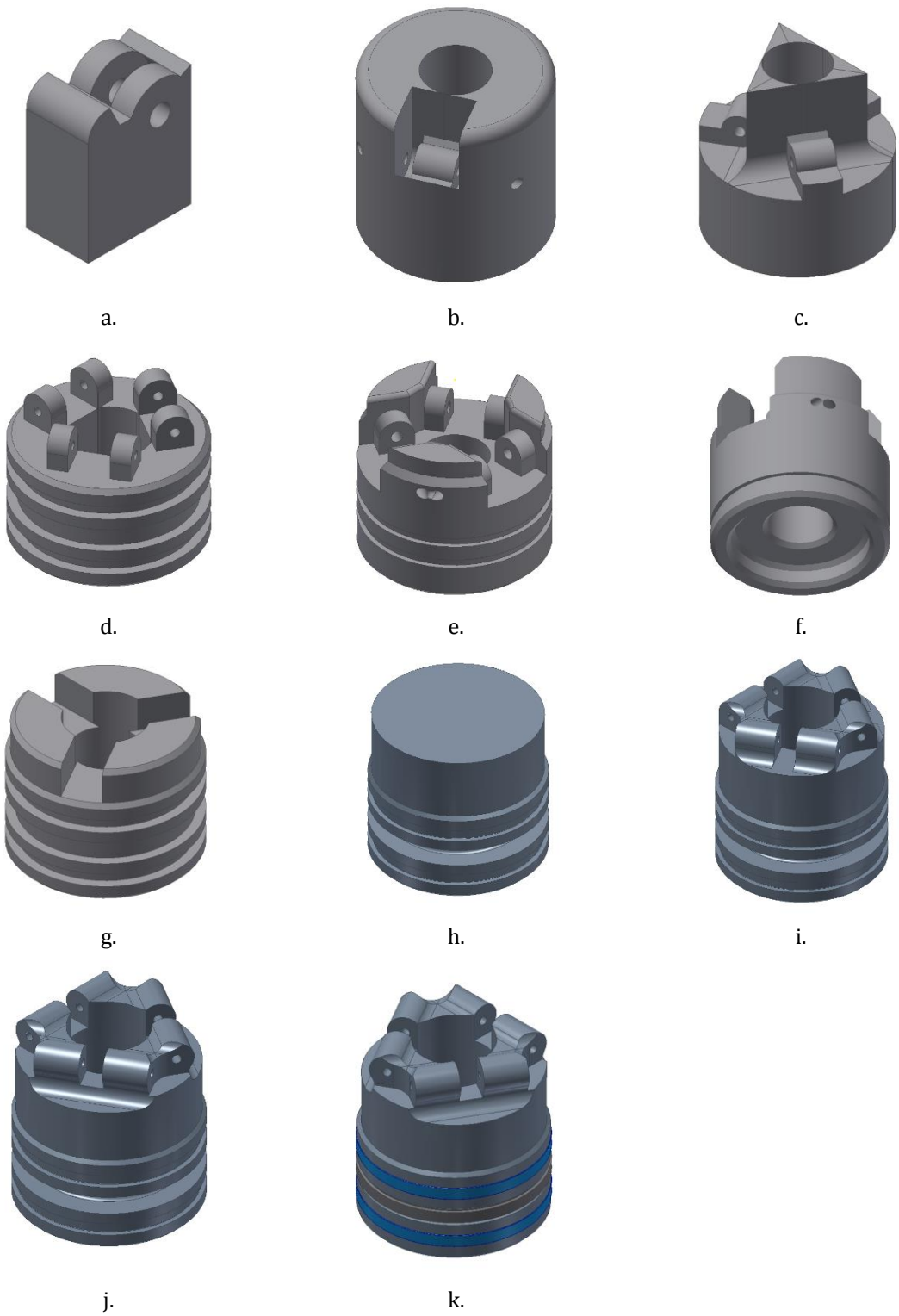

Figure 5.30: Piston development.

5.5.8. Grease cap

The primary function of the grease cap is to keep dirt away from the spring and prevent contamination of the lubricant around the spring. It is located within the core-assembly in between the upper-core and the bottom-core. The first step in the development involved a ring wedged between the upper and bottom-core parts, see figure 5.31.

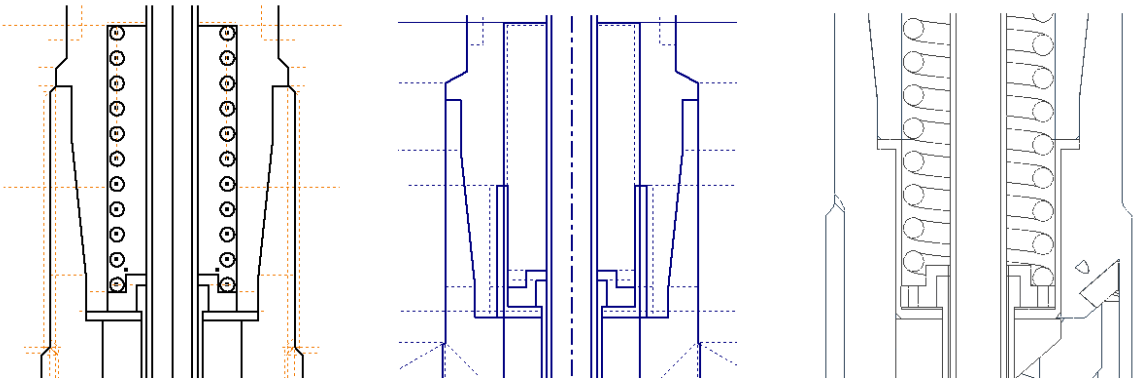

Figure 5.31: Development diagrams of the grease cap.

Initially the space of the stroke of the spring consisted of a single chamber. When the spring is compressed, the volume of this chamber decreased so fluid needs to flow through holes on the bottom of this chamber. When the spring is relaxed however, fluid flows in the chamber together with cutting debris. This could potentially damage the spring and clog the reamer from the inside out.

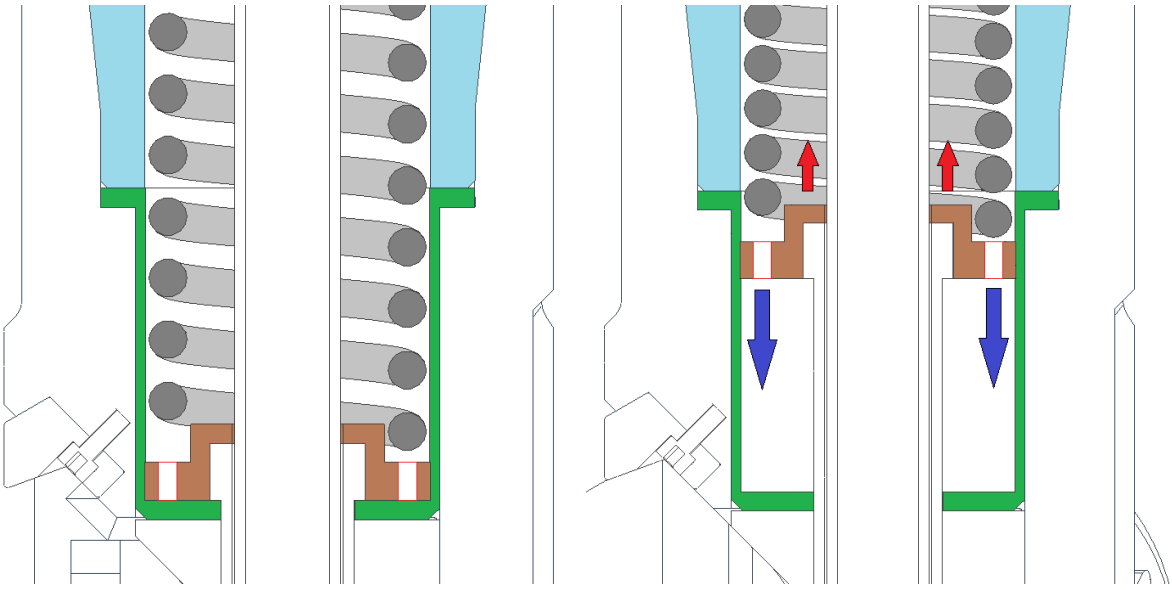

Figure 5.32: Left: spring (grey) in its pretension state. The retainer (brown) is located at the bottom of the grease cap (green). Right: when the retainer moves upwards (red arrows), fluid (blue arrows) flows through the holes of the retainer.

To solve this problem, the chamber had to be divided into two chambers (see figure 5.32). In case the spring is compressed or relaxed to fluid can be stored and retrieved from this second chamber without large chunks of debris being sucked in. Still, the combined volume of the two chamber changes because a part of the sleeve channel is being pushed upwards. The exchange of fluids with the exterior of the chamber is assumed negligible. Tests are needed to confirm whether this assumption is justified.

5.5.9. Mud channel

The mud channel is meant to transport the drilling fluid through the UR. The conceptual design shows that it is a straight pipe. No branches are present for converting the mudflow or for nozzles. No nozzles are present, because the bit would lose too much power. The annulus flow is also disturbed by the counter flow of the nozzles, which prevents proper flow through of the cuttings.

The mud channel is screwed in the upper core of the UR, underneath the pin connection. At the bottom, the mud channel is only laterally constrained by the piston. This means that the mud channel can be inserted during installation even when the other internal parts are already installed.

Because the blocks have to fold around the internal channels, the mud channel has been designed with the smallest diameter that is reasonably possible. As opposed to the old design, the new design has a flow channel with a constant internal and external diameter. This has been done to prevent a sudden contraction or expansion. Flow disturbances cause power loss, increased wear rates and leakage at the transition of pipe segments. The flow velocities present in the pipe are compared to the base case in table 5.9. The volumetric flow rate equals 28.4 l/s in both cases.

Table 5.9: Pipe flow velocities.

Design	Smallest diameter	Flow velocity
215.9 mm (8.5 inch) UR	23.5 mm	65.5 m/s
228.6 mm (9 inch) UR	22.0 mm	74.7 m/s

Because it is uncertain whether the mud channel can sustain these high flow velocities, it has been decided that the flow velocity must be kept the same in both designs for the maximum volumetric flow. This would result in the following allowable volumetric flow (table 5.10).

Table 5.10: Pipeline allowable volumetric flow.

Design	Smallest diameter	Flow velocity	Volumetric flow
215.9 mm (8.5 inch) UR	23.5 mm	65.5 m/s	1700 l/m
228.6 mm (9 inch) UR	22.0 mm	65.5 m/s	1500 l/m

A special tool is used to screw the mud channel into the top core. Therefore, notches are located on the bottom. The design of the mud channel is presented in figure 5.33.

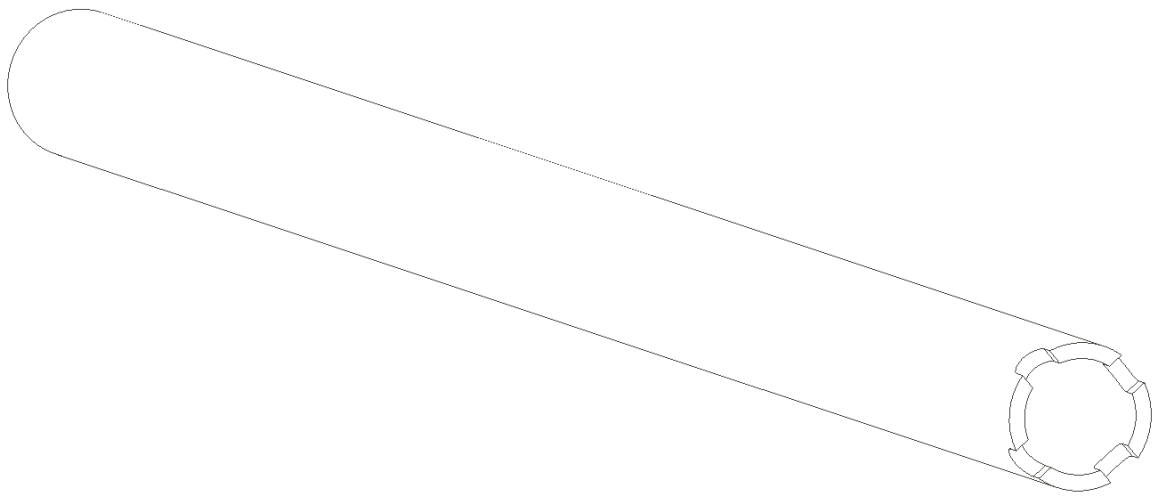

Figure 5.33: Mud channel

5.5.10. Sleeve channel

The sleeve channel is a pipe surrounding the mud channel. Its purpose is to convey the spring force from the top of the UR to the piston in the lower section. In case the cutter blocks are retrieved, the sleeve channel is pushed down together with the piston. The piston in its turn is connected to the coupling rods and pulls the blocks back into the UR. In case the blocks are extended, the motions are reversed.

The first concept (figure 5.34a) shows a wide diameter base that consists of three legs. These legs would fit in between the brackets of the piston. The couplings rods are then able to retract to their standing position with any interference of the channel. Since this design cannot be easily made from a hollow tube, the design needs to be adjusted.

Three small legs remained, which were very susceptible to bending (figure 5.34b). Since the outer perimeter resembles a circle, the channel has to be fitted with a thread or heated to fasten it, instead of using interlocking shapes.

To strengthen the tube, the perimeter was eventually closed. On three sides, slot recesses were made to accommodate for the coupling rods (figure 5.34c). The coupling rods had to be reduced in width for this to happen. On overview of the concepts is shown in figure 5.34.

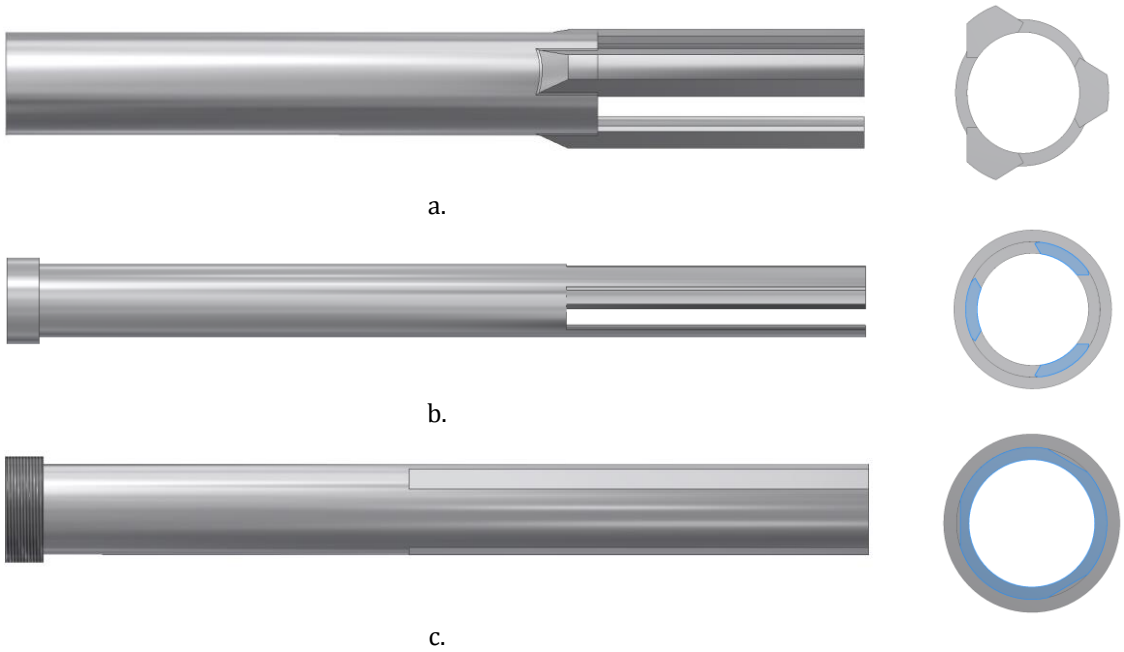

Figure 5.34: Development of the sleeve channel.

Jamming

Now that the final design for the sleeve channel is known, a calculation is performed to check whether *jamming due to tilting* might occur.

For this calculation, it is assumed that the spring disk does not make contact with the grease cap. It has also been assumed that the moving parts do not move with respect to each other, such that the assembly can be seen as one part. A free-body diagram is shown in figure 5.35.

The goal of the calculation is to determine the distance a, at which the assembly starts sliding. The solution can be determined analytically by solving the equilibrium equations of the system.

$$+\downarrow \Sigma F_y = F_{spring} - F_A \cdot \mu - F_B \cdot \mu = 0 \qquad [5.62]$$

$$+\rightarrow \Sigma F_x = F_B - F_A = 0 \qquad [5.63]$$

$$+\downarrow \Sigma F_y = F_A \cdot b + F_A \cdot \mu \cdot \left(c + \frac{d}{2}\right) - F_{spring}(c + a) = 0 \qquad [5.64]$$

For the conceptual design, the following parameters have been determined: b = 340 mm, c = 40 mm, d = 35 mm and μ = 0.2 [-]. This results in the following equation for a:

$$a = \frac{b}{2\mu} - 0.5c + \frac{d}{4} \qquad [5.65]$$
$$\rightarrow a = 839\ mm$$

This means the assembly is not likely to jam because the distance of the force to the centreline is in reality much smaller and cannot be this big.

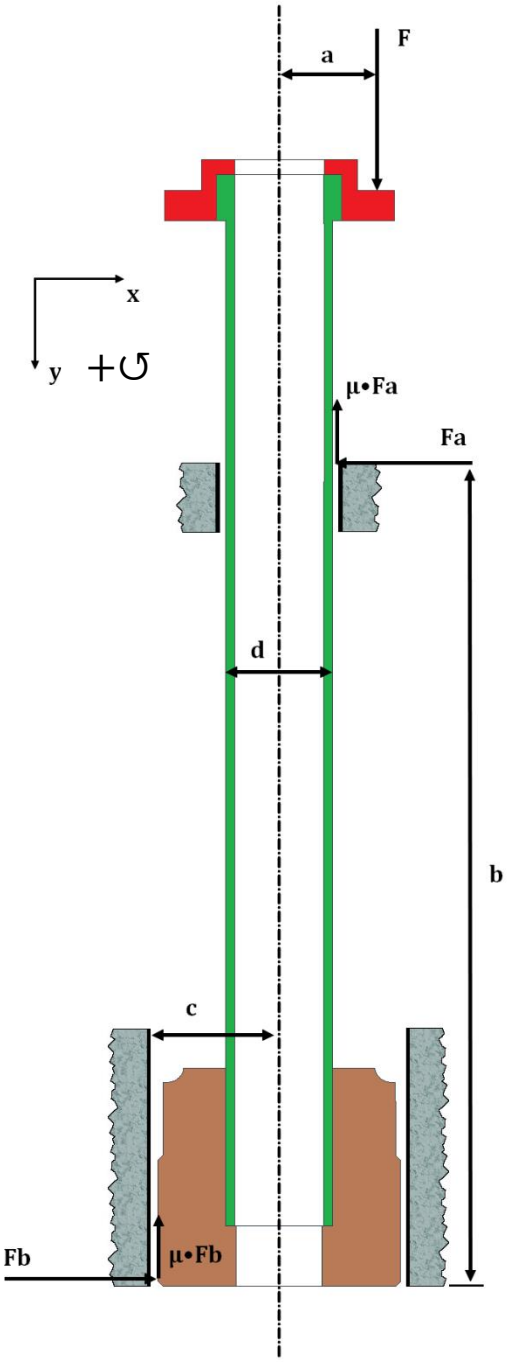

Figure 5.35: Simplified model of the sleeve assembly.

5.5.11. Plug

The plug is connected to the bottom of the grease cap and acts as a seal to prevent large cuttings from reaching the inner mechanism of the UR. Because the top angle of the blocks is directed towards the bore of the UR, an empty space would normally be present. Because the coupling rods and the piston do not reach this height, the plug can be fixed into position, also during operation.

The plug may be one of the most difficult parts to manufacture. Although it has a cyclic symmetric geometry, the grooves on the side have to match the sliding paths of the cutter blocks closely. The transition from this part to the bottom core also has to be smooth. A small stick-out at the bottom could result in the blocks refusing to retract.

The grease cap to which the plug is attached, is assumed to be tight fitted in between the top-core and main core bodies. However, by compressing the spring, a moment could result that wants to turn the plug around the mud channel. Therefore, an extra safety mechanism in the shape of a notch should be present to prevent any rotation of the part. This feature will be included in the 3D-printed model of the UR.

The absence of the plug could result in cuttings flowing towards the mud channel. The accumulation of these cuttings may cause the mud channel and piston assembly to wear much faster. If any cuttings dry up and are not removed before the next run, the cuttings might eventually prevent the UR from closing properly. As with the grease cap, the actual functionality of this parts needs to be tested in practice.

The plug is shown in figure 5.36. It can be seen that the 'legs' are cut of at a certain distance from the top. The reason for this is that elongating the legs would result in contact with the grooves of the block. Although this could be overcome, the decision was made to minimize the length and avoid the design of unnecessary details.

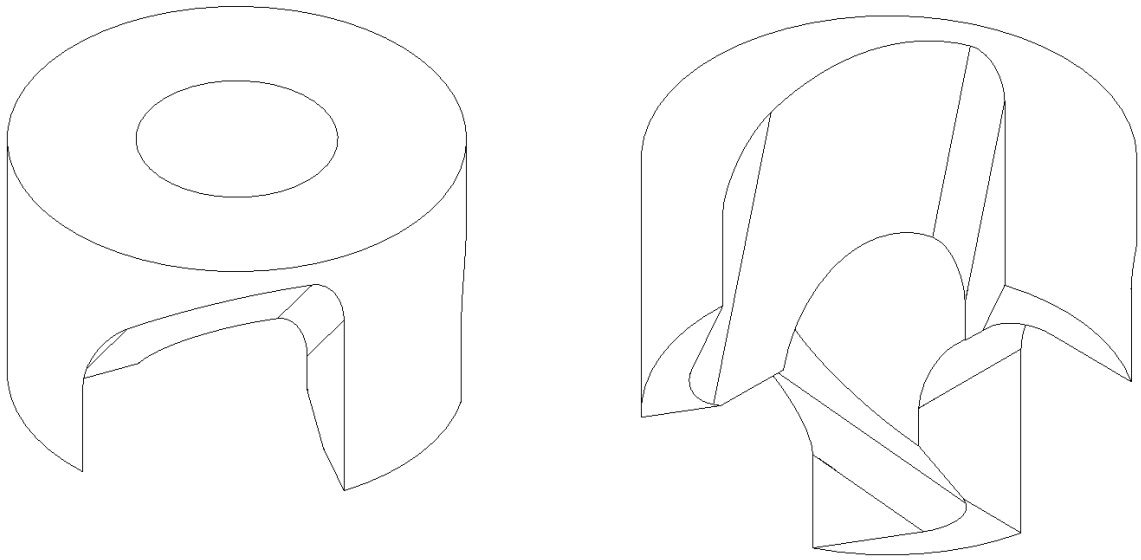

Figure 5.36: Dummy picture of the plug.

5.6. Assembly

5.6.1. Introduction

The UR consists of many parts with a variety of functions. Eventually these different parts have to be put together during the assembly of the UR. The design of the parts is closely related to this, since problems during assembly can lead to damage to the UR. Therefore, checks have to be carried out after the UR is assembled. Safety equipment should be worn throughout the entire process. The assembly procedure itself will be discussed in the next section. The internal parts have been colorized for clarity.

5.6.2. Procedure

The assembly procedure starts with lifting the **bottom core** to put it in an upright position (not depicted here). Slings can be used to hoist the bottom-core of the ground. Special care should be taken to prevent damage of the threads and the component should remain clean. Once the bottom-core has been lift up, the **grease cap** (red) and **plug** (green) should be slid onto the **sleeve channel** (yellow). The **spring disk** (blue) may also be screwed onto the sleeve channel. Next, the sleeve channel may be hammered carefully into the **piston** (gold). After the sleeve channel has been connected, **wear** and **slide rings** (light blue and grey) may be installed on the piston. Figure 5.37 shows a cross-section view of the sub-assembly.

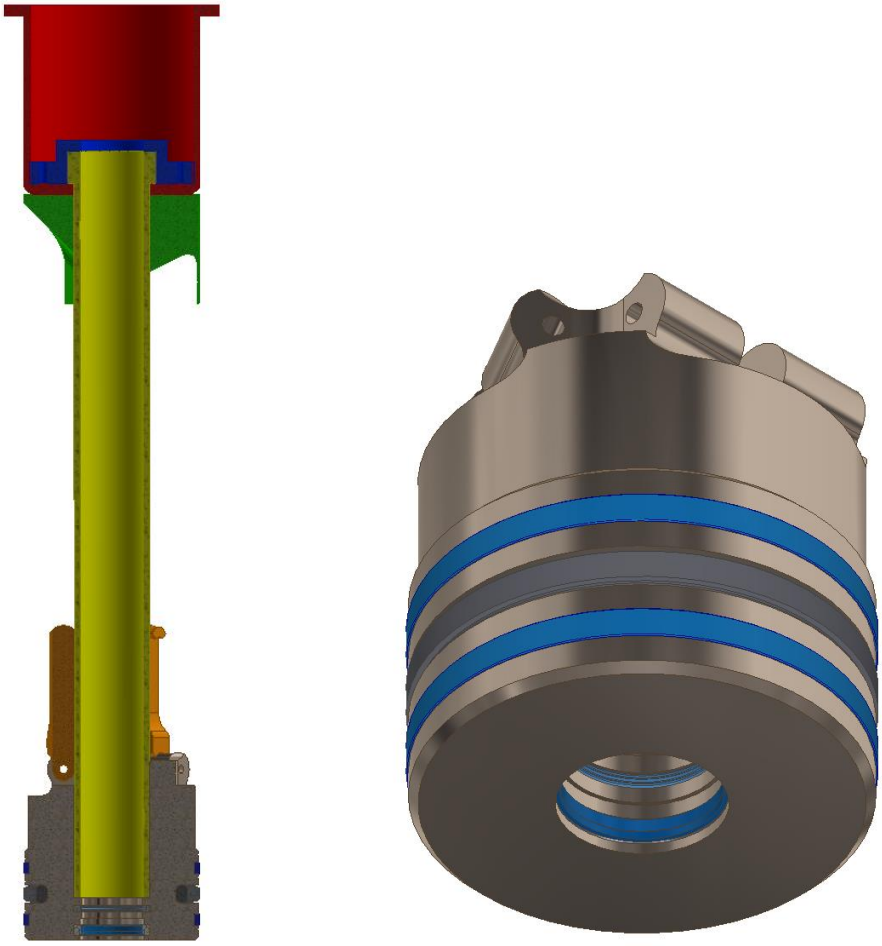

Figure 5.37: Left: Assembly of the internal parts. Right: Piston with wear and slide rings.

The assembly of parts now needs to be put in an upright position to install the **coupling rods** (orange). These rods are attached to the piston by means of pins that need to be inserted into the brackets on top of the piston. Now that most of the internal parts are put together, the resulting assembly of parts may now be inserted into the bore of the bottom-core.

Now, a special procedure follows in which the **cutter blocks** are attached to the coupling rods. Because there is no pin connection present between the block and coupling rods, the block has to slide sidewards onto the coupling rod. The coupling rod is bounded by the core body on the one side and the block on the other side. In order to enable the connection, the parts have been designed such that the block can move sideways only at a certain location. The following strip (figure 5.38) shows the connection procedure.

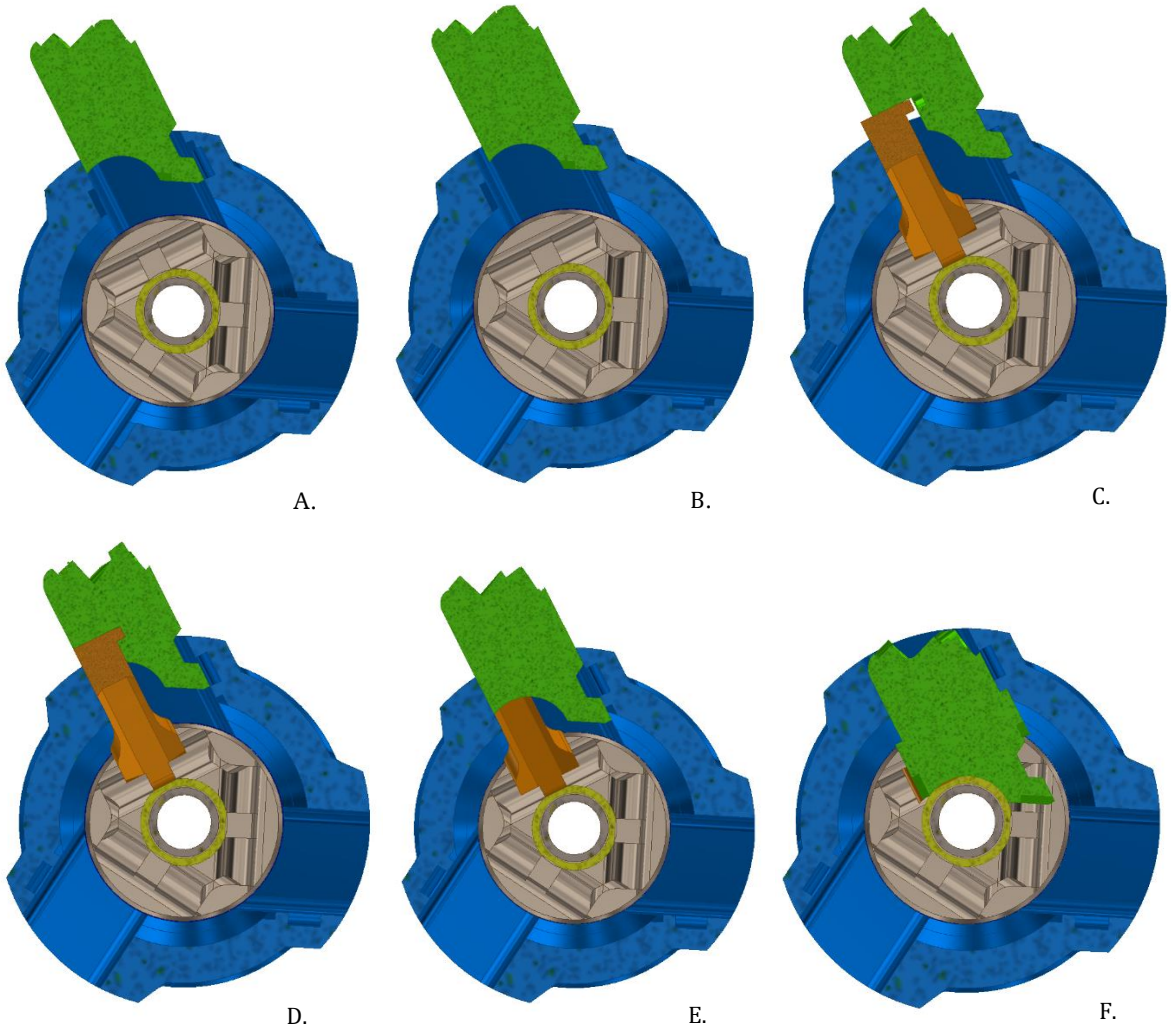

Figure 5.38: Procedure for connecting the coupling rods to the cutter blocks.

First, the block is partially inserted into the slot (A). At a certain depth, the block may be moved into the notch of the core body (B). Then, the coupling rod is retrieved from the inside and the protrusion is brought to the same height as the notch inside the block (C). The block can now slide back and a connection is made between the block and the coupling rod (D). For 9-inch reaming, the block will be moved as far as indicated in (E), so the notch will not cause problems during expansion. The retracted mode of the cutter block is shown in (F).

Now that the blocks are also connected, the piston may be lowered to its resting position at the bottom of the bore. At this point, the **armstoppers** can be installed with **hexagon socket screws** (figure 5.39). Next, the **spring** needs to be placed on top of the spring disk (figure 5.40). The **top section of the core** may be put on top of the spring. A force must be applied on top of this part to compress the spring. Simultaneously, the top-core needs to be screwed onto the bottom-core.

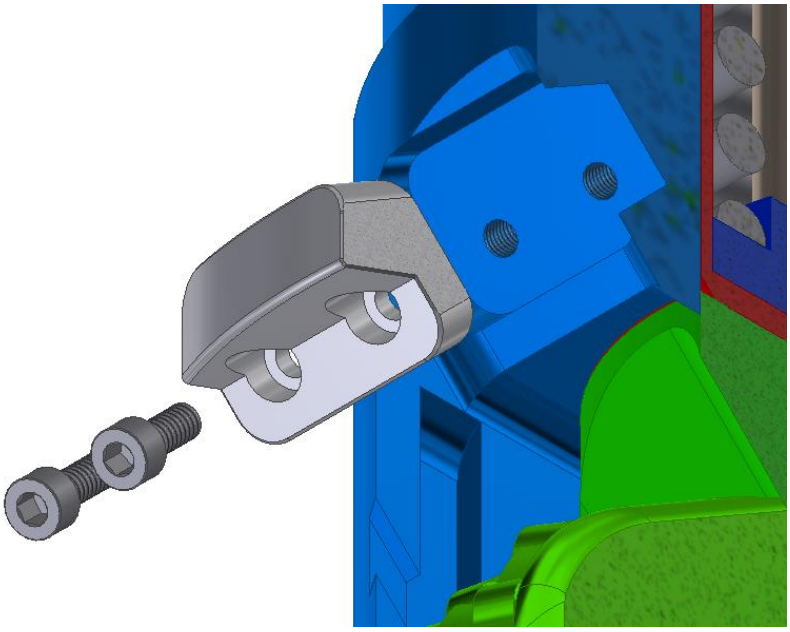

Figure 5.39: Armstopper installation.

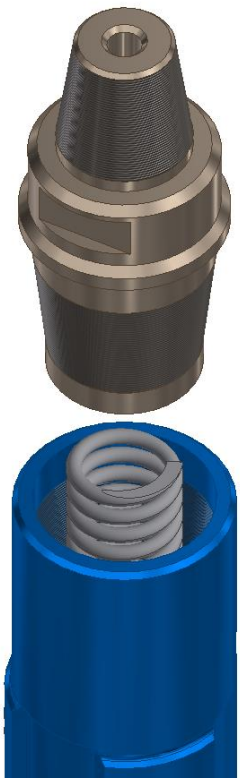

Figure 5.40: Spring put inside the bottom-core.

Installing the **mud channel** is the final step of the procedure. The mud channel can be inserted through the hole on the bottom of the core body (figure 5.41). The mud channel is then screwed onto the thread in the top part of the UR. For this, the mud channel is equipped with notches that form the point of application for the screw tool (figure 5.42).

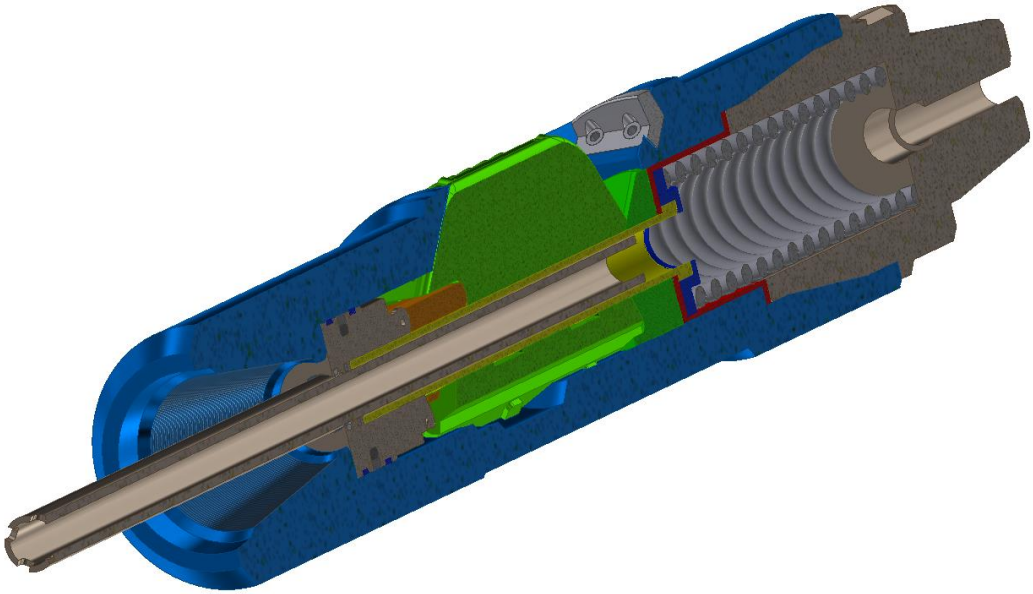

Figure 5.41: Insertion of the mud channel.

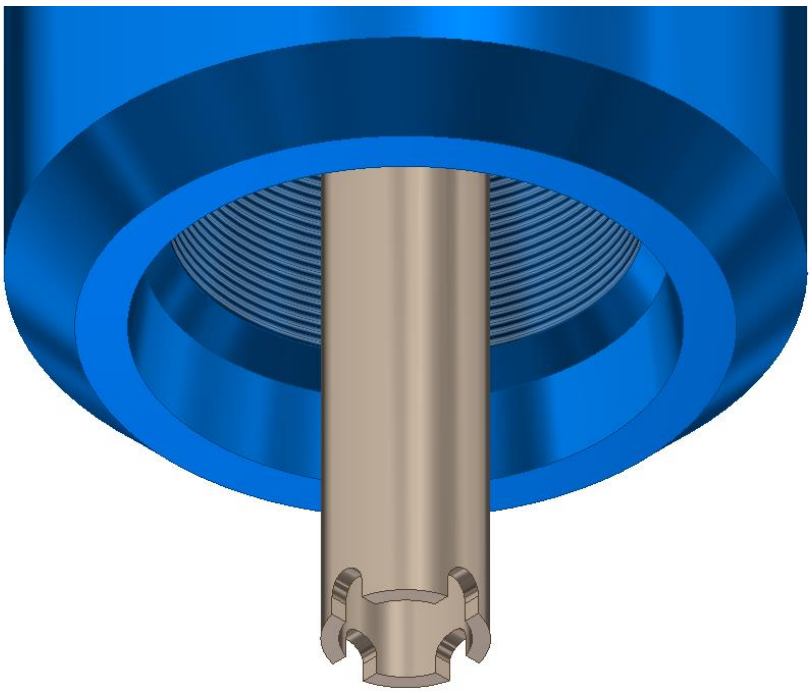

Figure 5.42: Notches for handling tool.

5.7. Manufacturing

5.7.1. Introduction

A variety of processing techniques is used during the production of the UR. The next sections will describe the basics of some *shaping* and *post-processing* techniques. It is also mentioned how they are applied in the production process of the UR and what tools are being used.

5.7.2. Hardfacing

To improve the wear resistance on the outside pads of the core body of the UR, the surface needs to be threated to become harder. A range of welding techniques can be used to bind crushed tungsten carbide or tungsten carbide inserts to the surface of the workpiece, see figure 5.43. First, stellite coating may be applied to the base metal. Then a torch is used to melt the particles together and other types of bonding powders can be applied on top. In the end, the top layer is grinded for a smooth surface finish. Especially the bottom edge of the pads need to be protected.

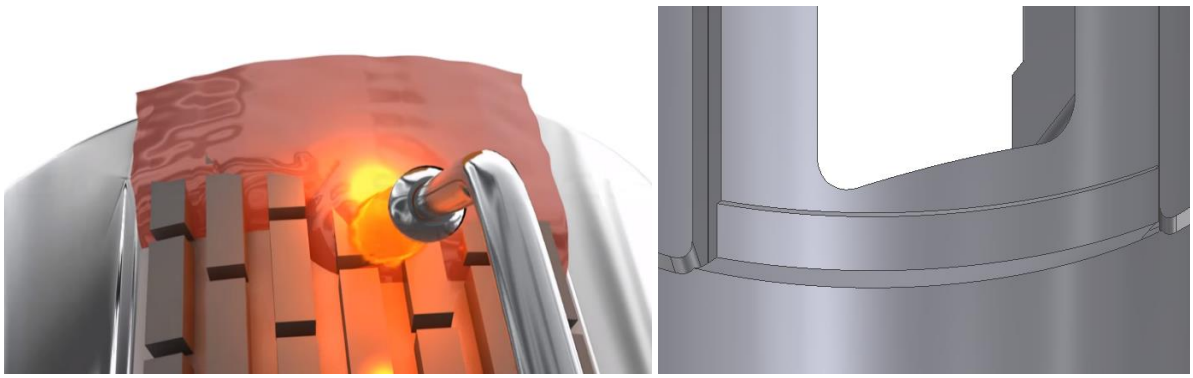

Figure 5.43: Left: hardfacing process with inserts on the side of the UR core-body. Right: bottom of the block slot.[23]

5.7.3. Brazing

Brazing or hard soldering is used to join metals together, by the solidifying of a filler material that adheres to the surfaces of the parts that need to be connected. The process of brazing takes place above a temperature of 450°C. These high temperatures may cause more thermal damage in comparison with soft soldering, but the connections made are stronger. For brazing the PDC cutters onto the cutter blocks, the solder alloy can be either thin and eutectic or viscous and with a melting range. This determines the layer thickness. For hard soldering steel, the most suitable solder alloys are Cu-Ag, Cu-Zn and Ag. The brazing process is shown in figure 5.44.[24]

Figure 5.44: Brazing PDC bits onto the cutter block of the UR.

5.7.4. Milling

To make the slots, pockets and grooves in the core body and other large parts, milling operations have to be performed. For this job a 4-axis milling machine is preferred. A 4-axis milling machine is able to translate around three axes and rotate around one, see figure 5.45. The milling process can be done with different tools. The pockets for the armstopper can be made using pocket milling, while the lengthwise grooves in the core body can be made with a keyway cutter.

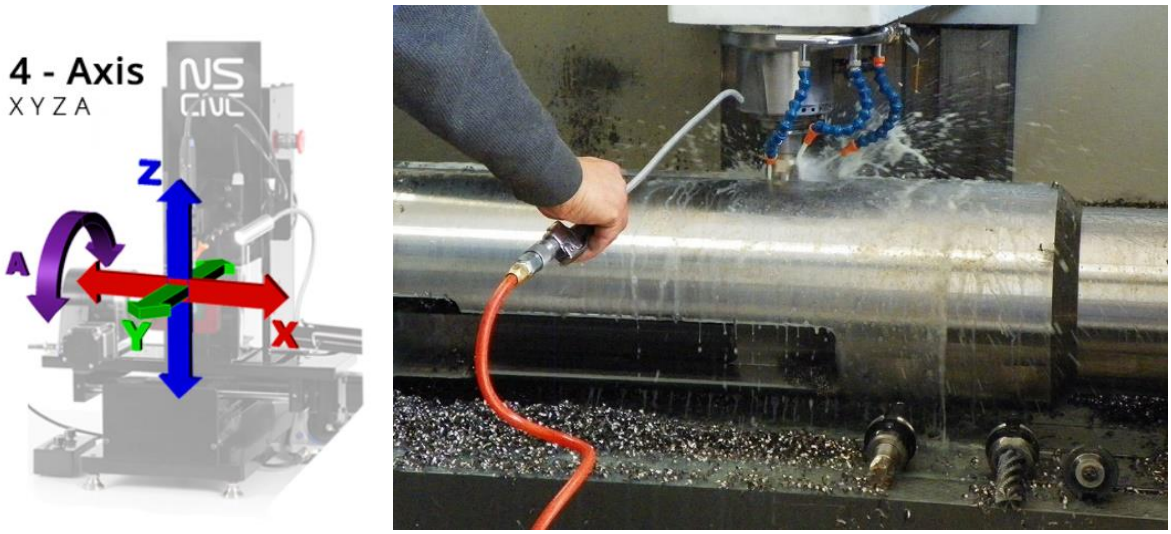

Figure 5.45: Left: milling machine degrees of freedom. Right: milling of the UR core body.[25],[26]

5.7.5. Boring

Boring is a machining technique where a chisel rotates eccentric by clamping it into a boring head, see figure 5.46. The bore in which is rotates has been drilled in advance. For the UR, it can be used to make a tapered hole, needed for the coupling rods to tilt outwards. The boring tool can both move parallel along the rotation axis and move at an angle relative to the rotation axis.

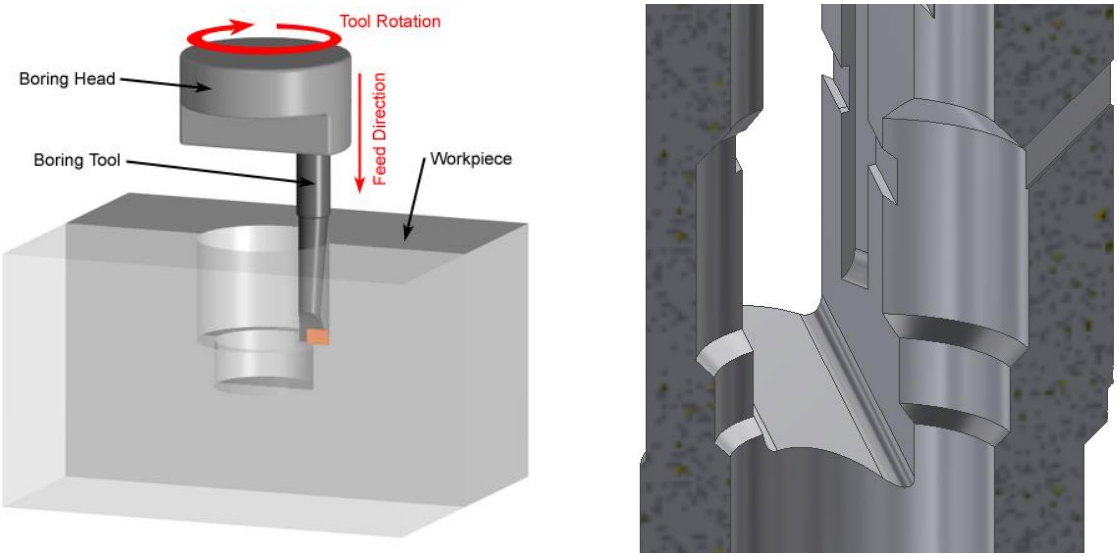

Figure 5.46: Left: the principle of boring. Right: part of the UR core body where boring needs to be performed.[27]

5.7.6. Sintering

Sintering is classified as a *shaping technique* that is being used within the branch of *powder metallurgy*. Powder is compressed into a mould, after which annealing takes place at high temperatures. This production technique can be used for manufacturing simple products with small tolerances, such as polycrystalline diamond composite (PDC) cutters, see figure 5.47.

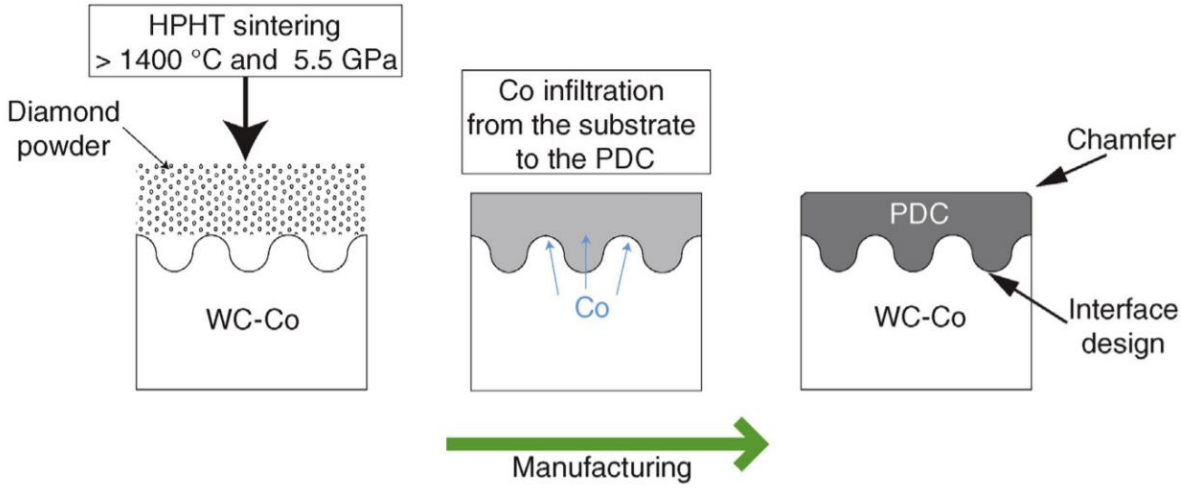

Figure 5.47: Manufacturing process of conventional PDC cutters.

These cutters consist of a WC-Co substrate bottom part. A diamond powder is put on top. The cutters are then sintered under high pressure (5.5 GPa) and high temperature (1400°C). The diamond particles then form a dense lattice structure. Some of the molten cobalt now advances through the boundary layer into the top layer and spreads homogenously. The cutter is post-processed by performing a surface finish and adding a chamfer on the side of the PDC part.[28]

5.7.7. Honing

Honing is a post-processing technique, which aims to improve the surface quality. A cylinder-honing tool consists of multiple honing stones, see figure 5.48. The stones contain abrasive grains like cubic boron nitride, silicon carbide, diamond or corundum. The characteristics of the work-piece determine which is these materials is the most favourable. The honing stones are pushed against the wall with a certain pressure to smoothen the surface. During honing, the stones both translate and rotate. These tools can be used to process the inside diameter of the UR, since the precision of the hole is important for the piston.[29]

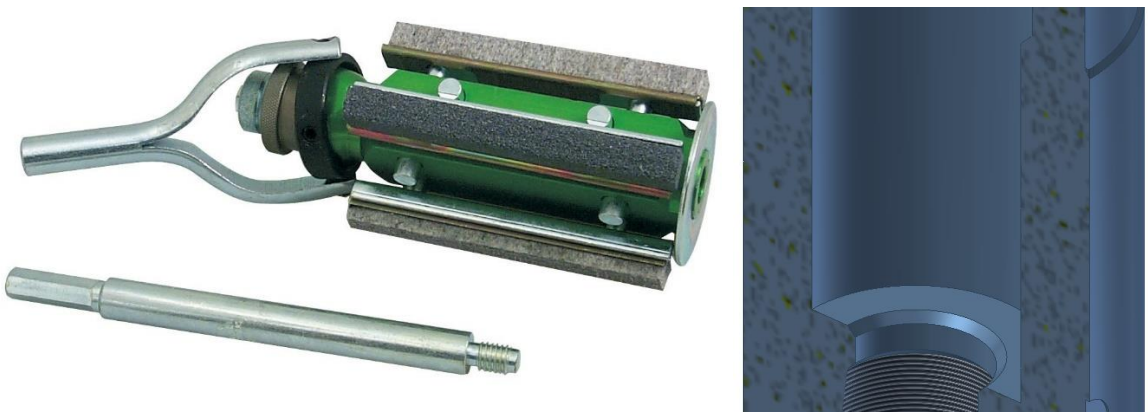

Figure 5.48: Left: honing tools for medium to hard workpiece materials. Right: UR bore hole.[30]

5.7.8. Broaching

With a broach tool, the material from the part is removed in one motion. A large number of teeth are arranged in a straight line. Each successive tooth reaches deeper into the part material and removes a thin layer, see figure 5.49. For the UR, a single keyway broach will be used to make the slides through which the blocks glide.

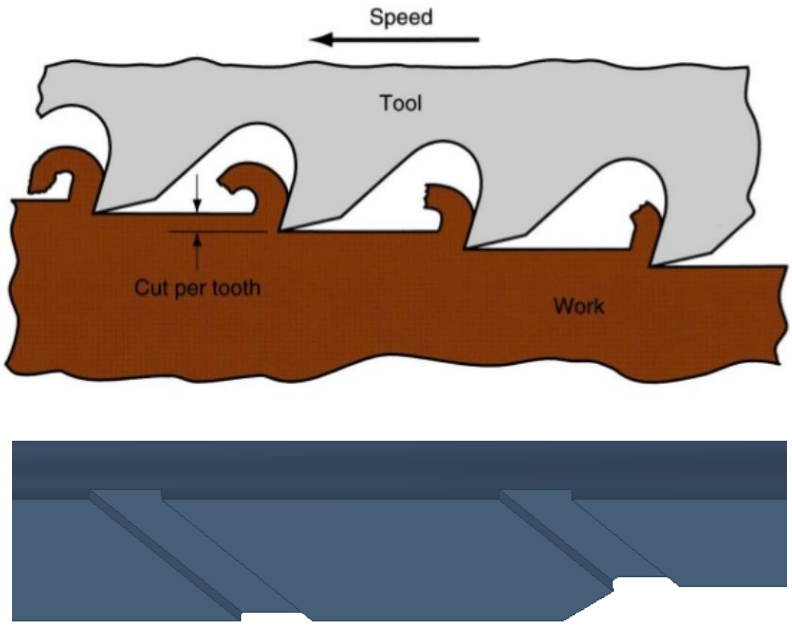

Figure 5.49: Top: broaching tool side-view. Bottom: part of the tongue-groove connection in the core of the UR.[31]

5.8. FEA using ANSYS Workbench

5.8.1. General introduction

For a finite element analysis (FEA), complex parts or constructions require strength calculations that are performed with the finite element method (FEM). To approximate the geometric domain by discretization, a grid is generated that consists of polygonal or polyhedral elements. Instead of using partial differential equations, matrix equations are used to estimate the displacement field, the stresses and the deformations, to obtain approximate solutions to boundary value problems. The accuracy of the solution will be dependent on the size of the elements relative to the domain and the type of element.

5.8.2. General procedure

To model a complex problem, approximate solutions are used. Due to the complexity of the equations, the use of the computing power of computers is preferred as hand calculations might become quite tedious. The finite element method uses systematically built up algorithms that can easily be implemented.

The elements that are used in the analysis are connected to each other with nodes, such that the displacement field is continuous for adjacent elements. These nodes have certain degrees of freedom. Since these degrees of freedom are unknown, they have to be determined by solving a system of constitutive and kinematic equations. The procedure followed by going through the following sequential steps[32]:

1. The domain is divided into elements by mesh generation and the type of element is being specified. The material properties and the support and loading conditions are known.
2. A system of equilibrium equations can be established according to Hooke's Law for linear elastic materials. Here, the multiplication of the (total) stiffness matrix and the displacement vector equals the force vector:

$$[K] \cdot \{D\} = \{F\} \qquad [5.66]$$

   The amount of elements in the displacement vector depends on the number of nodes. In 3-D, each node has six components; three translations in the x, y and z directions and three rotations about the x, y and z axes. Most components are unknown, but others are known because of the support conditions.
3. The system can now be solved for the nodal displacements:

$$\{D\} = [K^{-1}] \cdot \{F\} \qquad [5.67]$$

4. The displacement field of the mesh elements may now be determined by using so-called shape functions. The shape functions are multiplied with the degrees of freedom vector of the element:

$$\{u\} = [N] \cdot \{d\} \qquad [5.68]$$

5. The strain and stress fields can now be determined by using strain-displacement relations and stress-strain relations respectively:

$$\{\varepsilon\} = [B] \cdot \{d\} \qquad [5.69]$$

$$\{\sigma\} = [S] \cdot \{\varepsilon\} \qquad [5.70]$$

   Here, the B matrix relates the strains to the corresponding degrees of freedom for the element. The S matrix relates the strains to the stresses. The Newton-Raphson procedure could be using to solve for the set of simultaneous equations.

5.8.3. ANSYS element types

ANSYS Workbench chooses the element type from a library that contains over 100 different element formulations. Each element can be identified by an eight-character name. From the solution information available in ANSYS, the default element types used can be distinguished. The most common ones used in the following analysis are types SOLID187, CONTA174, TARGE170 and SURF154. To describe the form and the displacement field of these elements, shape functions are determined.

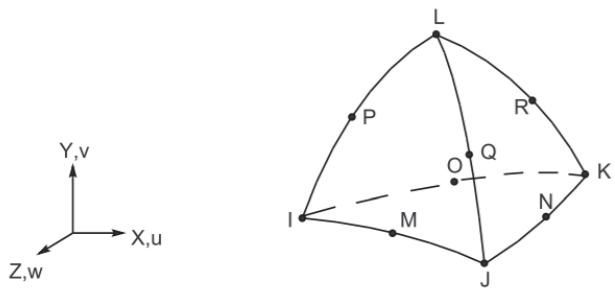

Figure 5.50: SOLID187.[33]

Figure 5.50 shows SOLID187. It is a 3-D 10-node tetrahedral structural solid element, suited for irregular meshes. Each node has three degrees of freedom, which are the translations in the x, y and z directions. The displacement in u direction of any point can be described by the following function[34]:

$$\begin{aligned} u = {} & u_I(2L_1 - 1)L_1 + u_J(2L_2 - 1)\mathrm{L}_2 + u_K(2L_3 - 1)L_3 \\ & + u_L(2L_4 - 1)L_4 + 4u_M L_1 L_2 + u_N L_2 L_3 + u_O L_1 L_3 \\ & + u_P L_1 L_4 + u_Q L_2 L_4 + u_R L_3 L_4 \end{aligned} \qquad [5.71]$$

The above function can be seen as the product of an interpolation or shape function matrix and a vector containing the nodal displacements, and has the same form for the other degrees of freedom. In this function, L_1 to L_4 represent the normalized coordinates. This means their value changes from 0 to 1 while 'travelling' along an edge, starting from a vertex and going to the opposite face or side. The letters with subscripts, u_M for example, are used to describe the u motion of node M.

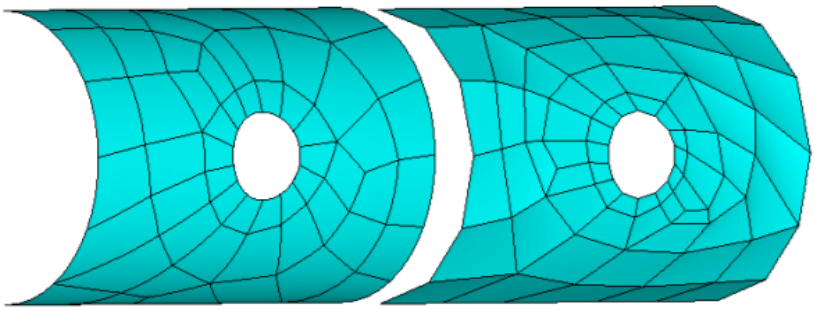

Figure 5.51: Left: SHELL93 Quadratic Elements (8 nodes), right: SHELL181 linear elements (4 nodes).[35]

Elements may also be distinguished based on their linear or quadratic properties. Quadratic elements like SOLID187 have midside nodes, which means that the shape function for the strains has a non-linear character between corner nodes. Since this means that the displacement varies in a non-linear fashion, linear variations of stress are supported within the element. Quadratic elements are also more suitable for curved surfaces and edges and are less sensitive to distortion when compared to linear elements. This is shown for shell elements in figure 5.51.

5.8.4. Support and boundary conditions

In modelling parts of the UR, several support conditions will be used to constraint the parts relative to each other. To get reliable results, these boundary conditions have to be applied correctly. The most important boundary conditions used for the UR are treated below.

Frictionless support
In some cases, surfaces need to slide along each other. This is the case with the coupling rods, since they are both connected to the piston and the blocks. The convex surface of the rod tip must be connected to the concave surface of the slot inside the block, such that deformations tangential to the faces are still allowed. The only direction constraint is the direction normal to the planes. A support with friction will not be used in the simulation since the coefficient of friction between the parts is unknown.[36]

Fixed support
This boundary condition inhibits the motion or deformation of nodes. This type of support condition is applied at places where assembly is in contact with the outside world. In most cases, this means that the blocks or the UR core will have a fixed constraint. The fixed support has to be placed at a distance far away from the area of interest, due to the possible unwanted influence of the Poisson effect.[37]

Contact regions
A solid body contact can be modelled by assigning contact and target elements. The corresponding surfaces of these elements are called contact and target surfaces, see figure 5.52. While a target element is allowed to pierce through the contact surface, a contact element is not allowed to pierce through the target surface. In case of a rigid-to-flexible contact, it seems obvious to choose the rigid element as the target element and the deformable element as the contact element. In the case of a flexible-to-flexible contact, both bodies are considered deformable. Most contacts for the UR can be described by the latter contact, because the bodies have a similar stiffness.

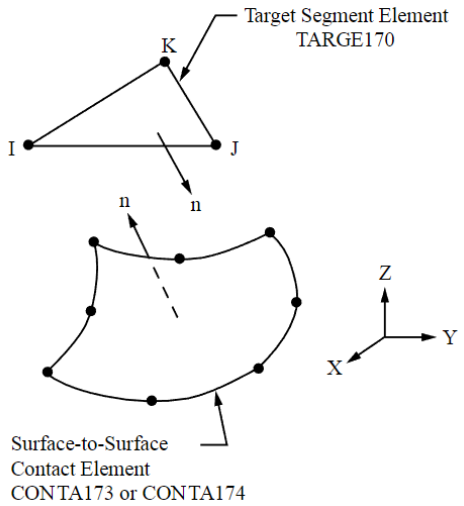

Figure 5.52: TARGE170 and CONTA174.[38]

In the case of the UR, an asymmetric or one-pass contact is defined. This means that the contact surfaces are all located on one surface while the target elements are all located on the other surface. This is decided based not only on the reduction in computational time but also on the relative sizes of the contacting faces.

In case of the blocks in the UR core, the blocks will tilt such that only the edges contact the slot walls. Therefore, the blocks are in this case assigned as the contact elements while the core is assigned as the target element. For the coupling rods, stiffness becomes a more important factor. Since the rods have to sustain a high load, they should be made from a very stiff material. This means that the rod should be assigned as the target element.

5.9. Detailed concept analysis

5.9.1. Introduction

To analyse the conceptual design in more detail, a finite element analysis will be performed. The most critical parts of the UR will be investigated for this. These parts will be isolated and simulated in separate sub-assemblies. The following *steps* will be performed:

1. *Simplify the sub-assembly and determine the load case to which the assembly is subjected.*
2. *Perform manual calculations that can later be compared to the FEA.*
3. *Determine the mesh size and apply mesh refinements where necessary.*
4. *Determine the locations of the contact regions and the type of contact.*
5. *Apply supports and constraints such that the model will behave in a realistic manner.*
6. *Solve the simulation for the equivalent stress and deformation.*
7. *Compare the results of the manual calculation and FEA and draw a conclusion.*

For the simulations, a distinction is made between *load cases* and *load combinations*. A load case describes the *loading principle*, in other words where loads are applied and with what reason. The load combination describes the combination of forces or pressures and their magnitude, which are applied in a certain load case. For the analysis, the load cases and load combinations as indicated in table 5.11 have been distinguished.

Table 5.11: Load cases and load combinations.

Sub-Assembly	Load case	Simulation number	Load combination
Link-piston assembly	Extension	1.	One link – 100 bar
		2.	One link – 300 bar
	Retraction	3.	One link – 1114 N
		4.	One link – 3341 N
UR-borehole assembly	UR contact only	5.	Nominal torque
		6.	Maximum torque
	Bit contact only	7.	Nominal torque – Nominal WOB
		8.	Nominal torque – Peak WOB
		9.	Maximum torque – Peak WOB
	Combined contact	10.	Nominal torque
		11.	Maximum torque
Armstopper assembly	Armstopper – block contact	12.	One armstopper – 34 kN
		13.	One armstopper – 103 kN
Sleeve channel assembly	Eccentric spring force application	14.	Spring disk – 3341 N

For each of the sub-assembly simulations the following research questions will be answered:

1. To what extend do the hand calculations correspond to the data required with the FEM analysis?
2. Where do peaks in the mechanical stresses occur and why?

Answering these questions helps to determine the reliability of the results. It is also determined whether the sub-assemblies could handle certain stresses or whether the loads are simply too high.

The areas of interest are shown in the overview below (figure 5.53) for clarity.

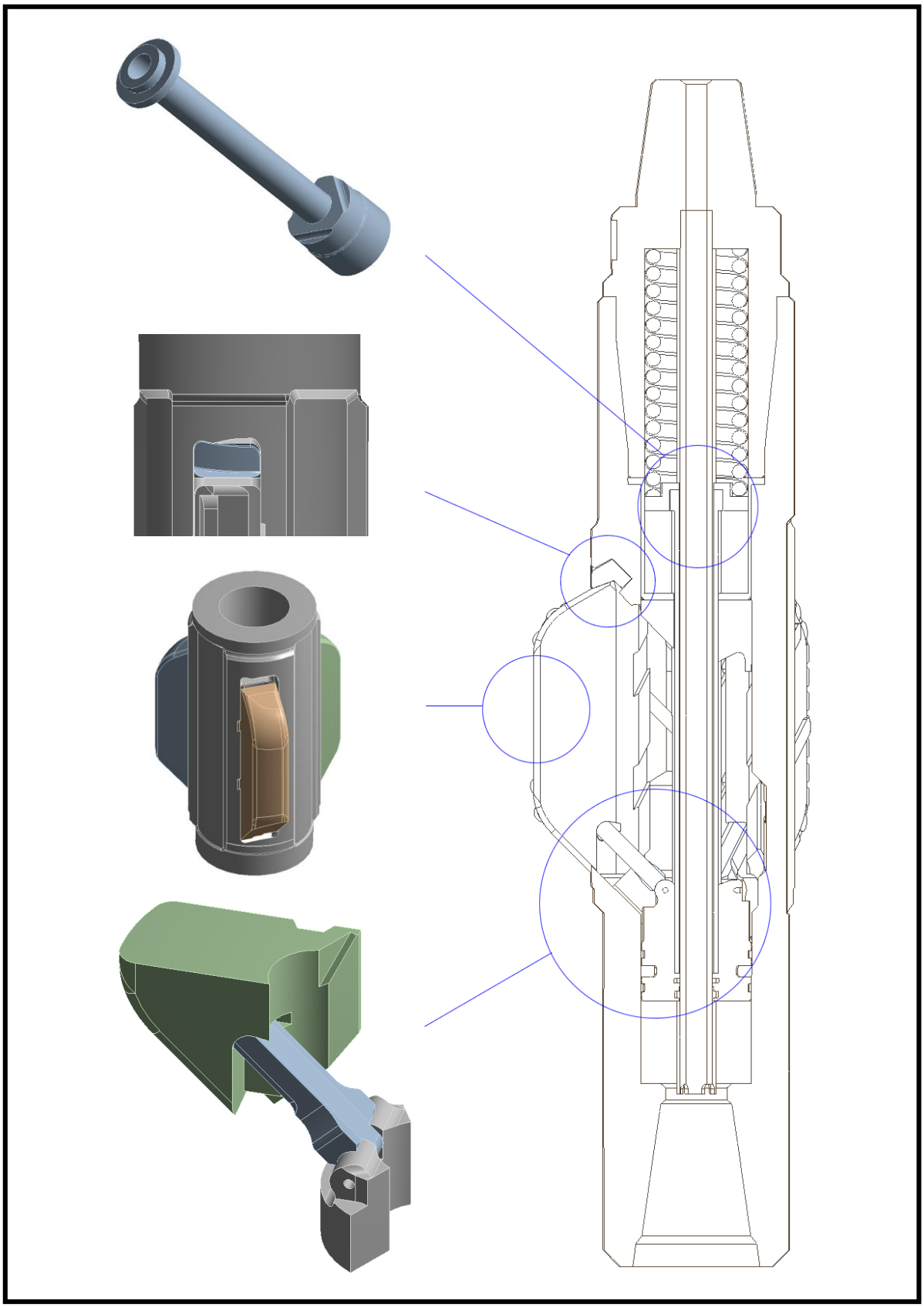

Figure 5.53: Overview of the sub-assemblies.

5.9.2. Link-piston analysis

Manual calculation

First, a manual calculation to determine the average compressive stress in the rod is made. It is known from practice that under certain conditions, the drill bit can be clogged. In that case, the pressure difference over the piston may rise to up to 30 MPa. The force that acts on the piston can be determined with eq. 5.72:

$$F = \Delta p \cdot \frac{\pi}{4}(D_{outer}^2 - D_{inner}^2) \qquad [5.72]$$

For a piston with an outer diameter of 80 mm and an inner diameter of 29 mm, this results in a force of 131 kN. The second worst-case scenario is considered here, which means one block has to convey one third of the force of the piston to the borehole wall. The narrowest cross-section of the rod has a surface area of approximately 180 mm^2. The compressive stress can be calculated as follows:

$$\sigma = \frac{F/\cos(45)}{A_{cross-section}} \qquad [5.73]$$

For the force that is computed above, this results in an average compressive stress of **343 MPa**.

In case the link pulls on the block, the maximum shear stress in the outer most fibre of the protrusion can be determined with the following simplified model, see figure 5.54. Here the shape of the protrusion is approximated by a rectangle with an equal surface area. For this calculation, the link is assumed to be jamming.

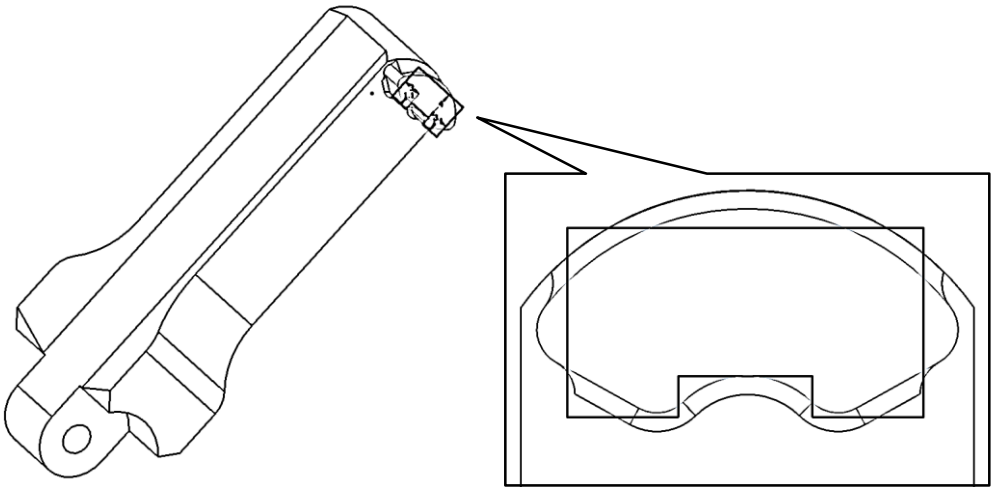

Figure 5.54: Simplified model of the link protrusion.

$$\sigma_{max} = \frac{Mc}{I} \qquad [5.74]$$

$$c = 2.727\ mm$$

$$M = 6.3\ Nm$$

$$I = \frac{1}{12}bh^3 + Ad^2 \qquad [5.75]$$

$$\bar{y} = \frac{\Sigma \tilde{y}_i A_i}{A} \qquad [5.76]$$

$$\rightarrow \bar{y} = 2.373\ mm$$

$$\rightarrow I = 88.65\ mm^4$$

$$\rightarrow \boldsymbol{\sigma_{max} = 194\ MPa}$$

Finite element analysis
The results of these manual calculations will now be verified by an analysis made in *Ansys Workbench*. To prepare the model for the analysis in Ansys, the parts must be constrained in the preferred orientation.

The rod is not only connected to the piston but also to the block. Since only the part of the block that contains the cavity for the rod is of interest, the top side of the block is cut away. The piston has also been simplified by removal of the bottom part. Due to its cyclic symmetry, only a third of the model is analysed to reduce calculation time. An overview of the model is shown in figure 5.55.

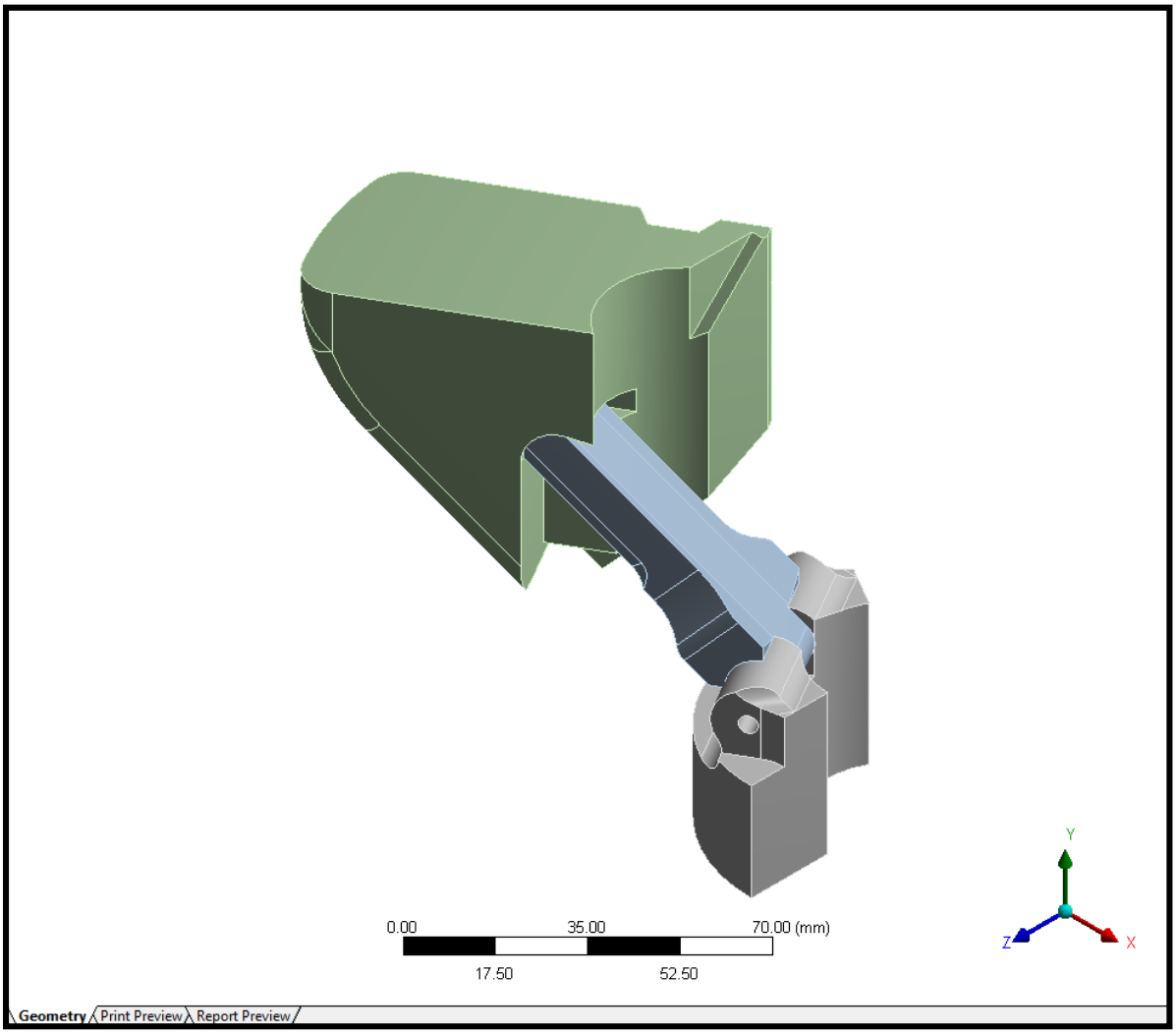

Figure 5.55: Link-piston model.

The second step involves defining the contact type between the rod and the other parts. A frictionless contact was chosen since the parts are assumed to have a smooth surface finish and remain in position. In case the link moves within the socket of the block, frictional forces will cause the pressure to redistribute. The total force can be found be integration but since the peak force and distribution itself is difficult to calculate, tests have to be carried out to determine the amount of friction and the effect it has on the link.

A no separation contact is defined at the side of the link and the block, because Ansys tends to shift the rod sideways. For clarity, these surfaces are shown in figure 5.56 below.

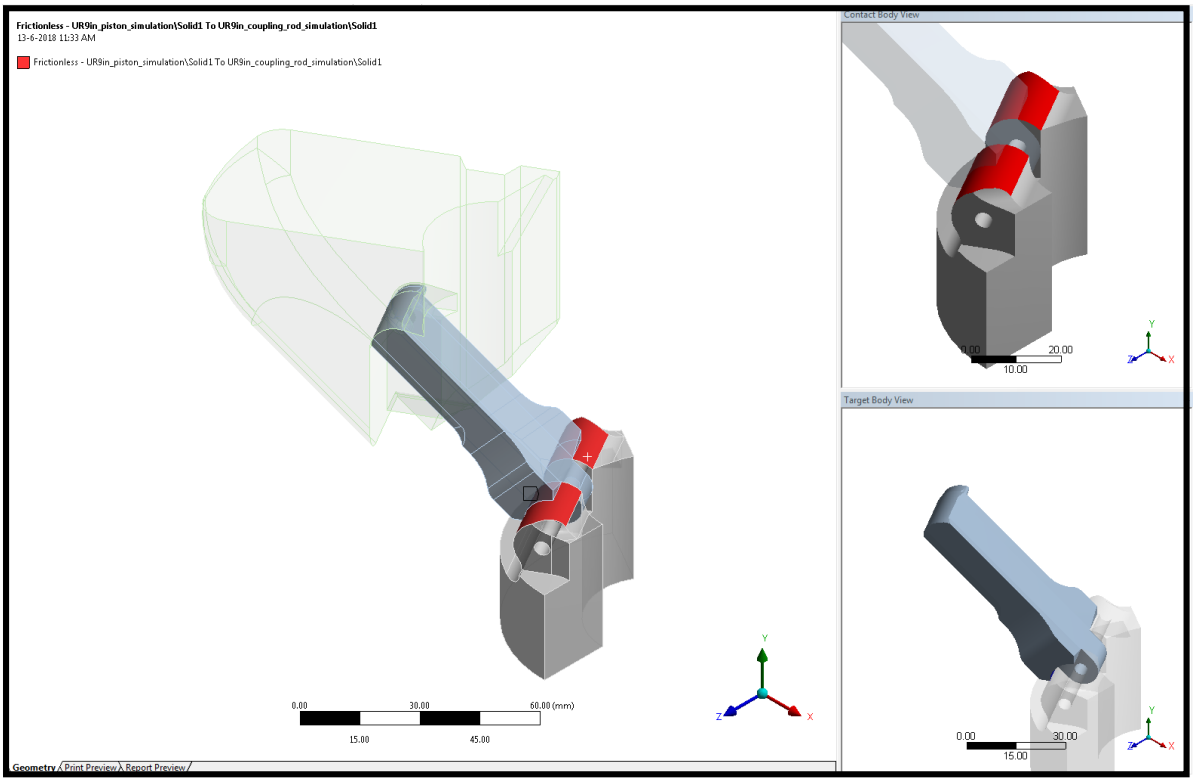

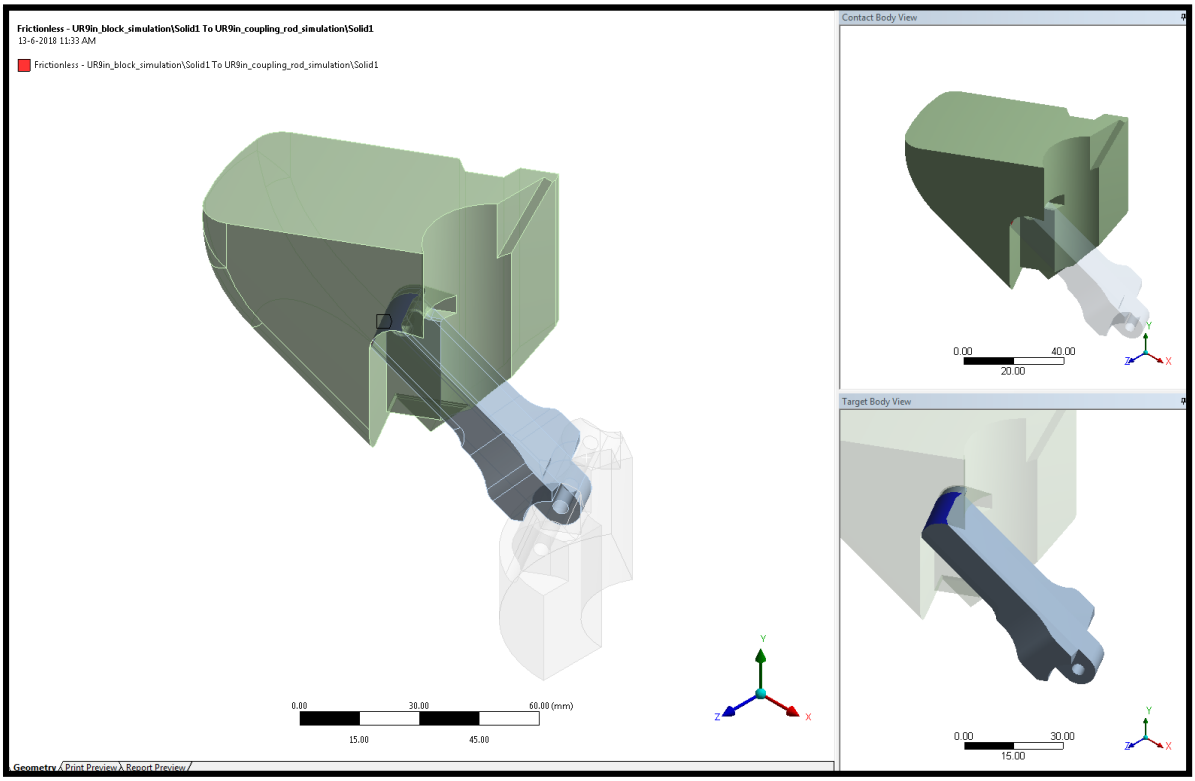

Figure 5.56: Manual contact regions.

The next step is to apply a suitable mesh. Since the bodies contain some curves, a more regular mesh can be created by setting the size function to 'curvature'. This size function locally refines the mesh and controls the growth of the mesh in regions of high curvature. A mesh refinement has been applied on the contact areas because high stresses are expected here. The generated mesh is shown in figure 5.57.

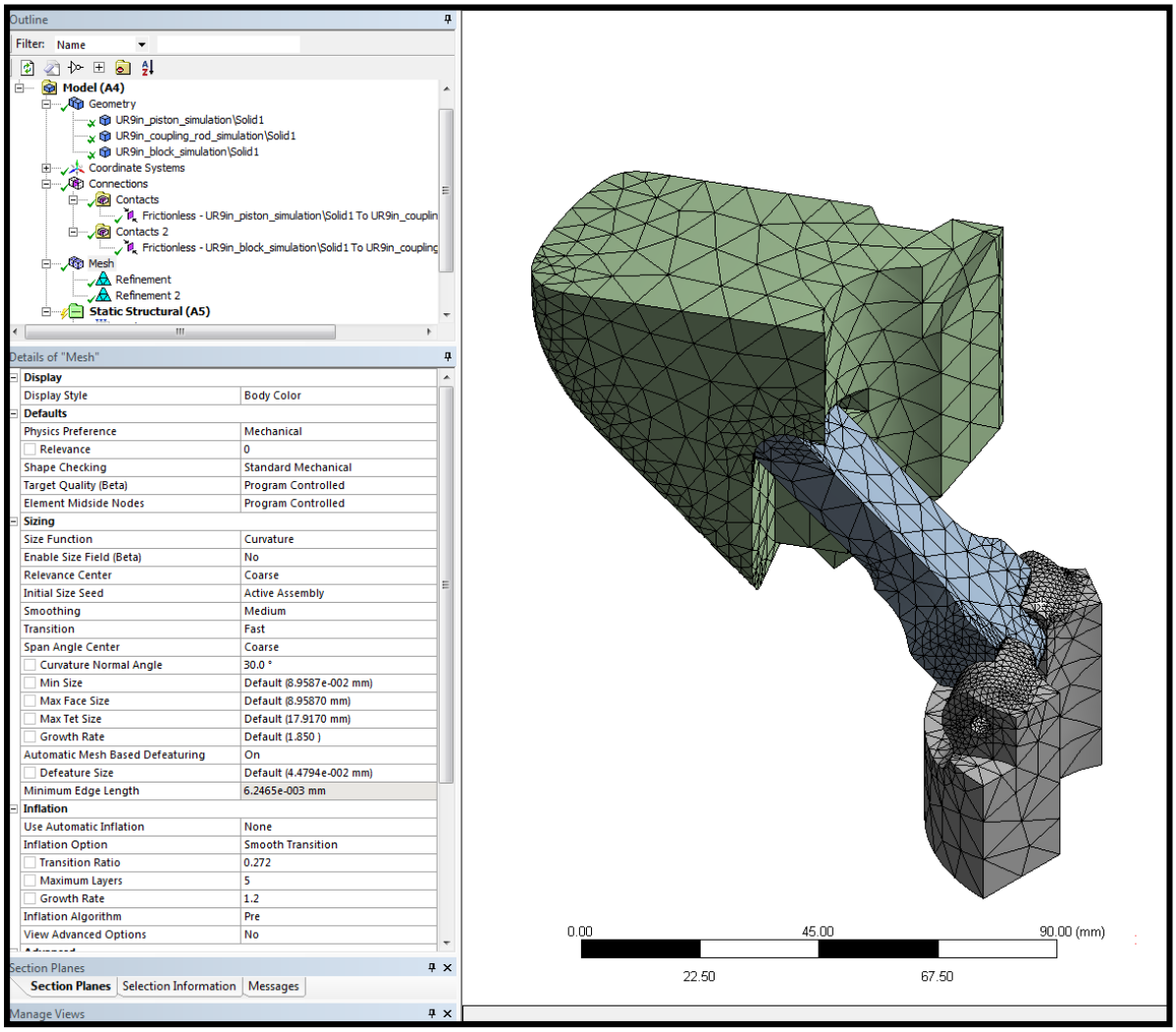

Figure 5.57: Mesh.

The mesh mainly consists of solid 3D elements. Default tetrahedral elements with midside nodes are used instead of hexahedral elements, because they mesh faster and are more suitable for double curved faces, if the element size is small enough.

Now that the connections and mesh are set, the constraints are implemented. The constraints include a two-sided fixed support for the block part, a frictionless support for the sides along which the piston-rod assembly is cut, one frictionless supports at the side of the link and a force constraint located at the bottom of the piston. These constraints are shown in figure 5.58.

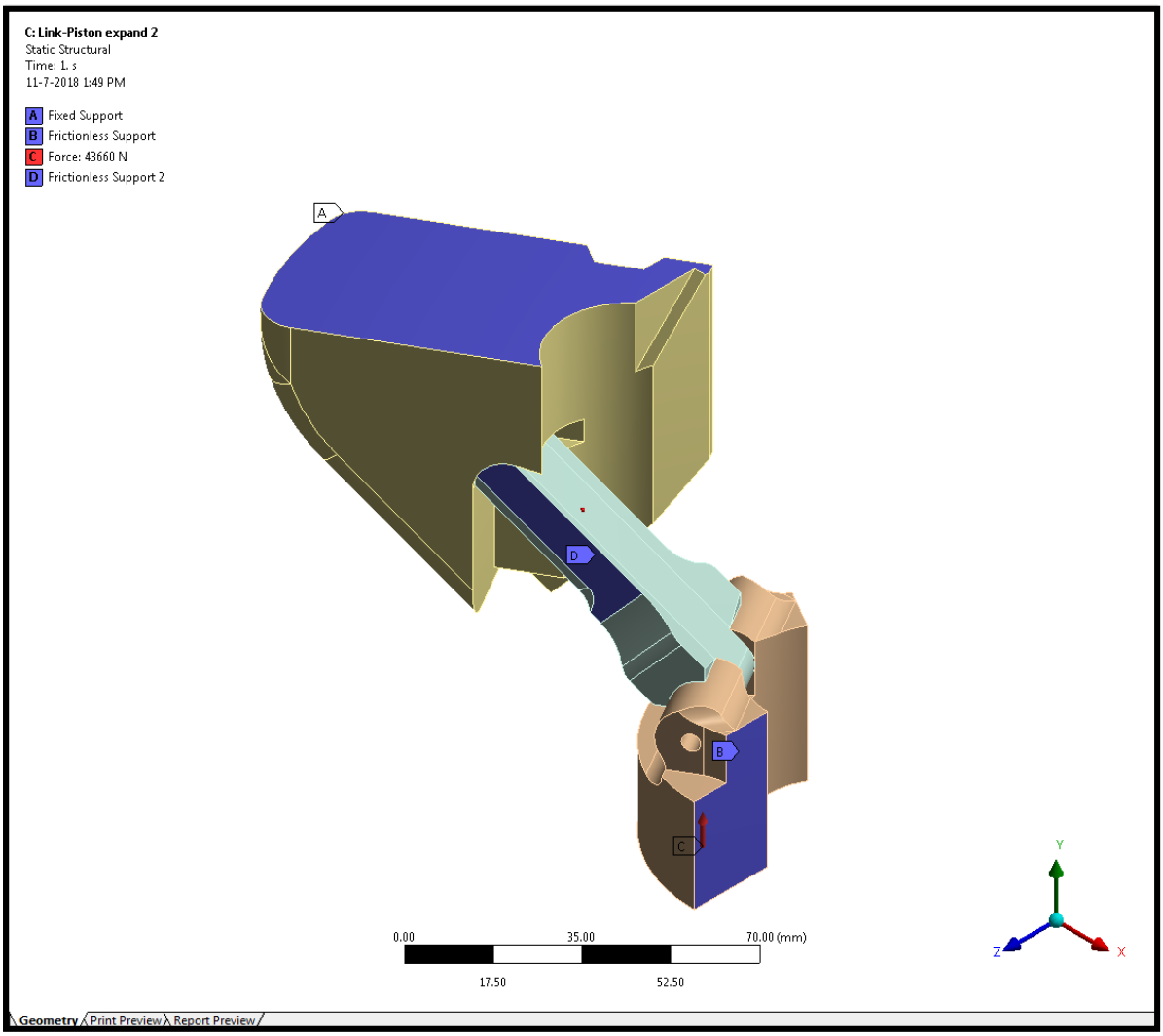

Figure 5.58: Supports and constraints.

A frictionless support type is chosen for the symmetry planes so that out-of-plane translations and rotations are fixed for both compression and tensile load cases. In-plane translations and rotations are not constraint, meaning that the surface is still able to slide upward and rotate about the normal axis. A frictionless support has also been added on the side of the link because for this position, it is constrained between the core assembly and the cutter block. It is also important to note that the frictionless support differs from a frictionless contact because the latter is nonlinear and may separate.

The fixed support has been placed on the outer surfaces of the block, as far away as possible from the contact area to avoid singularities due to the Poisson's effect. This would cause high stresses to become visible at the constrained nodes, which is undesirable.

The force vector has been defined in the global coordinate system by the values given up for the components in x, y and z direction.

The model is now ready to be solved. The solution in figure 5.59 show the resulting plot for the equivalent (von-Mises) stress for the case in which the rods each bear one-third of the piston load. The surface has been probed halfway the length of the link.

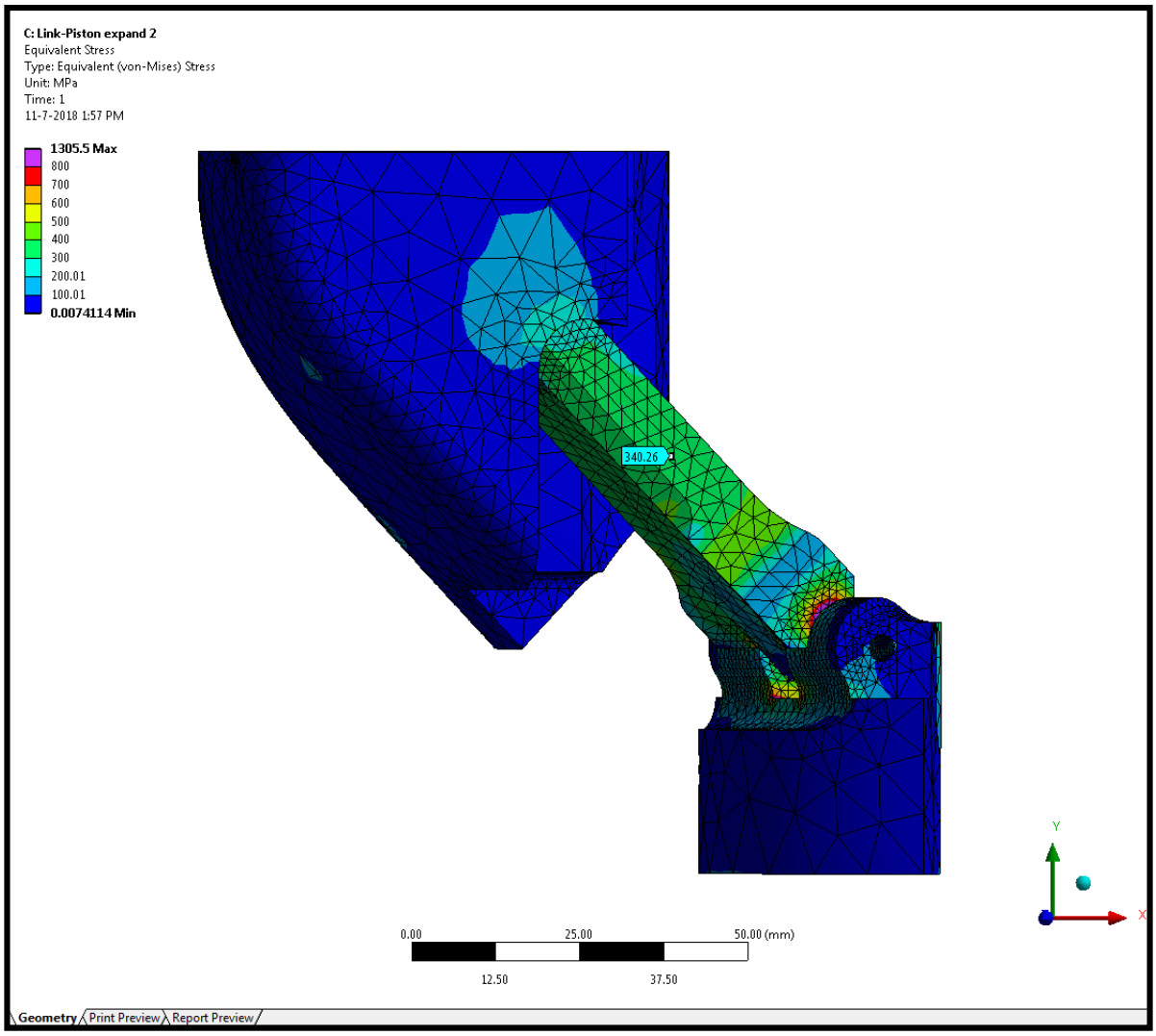

Figure 5.59: Equivalent von-Mises stress.

The same simulation is performed for the load combination in which one rod conveys the full force of the piston. The results of this simulation are shown in figure 5.60. It can be seen from the figure the stress within the rod exceeds the yield strength of common structural steel easily. The UR could stabilize itself within the hole in case one of the cutter blocks makes contact earlier than the other blocks. However, since the reamer might be constrained laterally by the bit, this is not always possible. Therefore, the maximum piston pressure had to be found that can be sustained by one coupling rod.

It turns out the previous load case can also be considered as the limiting load case for the link-piston assembly, in case a safety factor for the material of 1.25 is applied. The stress may not exceed 600 MPa in the rod. Minor stress peaks are still present along the brackets of the piston but due to material plasticity, these areas can be neglected.

This means that for the expansion of the blocks, a piston pressure of **100** bar is acceptable. The piston is able to bear 300 bars, but only if the load is distributed equally. This assumption is too optimistic and therefore not considered.

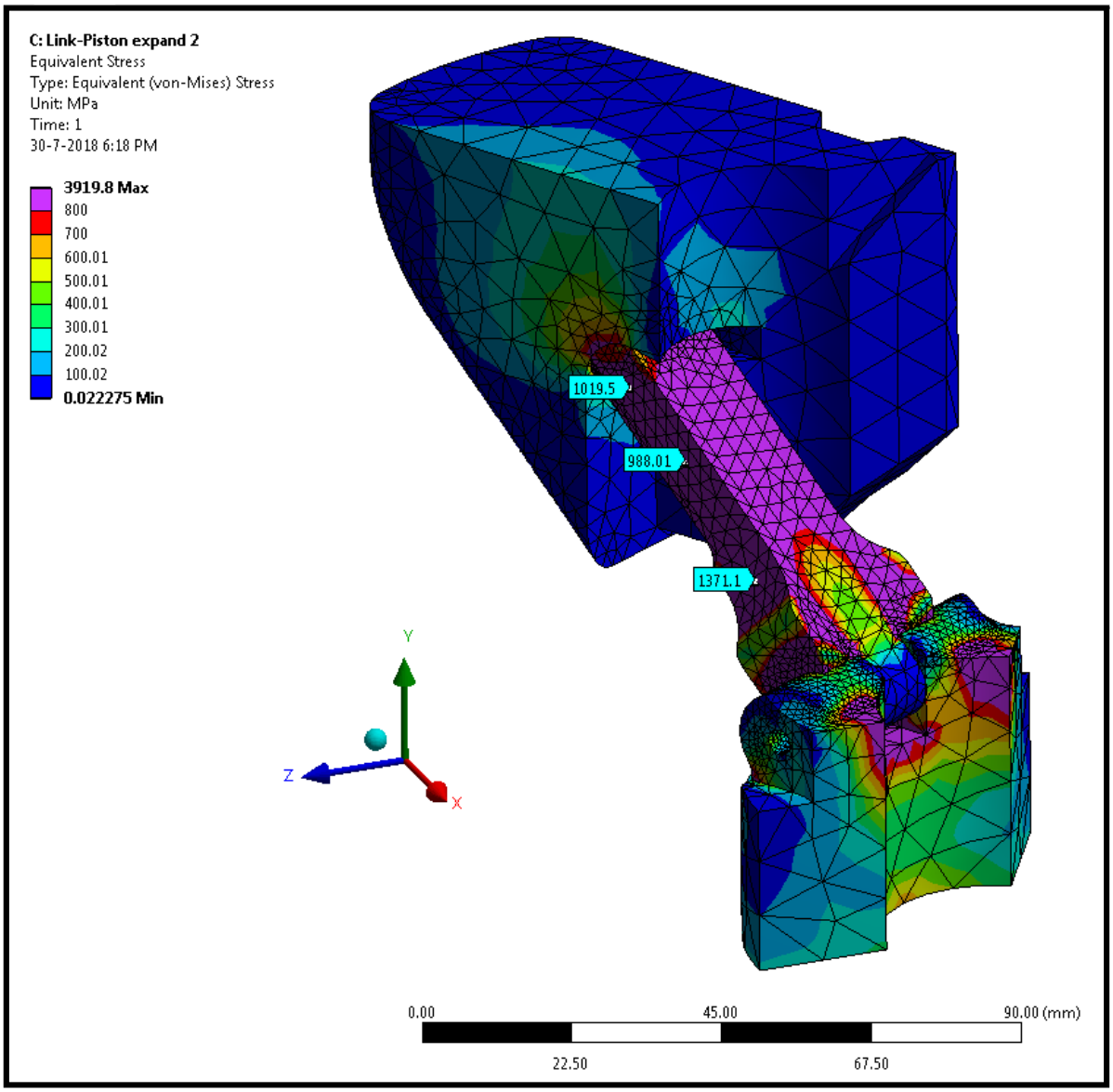

Figure 5.60: Equivalent stress plot for 300 bars of pressure conveyed through one coupling rod.

Now that the case for the extended position of the blocks has been examined, the case for retracting the block may be modelled. The result of this simulation is shown in figure 5.61. Here, the links are assumed to retract without jamming. In case one link is blocked, the full spring force will be conveyed through this link. The result of a simulation for this scenario is shown in figure 5.62. It must be noted that the stress scale has been adapted for visual purposes.

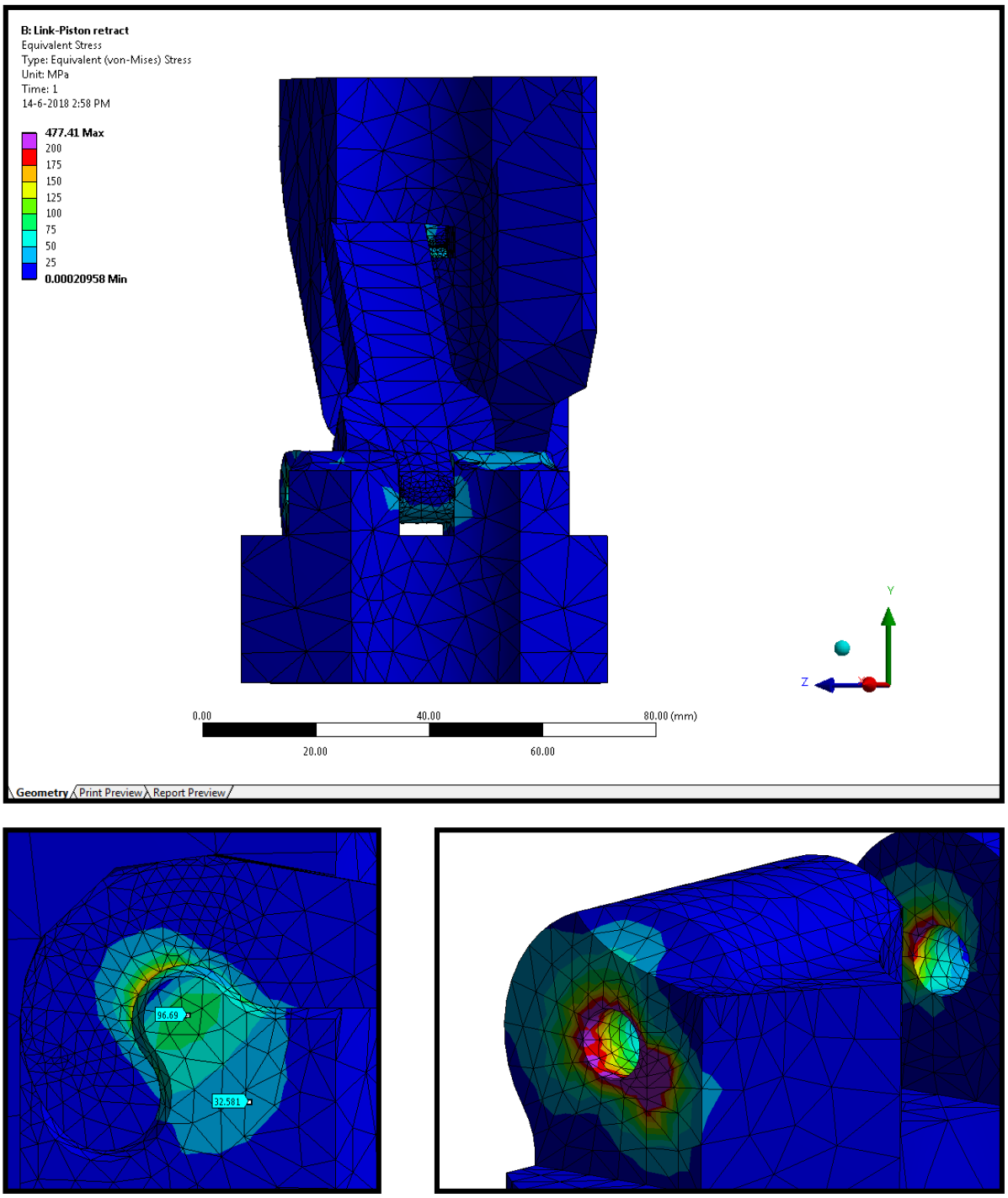

Figure 5.61: Equivalent von-Mises stress.

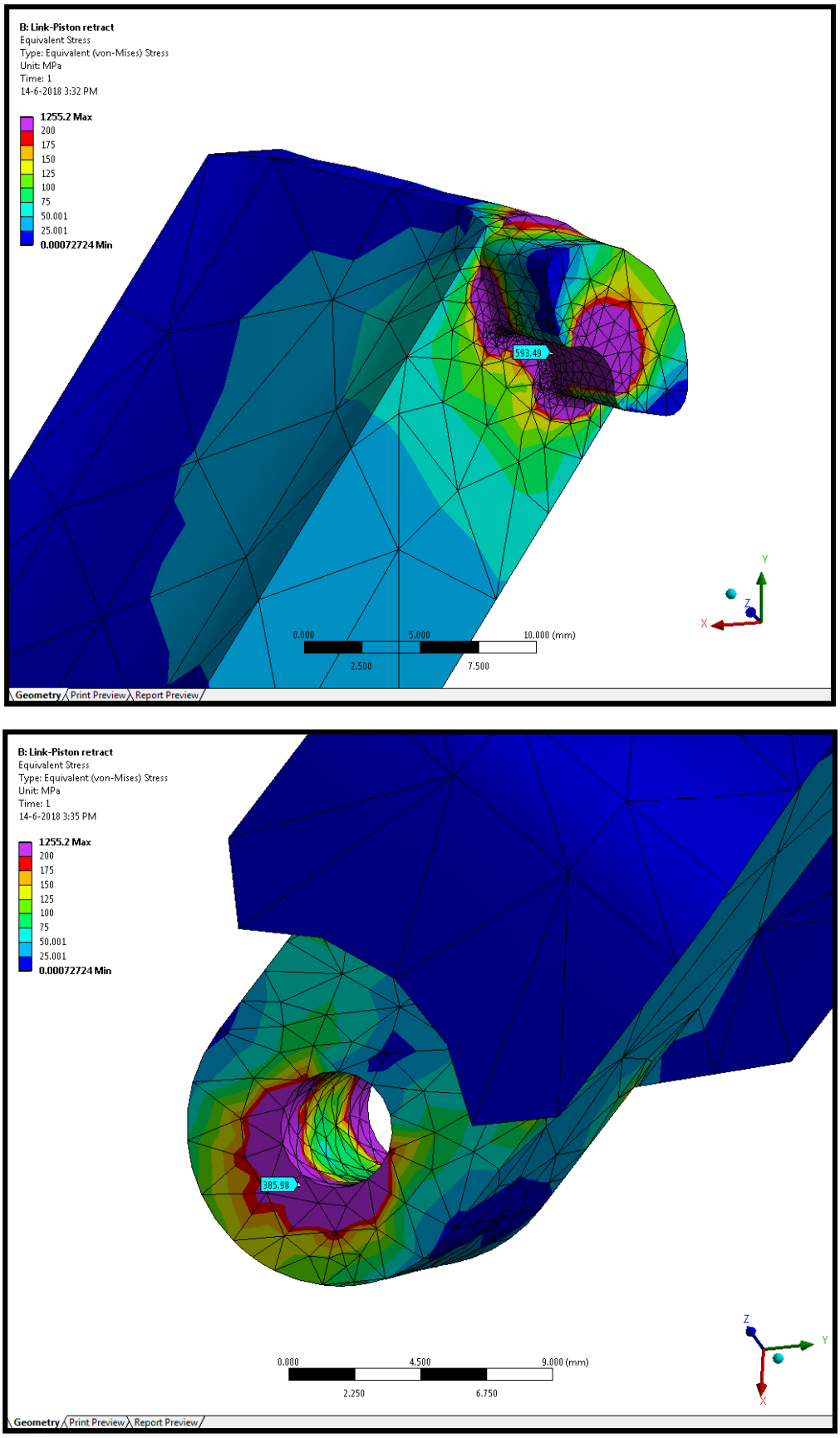

Figure 5.62: Retraction of the coupling rod with the full spring force.

Conclusion link-piston sub-assembly analysis

Now that the stress states and other phenomena have been identified, the research questions may be answered. For each question, the answer will be related to the parts in order to improve their design.

1. *To what extend do the hand calculations correspond to the data required with FEM analysis?*

The analytical calculations indicate that the average compressive stress in case the force is equally distributed should be approximately 343 MPa. In Ansys, values in ranging from 325 to 360 MPa were found by probing the surface at the smallest cross-section. For the case in which one rod transmits the full force, a stress of 1030 MPa has been hand calculated. The FEM model shows a sample values ranging from 850 MPa to 1100 MPa.

For the pin support, the stresses found with the FEA are higher compared to the hand calculations. A high stress concentration occurs under the fillet below the protrusion, which has not been accounted for in the hand calculation. In response to these results, a reaction force analysis is carried out. This analysis can be found in appendix D. The reaction force analysis showed that the model is solved properly. It is therefore concluded that the stress peaks are ordinary stress concentrations and no singularities.

By taking more probes, it turns out that the FEM model verifies what has been calculated by hand. Deviations are likely due to the presence of the pinholes and transitions in the geometry.

2. *Where do peaks in the mechanical stresses occur and why?*

From figure 5.61 and figure 5.62, it can be deduced that peak stresses mainly occur around the protrusion and pin support structures. Small corners and fillets cause a sharp transition in the stresses. In case the link retracts the block, there will be peak stresses inside the brackets. These stresses are likely caused by a counteracting moment that has a direction of rotation opposite to the rotation direction caused by the force that acts on the protrusion on top.

5.9.3. UR – borehole analysis

Introduction

The bottom-core part of the UR houses the blocks and the piston-rod assembly. It is the largest part in the UR. This cylindrical part contains one box at each end and has three rectangular grooves cut into it from the side. The inside is drilled out, such that a hole with a diameter of 80 mm remains through which the piston has to slide during assembly and operation of the UR. Because many edges are present, it will also be one of the hardest parts to manufacture. These edges are located inside the blocks slots and inside the recess along which the drilling fluid has to flow to the surface.

Three *load cases* have been distinguished for this part, see table 5.12. One in which the remaining torque is completely transmitted by the drill bit to the borehole, one in which the torque is entirely conveyed through the blocks of the UR and one case in which both the cutter blocks and drill bit convey some of the torque. For the first and second loading case, the assumption is made that the drill bit or UR blocks will not be in contact with the borehole wall at some point in time. For each of these three loading principles, three *load combinations* have been distinguished, see table 5.12 and 5.13.

Table 5.12: Load cases and load combinations.

	Load case	Load combination		
UR-borehole assembly	UR contact only	5.	Nominal torque	
		6.	Maximum torque	
	Bit contact only	7.	Nominal torque	Nominal WOB
		8.	Nominal torque	Peak WOB
		9.	Maximum torque	Peak WOB
	Combined contact	10.	Nominal torque	
		11.	Maximum torque	

Table 5.13: Measurements of torque and WOB.

Parameter	Value	Units
WOB - nominal	5000	[kg]
WOB - peak	10000	[kg]
Torque - nominal	8000	[Nm]
Torque - maximum	20000	[Nm]

Manual calculation

A simplified calculation can be used to determine the stress due to a moment and a force both directed along the axis of rotation of the UR. It is expected that the maximum stress occurs somewhere at the outer most radius. To determine the equivalent Von Mises stress, the in plane principal stresses are determined first, according to:

$$\sigma_{1,2} = \frac{\sigma_x + \sigma_y}{2} \pm \sqrt{\left(\frac{\sigma_x - \sigma_y}{2}\right)^2 + \tau_{xy}^2} \qquad [5.77]$$

$$\tau_{xy} = \frac{T c_0}{J} \qquad [5.78]$$

$$J = \frac{\pi}{2}(c_0^4 - c_i^4) \qquad [5.79]$$

$$\sigma_y = \frac{F}{A} \qquad [5.80]$$

$$A = \pi(c_0^2 - c_i^2) \qquad [5.81]$$

For the load case with the bit contact only, the inner radius c_i equals the piston radius, 40mm, while the outer radius c_0 equals 66.203 mm. By using a value of 8000 Nm for the torque T and a value of 49050 N for the force F, the following results can be obtained:

$$A = 1.03 \cdot 10^{-2}\ m^2$$

$$J = 3.3 \cdot 10^{-5}\ m^4$$

$$\rightarrow \sigma_y = 4.8\ MPa$$

$$\tau_{xy} = 16.75\ MPa$$

$$\rightarrow \sigma_1 = 14.5\ MPa, \sigma_2 = -19.3\ MPa$$

Now that the in-plane principle stresses have been determined, the equation below can be used:

$$\sigma_1^2 - \sigma_1\sigma_2 + \sigma_2^2 < \sigma_Y^2 \qquad [5.82]$$

$$\mathbf{35.4\ MPa} < \sigma_Y$$

Since the yield strength of the steel is much higher, the UR can sustain this load easily. The load due to the bending of the blocks will also be much higher.

In the UR contact only case, the blocks transmit the moment completely. Because of this, a force on the slot edge will be present that tends to yield the steel locally, since the blocks are 1-2 mm smaller in width than the slot.

For now, it is assumed that the blocks will be pressed against the wall along the entire edge. The yield strength of the material is assumed 600 MPa. In case the contact height would be 25 cm and the force 71 kN, the contact length should be equal to about **0.5 mm**.

Finite element analysis
The parts will now also be analysed with finite element software. The load mechanism where only the UR cutter blocks contact the borehole is considered first, see table 5.14.

Table 5.14: Considered load case.

Load case	Load combination	
UR contact only	5.	Nominal torque

The three cutter blocks have been placed in the grooves and are only constrained on the sides. The blocks have been modified for the test, such that the blocks are slightly smaller than the slots. In this way, the edges can be constrained to the surfaces on the sides of the slots and there will not be any interference of the parts. The core part has also been reduced in length, to reduce simulation time. The geometry is presented in figure 5.63.

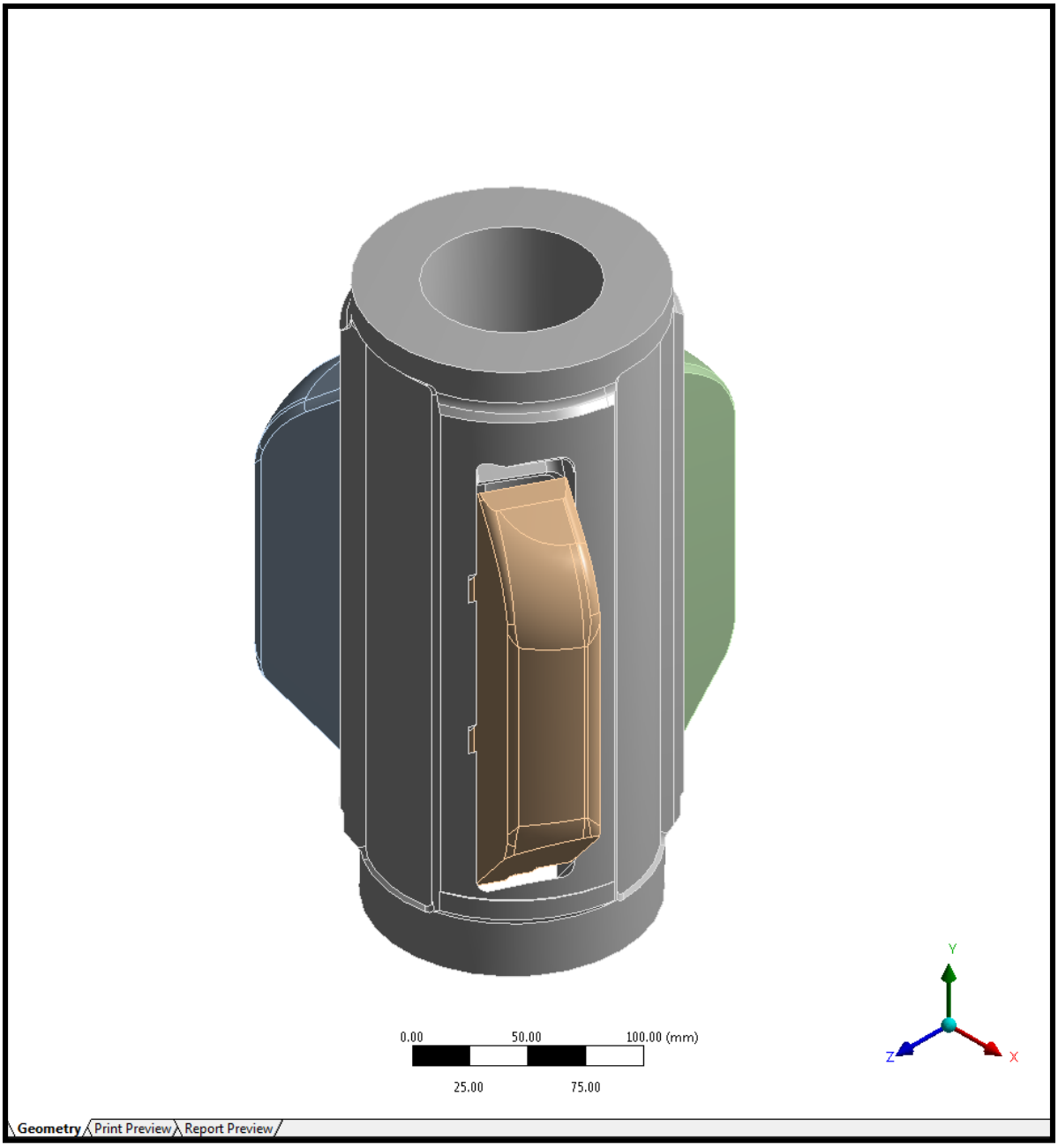

Figure 5.63: Block-bottom assembly geometry.

Now, the contact regions will be defined. The blocks are tilted slightly such that the sides are in contact with the block slot. On each side, the edges are connected to the contacting surface. Since the edges contain the elements that are the most likely to deform, they are assigned as the contact elements. The surfaces opposite to these edges will be assigned as target elements. These connections are shown in figure 5.64.

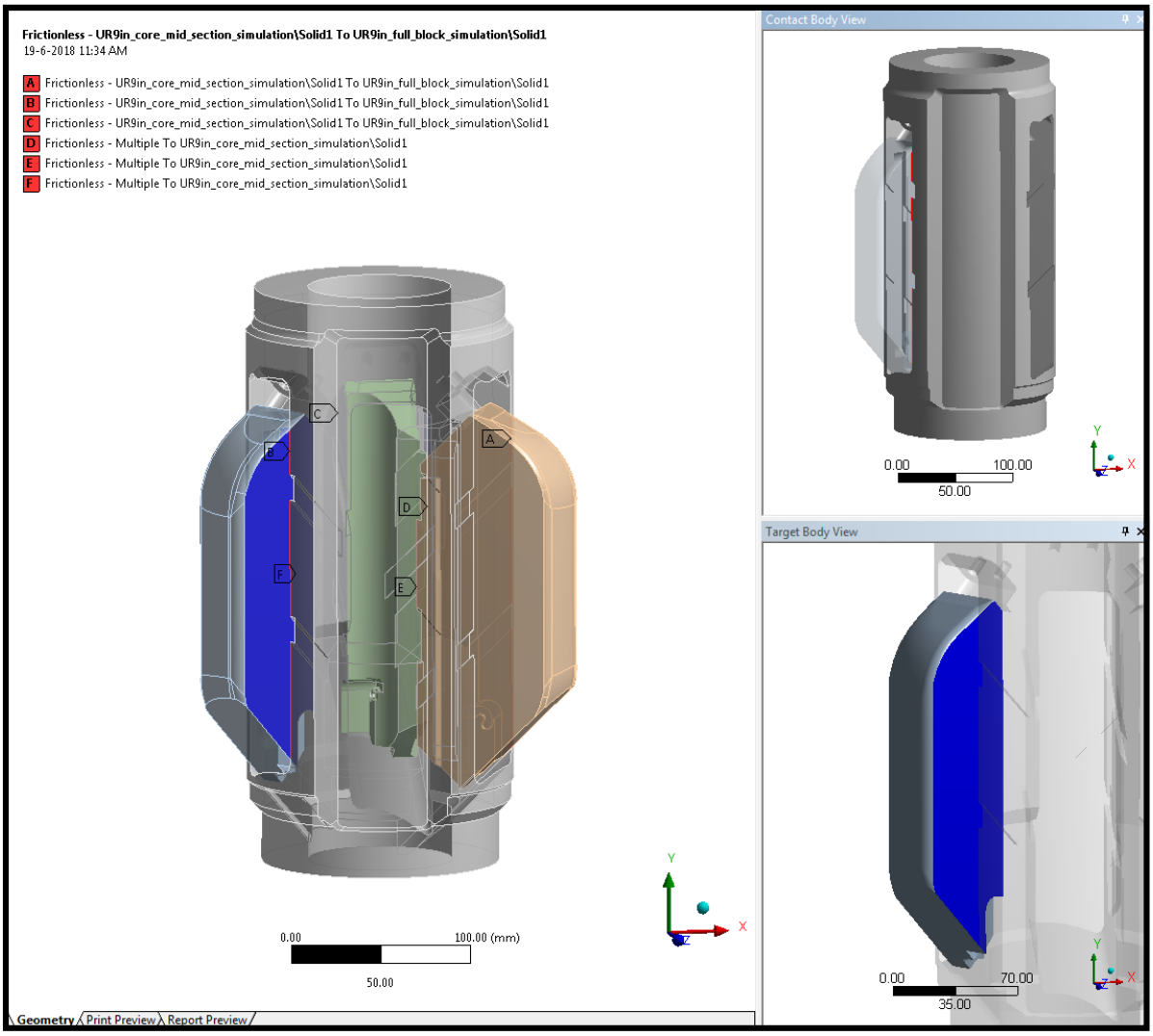

Figure 5.64: Connections.

Frictional and frictionless contacts are non-linear contact types. This means that only compressive forces can be transferred. In order to have results, non-linear calculations need to converge. For non-linear contacts, this can take a lot of time. Each non-linear simulation consists of sub-steps that involve an iterative process. *Ansys* uses the moment, rotation, displacement and force as convergence criteria.

In case of the force, the residual force has to be smaller than a certain force criterion for convergence. The solving process in *Ansys* can be monitored by changing the solution output in the solution information window. In case convergence problems are encountered, one might look at the contact stiffness or consult the analysis settings for the step and non-linear control options. By enabling '*auto time stepping*', the initial number of sub steps may also be defined.

Next, the mesh can be applied (figure 5.65). The size function is again set to 'curvature'. The body sizing function tool is used to set the element size to 5 mm. If the mesh size is too coarse, the stiffness of the model is not properly captured and stress gradients will not accurately be predicted.

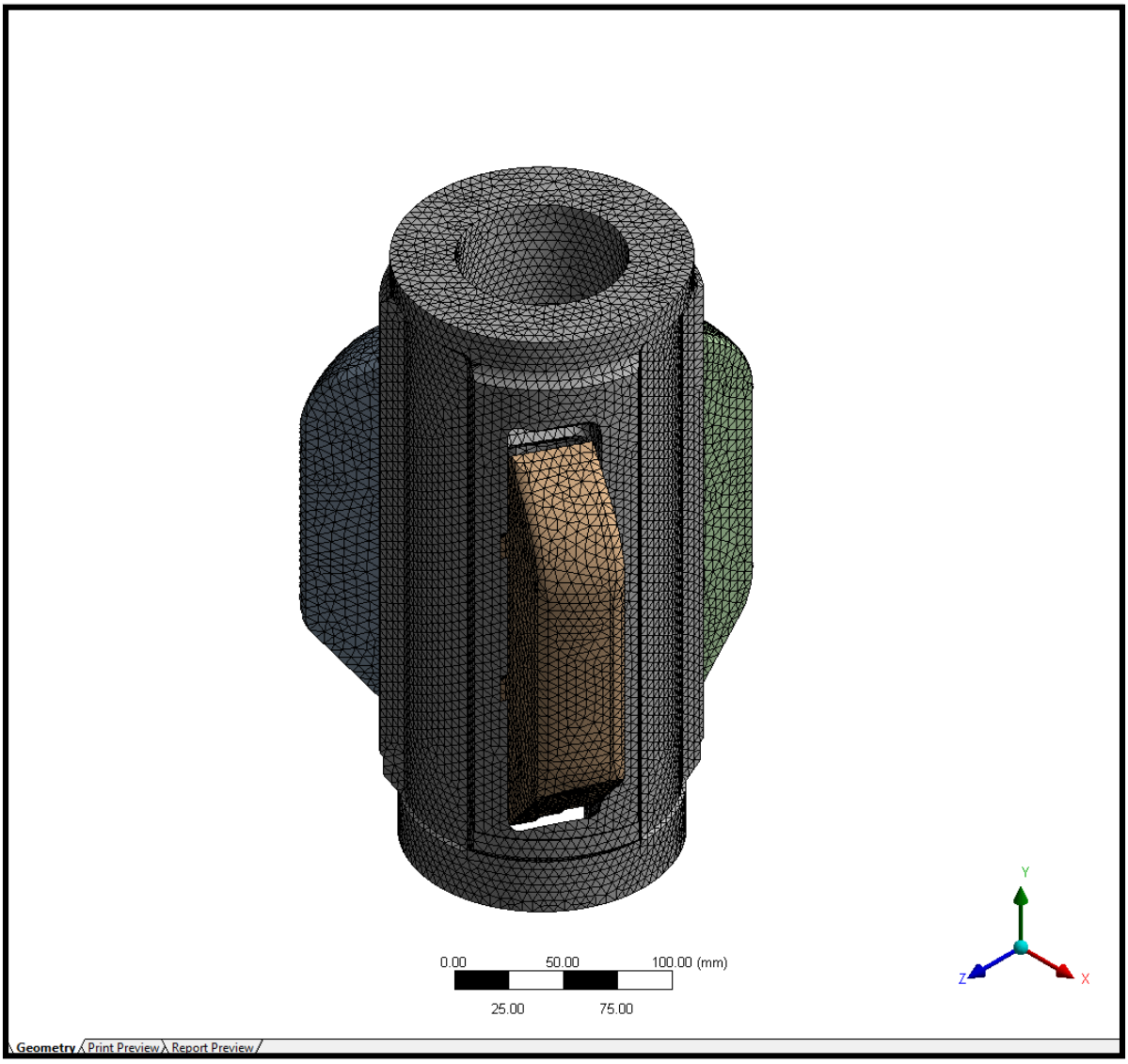

Figure 5.65: Mesh.

Next, support reactions are implemented. The blocks are fixed at the outer most edge with a displacement constraint. The core is allowed to rotate around all axis and allowed to translate sideways. Since the core is able to rotate around all axes, the blocks and the core can tilt with respect to each other. The support conditions are shown in figure 5.66.

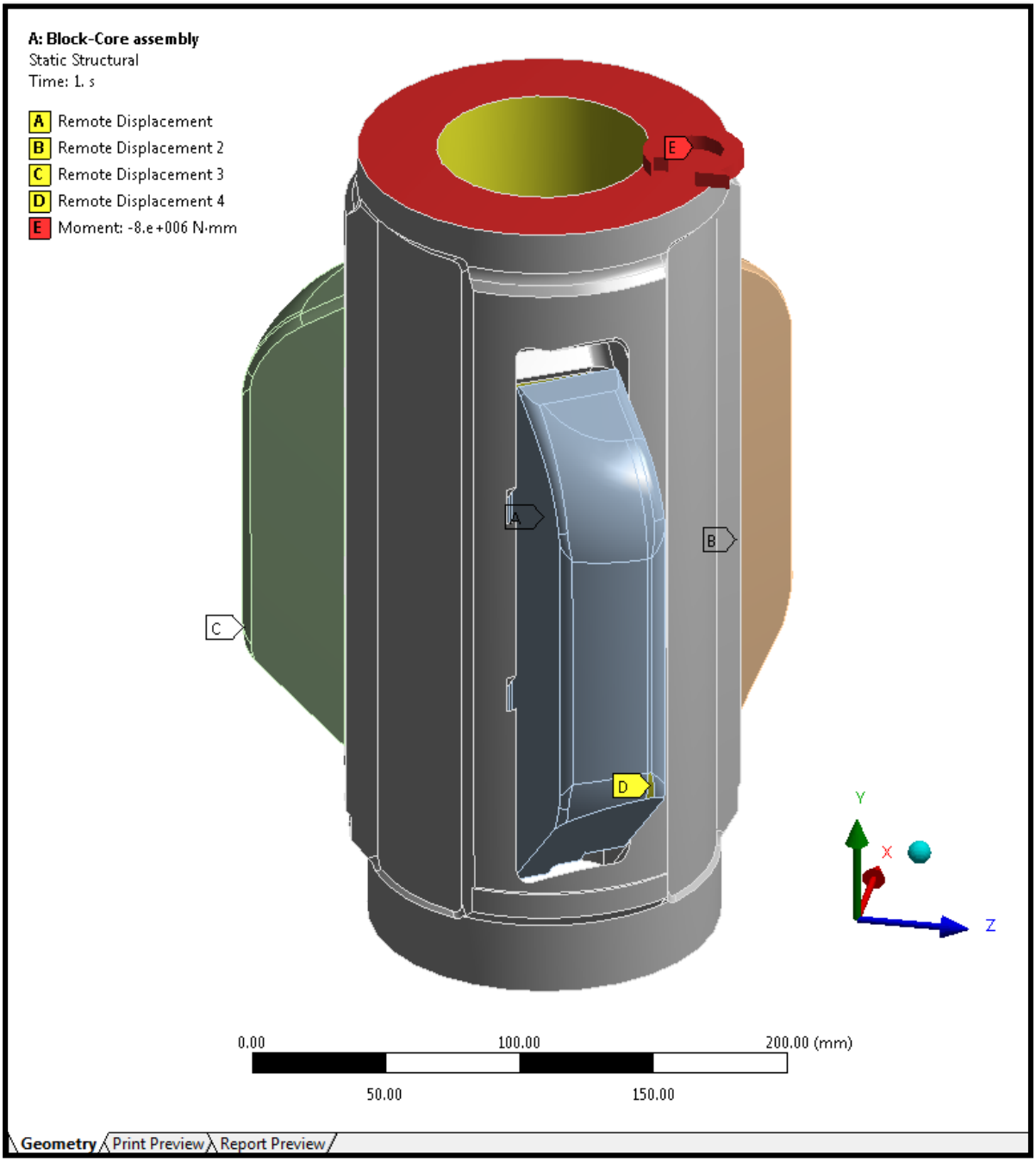

Figure 5.66: Support reactions.

A moment constraint has been applied at the top surface of the assembly while the displacement constraint has been placed at the bottom surface. It must be noted that the moment is given in *N·mm*. The moment vector is defined by its components in the global coordinate system.

By solving the model, the stress distribution as presented in figure 5.67 is found. It turns out that the area underneath the armstopper and the edges around the block slots contain relatively high stresses. A section-view of the backside of the block is shown in figure 5.68. It can be seen that a high stress peak is present here, which is likely a singularity. Because the area seems suspicious, a stress convergence study has to be carried out. This will be discussed in the next sub-chapter.

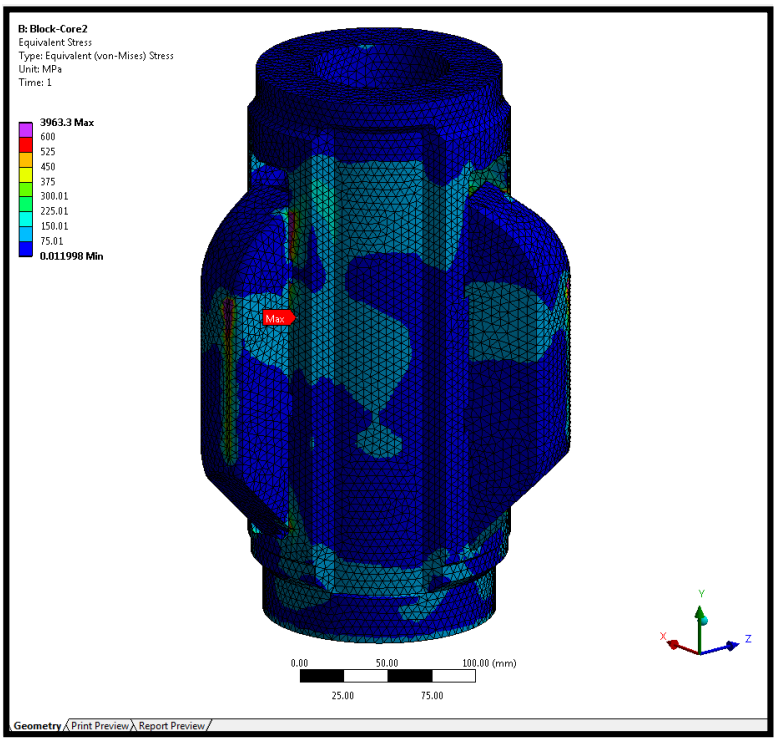

Figure 5.67: Stress distribution.

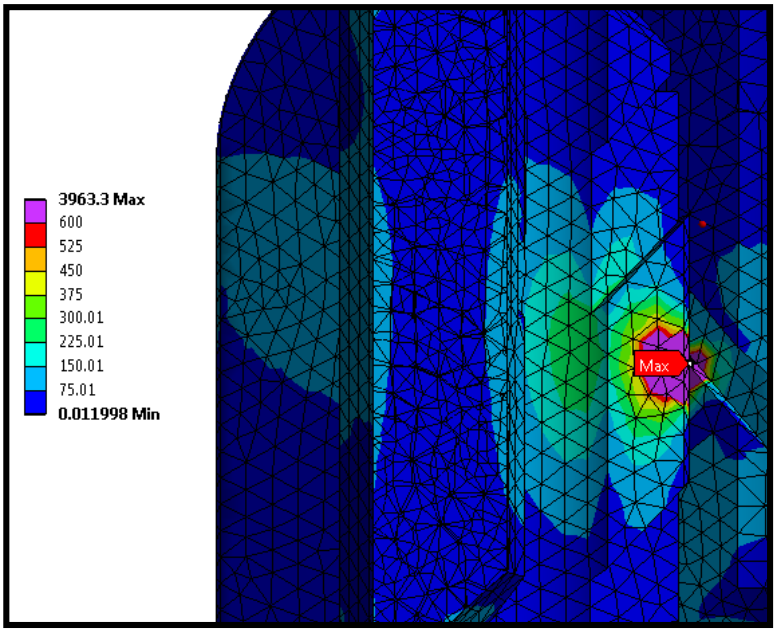

Figure 5.68: Peak stress.

FEA peak stresses

Introduction
There are situations where the stress becomes artificially high. Although more precise results and convergence should be reached with mesh refinement, the occurrence of geometry discontinuities, point-edge loads or stiffness transitions might prevent this from happening. In this case, the stresses are not actual static peak stresses but stress singularities, due to numerical problems in the FEA.

Admissibility of singularities
For actual static stress peaks, the material can be damaged by high strains and subsequent yielding. However, the effect of the disturbance remains confined to the contact zone or point of application of the load, see figure 5.69. According to *St. Venant's principle*, the stresses are not perturbed at some distance from the singularity and engineers might therefore dismiss the peak stress if the stress in the vicinity of the hotspot is not of interest. In case the high localized stresses are of a dynamic character, the risks involved are higher due to the occurrence of fatigue.[39]

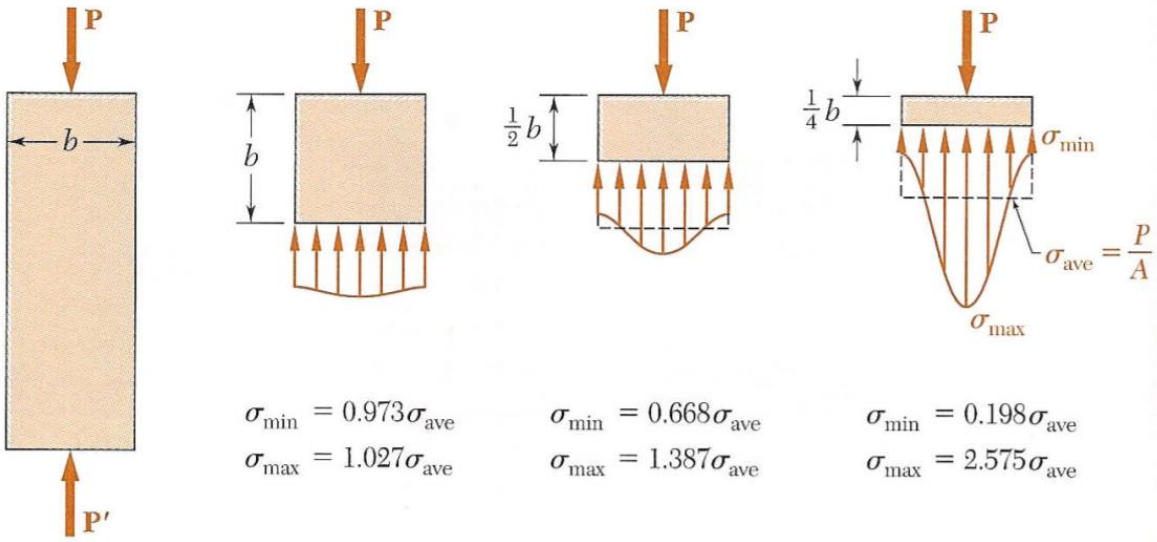

Figure 5.69: St. Venant's principle: normal stress distribution distorted in the vicinity of the point load.[40]

It may also be acceptable to leave singularities out of consideration in case only the displacement field is of importance. Displacements will remain finite at sharp corners. Since the stresses are derived from strains (eq. 5.83) and the strain is evaluated based on the gradient of the displacement field (eq. 5.84), the stress will still go to infinity.

$$\sigma_{i,j} = \sum_{k=1}^{3}\sum_{l=1}^{3} c_{i,j,k,l}\varepsilon_{k,l} \qquad [5.83]$$

$$\varepsilon_{i,j} = \frac{1}{2}\left(\frac{\partial u_i}{\partial x_j} + \frac{\partial u_j}{\partial x_i}\right) \qquad [5.84]$$

Lastly, the model may also include singularities in case the requested quantity results from an integral over the model domain. The total elastic strain energy inside a system is an example of this (eq. 5.85).

$$U = \frac{1}{2}\int_{\Omega} \sigma : \varepsilon \, d\Omega \qquad [5.85]$$

Singularity identification
To determine whether the peak stress can be categorized as a singularity, a mesh refinement study can be carried out. This may be done either manually or automatically with *Ansys*. The results of the mesh refinement analysis are used for the stress convergence analysis.

Ansys uses an adaptive mesh refinement technique in which a so-called *h-refinement* methodology is applied. To estimate the discretization error of finite element solutions, *a posteriori error estimators* are applied, which use the solution of the FEA itself to derive an estimate of the actual solution error. The h-refinement technique also decreases the mesh size in high stress regions.

Ansys utilizes the *Zienkiewicz-Zhu (ZZ)* error estimator:

$$\|U\|^2 = \sum_{i=1}^{m} \{\varepsilon\}_i^T \, [E] \, \{\varepsilon\}_i \, dV \qquad [5.86]$$

Here, m indicates the number of elements in the domain of interest, $\{\varepsilon\}$ indicates the strain vector and $[E]$ is the elasticity matrix. The left hand side shows the squared global energy norm, $\|U\|^2$. The global energy error norm may now be determined accordingly:

$$\|e\|^2 = \sum_{i=1}^{m} \int (\{\varepsilon^{\cdot}\}_i - \{\varepsilon\}_i)^T \, [E] \, (\{\varepsilon^{\cdot}\}_i - \{\varepsilon\}_i) dV \qquad [5.87]$$

The strain field that has been smoothened over the entire structure is indicates by $\{\varepsilon^{\cdot}\}$. In this way, the variation of the energy within a part can be used to quantify the global energy error. The relative error can now be determined with:

$$\eta = \left[\frac{\|e\|^2}{\|U\|^2 + \|e\|^2} \right]^{1/2} \qquad [5.88]$$

The discretization is considered sufficient if the relative error η obtains a value ≤ 0.05. An example of the mesh refinement cycle is shown in figure 5.70 for a plate, upon which a distributed load is applied.

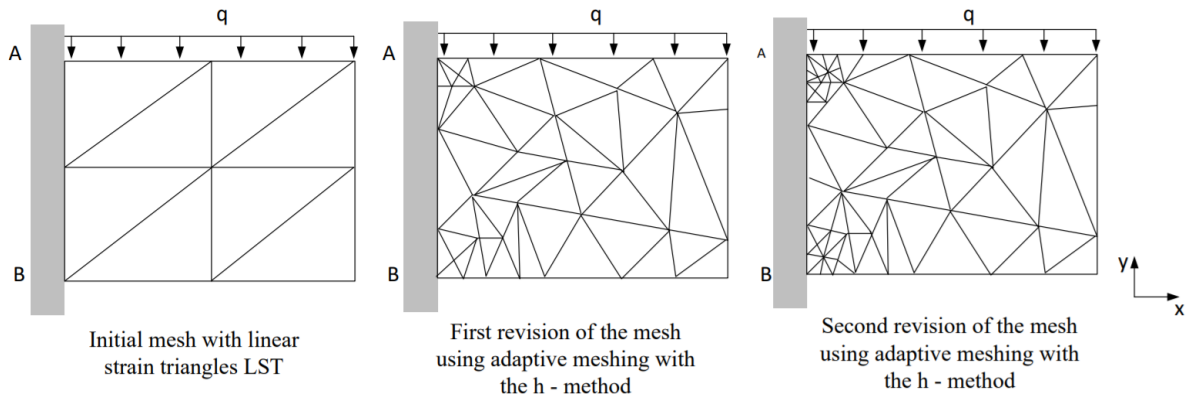

Figure 5.70: Adaptive meshing.[41]

To start the mesh refinement process, a convergence graph will be inserted by right clicking on the equivalent stress. Within details of 'convergence', the allowable change is set to 5%, meaning that the maximum von Mises stress may not have changed more than 5% from the previous iteration. At the solution details, the amount of refinement loops is set to 4, so that the mesh will only be refined a finite number of times. The program will now automatically refine the mesh locally, based on the error approximation technique. The results for the refinement procedure is shown below:

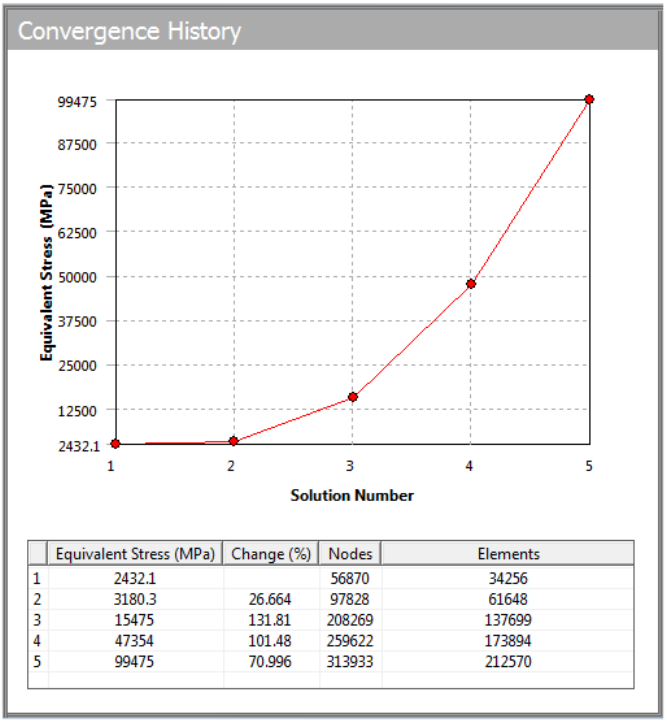

	Equivalent Stress (MPa)	Change (%)	Nodes	Elements
1	2432.1		56870	34256
2	3180.3	26.664	97828	61648
3	15475	131.81	208269	137699
4	47354	101.48	259622	173894
5	99475	70.996	313933	212570

Figure 5.71: Convergence history.

From the red exclamation mark before the convergence branch and the climbing line in figure 5.71, it can be concluded that the stress does not converge. From the simulation, it can also be seen that *Workbench* attempted to refine the mesh around the maximum stress area, see figure 5.72.

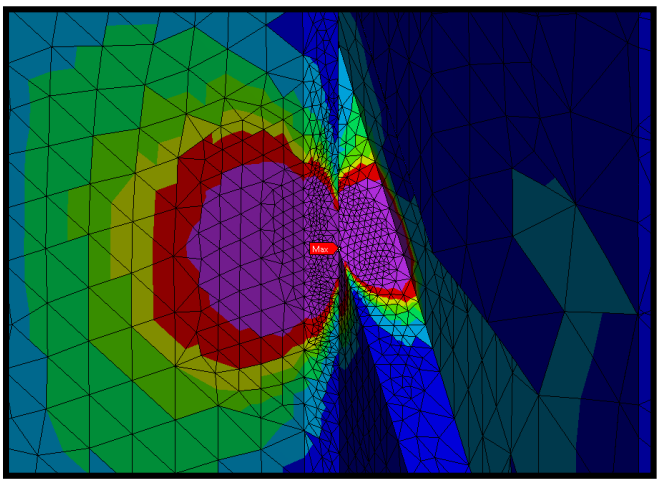

Figure 5.72: Mesh refinement at the high stress region.

Since the stress is of interest, another way has to be found to specify the stress along the inner edge of the block. Some ways to deal with singularities are mentioned in the next section.

Dealing with singularities
In case it has been decided that the singularity will not be ignored, there are several ways to deal with it. Some of the most common methods are mentioned below:

- Adjust the model geometry by adding chamfers or fillets to edges (figure 5.73) or increase the size of the contact area. A downside to this procedure is the use of finer mesh and consequently longer calculation times. Sometimes detailed features are deliberately removed from the model geometry, which is known as '*defeaturing*'.

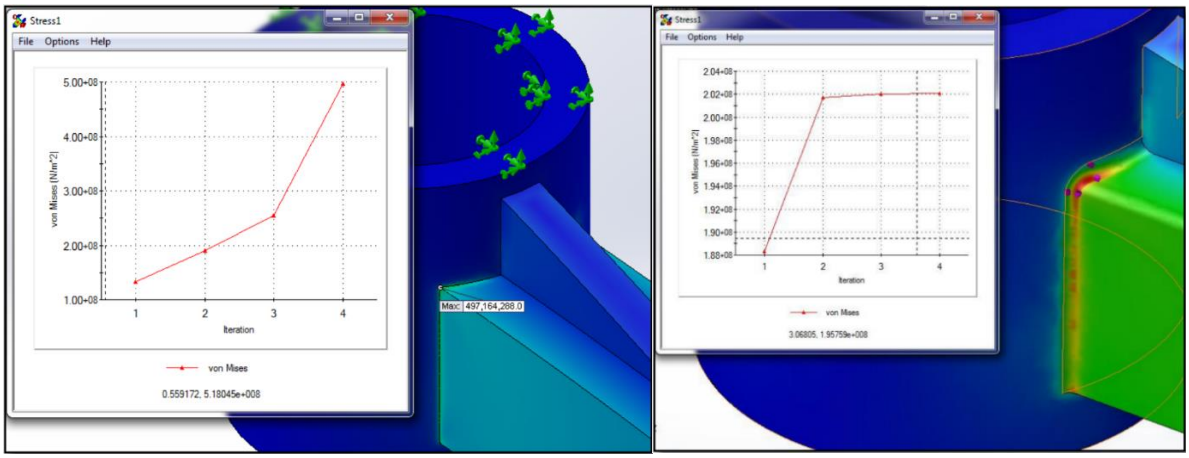

Figure 5.73: Model adjustments.[42]

- Adjust fixtures by applying them to faces instead of points or edges. Instead of fixing the faces, one may also include the actual part that represents the fixture. One condition for this modification is that part has to be very stiff compared to the part that is being studied.
- Adjust the loads such that they do not apply at small ridges or points. Loads are preferably applied as a distributed load.
- Use break-out modelling or sub-modelling. First, a large model is meshed using a relatively coarse mesh. The solution information is then used for a smaller sub model with more details.
- Using elastic-plastic materials. In reality, the material will deform and the stress is redistributed.
- Use of the hotspot method, which uses a linear extrapolation of the stresses. In case of plates welded together, the stresses at half and one and a half times the plate thickness away from the hotspot. Figure 5.74 shows the stress distributions.

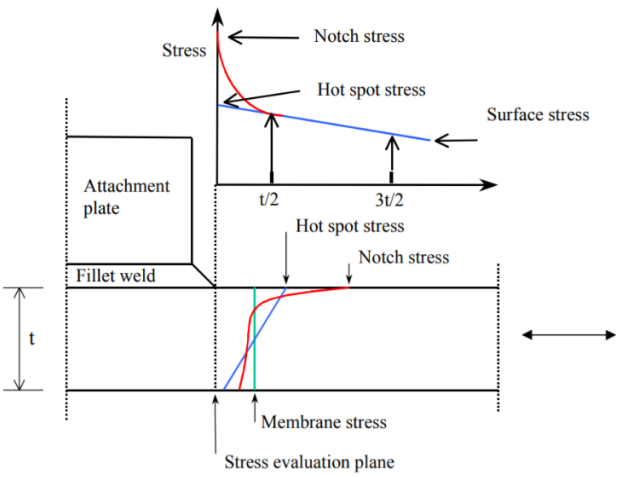

Figure 5.74: schematic stress distribution at a hot spot.[43]

For this problem however, a hand calculation seems sufficient, based on the theory discussed in the first section. Due to plastic deformation, the stress is distributed along the edge. The edge that first encounters the slot inside the core is 50 mm long. A simple hand calculation is performed to determine the amount of deformation for a material having a yield strength of 600 MPa. The reaction force was previously calculated to be 71 kN.

$$w = \frac{F}{\sigma \cdot h} \qquad [5.89]$$

$$\rightarrow \boldsymbol{w = 2.37\ mm}$$

This amount seems reasonable for the width of the contact surface.

Conclusion

The research questions may now be answered.

1. *To what extend do the hand calculations correspond to the data required with the FEM analysis?*

The contact width will be different from what has been calculated with the analytical calculation. Initially a contact length of 25 cm was assumed but the simulation shows that the block will contact the block along a 50 mm line. This means that the contact width will be almost five times as high. It is not expected to be a problem.

The simulation also shows that the stress at the surface is not constant along the y-direction inside the cavities on the side of the bottom-sub. This is because the effect of the pressure that is exerted by the blocks was not taken into account. The stresses also have higher values in the simulation. The loading principle is different from what has been assumed with the hand calculations.

In earlier hand calculations, a distributed load was placed along the entire outside edge. The contact width was estimated by assuming a yield strength of 600 MPa of the material. In reality, there will only be two contact areas. The material will yield locally until the material has been deformed enough to sustain the load without yielding further. Since the contact areas are smaller due to the slots being bent open, the contact width will be larger locally.

2. *Where do peaks in the mechanical stresses occur and why?*

Stress peaks occur around the edges of the slots, in particular along the edges behind the armstopper. A front view showing the sharp edge is shown in figure 5.75. The stress peak here is likely caused by the pressure of the block, which tends to bend open this narrow section, although it has been redesigned before, after a previous FEA was carried out. The location of the peak stresses are the same for the maximum loads.

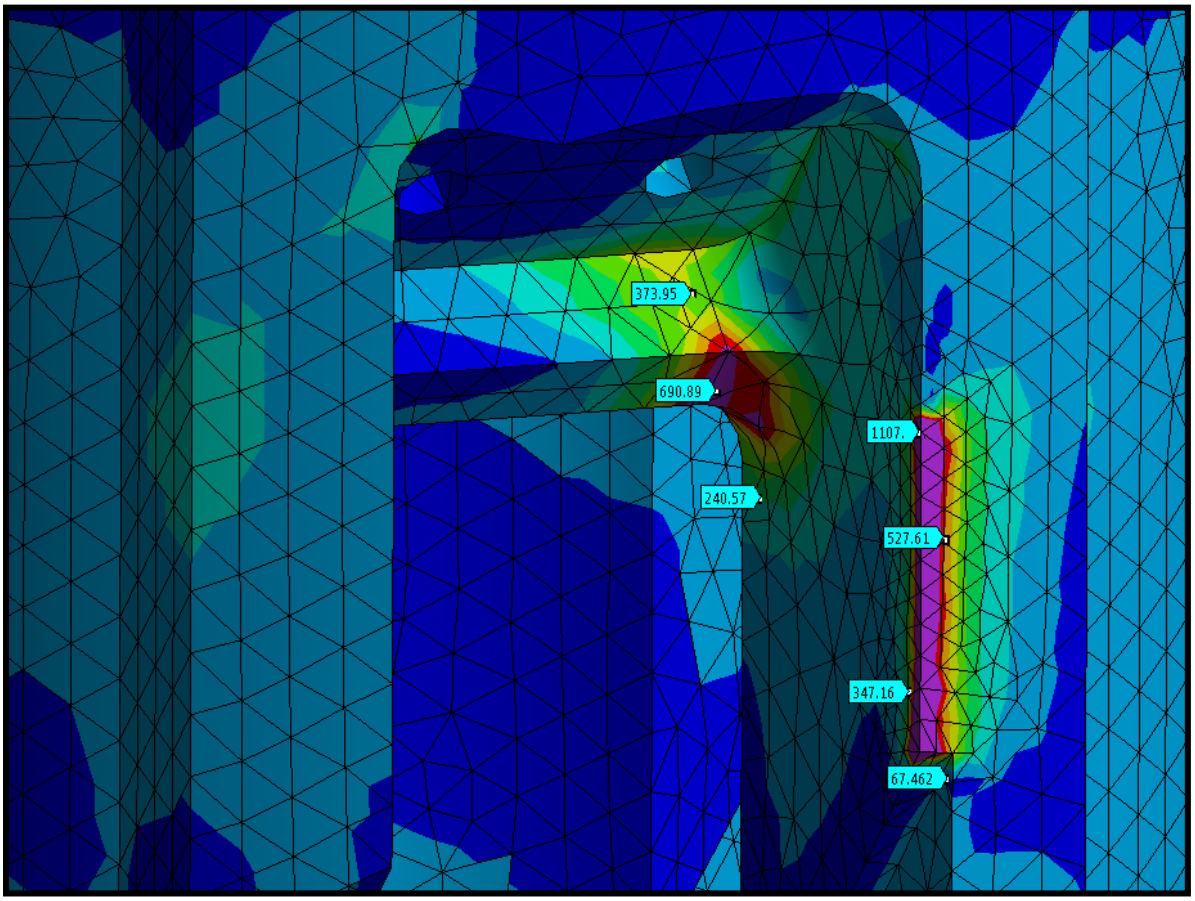

Figure 5.75: Stress concentration around the armstopper edge.

Now, the load case in which the bit contacts the borehole is considered, see table 5.15.

Table 5.15: Considered load case.

Loading case	Load combination		
Bit contact only	7.	Nominal torque	Nominal WOB

To simulate the behaviour of the bottom-core, the part will be elongated by 25 cm to resemble a bottom-core – bit assembly. Next, the model is meshed. This is shown in figure 5.76.

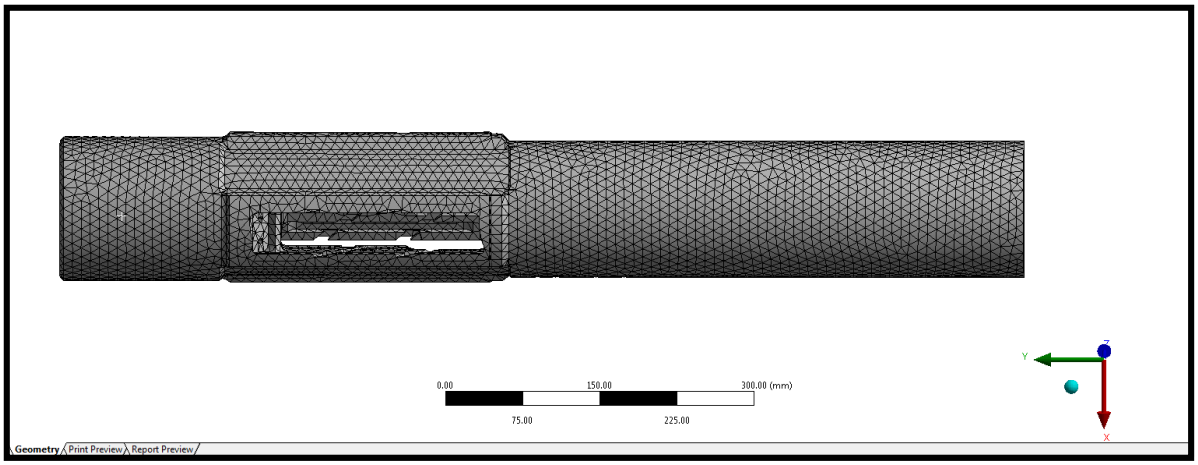

Figure 5.76: Mesh.

After this is done, the boundary conditions are determined. In this case, the bottom is fixed and at the top, a force and moment of 49050 N and 8000 Nm are applied, respectively. This is shown in figure 5.77.

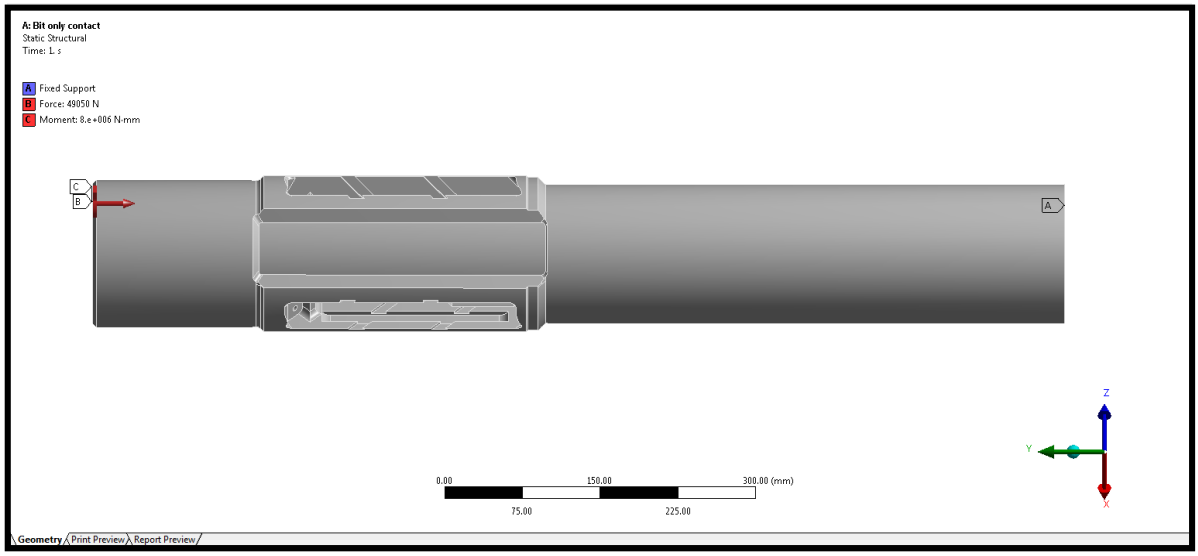

Figure 5.77: Supports and constraints.

At last, the equivalent stress distribution along the bottom-core can be determined. The top and bottom of the cutter block slots are shown in figure 5.78.

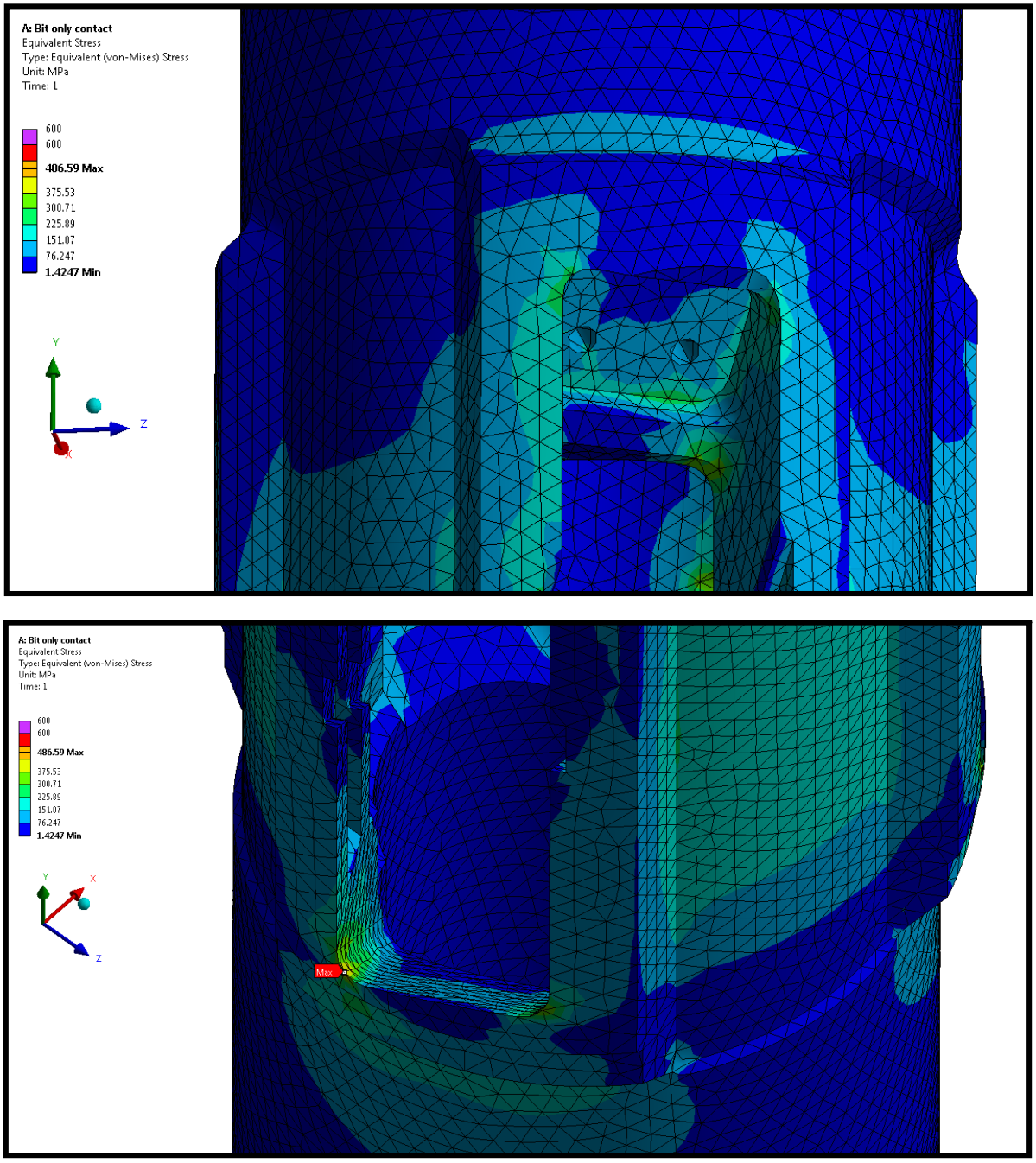

Figure 5.78: Equivalent Von Mises stress plots.

It can be seen that the highest stress occurs at the bottom of the slot on the left side. The stress peak has a value of about 490 MPa. Lower stresses are present above the pocket cut-outs. High stress locations stay the same for higher WOB (10 ton) and higher torque (20000 Nm) but the stress peak increases to 1216 MPa. The stress will also be higher in the pockets on the outside but a stress of 600 MPa is not exceeded for these parts. The equivalent stress plots for this simulation, along with the plot for the nominal torque, peak WOB case and the limiting load case can be found in appendix H. As it turns out, the WOB is not limiting. The maximum torque however has a large influence.

The stress along the outer perimeter at the bottom of the core body has been plotted in figure 5.79.

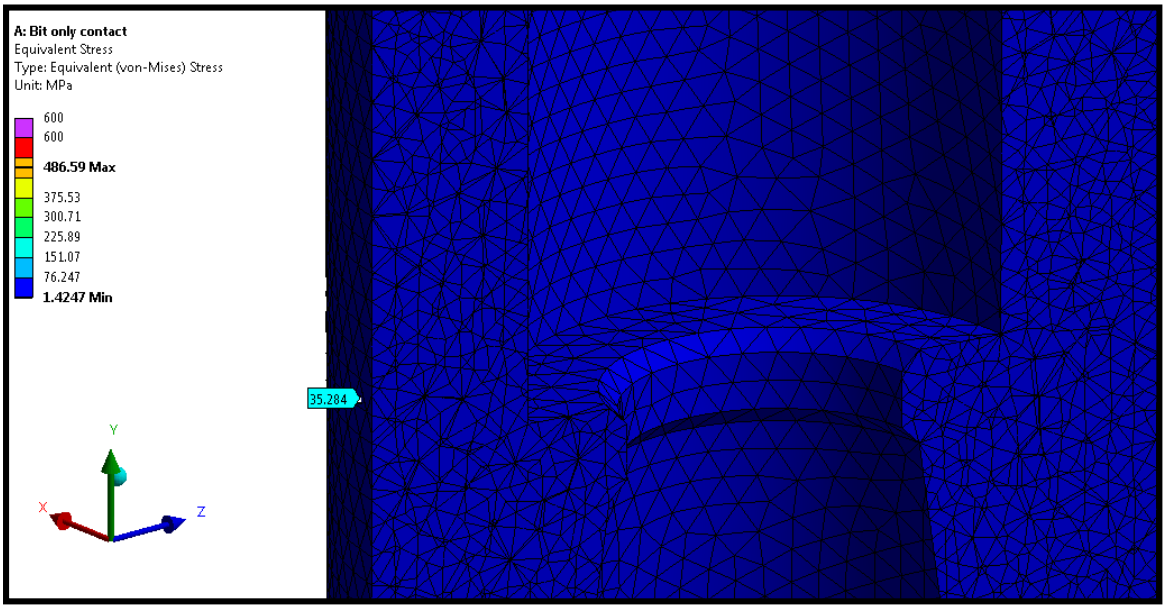

Figure 5.79: Stress along circumference.

Conclusion

1. *To what extend do the hand calculations correspond to the data required with FEM analysis?*

The static structural analysis and hand calculation seem to predict the same result for the stress at the considered cross-section. With the hand calculation, a stress of 35.4 MPa was predicted. A cross-section with a stress-probe displays 35.3 MPa. Some stress peaks occur on the inside of the slots, but these do not exceed the yield stress.

Higher stresses occur at the height of the pockets next to the block slots, but these stresses do not exceed 600 MPa, even for the heaviest load case. It can be concluded that the stress along the outside is not limiting for this load case.

2. *Where do peaks in the mechanical stresses occur and why?*

Stress peaks occur at the bottom of the slots and at the top around the armstopper pocket. These stress peaks exceed 600 MPa, which has been taken as the highest allowable stress for the design. High stress peaks occur at these locations because the slots form a weak point in the design. Due to the torque load, the columns that run alongside the slots will bend and rotate simultaneously. This causes the fillets to deform.

Now that the research question have been answered, the limiting load case may be stated. It was found that this load case could withstand a load combination of **10000** kg WOB and **12000** Nm torque. Stress peaks in the slots just reach the yield stress of the material. Since these peak stresses only occur in small areas, the design should be capable to withstand them.

Lastly, the load case in which the UR and bit contact the borehole is considered, see table 5.16.

Table 5.16: Considered load case.

Load case	Load combination	
Combined contact	10.	Nominal torque

In case both the UR blocks and the drill bit are in contact with the borehole, the applied torque must be distributed. From soil mechanics, it is know that the power needed for cutting equals the product of the cutting volumetric production and the specific cutting energy (Miedema (2016)):

$$E_{sp} \cdot Q_c = P_c \qquad [5.90]$$

The cutting volumetric production is equal to the product of the surface area, over which the cutters act, and the ROP:

$$Q_c = A_{cutters} \cdot ROP \qquad [5.91]$$

The power that being transferred to the soil can be approximated by the product of the torque, generated by soil-cutter interaction, and the angular velocity of the drill string assembly:

$$P_c = T \cdot \omega \qquad [5.92]$$

Equation 5.91 and 5.92 can be filled in equation 5.90, and the ratios of power can now be written as:

$$\frac{E_{sp,1} \cdot A_{1,cutters}}{E_{sp,2} \cdot A_{2,cutters}} = \frac{T_1}{T_2} \qquad [5.93]$$

The specific energy may be dependent on the cutter shape, the thickness of the layer cut and the cutting velocity. The cutters used on the bit and UR are both PDC cutters. For now, the assumption is made that the influence on the specific energy of the difference in cutting velocities between the UR and the drill bit may be neglected, in which case $E_{sp,1} \approx E_{sp,2}$ is assumed. This results in:

$$\frac{A_{1,cutters}}{A_{2,cutters}} = \frac{T_1}{T_2} \qquad [5.94]$$

It can be seen that the required torque ratio now equals the surface area ratio. Since the hole diameter and the drill bit diameter are known, this ratio can now be determined:

$$\frac{A_{1,cutters}}{A_{2,cutters}} = \frac{\frac{\pi}{4}(0.2286^2 - 0.14923^2)}{\frac{\pi}{4} \cdot 0.14923^2} = \frac{T_1}{T_2} = 1.35 \qquad [5.95]$$

The torque values on the top and bottom of the assembly may now be determined. Values that are used for the simulations are shown in table 5.17.

Table 5.17: Distribution of torque and WOB.

Torque levels	Value at the UR shoulder	Value at the bit
Nominal torque	8000 Nm	3404 Nm
Maximum torque	20000 Nm	8511 Nm

First, a mesh will be generated and contact regions are defined. After this has been done, the supports have to be inserted. The displacements prevent motion in all directions, while the remote displacement only fixes the displacement in y direction. The force that acts on the cutter blocks is assumed to transmit its load through the armstopper slots. The supports are shown in figure 5.80. Finally, the solution can be obtained. This is shown in figure 5.81.

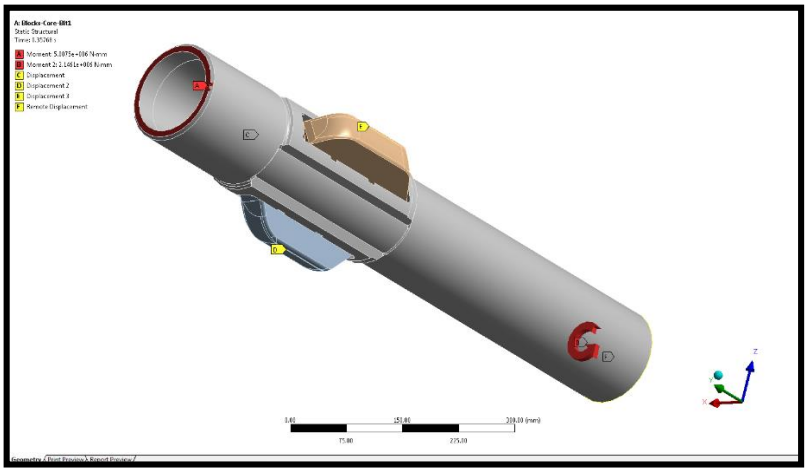

Figure 5.80: Supports and constraints.

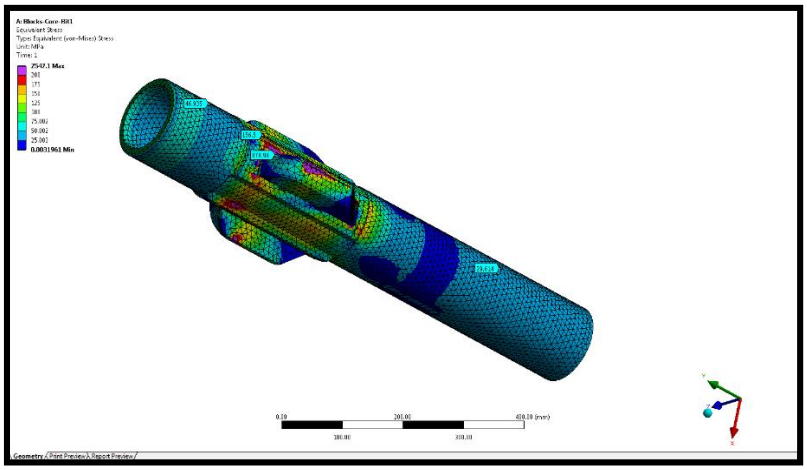

Figure 5.81: Equivalent stress plot.

Conclusion

In this load case, the torque applied on top of the UR is divided over the drill bit and the UR cutter blocks. Therefore the allowable torque level will be higher than for the load case in which only the UR cutter blocks contact the bore hole. The torque level at the cutter blocks will be limiting. Therefore, the total applied torque at the top may not exceed **14000** Nm.

5.9.4. Armstopper part analysis

The armstoppers are located above the blocks inside a pocket in the core-assembly. Their main purpose is to prevent the cutter blocks from sliding out of the core body. The armstopper is connected to the core body by means of two bolts. This is because the armstoppers need to be detachable for maintenance purposes. The blocks can only be inserted when the armstoppers are taken out.

To simulate the loads on the armstopper, a pretension is applied to the bolts first, to take the tightening from the installation into account. The surface area that bears the block loads will be tested for the force that is due to a 100 bar pressure difference between the interior and exterior of the UR. Two cases will be investigated, one where three stoppers convey the piston load and one where a single armstopper conveys the full piston load. Afterwards the limiting case will be determined. Cutting forces are not taken into account here.

The force has to be transmitted from the piston to the armstopper. Therefore, the coupling rod and the cutter block have to convey this force. A schematic overview of the forces is presented in figure 5.82.

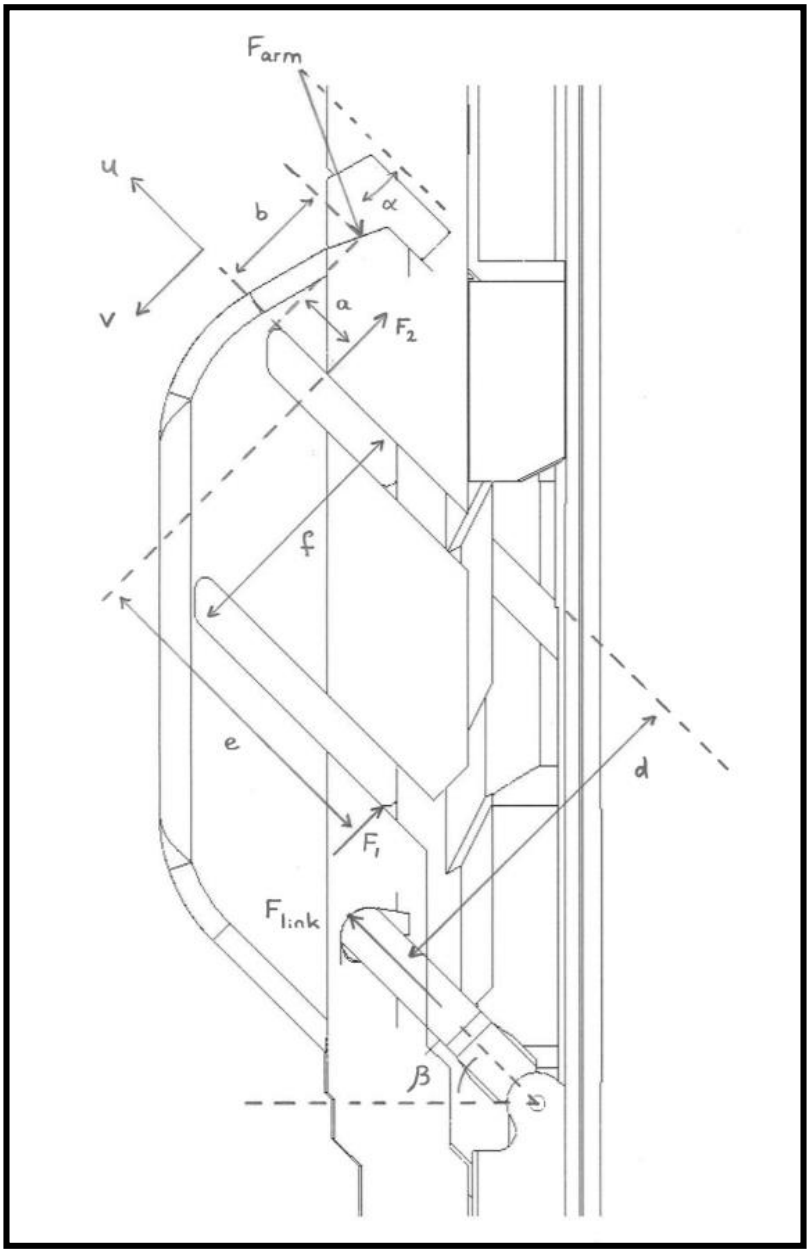

Figure 5.82: Schematic overview of the forces acting on the cutter block in the extended position.

Next, the forces have to be calculated. In this analysis, the unknown forces are F_{arm} , F_1 and F_2. Force and moment equilibria can be established in a way similar to the *case 3* cutter block analysis. This results in:

$$F_u = F_{link} - \mu_2(F_2 - F_1) \quad [5.96]$$

$$F_v = F_1 + F_2 \quad [5.97]$$

$$F_v \cdot a + F_1 \cdot e = F_u \cdot b + F_{link} \cdot d + \mu_2 \cdot F_1 \cdot f \quad [5.98]$$

The forces are defined in the *u*, *v* system of coordinates. Because the armstopper force is not aligned with one of the axis, it is decomposed in the following components:

$$F_u = F_{arm} \cdot \cos\alpha \quad [5.99]$$

$$F_v = F_{arm} \cdot \sin\alpha \quad [5.100]$$

The inner and outer diameter (ID and OD) of the piston are known, together with the pressure difference and the distances of the forces to the reference point for the moment equilibrium. The angles and friction coefficient have also been determined.

$$OD = 80\ mm, ID = 29\ mm$$

$$\Delta p = 10\ MPa$$

$$a = 17.5\ mm$$
$$b = 30\ mm$$
$$d = 90\ mm$$
$$e = 84\ mm$$
$$f = 65\ mm$$

$$\mu_2 = 0.2$$
$$\alpha = 25°$$
$$\beta = 45°$$

The piston force and force in the direction of the coupling rods can be determined as follows:

$$F_{piston} = \Delta p \cdot \frac{\pi}{4}(OD - ID)^2 = 44\ kN \quad [5.101]$$

$$F_{link} = \frac{F_{piston}}{\cos\beta} = 62\ kN \quad [5.102]$$

The system of equations can now be solved by filling in the known parameters. This results in:

$$F_{arm} = 103\ kN$$

$$F_1 = 101\ kN$$

$$F_2 = -58\ kN$$

Since $F_1 > 0$ and $F_2 < 0$, the calculation is valid. It can be concluded that the tongue-groove forces cause the blocks to have a tendency of rotating anti-clockwise. This seems plausible.

Now, the bolt pretension will be determined. The bolts used for the armstoppers are standard M6 8.8 bolts. This type of bolt has to following properties:

Stress area: 20.1 mm^2 for ISO898 bolts

Nominal tensile strength: 800 N/mm^2

Yield strength: 640 N/mm^2

For testing, a certain proof load has also been defined. From the proof load stress, the tensioning stress can be determined. Factors of 0.9 and 0.7 have been used to determine the proof load stress and tensioning stress, respectively:

Proof load stress: $0.9 \cdot yield = 576\ N/mm^2$

Tensioning stress: $0.7 \cdot proof = 403\ N/mm^2$

The pretension load can now be determined by multiplying the tensioning stress with the stress area:

$$Force: \sigma \cdot A = 403 \cdot 10^6 \cdot 20.1 \cdot 10^{-6} = 8100\ N = 8.1\ kN \qquad [5.103]$$

Now, that the loads have been determined, a static structural simulation can be performed in Ansys. Three armstoppers have been fitted inside a part of the core structure. For the analysis with only one armstopper, the two other armstoppers have been suppressed. The geometry is shown in figure 5.83.

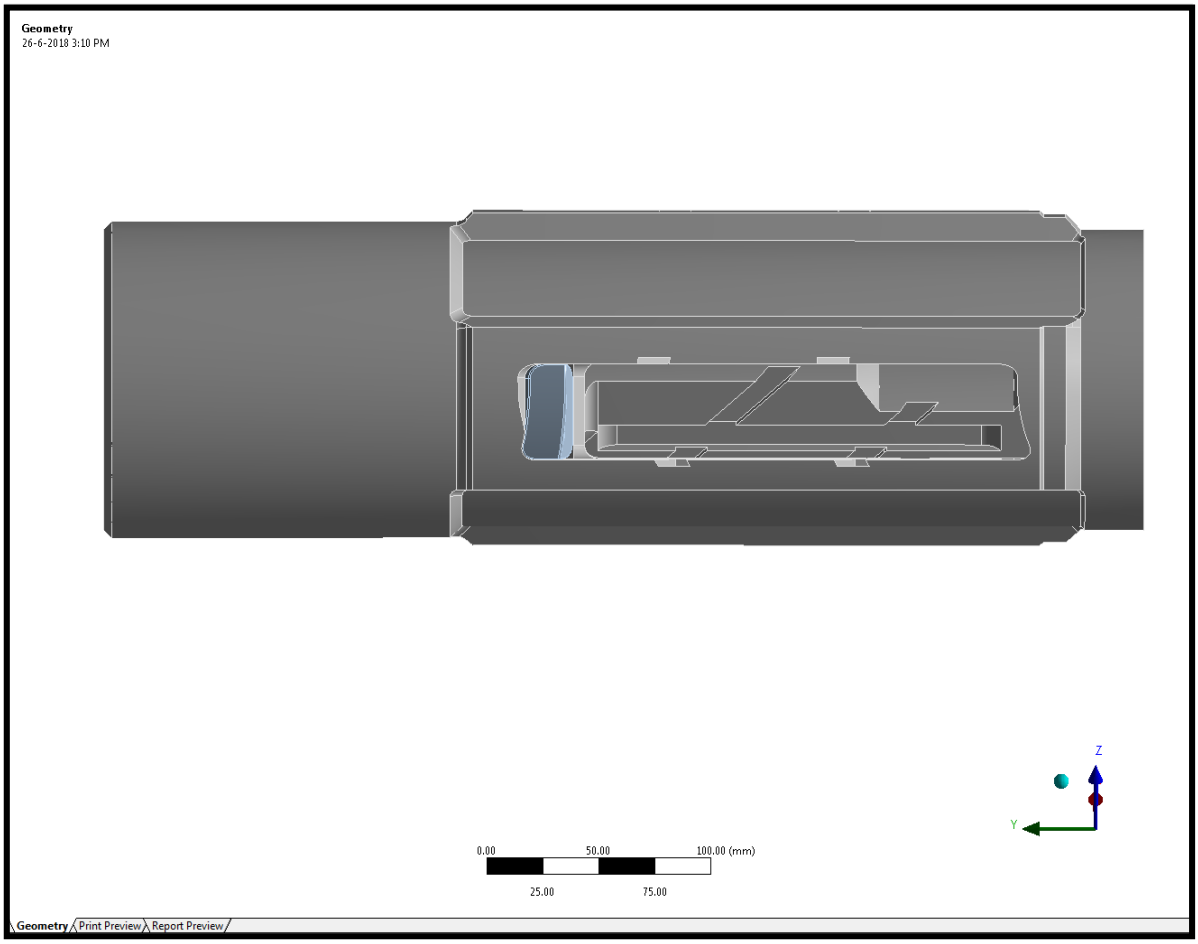

Figure 5.83: Armstopper simulation geometry.

Next, the contact have been defined. The armstopper is surrounded by frictionless contacts, see figure 5.84. A frictionless contact may separate and can only handle compressive forces. The mesh is presented in figure 5.85. For the core body, mesh size of 10 mm is used while for the armstopper, a mesh size of 2 mm is used. Refinements have been added to the bolthole and the surrounding edges in the core body. The size function inside details of 'mesh' has been set to curvature again.

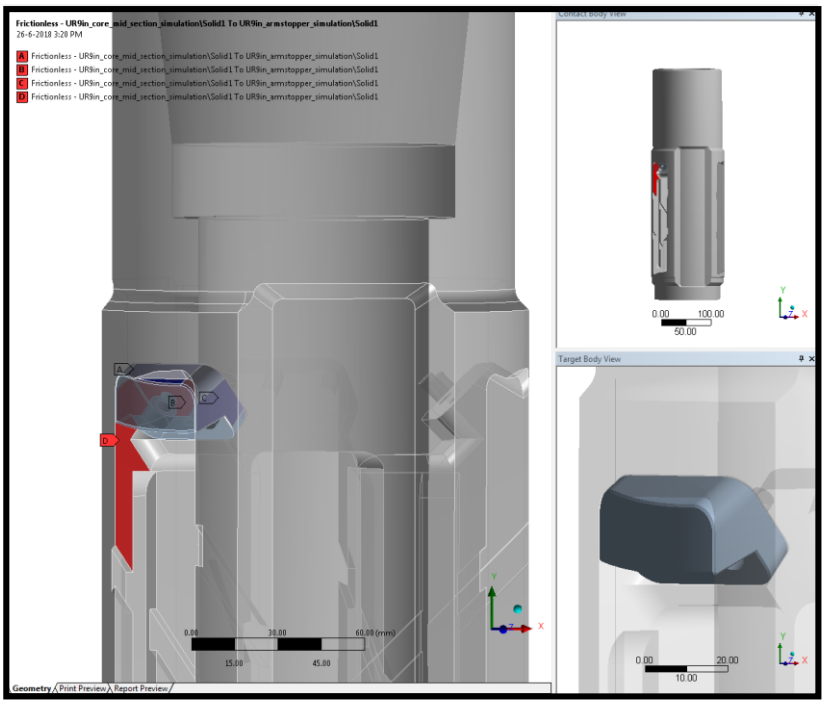

Figure 5.84: Contacts.

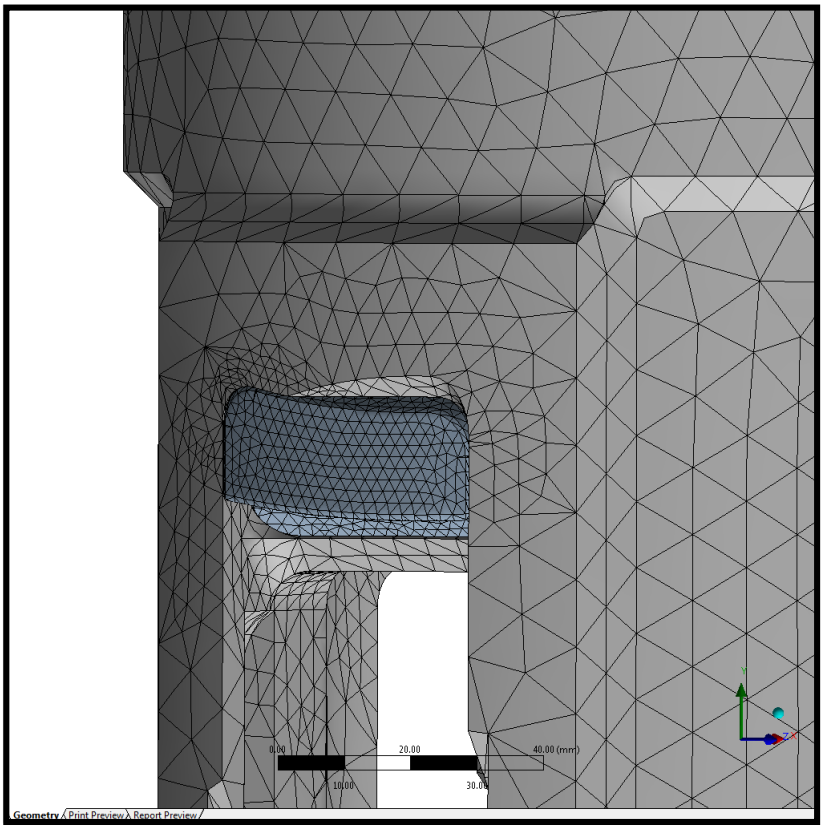

Figure 5.85: Mesh.

The load combination for a piston load of 10 MPa that has been distributed over three blocks is simulated first. The result of this simulation is shown in figure 5.86. The force on the armstopper equals **34** kN.

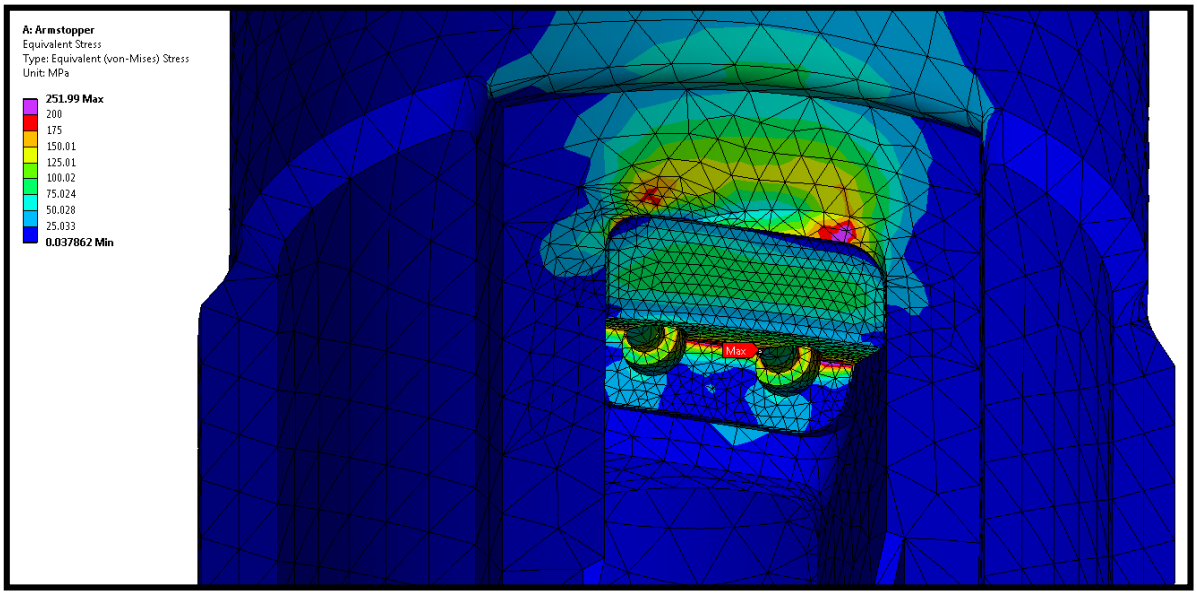

Figure 5.86: Armstopper loaded with distributed 10 MPa piston load.

It can be seen from figure 5.86 that this case is not limiting for the design, since the peak load will not exceed 252 MPa. Therefore, a second simulation is run where a piston load of 100 bars is conveyed through one armstopper. This corresponds to a force on the armstopper of **103** kN.

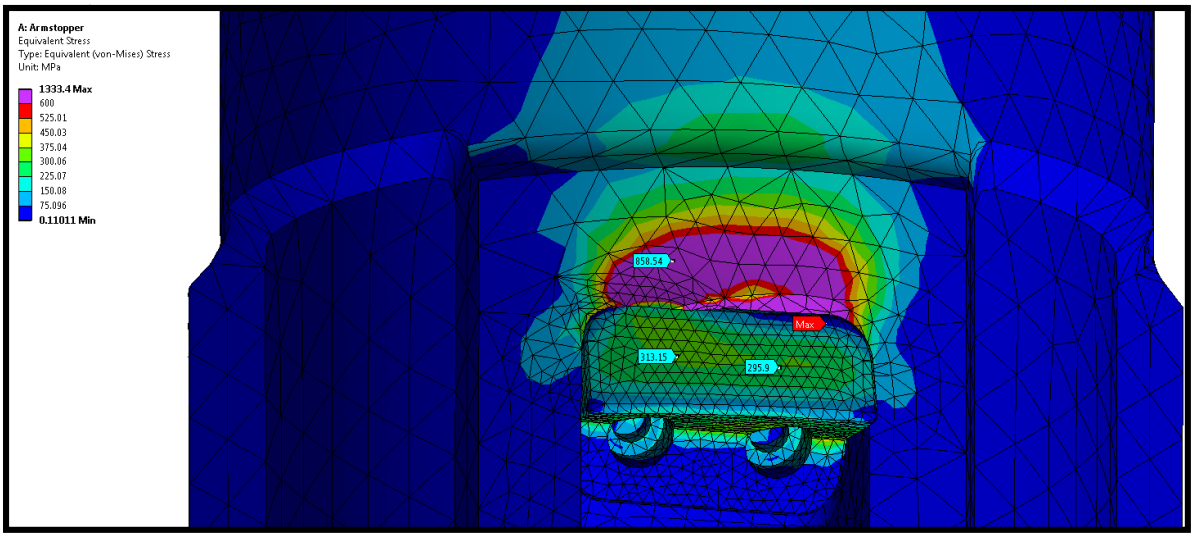

Figure 5.87: Armstopper loaded with full 10 MPa piston load.

The results from figure 5.87 show that area above the armstopper contains stresses higher than the yield stress of AISI 4145, which is about 760 MPa. When a safety factor of 1.25 is applied, the stresses should remain below 600 MPa. For an armstopper force of 65000 N, the maximum stress will not exceed 635 MPa. Since this stress only occurs in a single node and the surrounding stresses do not exceed 600 MPa, this load is considered safe. The armstopper force in this case corresponds to a piston pressure of **63** bar or 6.3 MPa. This will be considered as the limiting case. The result of this simulation can be found in appendix I. The armstoppers will be able to handle a piston pressure of 189 bar, only if the load is equally distributed between the armstoppers. For the design however, this assumption is too optimistic.

5.9.5. Sleeve channel analysis

The sleeve channel has to transmit a force from the spring to the piston. This force causes compressive stresses and bending stresses, in case an eccentric load is applied. To check whether the deflection and maximum compressive stress are sufficiently low, manual calculations and FEM calculations are performed and compared to verify the results.

Manual calculation

Since the spring load may not be applied through the centroid and the tube may not be perfectly straight, it should be checked whether the spring load could be sustained by the channel when restrictions on the maximum allowable stress and deflection are imposed.

The sleeve channel has been indicated in red in figure 5.88. One end of this channel is clamped into the piston (brown, bottom), while the other end is clamped into the spring disk (brown, top). The piston and the spring disk are both located inside the bore of the UR core assembly.

Because of the play between these parts and the hole, it is assumed that small rotations possible. Lateral movement however neglected. This means that both ends can be seen as pin supports, see figure 5.89.

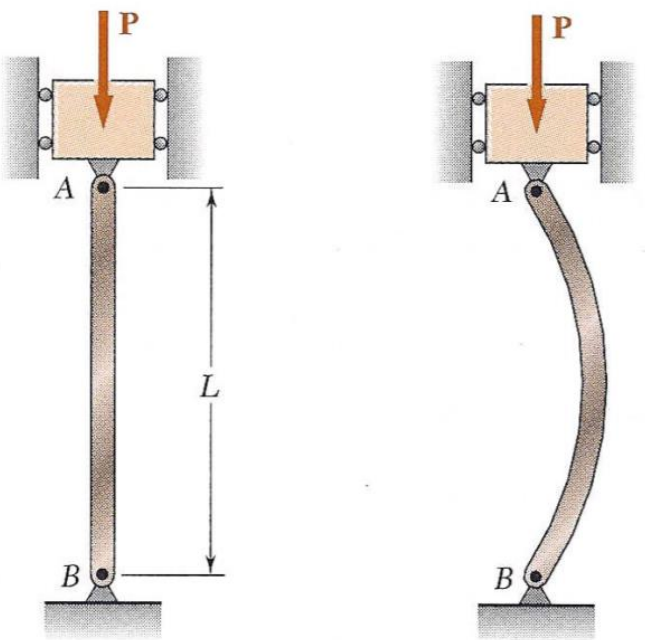

Figure 5.89: Schematic representation of the pin supports.[44]

Since the cross-section is circular and the support-principle is not depending on the direction of deflection, only one value can be used for the effective length factor K and the moment of inertia I of the cross-section.

It is assumed that the sleeve channel will bend around the undeformed mud channel (green) and that the deformation of the sleeve channel is not hindered by other surrounding parts. For the load P, the full force of the spring (grey) is taken. It must be noted that the load conditions shown represent a very conservative case.

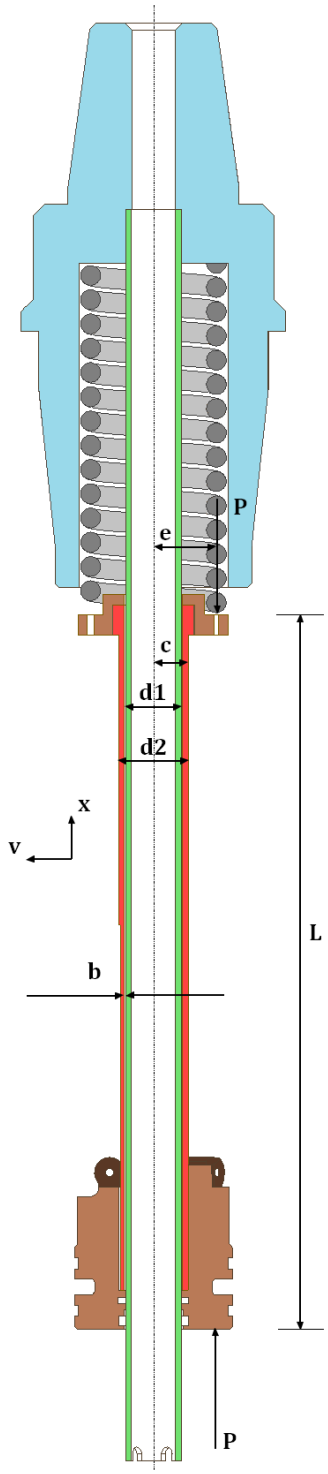

Figure 5.88: Situation drawing.

The spring force is applied at a distance e from the centreline of the sleeve channel. By considering an arbitrary cross-section of the channel, the internal moment can be determined[45]:

$$M = -P(e + v) \qquad [5.104]$$

Here, v is the deflection due to bending. To find the elastic curve, it is necessary to solve the following equation:

$$EI\frac{d^2v}{dx^2} = -P(e + v) \qquad [5.105]$$

The general solution to this equation consists of a complementary and a particular solution:

$$v = C_1 \sin\sqrt{\frac{P}{EI}}x + C_2 \cos\sqrt{\frac{P}{EI}}x - e \qquad [5.106]$$

Since the top and bottom of the channel are prevented from moving sideways, the deflection of the channel at the bottom and the top of the channel is equal to zero. By using these boundary conditions, an equation for the deflection curve can be found:

$$v = e\left[\tan\left(\sqrt{\frac{P}{EI}}\frac{L}{2}\right)\sin\left(\sqrt{\frac{P}{EI}}x\right) + \cos\left(\sqrt{\frac{P}{EI}}x\right) - 1\right] \qquad [5.107]$$

The maximum deflection and maximum stress both occur at the halfway length of the channel for symmetry reasons. It now follows that the maximum deflection can be determined by:

$$v_{max} = e\left[\sec\left(\sqrt{\frac{P}{EI}}\frac{L}{2}\right) - 1\right] \qquad [5.108]$$

The maximum stress in the channel is the result of bending due to a moment and an axial load:

$$\sigma_{max} = \frac{P}{A} + \frac{Mc}{I} \qquad [5.109]$$

$$M = |P(e + v_{max})| = P \cdot e \cdot \sec\left(\sqrt{\frac{P}{EI}}\frac{L}{2}\right) \qquad [5.110]$$

Here, A represents the cross-sectional area of the channel and c denotes the distance to the outermost fibre. By filling in the result from equation 5.110 into equation 5.109 and by using the definition of the radius of gyration, which defined as $\sqrt{I/A}$, a formula for the maximum stress called the *secant equation* can be obtained:

$$\sigma_{max} = \frac{P}{A}\left[1 + \frac{e \cdot c}{r^2}\sec\left(\frac{L}{2r}\sqrt{\frac{P}{EA}}\right)\right] \qquad [5.111]$$

For both equations, the argument of the secant needs to be in radians.

Since the geometric and force parameters are known, the maximum stress and deflection can readily be determined. Values for the parameters are shown in table 5.18.

Table 5.18: Parameter values.

Parameters	
L = 357 mm	e = 31.5 mm
d_1 = 29 mm	F = 3340.70 N
d_2 = 35 mm	E = 210 GPa
c = d_2/2 mm	r^2 = I/A

For the tubular cross-section, the following values were determined for the area, the moment of inertia and consequently the radius of gyration:

$$A = \frac{\pi}{4}(d_2^2 - d_1^2) = 3.02 \cdot 10^{-4}\ m^2 \qquad [5.112]$$

$$I = \frac{\pi}{64}(d_2^4 - d_1^4) = 3.89 \cdot 10^{-8}\ m^4 \qquad [5.113]$$

$$\rightarrow r = 0.011\ m$$

By assuming a complete circular cross-section, which is the case for the top section of the sleeve channel the stress due to axial loading becomes:

$$\sigma = \frac{P}{A} = \frac{3340.70\ N}{0.00030\ m^2} \approx 11.08\ MPa \qquad [5.114]$$

Now, that the data is known, the maximum deflection and compressive stress due to the eccentric force can be determined:

$$v_{max,unsupported} = 0.206\ mm$$

$$\sigma_{max} = 58.675\ MPa$$

The value for the maximum stress seems reasonable and causes no problems in the design. The maximum deflection however is higher than the 0.15 mm of clearance between the mud channel and the sleeve channel. The full force however is only present in case the spring is at its shortest meaning that the sleeve channel moved up inside the core. Then it will be supported approximately halfway by internal parts. The maximum deflection will then be:

$$v_{max,supported} = 0.106\ mm$$

This is an allowable amount of deflection. Now that the amount of deflection has been determined, a simulation in Ansys will be performed to compare the results.

The sleeve channel was first modelled as a simple hollow tube. The pin supports and remote force support that are applied can be seen in figure 5.90 below:

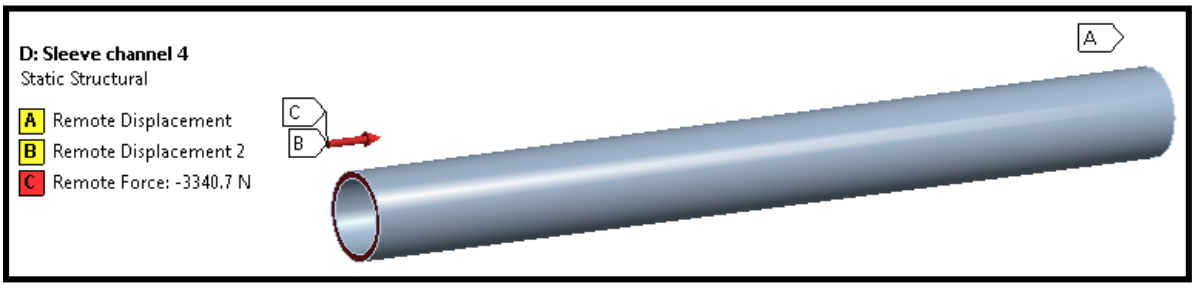

Figure 5.90: Support conditions for the sleeve channel.

Next, the model could be solved. For solving, the analysis setting 'large deflection' was turned on, which means that Ansys takes changes of stiffness due to a changing shape into account. A detail of the von-Mises plot and deformation plot are shown in figure 5.91.

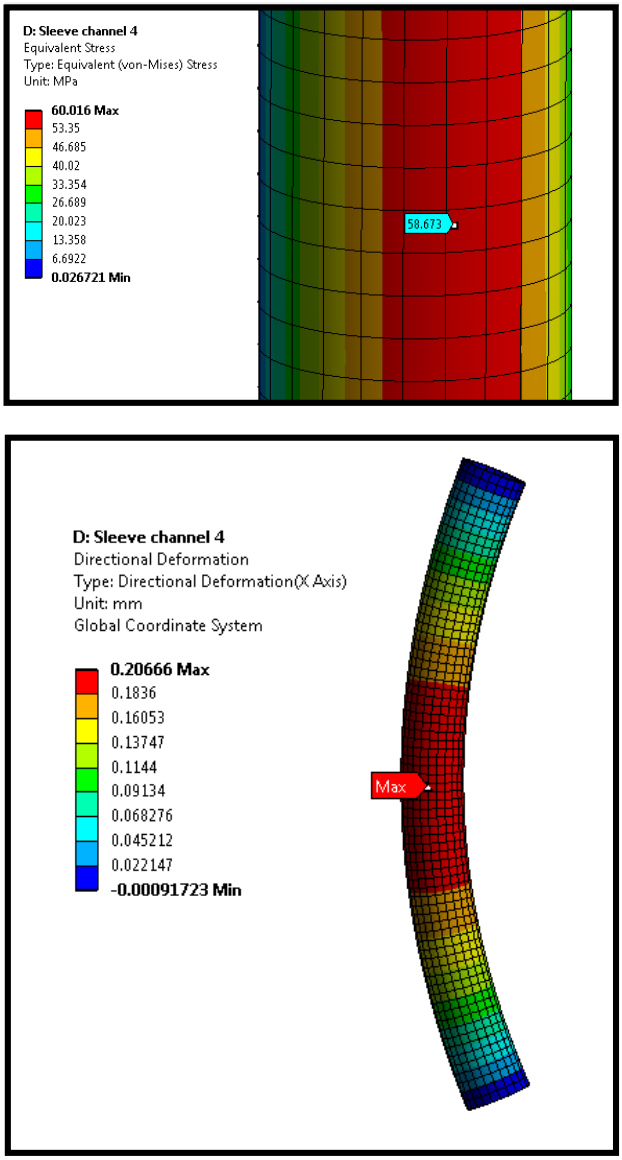

Figure 5.91: Top: von Mises stress. Bottom: deflection.

The analysis has also been performed with the piston and spring disk attached to the sleeve channel. The outcome of these simulations is shown in figure 5.92.

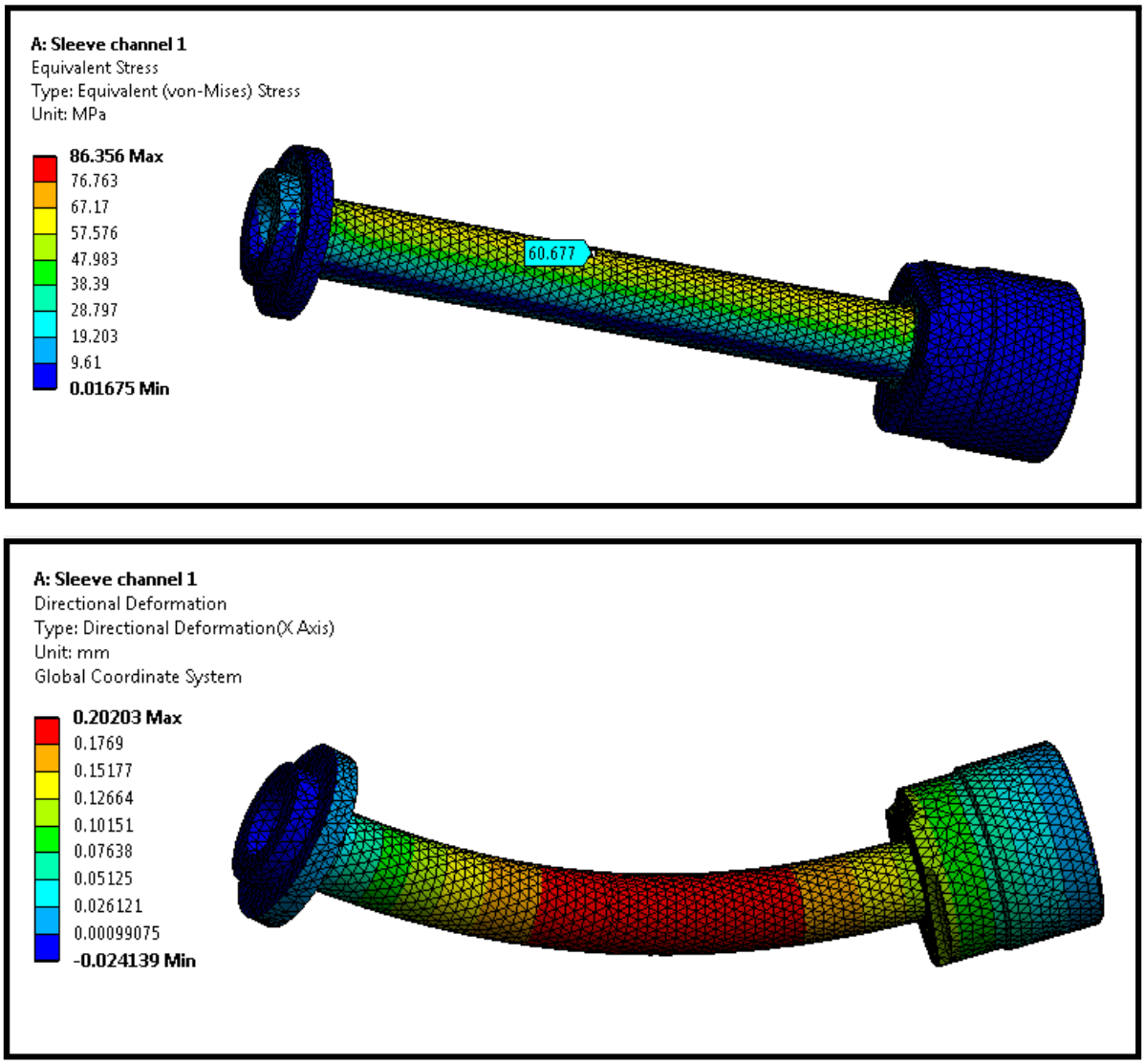

Figure 5.92: Top: von Mises stress of the assembly. Bottom: Directional deformation of the assembly.

Conclusion sleeve-channel analysis

Now that the stress states and other phenomena have been identified, the research questions may be answered. For each question, the answer will be related to the parts in order to improve their design.

1. *To what extend do the hand calculations correspond to the data required with FEM analysis?*

The hand calculations indicate that the maximum compressive stress in the channel wall should be approximately 59 MPa. In Ansys, exact same value was found by probing the surface. Because the first model has exactly the same parameters, these close matching results were predicted. The second model deviates from the hand calculations by a fraction of the stress. This is likely due to the new geometry and its mesh.

2. *Where do peaks in the mechanical stresses occur?*

From figure 5.91 and 5.92, it can be deduced that peak stresses mainly occur along the circumference of the column. The peak stress and deflection will be the highest at half of the length, but are not causing any problems because the assumptions made are very conservative.

6. Evaluation and recommendations

6.1. Process evaluation

For the design of the UR, the following requirements were determined in consultation with Huisman:

- *The UR must have a drill diameter of 9 inch (228.6 mm) or more.*
- *The UR can have a maximum body diameter of 5 7/8 inch (149.225 mm).*
- *The length of the underreamer should be as short as possible and be no longer than 750 mm.*
- *The current design of DRILLSTAR will serve as a base-case and the specifications of the base-case determine the minimal requirements for the new concept design.*
- *The reamer blades have to move outwards under the influence of mud pressure.*
- *The reamer blades have to retract by using one or more springs.*

One may ask why these specific sizes have been set. The answer is that the reamer diameter needs to become larger to lower the pressure drop between the outside of the casing and the borehole. The body diameter however has a limitation on the diameter to allow it to pass through the casing. The length of the UR is restricted because it might be used in directional drilling applications, for which steerability plays an important role. The steering angle becomes larger for shorter tools. Since electricity is difficult to generate down hole, mud is used to expand the cutter blocks. Springs are used to retract the blocks and make sure that they stay in their closed position. In this way, the blocks only expand when a certain initial pressure is reached.

The UR has been designed in two phases. The conceptual design and selection phase was used to determine which concept has the most promising characteristics in terms of:

- *Clogging and jamming*
- *Moving parts*
- *Internal space*
- *Vibration resistance*
- *Wear resistance*
- *Hole enlargement*
- *Complexity and cost*
- *Range of applications*
- *Proven technology*
- *Technical feasibility*
- *Reliability and durability*
- *Maintenance*
- *Ease of assembly*
- *Design flexibility*
- *Expected cutting performance*

Why has this been done? The answer is that not every concept can be worked out in detail and concept may perform well for one boundary condition while they perform poor for other boundary conditions. Therefore, the boundary conditions were considered as a whole to come to a well-founded choice.

In chapter 4, it was concluded that the concept with the eccentric blade configuration had scored the highest for the boundary conditions and has the highest chance to meet the requirements. The preliminary design of this concept had to be worked out further in the detailing phase. First, the general layout of components had to be determined. It was decided that the spring and piston assembly had to be separated and relocated.

After this was done, distinctive parts of the UR were thoroughly analysed. The following subjects have been discussed in detail:

- *The expansion mechanism*
- *The link extension model*
- *The mechanical spring*
- *The cutter block shape analysis*
- *Component development*
- *Assembly and manufacturing*
- *FEA of the sub-assemblies*

The results that were acquired helped in the development of the first functional prototype of the new UR. This prototype is a 1:2 scaled version of the actual reamer. The prototype and its working principles will be discussed next.

6.2. Prototype evaluation

6.2.1. Printer

To test whether the parts can function together properly in the assembly, a 1:2 prototype has been developed. The *Fortus 250mc stratasys*, a professional 3D printer, has been used to print the parts. The printer uses *ABS* plastics to print, which is very tough and impact resistant. However, to work with ABS, the bed and chamber need to be heated, to prevent parts from bending during the cooling process. To manufacture the prototype, the printer uses a *rapid prototyping technique* called *fused deposition modelling* (FDM). This means that a plastic filament is extruded through a nozzle after which multiple molten layers are printed on top of each other.

The preparation of the parts starts with loading the Inventor part into the *Insight 3D printing software*. Next, the model is cut into slices, support material is added and the tool path is defined. This is shown in 6.1.

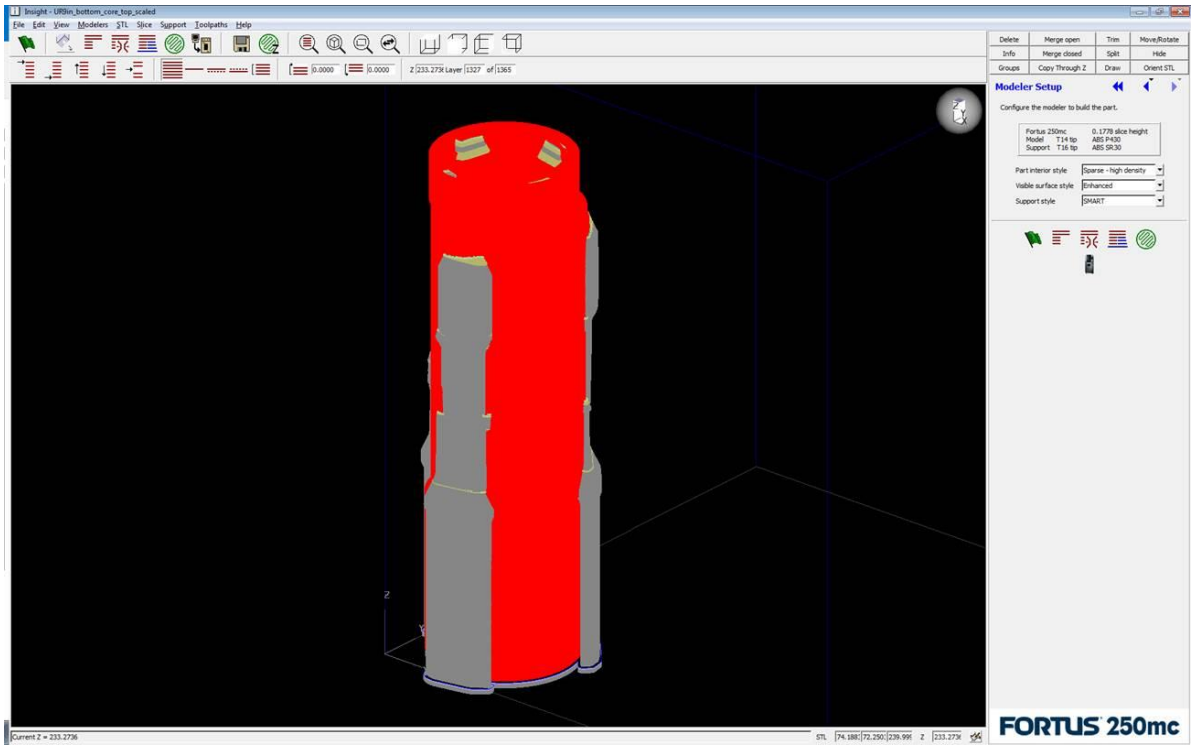

Figure 6.1: Model of the UR core (red) with support material (grey).

The layers of the model have a certain thickness. Depending on the desired accuracy, the layer height could be either 0.3302, 0.2540 or 0.1778 mm. Since the deposition nozzle of the printer has a fixed diameter, the layer thickness is controlled by the volume flow of molten plastic through the nozzle and the velocity of the nozzle head itself.

The layer properties are not only important with respect to accuracy but also with respect to cost and the duration of printing. If the layer consists of thin filament layers with no spacing, only small voids are present. The model with be very solid as a result but a lot of printing material is used and it takes a considerable amount of time to print the parts. Using *sparse fills* and large rasters can provide a solution to these problems.

After the model has been generated by the program, it needs to be checked whether the supports and layers are properly defined per layer. The infill of the slices also has to be checked. While investigating these areas, adjustments to the layers can be made to prevent future printing problems. A slice from the UR-bottom core is shown in figure 6.2 as an example.

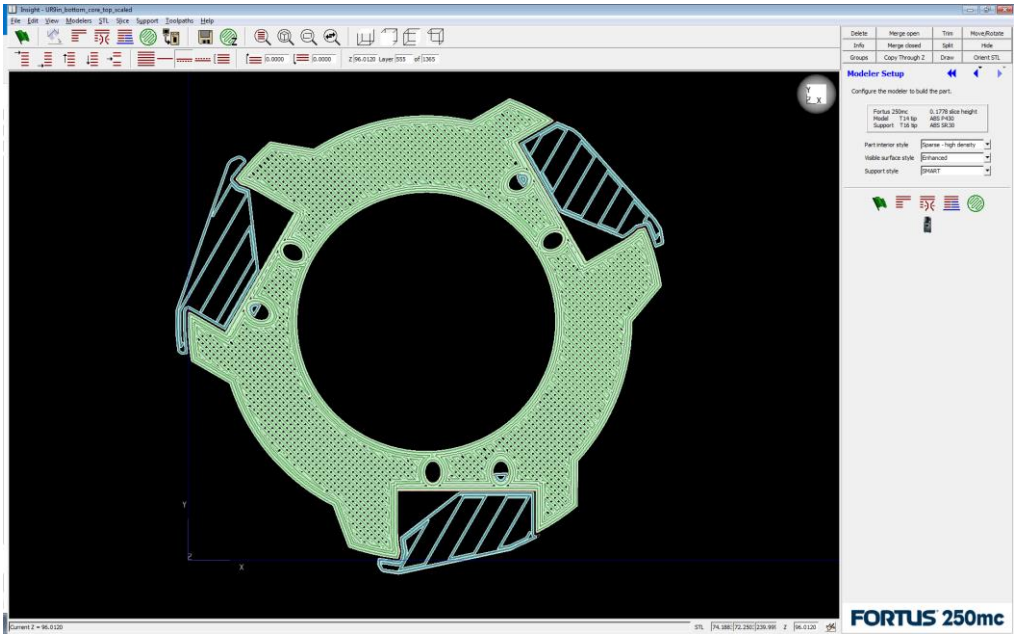

Figure 6.2: Check of the infill and layering.

The final step is to open the parts in the *Control Center* software to see how the parts are going to be printed on the bed. Only parts with equal colour and layer height can be printed at the same time. The arrangement of the grey parts is shown in figure 6.3. This software calculates the amount of model and support material that is going to be used, together with the time that is needed for printing, which in this case is 80 hours.

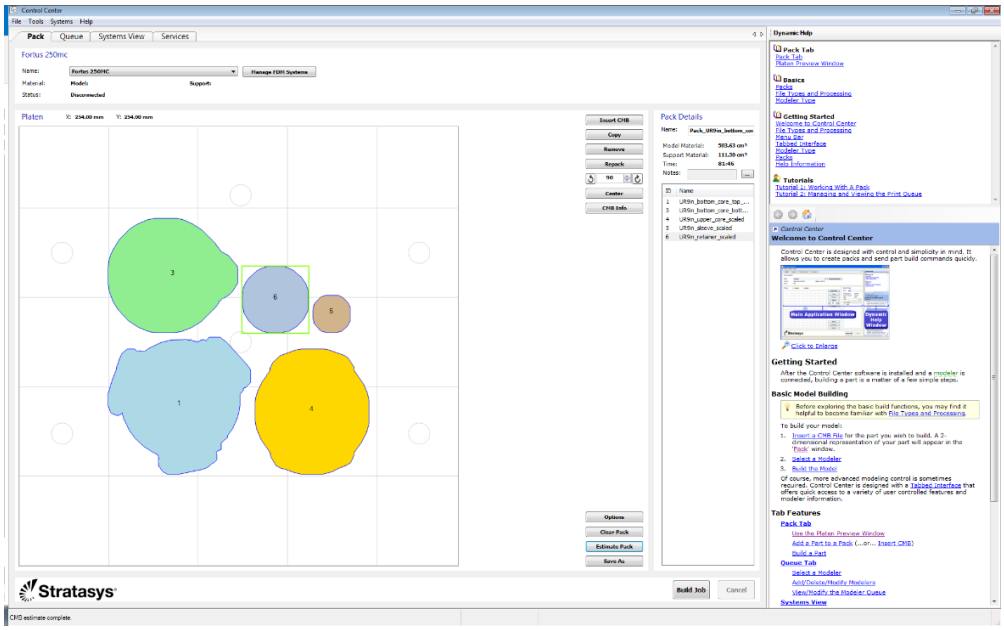

Figure 6.3: Parts arrangement and pack details.

6.2.2. Model adaption

The parts have been adapted such that a play of (at least) 0.25 mm is present in between all the parts. Since threaded connections are not present, all parts have to either fit together with a tight connection, an interlocking connections or a fitting where the components are at all times pushed against each other.

A tight connection was only applied at the mud channel because there was no room for any fitting mechanism. Interlocking fittings have been applied for the box and pin connection. These fittings are called bayonet mounts and are shown in figure 6.4. It must be noted that these type of connections are not used in the actual design. The particular connection shown below was made because of the printers net build size, which is 254 x 254 x 305 mm.

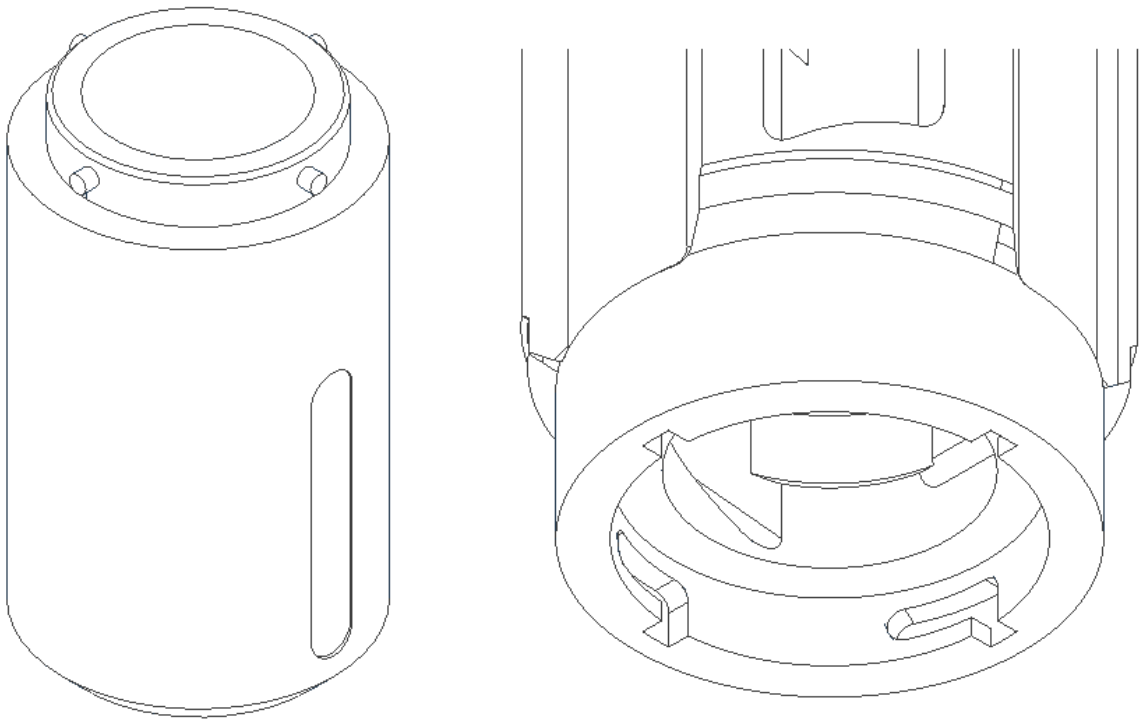

Figure 6.4: Bayonet mount.

Besides the connections and tolerances, several other adaptions were made. Because the mud channel was scaled, the inner diameter also became smaller. For cosmetic and support reasons, the hole above was narrowed down to serve as a resting position.

Because many parts have circular symmetric features, they are able to rotate within the UR assembly. However, for some sliding connections, it is essential that the parts remain in one position. This is achieved by designing a keyed joint onto the part.

Other minor adjustments included simplifying the details on small parts like the coupling rods, to prevent printer errors and to extend partially drilled holes so that they are drilled completely through. This has been done so that support material could be removed more easily afterwards.

6.2.3. Conclusions

The tolerances that are applied were the same for all parts. It is clear that for some parts, the play is too big. This means that smaller tolerances must be applied at these locations. From the model, it became also clear that due to a rotation of the piston, the coupling rods could disconnect from the blocks somewhere halfway the opening stroke. This can be a problem in case severe vibrations down hole occur. The problem may also prevent the tool from opening.

So why does this problem still occur? Locking the piston to which the coupling rods are connected proved to be very difficult. The piston must be able to move up and down. The slide and wear rings are in contact with the hole along the complete circumference. A predecessor of the base case design contained a pin that would penetrate the piston from the bottom. Moments applied to the piston caused this pin to bend, preventing the reamer from closing. The pin would also need to run in between the internal and external wear and slide ring grooves. This put limitations on the diameter of the pin. A temporary solution was found be making a small chamfer on the outside, so that the link could still fold out along the slot wall. The current model of this link is shown in figure 6.5.

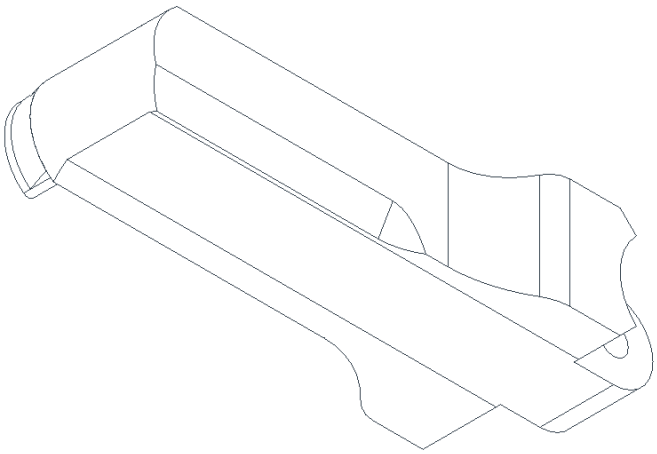

Figure 6.5: Coupling rod design.

The model also showed that putting the parts together might also be a problem. Because the parts were scaled down and opening sizes were reduced, assembling the model became difficult. For the actual reamer, special tools are probably needed to hold to coupling rods into position so that the blocks could slide in place. These tools are needed and need to be designed unless a better solution to the problem is found.

An overview of the complete assembly is shown in appendix G.

6.3. Design evaluation

6.3.1. UR specifications and operating parameters

Now that the prototype has been evaluated, a comparison can be made between the base-case design and the renewed design. The outcome is presented in table 6.1.

Table 6.1: Comparison Hydraulic Reamer 600 and renewed design.

Specification	Hydraulic Reamer 600		Renewed design
Max. body OD (hardfaced)	5 ¾“	146 mm	149.225 mm
Shoulder to shoulder length (A)	32“	813 mm	750 mm
Bit to blade length (B)	20,7”	525 mm	278.8 mm
Blade length (C)	7,7”	195 mm	200.7 mm
Approx. Weight	170 lbs	77 kg	70 kg
Top thread	3 ½” API REG Pin	-	3 ½” API REG Pin
Top shank OD	4 ¾”	121 mm	121 mm
Bottom thread	3 ½” API REG Box	-	3 ½” API REG Box
Rec. m/u torque 3 ½” REG	Min 10.000 ft-lbs Max 11.500 ft-lbs	13.558 N·m 15.592 N·m	13.558 N·m 15.592 N·m
Rec. m/u torque 4 ¼” XHTDI	13.500 ft-lbs	18.300 N·m	18.300 N·m
Min. ID (operating)	1.1”	28 mm	22 mm
Operating Parameters			
Min. pilot hole size	5 7/8”	149 mm	149 mm
Opening range	6 ¼” – 8 ½”	159 – 216 mm	159 – 228.6 mm
Collapsed diameter	5 ¾”	146 mm	149.225 mm
Max flow rate	450 GPM	1.700 lpm	1.500 lpm
Min. operating pressure	150 psi	10 bar	10 bar
Max. operating pressure	725[1] psi	50[1] bar	63 bar
Max. WOB	14.300 lbs	6.5 mt	10.5 mt
Max. torque	7000 lbs·ft	9.490 N·m	8000 N·m
Max. operating temp (std. seals)	392 °F	300 °C	200 °C
Base material	AISI 4145 H	-	AISI 4145 H
Seal material	Viton 80 Shores	-	Turcite and Zurcon
Shear value (for 1 shear pin)	101 – 116 psi	7 – 8 bars	-

It can be seen from table 6.1 that the shoulder-to-shoulder distance has been reduced. According to test carried out by Huisman, this will improve steerability. The blade length has been increased slightly, which has a positive effect if the UR acts as a stabilizer. The bit to blade length has been reduced drastically. This will also have a positive effect on the steerability. Other dimensions changed include the diameter of the mud channel, which has been decreased by 6 mm. The flow rate has therefore been reduced to keep the same flow velocity. For Huisman, this will not be a problem because these flow rates are still much higher than the flow rates used by Huisman. It can also be seen that the opening range has been broadened. This will reduce the annulus pressure losses.

The UR has also become 7 kg lighter. In this way, the material costs might be reduced. Besides the design related variables, material variables were also determined. For the current design, standard seals (o-rings) are used. These rings are made from fluoroelastomers and are designed as ‘FKM ‘. Although these seals can withstand temperatures above 200 °C, the friction properties are worse than those of specially designed Turcite and Zurcon Slyd and wear rings from Trelleborg. Therefore, the decision was made to opt for these type of seals. The base material of the UR was not changed since the current material already has sufficient wear resistance and strength.

6.3.2. Annulus pressure loss – calculation

To calculate the annular pressure losses between the casing and borehole, the dimensions of the annulus have to be determined first. The casing used for the UR will have the following properties (table 6.2):

Table 6.2: Casing properties.

Casing OD		Weight		Casing ID		Drift	
7”	177.8 mm	35 lbs/ft	52 kg/m	6.004”	152.4 mm	5.879”	149.3 mm

Since the UR enlarges the diameter of the borehole, a new annulus area needs to be determined. In combination with the volumetric flow rate, the bulk velocity of the fluid can be determined. The properties are again both expressed as field units and metric units, see table 6.3.

Table 6.3: Annulus ID and OD along casing joint, and pump rate.

Current annulus (ID – OD)		New annulus (ID – OD)	
7” – 8.5”	177.8 – 215.9 mm	7” – 9”	177.8 – 228.6 mm

Pump rate (Q)
450 GPM = 1703 l/m = 28.4 l/s = 0.0284 m³/s

The annular pressure losses per unit of length for laminar flow are given by:

$$\frac{\Delta P}{L} = \frac{(PV)\bar{V}}{60\,000(D_h - D_c)^2} + \frac{YP}{200(D_h - D_c)} \qquad [6.1]$$

Here, D_h and D_c are the hole diameter and casing diameter, respectively. The PV and YP values describe the plastic viscosity and yield point of the fluid, according to the Bingham Plastic model. The average velocity $\bar{V}$ can be obtained directly with the following equation:

$$\bar{V} = \frac{24.51 \cdot Q}{\left({D_h}^2 - {D_c}^2\right)} \qquad [6.2]$$

However, for eq. 6.1 to be valid, the laminar assumption will be checked first. A critical velocity is determined by setting YP equal to zero and by introducing an effective viscosity. The relation for the Newtonian flow is set equal to eq. 6.1. The effective viscosity can now be written explicitly and is used in the calculation of the Reynolds number. The transition from laminar to turbulent is assumed to happen at 3000 [-]. By solving this intermediate relation for the flow velocity, an equation for the critical flow velocity can be obtained:

$$V_c = \frac{97 \cdot PV + 97 \cdot \sqrt{PV^2 + 6.2\rho {D_e}^2 (YP)}}{\rho D_e} \qquad [6.3]$$

$$D_e = D_h - D_c \qquad [6.4]$$

Here, D_e is the annular hydraulic diameter. Now that the method has been set up, the values for the PV, YP and ρ have to be determined. The PV value is influenced by the colloidal solids content of the mud. The YP of the mud is often used as an indication for carrying cuttings. The rheological parameters of the mud may also depend on the casing rpm, downhole pressures and downhole temperatures, but these effects will not be discussed in detail here.

The values for the PV, YP and ρ that will be used in the calculation are presented below:

PV	= 20 cP	= 0.02 Pa·s
YP	= 20 lb/100 ft^2	= 9.6 Pa
ρ	= 10 ppg	= 1198 kg/m^3

Now that the parameters are determined, the average velocities are determined first, which are then compared to the critical velocity. If the average velocity is lower than the critical velocity, eq. 6.1 can be used to calculate the pressure loss per meter length. The results are presented in table 6.4.

Table 6.4: Results.

Current design		New design	
Annulus area		Annulus area	
18.3 in^2	0.012 m^2	25.1 in^2	0.016 m^2
Average velocity		Average velocity	
474 ft/min	2.40 m/s	345 ft/min	1.75 m/s
Critical velocity		Critical velocity	
495 ft/min	2.51 m/s	452 ft/min	2.30 m/s
CHECK		CHECK	
Pressure losses		Pressure losses	
0.14 psi/ft	3167 Pa/m	0.08 psi/ft	1810 Pa/m

It can be seen that both flow velocities stays below the critical velocity, so the laminar flow regime assumption is valid. It can be seen that the pressure loss per unit of length has been reduced by a significant amount. The decrease in pressure and percentage of decrease are presented below:

$$Decrease = 3167 - 1810 = \mathbf{1357}\ Pa/m$$

$$Percentage\ of\ decrease = \frac{1357}{3167} \cdot 100 = \mathbf{43}\%$$

Example

Now that these numbers have been determined, an example case can be considered. Here, both the casing joints and casing couplings are considered. The casing couplings have an OD of **8**". For Huisman the volumetric flow is limited to **1200** l/m or **0.02** m^3/s. For every **40** ft of casing, **39** ft consists of joints and **1** ft consists of couplings. For now, a well of **6600** ft or **2012** m depth is assumed to calculate the pressure drop for both the current and new design. Relevant parameters are shown in table 6.5 below:

Table 6.5: Example parameters.

Current design		New design	
Annulus area at casing coupling		Annulus area at casing coupling	
6.5 in^2	0.004 m^2	13.4 in^2	0.009 m^2
Flow velocity at casing coupling		Flow velocity at casing coupling	
940 ft/min	4.78 m/s	457 ft/min	2.32 m/s
Pressure losses		Pressure losses	
1.45 psi/ft	32800 Pa/m	0.25 psi/ft	5655 Pa/m

The assumption was made that the flow remains laminar and that no flow disturbances are present at the couplings. In reality, this is not the case, and turbulence should be accounted for.

Since 6600 ft consist of 165 repeating segments, the casing couplings take up a length of **165** ft while the casing joints take up a length of **6435** ft.

For the current casing, the pressure drop can be determined as follows:

$$6435\ ft \cdot 0.14 \frac{psi}{ft} + 165 ft \cdot 1.45 \frac{psi}{ft} = 1140\ psi$$

$$\rightarrow \mathbf{79}\ bar$$

For the new casing, the pressure drop can be determined as follows:

$$6435\ ft \cdot 0.08 \frac{psi}{ft} + 165 ft \cdot 0.25 \frac{psi}{ft} = 556\ psi$$

$$\rightarrow \mathbf{38}\ bar$$

Which is a decrease of **41** bar. The percentage of decrease in this case would be **52** %.

It can be concluded that for the smaller casing sizes, increasing the diameter of the reamed hole can have a huge impact on the pressure drop and eventually the required pump power.

6.3.3. Steerability – calculation

Method 1

As mentioned in the introduction, the steerability of the UR should improve by shortening the length of the UR. To give an indication of the improvement in terms of numbers, a basic model is presented in figure 6.6:

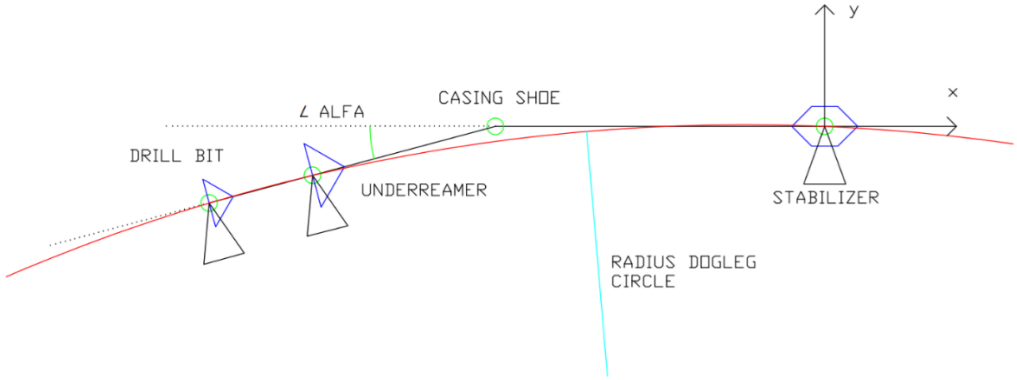

Figure 6.6: Exaggerated representation of a simplified model to determine the dogleg.

The distance between the centre of the drill bit, the midpoint of the underreamer at the cutters and the second casing stabilizer needs to be determined. The angle at the casing shoe also needs to be determined. The goal of the analysis is to determine the *dogleg* or directional change of the steering assembly in degrees per 100 ft of drilling. A drawing of the assembly is presented in figure 6.7.

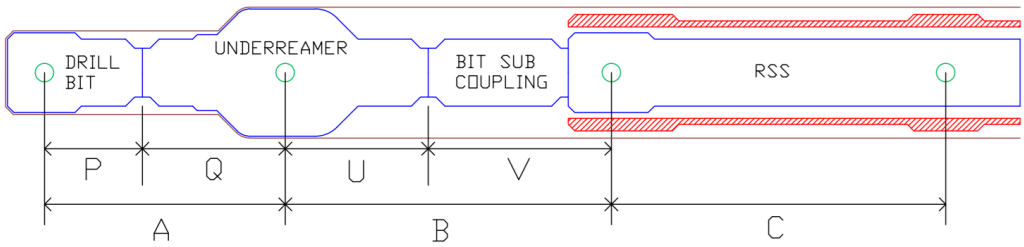

Figure 6.7: Situation drawing of the BHA assembly.

The BHA-casing clearance and casing-borehole clearance are neglected in this analysis. The new design only changes distance Q, U, A and B. Distances P, V and C remains fixed. Table 6.6 shows the values that are used for the analysis. The angle α has been fixed at 0.7°, which is determined by the design of the RSS.

Table 6.6: parameters.

Current design		New design	
A	822 mm	A	559 mm
B	634 mm	B	831 mm
C	2000 mm	C	2000 mm
P	200 mm	P	200 mm
Q	622 mm	Q	359 mm
U	284 mm	U	481 mm
V	350 mm	V	350 mm

When the bit-underreamer assembly is tilted by the point-the-bit rotary steerable system, a circle can be described that passes through the drill bit, underreamer and stabilizer centres. The radius of this circle needs to be determined to derive the *dogleg severity* (DLS).

From the drawing in Inventor, the borehole radius can be determined easily. The centre and radius of the circle can also be determined algebraically. In this case, the general equation for a circle needs to be considered:

$$(x - x_c)^2 + (y - y_c)^2 - r^2 = 0 \qquad [6.5]$$

At this point, the centre of the circle (x_c, y_c) and its radius r are unknown. However, the three points that lay on the circle are known. If the centre and radius were known, filling in the equation above should result in zero. Therefore, three equations can be established. The origin of the system of coordinates is set at the midpoint of the second stabilizer.

For this point, the following equation should hold:

$$(0 - x_c)^2 + (0 - y_c)^2 - r^2 = 0 \qquad [6.6]$$

For the underreamer, the following equation should hold:

$$((-C - B \cdot \cos\alpha) - x_c)^2 + ((-B \cdot \sin\alpha) - y_c)^2 - r^2 = 0 \qquad [6.7]$$

For the drill bit, the next equation should hold:

$$((-C - (A + B) \cdot \cos\alpha) - x_c)^2 + ((-(A + B) \cdot \sin\alpha) - y_c)^2 - r^2 = 0 \qquad [6.8]$$

Since the lengths of these segments are known, they can be filled into the equations. For the **current design**, this results in:

$$(-x_c)^2 + (-y_c)^2 - r^2 = 0 \qquad [6.9]$$

$$(-2633.95 - x_c)^2 + (-7.75 - y_c)^2 - r^2 = 0 \qquad [6.10]$$

$$(-3455.89 - x_c)^2 + (-17.79 - y_c)^2 - r^2 = 0 \qquad [6.11]$$

Working out equation 6.10 and 6.11 results in:

$$6937692.60 + 5267.9 \cdot x_c + {x_c}^2 + 60.06 + 15.5 \cdot y_c + {y_c}^2 - r^2 = 0 \qquad [6.12]$$

$$11943175.69 + 6911.78 \cdot x_c + {x_c}^2 + 316.48 + 35.58 \cdot y_c + {y_c}^2 - r^2 = 0 \qquad [6.13]$$

By subtracting equation 6.9 from these equations, a set of two equations with two unknown's remains, which can be solved for the coordinates of the centre of the circle. The values for x_c and y_c that are found this way could directly be used with the Pythagoras Theorem to calculate the radius:

$$x_c = -769\ mm$$

$$y_c = -186272\ \ mm$$

$$\rightarrow R = 186\ m$$

This result can be used directly to calculate the dogleg:

$$\frac{s \cdot 180}{R \cdot \pi} = \varphi\ [deg] \qquad [6.14]$$

$$\rightarrow \frac{30 \cdot 180}{186 \cdot \pi} = 9.2\ deg/30\ m$$

The same set of equations can be solved for the **new design**. This results in:

$$\rightarrow R = 196\ m$$

$$\frac{30 \cdot 180}{196 \cdot \pi} = 8.8\ deg/30\ m$$

This result was not expected. According to this method, the steerability becomes worse by 4%. This result it most likely due to either the placement of the tipping points or not considering the aggressiveness of the bit. Since tests at the Huisman drilling rig in the Czech Republic indicate that this is not the case, another method will be considered.

Method 2
The rotary steerable system used by Huisman uses point the bit technology in which the UR and drill bit are set under an angle with respect to the remaining part of the BHA. Inside the RSS and a steering arm called the eccentre is used to steer the part below the casing shoe, known as the stick-out. In this new model, a force is applied at the tip of the excenter. This causes the stick-out to have a tendency to turn. Because the hole is straight, the problem could be seen as stinking a crooked assembly down a straight hole. The situation is shown in figure 6.8.

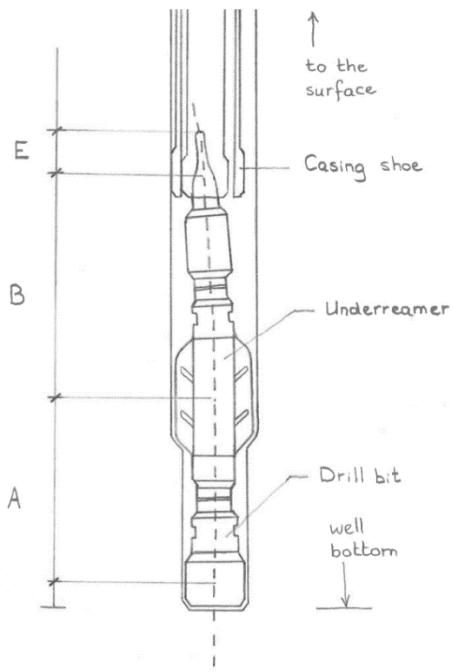

Figure 6.8: Crooked stick-out inside the borehole.

Some assumptions are made for the following model. These assumptions are summarized below:

- The BHA is *suspended vertically*. Therefore, the effect of *gravity is neglected*.
- The casing string is assumed to be *infinity long*, compared to the stick-out. Therefore, *the casing goes straight up and does not bend*.
- The drawing indicates that there is some play in between parts at the casing shoe. When the stick-out is pointed to the right, the casing shoe is pushed to the left. For the analysis, *the BHA-casing shoe and casing shoe-borehole play will be present*.
- Although the BHA has a rotation point at the casing shoe in between section B and E, *this rotation point is assumed not to be present here* as this point is allowed to move sideways to some extent and the casing shoe does not exert a force at this point due to the infinite length of the casing.
- The UR acts as a stabilizer while the bit is fitted with aggressive cutters. Therefore, the UR will acts as a pivoting point.
- The stick-out assembly is assumed to be rigid.

By applying the assumptions, a simple beam model can be drawn. This model is shown in figure 6.9.

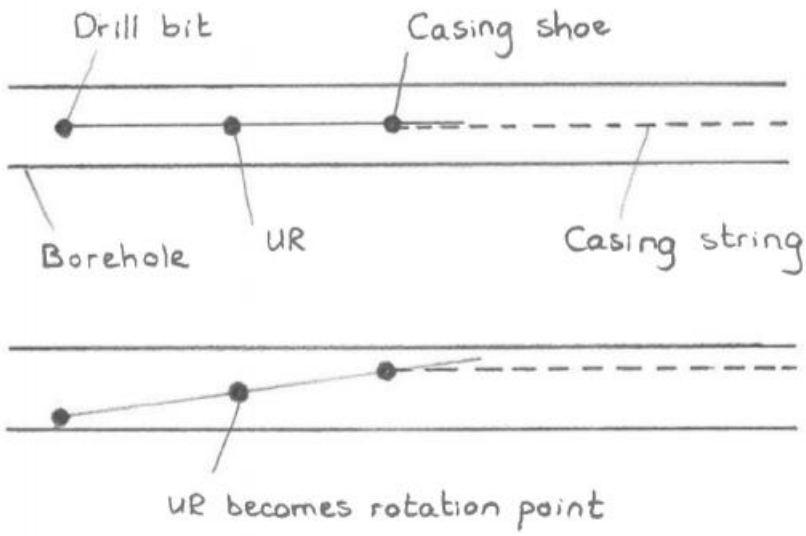

Figure 6.9: Beam model of the stick-out assembly.

The model shows a level system where the UR acts as a pivoting point. When a force is applied at the excenter, the right side of the lever moves up while the bit side moves down. The force at the bit will be higher when the rotation point moves closer to the bit. To attain the same angle, the bit also has to cut less material. The following lever relation may be established to prove the concept:

$$F_{Drill\ bit} \cdot A = F_{excenter} \cdot (B + E) \qquad [6.15]$$

$$\rightarrow F_{Drill\ bit} = \frac{F_{excenter} \cdot (B + E)}{A} \qquad [6.16]$$

It can be seen (figures 6.8 and 6.9) that for a smaller A, the bit force will be higher. Distances B and E on the other hand need to be larger in order to increase the bit force. An example for the current and new design is worked out below. The excenter force is assumed to be 10000 N. The arm of the excenter is equal to 1.2 m.

Current:

$$F_{Drill\ bit} = \frac{10000 \cdot (0.634 + 1.2)}{0.822} = 22311\ N$$

New:

$$F_{Drill\ bit} = \frac{10000 \cdot (0.831 + 1.2)}{0.559} = 36333\ N$$

This means that the new design will, due to shortening the UR and lowering the cutter blocks, increase the force at the bit by **63**%. This corresponds to experience from practice and it seems to be a reasonable result. From this calculation, it can be concluded that the steerability is indeed improved.

6.4. Recommendations

Now that the development process and the results have been treated, some recommendations on how to proceed can be given. The recommendations mentioned below relate to all aspects of the research.

- It is clear that some part may be jamming because of debris or high loads. This is for example the case for the blocks. The exact amount of friction between the blocks remains unknown. It must be investigated which tolerances must be applied in order to make the sliding process smooth.

- Operational issues like bit balling can cause a high pressure differential over the UR assembly, see figure 6.10. This causes high loads on the coupling rods, which may bend inside the UR. This can cause retraction problems. Bit balling at the UR itself may also reduce the ROP. It must be investigated whether the flow of mud is not hindered and if the blocks are susceptible to bit balling. In case bit balling occurs, a build-in safety valve in the mud motor could prevent damage to the internal mechanism of the UR.

Figure 6.10: Bit balling at the drill bit.[46]

- Because is it desired for the UR to have a 'closed' structure, the cutter blocks have been designed such that it fits exactly through the slots inside the UR-core body. However, the cutters attached to the outside of these blocks need to stick out further than the underlying steel. For this to happen, there needs to be a certain clearance between the bottom of the cutters and the sliding surface below. This means that the edge underneath the blocks has to be open. A solution to this problem must be found to complete close off the internal structure.

- The current cutter block has a stabilizer side with a length of about 85 mm. The conceptual design has a stabilizer side of about 110 mm. The effects of this increase in length needs to be examined.

- The base-case had three nozzles incorporated into the design. These nozzles would mix up the flow in the pockets next to the cutter blocks and reduce the amount of power transferred to the bit. The application purposes of these nozzles is unclear and they seem to be obsolete, since the nozzle are plugged according to the DRILLSTAR design drawings. Therefore, the nozzle have been left out of the new design. The effects of removing the nozzles needs to be investigated further.

- The cutter blocks have been designed with a certain top angle. Tests have to be carried out with the blocks in retrieval operations to see if the casing is capable of pushing the blocks inwards.

- The motion and mechanical properties have been investigated for bending and jamming. The model used for this analysis had some simplifications applied to it. In reality, the sleeve channel has slightly smaller cross section and therefore it might be more susceptible to buckling. Debris might also flow in between the mud channel and sleeve channel. When this mud dries up after operations have ended, disassembly might become difficult or the channel could be stuck during the next run. It has to be examined whether this is really the case. The problems will probably also relate to the type of formation rock that is being drilled and the kind of mud used.

- The design of the UR includes a grease cap to shield the spring from debris. The efficacy of this part has not been proved and its use is contested by some engineers of R&D. Although spring chamber has been split into two compartments and the volume change of the chamber is almost negligible, the effect of this cap needs to be investigated.

- *Glyd* and *Slyd* rings have been used in the design for the piston. In general, these rings will slide smooth but their temperature resistance is inferior to that of FKM O-rings. However, these O-rings have other sliding properties that could possibly cause the piston to seize. It needs to be investigated whether a low coefficient of friction or higher temperature resistance is more advantageous.

- The connection of the coupling rod to the cutter block has been designed such that no extra pin part is used. Consequently, the maintenance properties are improved but the tip of the coupling rod is not constrained sideways. In an intermediate extension position, the left side of the rod is not resting against the opposite cutter block or the slot side, see figure 6.11. In case severe vibrations occur during extension, the rods might turn outward a little bit depending on the play they have. The probability of the occurrence of this event must be investigated. If possible, the design needs to be adapted to rule out this kind of failure.

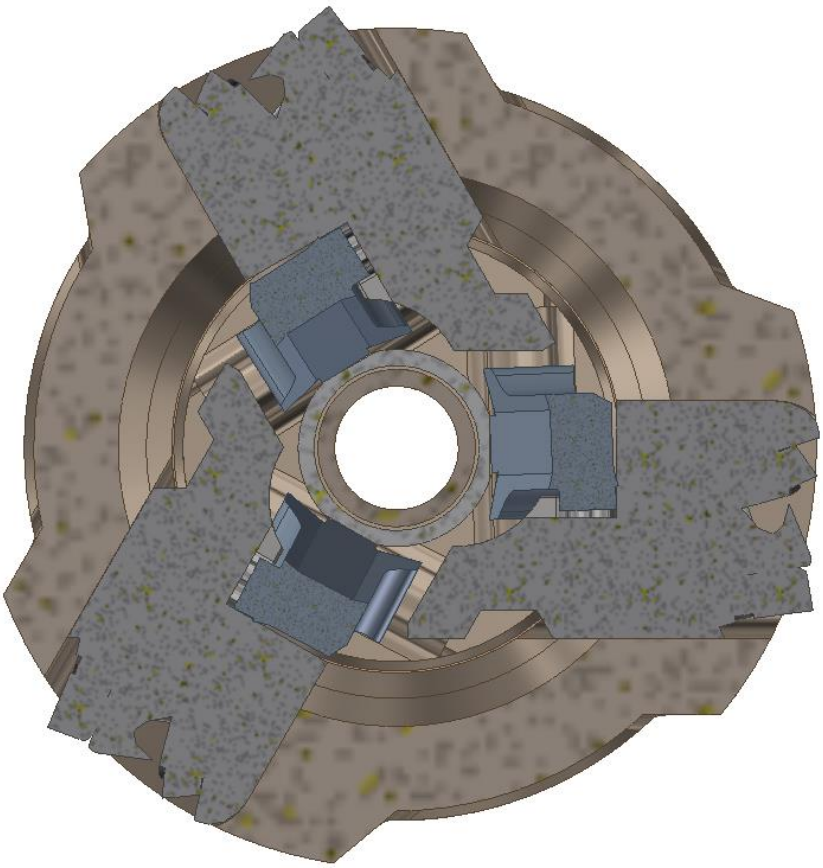

Figure 6.11: Intermediate position of the coupling rods.

- There is still a discussion on whether the fluid flow around the outer perimeter of the UR is sufficient to transport cuttings. There might be an opportunity to adjust the pockets on the outside of the reamer. Because the reamer rotates while cuttings are transported upward, a helical shape of the pockets could support the transport of cuttings by drawing in fluid from below. Whether this effect contributes to better transport has to be investigated.

- The volume flow has been reduced in order to have the same flow speed within the channel. From practice, it is known that high flow velocities can lead to *washout*. Due to turbulent slurry flow, the pin and box connections at the end of the UR may wear out, see figure 6.12. During the design phase, attention has been paid to the flow path. The mud channel is made completely straight. No lateral branches and diameter transitions are present in order to prevent phenomena like flow contraction and expansion. However, the end of the mud channel might be susceptible to washout. The wear mechanisms caused by fluid flow have to be investigated in more detail in order to predict the amount of pipe erosion.

Figure 6.12: Wear of the pin connection of a drill pipe.

- During the spring test, the length and diameter of the spring were measured by hand. Because of this, the results have a relative low reliability and relatively high random error. It is recommended that spring are carried out with calibrated spring testing machines for more accuracy.

- Research the combined effect of WOB and torque loads.

- Shear pins have not been implemented in the design. The use of these shear pins depends on the application of the reamer. In case the reamer needs to drill out cement. The reamer first needs to expand to the diameter of the previous set casing, before going to the full reaming diameter of 9 inch. Shear pins are also used as a safety mechanism to guaranty that the reamer does not open at low pressures and is set to open only when a certain pressure is reached. The location of the shear pins should also be reconsidered. The current design involves pins that are inserted around the piston. This causes the piston to be constrained but in case the block is slid out halfway it will not contact the arm stoppers and violent vibrations might occur. To prevent this, the shear pins should be inserted in the cutter blocks themselves.

- The calculation for the annular pressure losses depend on some calculations. It is assumed that the UR is placed concentric inside the hole and that the rheological properties of the mud were known. To a more detailed analysis, the temperature and the amount of colloids in the mud should also be considered more carefully. The properties may also change along the casing. All of these different effects have to be researched in more detail.

- Look more in detail to the design of the tongue-groove connections at the blocks. More tongue groove-connections could be better in terms of vibrations but the blocks are more likely to seize due to the larger surface area on the sides.

7. Conclusion

The main goal of this thesis was to determine whether it would be possible to design an UR, having a (maximum) body diameter of 149.23 mm (5 7/8 in.), with a diameter of at least 228.6 mm (9 in.) and a shoulder-to-shoulder length of at most 750 mm.

To determine whether the new design would be feasible, some additional requirements were imposed. These requirements are related to the opening mechanism and specifications of the current design. The most promising design has been selected by means of a MCA. Analytical calculations and Ansys simulations have been carried out to determine whether certain strength requirements are met.

Now it can be determined whether the goals set in the thesis assignment are fulfilled:

1. ***Is it possible to design an UR with a body diameter of 149.23 mm (5 7/8 in.) and a reaming diameter of at least 228.6 mm?***

Yes. By putting the blocks in an eccentric configuration around the mud channel, the blocks may reach a diameter of *228.6 mm* instead of 215.9 mm (8.5 in.).

2. ***Is it possible to design an UR with a body diameter of 149.23 mm and a shoulder-to-shoulder length of at most 750 mm?***

Yes. By moving the spring to the top of the UR and shortening the piston length. To reduce the overall length further, the extension angle of the blocks has been changed from 60 degrees to 45 degrees. The shoulder-to-shoulder length has been decreased by *66 mm*, from 816 mm to 750 mm.

By design, most of the remaining requirements are automatically met. Analytical calculations and Ansys calculations suggest that the conceptual design has superior strength characteristics compared to the base-case design.

Bibliography

[1] DRILLSTAR (n.d.). Z-reamer - your advanced compact underreamer. Retrieved November 6, 2017, from http://drillstar-industries.com/oil-and-gas/drilling/z-reamer/

[2] Casing drilling marks a century of progress. (2012, October 01). Retrieved November 6, 2017, from https://www.offshore-mag.com/articles/print/volume-72/issue-10/drilling-and-completion/casing-drilling-marks-a-century-of-progress.html

[3] Bojan, P. (2016). REVIEW OF CASING WHILE DRILLING TECHNOLOGY. Retrieved November 7, 2017, from https://scindeks-clanci.ceon.rs/data/pdf/0354-2904/2016/0354-29041629011P.pdf

[4] DrillingFormulas.Com (2016). Basic Knowledge of Casing while Drilling (CwD). (n.d.). Retrieved November 7, 2017, from http://www.drillingformulas.com/basic-knowledge-of-casing-while-drilling-cwd/

[5] Society of Petroleum Engineers (2015). Functions of drilling fluid. (n.d.). Retrieved November 9, 2017, from https://petrowiki.org/Functions_of_drilling_fluid

[6] McCaskill, J. (2006). Managing wellbore pressure while drilling. Retrieved November 12, 2017, from http://iadc.org/dcpi/dc-marapr06/Mar06-mccaskill.pdf

[7] Ikon Science solutions (n.d.). *Example of well plan with mud-weight, fracture pressure and pore pressure in Equivalent mudweight (EMW) gradient.* Retrieved November 14, 2017, from https://www.ikonscience.com/Portals/0/adam/Content/dFJiyunn-kyWWTuhYH6eDg/Image/fig2.1.png

[8] E. R. Crain (2015).Crain's Petrophysical Handbook - Measurements While Drilling (MWD) And Geosteering. (n.d.). Retrieved November 20, 2017, from https://www.spec2000.net/08-mwd.htm

[9] Akiet B.V. (n.d.). Composite Casing Drilling with High Strength Composite Tubular (HSCT). Retrieved November 22, 2017, from https://akiet.com/industry/casing-drilling

[10] Kyle R. Fontenot, Bill Lesso, R. D., StricklerTommy M. Warren, 2005. Using Casing to Drill Directional Wells, Oilfield Review Summer 2005: 44–61. Retrieved November 23, 2017, from https://pdfs.semanticscholar.org/75e8/bf875c12326d872012831fdbd5f4815d5fc4.pdf

[11] Maintenance Instructions (MI), HYDRAULIC Z-REAMER Z600H - 5 3/4" Max Body OD, no. D00003008, DRILLSTAR, Sep. 9, 2016. Accessed November 24, 2017.

[12] Wieling, I. (2017). "FYI". Message to Philip Kamp. November 16, 2017. Outlook 2013.

[13] DRILLSTAR. (2016). HYDRAULIC Z-REAMER Z600H - 5 3/4" OD F/6" PILOT HOLE 3 ½" REG PIN X BOX [PDF file]. Retrieved December 4, 2017.

[14] Harvest Tool Company. (n.d.). Rotor Underreamer. Retrieved January 8, 2018, from http://www.harvesttool.com/rotorunderreamer.html

[15] Schlumberger Technical Report, 2010. Drillstring vibrations and vibration modeling. Retrieved January 8, 2018, from http://www.slb.com/~/media/Files/drilling/brochures/drilling_opt/drillstring_vib_br.pdf

[16] Eriksen, E. (2009). Jetted underreamer assembly. Retrieved January 17, 2018, from https://patents.google.com/patent/US8113301

[17] Engineering 360. (n.d.). Compression Springs Information. Retrieved February 5, 2018, from https://www.globalspec.com/learnmore/mechanical_components/springs/helical_compression_springs

[18] Budynas, R. G., Nisbett, J. K., & Shigley, J. E. (2011). Shigley's mechanical engineering design. New York: McGraw-Hill.

[19] Tevema. (n.d.). D24610. Retrieved February 7, 2018, from https://www.tevema.com/d24610

[20] Martenelli, E. (2008). Elastic Buckling of Columns. Retrieved February 9, 2018, from http://www.enzomartinelli.eu/MaterialeDidattico/stabilita/StabilityChapter02.pdf

[21] Tevema. (n.d.). Compression Spring. Retrieved February 7, 2018, from https://www.tevema.com/technische-product-info/drukveren?__store=engels&__from_store=frans

[22] NACE International. (n.d.). Hydrogen Embrittlement. Retrieved February 7, 2018, from https://www.nace.org/Corrosion-Central/Corrosion-101/Hydrogen-Embrittlement/

[23] Lion Engineering Services Ltd. [LionEngServices]. (2018, 21, 2). Lion Engineering Services - Welding & Hardfacing animation. Retrieved from https://www.youtube.com/watch?v=p5Dk6YVdQiQ
[24] Kals, H.J.J., (2003). Industriële productie: Het voortbrengen van mechanische producten, SDU Uitgeverij.
[25] Admin (2018). Mill axis diagram. Retrieved February 12, 2018, from http://tinyforge.co/mill-axis-diagram.html
[26] Bakerfield Bit & Tool. (2018). Multi-Purpose Underreamers. Retrieved February 12, 2018, from http://www.bakersfieldbitandtool.com/underreamer/
[27] CustomPartNet. (2018). Hole-making operations. Retrieved February 14, 2018, from http://www.custompartnet.com/wu/hole-making
[28] Yahiaoui, Malik and Paris, Jean-Yves and Delbé, Karl and Denape, Jean and Gerbaud, Laurent and Colin, Christophe and Ther, Olivier and Dourfaye, Alfazazi Quality and wear behavior of graded polycrystalline diamond compact cutters. (2016) International Journal of Refractory Metals and Hard Materials, vol. 56. pp. 87-95. ISSN 02634368
[29] Engineerings Edge. (2018). Honing Manufacturing Review. Retrieved February 15, 2018, from https://www.engineersedge.com/manufacturing/honing-manufacturing.htm
[30] Amazon (2018). Lisle 15000 Engine Cylinder Hone. Retrieved February 15, 2018, from https://images-na.ssl-images-amazon.com/images/I/61ughCx1yLL._SL1275_.jpg
[31] ISE 316 - Manufacturing Processes Engineering Chapter 22 MACHINING OPERATIONS AND MACHINE TOOLS Turning and Related Operations Drilling and Related Operations. Retrieved February 16, 2018, from https://slideplayer.com/slide/1544470/
[32] Keulen, F. (2016). Advanced Mechanics Part: Continuum Mechanics.
[33] SAS IP, Inc. (n.d.). 13.187. SOLID187 - 3-D 10-Node Tetrahedral Structural Solid. Retrieved February 21, 2018, from https://www.sharcnet.ca/Software/Ansys/17.0/en-us/help/ans_thry/thy_el187.html
[34] SAS IP, Inc. (n.d.). 11.9.2. 10-Node Tetrahedra. Retrieved February 21, 2018, from https://www.sharcnet.ca/Software/Ansys/17.0/en-us/help/ans_thry/thy_shp8.html
[35] Dufour, P. (2003). Picking an Element Type For Structural Analysis. Retrieved February 23, 2018, from https://www.slideshare.net/gopalvrushali/struct-element-types
[36] SAS IP, Inc. (n.d.). Frictionless Face. Retrieved February 26, 2018, from https://www.sharcnet.ca/Software/Ansys/17.0/en-us/help/wb_sim/ds_Frictionless_Surface.html
[37] SAS IP, Inc. (n.d.). Fixed Supports. Retrieved February 26, 2018, from https://www.sharcnet.ca/Software/Ansys/16.2.3/en-us/help/wb_sim/ds_Fixed_Supports.html
[38] SAS IP, Inc. (n.d.). TARGE170. Retrieved February 26, 2018, from https://www.sharcnet.ca/Software/Ansys/16.2.3/en-us/help/ans_elem/Hlp_E_TARGE170.html
[39] Sönnerlind, H. (2018). Applying and Interpreting Saint-Venant's Principle. Retrieved April 2, 2018, from https://www.comsol.com/blogs/applying-and-interpreting-saint-venants-principle/
[40] Mechanical Design in Optical Engineering. Retrieved April 3, 2018, from https://wp.optics.arizona.edu/optomech/wp-content/uploads/sites/53/2016/10/OPTI_222_W1.pdf
[41] Svenninggaard, J. (2017). How to deal with the annoying Hot Spots in FEA. Retrieved April 5, 2018, from https://www.ucviden.dk/portal/files/40294494/How_to_deal_With_Hot_Spots.pdf
[42] Patel, S. (n.d.). Simulation – Avoiding Singularities. Retrieved April 6, 2018, from http://files.goengineer.com/docs/support/SolidWorks%20Simulation%20-%20Avoiding%20Singularities.pdf
[43] DNV GL (n.d.). RP-C203: Fatigue design of offshore steel structures. pg. 64. Retrieved April 10, 2018, from https://rules.dnvgl.com/docs/pdf/DNVGL/RP/2016-04/DNVGL-RP-C203.pdf
[44] Mechanical Design in Optical Engineering. Retrieved April 3, 2018, from https://wp.optics.arizona.edu/optomech/wp-content/uploads/sites/53/2016/10/OPTI_222_W18.pdf
[45] Hibbeler, R. C. (2011). Mechanics of materials. Upper Saddle River, N.J: Pearson Education.

[46] DrillingFormulas.Com (2014). What You Need To Know About Drilling Bit Balling Up and How To Troubleshooting It. Retrieved, June 21, 2018, from http://www.drillingformulas.com/what-you-need-to-know-about-drilling-bit-balling-up-and-how-to-troubleshooting-it/

[47] FONTENOT, K., et al., 2005. Using Casing drilling to drill directional wells. Oilfield Review, 17(2), pp.44- 61.

[48] Ghiselin, D. 2012. Casing drilling marks a century of progress. Offshore Magazine, volume 72, issue 10. https://www.offshore-mag.com/articles/print/volume-72/issue-10/drilling-and-completion/casing-drilling-marks-a-century-of-progress.html

Nomenclature

Symbols		Description	Units	Page
$[B]$		Matrix relating strain to displacement	-	104
$[E]$		Elasticity matrix	-	127
$[K^{-1}]$		Inverse stiffness matrix	-	104
$[K]$		Total stiffness matrix	-	104
$[N]$		Interpolation matrix	-	104
$[S]$		Matrix relating stress to strain	-	104
A		Area, shoulder to shoulder length, outer diameter previous casing, drill bit – UR distance	[m²], [mm], [mm], [mm]	53/55, 11, 22/23, 157
a		Short side internal length cutter block, distance between node A and B in beam-model, kite dimension, eccentricity of applied force, top groove to casing contact point	[mm], [mm], [mm], [mm], [mm]	32, 33/34, 43, 94, 65
A_2		Area on the long side of the cutter block	[m²]	32
A_3		Area on the short side of the cutter block	[m²]	32
$A_{cross\text{-}section}$		Cross-section area	[m²]	109
$A_{cutters}$		Surface area over which the cutters act	[m²]	135
A_{flow}		Flow area annulus	[m²]	76
A_i		Local area	[m²]	109
b		Long side internal length cutter block, distance between node B and C in beam-model, kite dimension, line contact length, clearance between mud channel and sleeve channel, top groove to casing contact point	[mm], [mm], [mm], [mm], [mm], [mm]	32, 33/34, 43, 87, 142, 65
B		Blade to bit length, UR – knuckle joint distance	[mm], [mm]	11, 156
BH		Brinell hardness	[N/mm²]	87
c		Short side external length cutter block, kite dimension, groove length in core body of the UR, piston radius, distance to the outer most fibre	[mm], [mm], [mm], [mm], [mm]	32/33, 43, 65, 94, 109
C		Blade length, constant of integration, spring stiffness, knuckle joint – second stabilizer distance	[mm], -, [N/m], [mm]	11, 38/143, 54, 156
c_0		Outer radius of the UR core body	[mm]	119/120
c_1		Inner radius of the UR core body	[mm]	119/120
d		Side length cutter block, kite dimension, wire diameter, mud channel outer diameter, perpendicular distance used in parallel axis theorem	[mm], [mm], [mm], [mm], [mm]	32/33, 43, 53/54/58, 94, 109
D		Casing outer diameter, (enlarged) hole diameter, mean spring diameter	[mm], [mm], [mm]	22/23, 45, 53/58
D_1		Diameter of convex or concave surface	[mm]	86
d_1		Mud channel outer diameter	[mm]	142
d_2		Sleeve channel outer diameter	[mm]	142
D_2		Diameter of convex or concave surface	[mm]	86
$D_{bore,min}$		Minimum bore diameter	[mm]	54
D_c		Casing diameter	[mm]	153
$D_{drill,max}$		Maximum drill diameter	[mm]	54
$D_{drill\ string}$		Drill string diameter	[mm]	76
D_e		Annular hydraulic diameter	[mm]	153
D_h		Hole diameter	[mm]	153
D_{inner}		Inner diameter piston	[mm]	53/109
D_m		Mud channel diameter, mean coil diameter	[mm], [mm]	46, 54/58
D_{out}		Coil outer diameter	[mm]	54

D_{outer}		Outer diameter piston	[mm]	53/109
$D_{pilot\ hole}$		Pilot hole diameter	[mm]	76
D_{pocket}		Pocket diameter	[mm]	76
D_{rel}		Relative diameter	[mm]	86/87
D_{UR}		Underreamer diameter	[mm]	76
e		Groove distance, eccentricity	[mm], [mm]	65, 142
E		Casing inner diameter, modulus of elasticity	[mm], [GPa]	22/23, 55/56
E_1		Elastic modulus of body 1	[GPa]	86
E_2		Elastic modulus of body 2	[GPa]	86
E_{eq}		Equivalent modulus of elasticity	[GPa]	86
E_{sp}		Specific cutting energy	[kN/m^2] or [MN/m^2]	135
F		BHA component diameter, force on the cutter block, (maximum) spring force	[mm], [N], [N]	22/23, 35, 54/58
f		Spring deflection, distance between sliding grooves	[mm], [mm]	54, 65
F_1		External force on cutter block, force on lower sliding rail cutter block	[N], [N]	32/33, 65/67-70
F_2		Force applied to the cutter block by the core body, force on upper sliding rail cutter block	[N], [N]	32/33, 65/67-70
F_3		Force applied to the cutter block by the core body	[N]	32/33
F_{arm}		Force on the armstopper	[N]	138
F_{bottom}		Force on the bottom of the cutter block	[N]	174
$F_{drill\ bit}$		Force on the drill bit	[N]	160
F_{lift}		Additional lifting force	[N]	70
F_{link}		Force on the link	[N]	138
FoS		Factor of safety	[-]	174
F_{piston}		Force on the piston	[N]	138
F_{spring}		Spring force	[N]	93
F_u		Force parallel to tongue groove connection	[N]	65-67
F_v		Force perpendicular to tongue groove connection	[N]	65-67
F_w		Cutter block maximum friction force	[N]	65
$F_\perp$		Force perpendicular to the top side of the cutter block	[N]	65/67
g		Gravitational acceleration	[m/s^2]	174
G		UR DRILLSTAR ream diameter, modulus of elasticity in shear	[mm], [GPa]	22/23, 54
h		Height of cutter block	[mm]	32/33/35
H		Drill bit diameter	[mm]	22/23
I		Second moment of area	[mm^4]	55/109
J		Polar moment of inertia	[mm^4]	53/120
k		Spring stiffness	[N/m]	53
k_h		Stribeck value	[-]	87
L		Normalized coordinates, length from spring disk to bottom of the piston	[-], [mm]	105, 142
L_0		Free spring length	[mm]	54/58
$l_{buckling}$		Buckling length	[mm]	55
L_{closed}		Closed length of the spring	[mm]	54
$L_{extension}$		Extension length	[mm]	52
L_n		Solid height	[mm]	54/58
L_{rod}		Coupling rod length	[mm]	52
L_{slide}		Slide length	[mm]	52
L_{stroke}		Stroke length rod, stroke length spring	[mm], [mm]	52, 53
L_{thread}		Spring thread length	[mm]	58
m		Number of elements in domain of interest for adaptive meshing	[-]	127

M		Torque, internal moment	[N·m], [N·m]	32/109, 35
$M_{1,2}$		Internal moment beam-model	[N·m]	34
M_{max}		Maximum internal moment in beam-model	[N·m]	34
n		Parameter to indicate how many blades are in contact with the borehole (n=1,2,3), number of active coils, number of rotations for bearings	[-], [-], [-]	32/33, 54, 87
N_f		Fixed number of coils	[-]	58
N_t		Total number of coils	[-]	54/58
N_w		Number of active coils	[-]	54
$OD_{expansion}$		Expansion of the outer diameter of the spring	[mm]	58
P		Force	[N]	142
P_c		Power needed for cutting	[Watt]	135
p_{max}		Maximum pressure	[N/m²]	87
PV		Plastic viscosity	[Pa·s]	153/154
Q_c		Cutting volumetric production	[m³/s]	135
r		Reaming radius, distance to outer fibre	[mm]	32/33, 53
R		Reaming radius, mean coil radius, dogleg radius	[mm], [mm], [m]	45, 53/54, 157/158
ROP		Rate of penetration	[m/s]	135
S_n		Maximum spring deflection	[mm]	54
T		Torque	[N·m]	120
U		Total elastic strain energy	[Joule]	126
u		axis of coordinate system, displacement in u direction	-, [mm]	67, 105
$u_{i\text{-}r}$		Displacement in u direction of nodes i-r	[mm]	105
$\bar{V}$		Average velocity	[m/s]	153
V		Shear force	[N]	34
v		Deflection of a beam, axis of coordinate system	[mm], -	143, 67
$V_{1,2}$		Internal shear force beam-model	[N]	34
V_c		Critical flow velocity	[m/s]	153
V_{max}		Maximum internal shear force in beam-model	[N]	34
w		Width of cutter block	[mm]	35/43/46
WoB		Weight on bit	[kg]	174
x		axis of coordinate system	-	156
x_1		Coordinate used to represent the internal shear force and moment throughout a beam, extension length	-, [mm]	33/34, 46
x_2		Coordinate used to represent the internal shear force and moment throughout a beam, extension length	-, [mm]	33/34, 46
x_c		X-coordinate of dogleg circle center	[mm]	157
$\bar{y}$		y-coordinate of centroid of total area	[mm]	109
$\tilde{y}_t$		y-coordinate of centroid of local area	[mm]	109
y		axis of coordinate system, distance furthest away from the vertical axis	-, [mm]	156, 35
y_2		Width of contact surface along the edge on the short side of the cutter block	[mm]	32
y_3		Width of contact surface along the edge on the long side of the cutter block	[mm]	32
y_c		Y-coordinate of dogleg circle center	[mm]	157
YP		Yield point	Pa	153/154
$\{D\}$		Nodal displacement vector for all elements	-	104
$\{d\}$		Degrees of freedom vector for one element	-	104
$\{F\}$		Force vector	-	104
$\{u\}$		Displacement field vector	-	104
$\{\varepsilon\}$		Strain vector	-	104

$\{\sigma\}$		Stress vector	-	104
α		Kite angle, angle between vertical and block extension path, block outside face angle with horizontal, RSS angle	[deg], [deg], [deg], [deg]	43, 52
β		Block departure angle, angle between rod and horizontal	[deg], [deg]	43/65, 52
γ		Kite angle, angle between casing force and $F_{\perp}$	[deg], [deg]	43, 65/66
δ		Angle between $F_{\perp}$ and the horizontal	[deg]	65
η		Relative error	[-]	127
θ		Angle between rod and vertical, contact angle	[deg], rad	52, 87
λ		Slenderness	[-]	55/56
μ_1		Coefficient of friction	[-]	65
μ_2		Coefficient of friction	[-]	66/67
ν		Poisson ratio	[-]	86
ρ		Density	[kg/m^3]	153/154
σ		Normal stress	[N/m^2]	35
$\sigma_{1,2}$		In-plane principle stresses	[N/m^2]	120
$\sigma_{abs,max}$		Absolute maximum normal stress	[N/m^2]	35
$\sigma_{buckling}$		Buckling stress	[N/m^2]	56
σ_H		Hertz contact stress	[N/m^2]	87
σ_{max}		Maximum normal stress, maximum shear stress	[N/m^2], [N/m^2]	35, 109
σ_{yield}		Yield stress	[N/m^2]	32/33/53
τ		Internal shear stress, spring maximum shear strength	[N/m^2], [N/m^2]	53, 58
τ_{xy}		Shear stress component	[N/m^2]	120
υ_{max}		Maximum deflection	[mm]	143
$\upsilon_{max,supported}$		Maximum deflection while supported	[mm]	144
$\upsilon_{max,unsupported}$		Maximum deflection while unsupported	[mm]	144
φ		Angle between cutter force line of action and line tangential to the rotation direction of the cutter block	[deg]	32/33
ω		Angular velocity of drill string assembly	[1/s]	135
$\|\|e\|\|$		Global energy error norm	[Joule]	127
Δp		Pressure differential	[MPa]	53

Symbol	Meaning	
,	'separation'	
/	'and'	
-	'inapplicable' or 'indeterminate'	For units
	'to'	For pages

List of abbreviations

BHA	Bottom Hole Assembly
CPN	Casing Profile Nipple
CRT	Casing Running Tool
CwD	Casing while Drilling
DLA	Drill Lock Assembly
DTU	Drilling Type Underreamer
DwL	Drilling with Liner
ECD	Equivalent Circulating Density
ECI	Enhanced Casing Installation
EDR	Expandable Drilling Reamer
EMW	Equivalent Mud Weight
ERD	Extended Reach Drilling
FDM	Fusion Deposition Modelling
FEA	Finite Element Analysis
FEM	Finite Element Method
FoS	Factor of Safety
GPM	Gallon Per Minute
HEWD	Hole Enlargement While Drilling
HSP	Hydrostatic Pressure
HWT	Huisman Well Technology
ksi	Kilopound per square inch
LCM	Lost Circulation Materials
LDD	Lockdown Device
LWD	Logging While Drilling
mt	Metric ton
MW	Mud Weight
MWD	Measurements While Drilling
NBR	Near-Bit Reamer
NPT	Non-Productive Time
OCTG	Oil Country Tubular Goods
PCPD	Progressive Cavity Positive Displacement
PDC	Polycrystalline Diamond Compact
POOH	pull out of the hole
ppg	Pound-mass per gallon
psi	Pound-force per square inch
REG	regular (API connection)
RFID	Radio-Frequency-identification
RIH	Run In Hole
RoD	Ream on Demand
ROP	Rate Of Penetration
RPM	Rounds Per Minute
RSS	Rotary Steerable System
RWD	Ream While Drilling
TD	Total Depth
TIH	Trip In Hole
TSP	Thermally Stable Polycrystalline
TVD	True Vertical Depth
UR	Underreamer
VST	Verenstaal
WOB	Weight on Bit

Metric and U.S. measurement equivalences

Metric	Imperial	Imperial	Metric
1 m	*39.37 in.*	*1 in.*	*0.025 m*
1 m	*3.28 ft*	*1 ft*	*0.305 m*
1 m^3/s	*15850 GPM (US)*	*1 GPM (US)*	*$6.3 \cdot 10^{-5}$ m^3/s*
1 litre/minute	*0.264 GPM (US)*	*1 GPM (US)*	*3.79 litre/minute*
1 kg/m^3	*0.0083 ppg*	*1 ppg*	*119.8 kg/m^3*
1 kg	*2.207 lbm*	*1 lbm*	*0.454 kg*
1 N	*0.225 lbf*	*1 lbf*	*4.45 N*
1 MPa	*145 psi*	*1 psi*	*0.0069 MPa*
1 kg/m^2	*0.0014 $lbm/in.^2$*	*1 $lbm/in.^2$*	*703.1 kg/m^2*
1 N·m	*0.738 lbf·ft*	*1 lbf·ft*	*1.36 N·m*
1 m/s	*196.85 ft/min*	*1 ft/min*	*0.0051 m/s*
1 Pa/m	*$4.42 \cdot 10^{-5}$ psi/ft*	*1 psi/ft*	*22621 Pa/m*
1 Pa·s	*1000 cP*	*1 cP*	*0.001 Pa·s*
1 kg/m	*0.672 lbs/ft*	*1 lbs/ft*	*1.49 kg/m*

Note: lbs has units of mass.

Inches to millimeter conversion chart for commonly used dimensions.

Inch	Millimeter
1	25.4
2	50.8
3	76.2
$3\frac{1}{2}$	88.9
4	101.6
$4\frac{3}{4}$	120.7
5	127
$5\frac{1}{2}$	139.7
$5\frac{3}{4}$	146.1
$5\frac{7}{8}$	149.2
6	152.4
7	177.8
8	203.2
$8\frac{1}{2}$	215.9
9	228.6
9.45	240.0
$9\frac{5}{8}$	244.5
10	254
11	279.4

List of figures

Figure 1.1: DRILLSTAR Z1225H type underreamer.[1] ... 1
Figure 2.1: Overview of a conventional drilling method and the main types of CwD methods.[47, [48] ... 4
Figure 2.2: Depth vs pressure gradient plot.[7] ... 6
Figure 2.3: Axial (left) and torsional (right) sections. ... 7
Figure 2.4: Composite (top and middle) and stainless steel (bottom) casing joints. ... 7
Figure 2.5: The matrix body structure (left) and the PDC cutting elements (right). ... 8
Figure 2.6: Drilling stabilizer. ... 8
Figure 2.7: Drill pipe float valve. ... 8
Figure 2.8: Mud motor principle (left) and rotor (right). ... 9
Figure 2.9: Push-the-bit (left) and point-the-bit (right). ... 9
Figure 3.1: DRILLSTAR Z600H layout in section view. ... 10
Figure 3.2: Telescopic blocks consisting of a shell (red) and inner block (green). ... 12
Figure 3.3: Side-view with blocks extended. ... 12
Figure 3.4: Vertical sliding blocks. ... 13
Figure 3.5: Diaphragm mechanism. Left and middle: three-bladed design. Right: five-bladed design. ... 14
Figure 3.6: Eccentric blade interfaces. Left: straight blocks. Right: curved blocks. ... 15
Figure 3.7: Multi-disk blades. ... 16
Figure 3.8: Blocks with finger joints. ... 17
Figure 3.9: Arrow shaped sliding grooves. ... 18
Figure 3.10: Multimember extendable arms (XR™ Reamer Hole Enlargement Tool – Halliburton, 2016). ... 19
Figure 4.1: Section view of the base-case including dimensions.[13] ... 22
Figure 4.2: Diameters of string elements. ... 23
Figure 4.3: Coupling rod that connects to the inner and outer block with pins. ... 24
Figure 4.4: Groove overlap with slot. ... 25
Figure 4.5: Views of the preliminary basic concept. ... 25
Figure 4.6: Telescopic concept with extended blocks including dimensions in mm. ... 26
Figure 4.7: Diaphragm concept drawn in reference framework. ... 27
Figure 4.8: Vanes adjusted rotation angle and rotation axis (bottom view). ... 28
Figure 4.9: Groove-ridge connection (bottom view). ... 28
Figure 4.10: Rotor underreamer of the Harvest Tool Company, LLC.[14] ... 29
Figure 4.11: Stick-slip phenomenon.[15] ... 30
Figure 4.12 A: Full eccentric (triangular) configuration. ... 31
Figure 4.12 B: Partial circumjacent configuration. ... 31
Figure 4.12 C: Full adjacent configuration. ... 31
Figure 4.13: Parametric model. ... 32
Figure 4.14: Beam model of the block. ... 33
Figure 4.15: Shear (left) and moment (right) diagram. ... 34
Figure 4.16: Bending stress at section B. ... 35
Figure 4.17: Schematic representation of the elastic curve. ... 36
Figure 4.18: Tilting and clearance of the block in the UR core structure. ... 36
Figure 4.19: Free-body diagrams of the segments of the block. ... 37
Figure 4.20: Exaggerated representation of the column deformation. ... 39
Figure 4.21: Finite element analysis of the UR core structure. ... 40
Figure 4.22: Local stress maximum. ... 40
Figure 4.23: stages in designing the block joints and shapes. ... 41
Figure 4.24: Top view of the meeting interface between three cutter blocks. ... 41
Figure 4.25: Block with finger joints. ... 42
Figure 4.26: Block slide-out position. ... 42
Figure 4.27: Block geometry. ... 43
Figure 4.28: Block edges around the top (left) and bottom (right) corners. ... 44
Figure 4.29: Exploded view of the second prototype of the finger joint concept. ... 44
Figure 4.30 A: Tongue-groove fittings 1 and 2 meeting along the edge of the blocks. ... 45
Figure 4.30 B: Graphical representation of drill diameter calculation. ... 45
Figure 4.31: Relation between block width and stick-out length. ... 46

Figure 4.32: Impact of including the coupling rod into the design. 46
Figure 5.1: Rack and pinion actuator.[16] 49
Figure 5.2: Spring with piston. 49
Figure 5.3: Conceptual designs for the expansion mechanism. 50
Figure 5.4: Model to determine the required stroke length. 52
Figure 5.5: Buckling shape.[20] 55
Figure 5.6: Springs that will be tested. 59
Figure 5.7: Experiment setup and schematic setup drawing. 59
Figure 5.8: Measurement method. 60
Figure 5.9: Tapping tool to repair the damaged thread. 60
Figure 5.10: Spring end closed completely after compression and relaxation. 63
Left: uncompressed, Right: compressed and relaxed. 63
Figure 5.11: Geometric model of a block with two tongue groove fittings. 65
Figure 5.12: Upper-core. 72
Figure 5.13: Core assembly consisting of top and bottom sub. 73
Figure 5.14: Spring moved to the top of the UR. 73
Figure 5.15: Spring moved down. 74
Figure 5.16: Sizing of the links. 74
Figure 5.17: Sizing of the spring. 75
Figure 5.18: Cross-sections with flow area (hatched) bounded by the pilot hole contour (red) and UR contour (blue). 76
Figure 5.19: Conceptual design of the bottom-core. 77
Figure 5.20: Fillets added to the slots. 77
Figure 5.21: UR contour adjusted for manufacturing. 77
Figure 5.22: Section view of the internal grooves. The pin connection is located at the top of this picture. 78
Figure 5.23: Sketches of the block shapes with varying top angles. 79
Figure 5.24: Rough 3D model of the cutter block. 80
Figure 5.25: Block with room for the link connection (left) and cut out for the support legs (right). 80
Figure 5.26: Connection for the coupling rod. 81
Figure 5.27: Rough shape (left) and detailed shape (right) of the cutter block. 82
Figure 5.28: Arm stopper concepts. 83
Figure 5.29: Link development. 85
Figure 5.30: Piston development. 89
Figure 5.31: Development diagrams of the grease cap. 90
Figure 5.32: Left: spring (grey) in its pretension state. The retainer (brown) is located at the bottom of the grease cap (green). Right: when the retainer moves upwards (red arrows), fluid (blue arrows) flows through the holes of the retainer. 90
Figure 5.33: Mud channel. 91
Figure 5.34: Development of the sleeve channel. 92
94
Figure 5.35: Simplified model of the sleeve assembly. 94
Figure 5.36: Dummy picture of the plug. 95
Figure 5.37: Left: Assembly of the internal parts. Right: Piston with wear and slide rings. 96
Figure 5.38: Procedure for connecting the coupling rods to the cutter blocks. 97
Figure 5.39: Armstopper installation. 98
Figure 5.40: Spring put inside the bottom-core. 98
Figure 5.41: Insertion of the mud channel. 99
Figure 5.42: Notches for handling tool. 99
Figure 5.43: Left: hardfacing process with inserts on the side of the UR core-body. Right: bottom of the block slot.[23] 100
Figure 5.44: Brazing PDC bits onto the cutter block of the UR. 100
Figure 5.45: Left: milling machine degrees of freedom. Right: milling of the UR core body.[25],[26] 101
Figure 5.46: Left: the principle of boring. Right: part of the UR core body where boring needs to be performed.[27] 101
Figure 5.47: Manufacturing process of conventional PDC cutters. 102
Figure 5.48: Left: honing tools for medium to hard workpiece materials. Right: UR bore hole.[30] 102

Figure 5.49: Top: broaching tool side-view. Bottom: part of the tongue-groove connection in the core of the UR.[31] 103
Figure 5.50: SOLID187.[33] 105
Figure 5.51: Left: SHELL93 Quadratic Elements (8 nodes), right: SHELL181 linear elements (4 nodes).[35] 105
Figure 5.52: TARGE170 and CONTA174.[38] 106
Figure 5.53: Overview of the sub-assemblies. 108
Figure 5.54: Simplified model of the link protrusion. 109
Figure 5.55: Link-piston model. 110
Figure 5.56: Manual contact regions. 111
Figure 5.57: Mesh. 112
Figure 5.58: Supports and constraints. 113
Figure 5.59: Equivalent von-Mises stress. 114
Figure 5.60: Equivalent stress plot for 300 bars of pressure conveyed through one coupling rod. 115
Figure 5.61: Equivalent von-Mises stress. 116
Figure 5.62: Retraction of the coupling rod with the full spring force. 117
Figure 5.63: Block-bottom assembly geometry. 121
Figure 5.64: Connections. 122
Figure 5.65: Mesh. 123
Figure 5.66: Support reactions. 124
Figure 5.67: Stress distribution. 125
Figure 5.68: Peak stress. 125
Figure 5.69: St. Venant's principle: normal stress distribution distorted in the vicinity of the point load.[40] 126
Figure 5.70: Adaptive meshing.[41] 127
Figure 5.71: Convergence history. 128
Figure 5.72: Mesh refinement at the high stress region. 128
Figure 5.73: Model adjustments.[42] 129
Figure 5.74: schematic stress distribution at a hot spot.[43] 129
Figure 5.75: Stress concentration around the armstopper edge. 131
Figure 5.76: Mesh. 132
Figure 5.77: Supports and constraints. 132
Figure 5.78: Equivalent Von Mises stress plots. 133
Figure 5.79: Stress along circumference. 134
Figure 5.80: Supports and constraints. 136
Figure 5.81: Equivalent stress plot. 136
Figure 5.82: Schematic overview of the forces acting on the cutter block in the extended position. 137
Figure 5.83: Armstopper simulation geometry. 139
Figure 5.84: Contacts. 140
Figure 5.85: Mesh. 140
Figure 5.86: Armstopper loaded with distributed 10 MPa piston load. 141
Figure 5.87: Armstopper loaded with full 10 MPa piston load. 141
Figure 5.89: Schematic representation of the pin supports.[44] 142
Figure 5.88: Situation drawing. 142
Figure 5.90: Support conditions for the sleeve channel. 145
Figure 5.91: Top: von Mises stress. Bottom: deflection. 145
Figure 5.92: Top: von Mises stress of the assembly. Bottom: Directional deformation of the assembly. 146
Figure 6.1: Model of the UR core (red) with support material (grey). 148
Figure 6.2: Check of the infill and layering. 149
Figure 6.3: Parts arrangement and pack details. 149
Figure 6.4: Bayonet mount. 150
Figure 6.5: Coupling rod design. 151
Figure 6.6: Exaggerated representation of a simplified model to determine the dogleg. 156
Figure 6.7: Situation drawing of the BHA assembly. 156
Figure 6.8: Crooked stick-out inside the borehole. 158
Figure 6.9: Beam model of the stick-out assembly. 159
Figure 6.10: Bit balling at the drill bit.[46] 160
Figure 6.11: Intermediate position of the coupling rods. 161
Figure 6.12: Wear of the pin connection of a drill pipe. 162

FIGURE H.1: UR LOADED WITH NOMINAL TORQUE AND PEAK WOB. 190
FIGURE H.2: UR LOADED WITH NOMINAL TORQUE AND PEAK WOB. 190
FIGURE H.3: UR LOADED WITH MAXIMUM TORQUE AND PEAK WOB. 191
FIGURE H.4: UR LOADED WITH MAXIMUM TORQUE AND PEAK WOB. 191
FIGURE H.5: UR SUBJECTED TO THE LIMITING TORQUE AND WOB LOAD. 192
FIGURE H.6: UR SUBJECTED TO THE LIMITING TORQUE AND WOB LOAD. 192
FIGURE I.1: ARMSTOPPER SUBJECTED TO THE LIMITING PISTON LOAD. 193

List of tables

Table 1.1: Standard dimensions. 1
Table 3.1: Product Data Sheet Hydraulic Reamer 600.[12] 11
Table 3.2: Boundary conditions. 20
Table 3.3: Weighing factors. 21
Table 3.4: MCA. 21
Table 4.1: Base – case dimensions. 22
Table 4.2: Important reference dimensions. 22
Table 4.3: Input and output values for the current design. 33
Table 4.4: Measurements of torque and WOB. 39
Table 4.5: Boundary conditions. 47
Table 4.6: Weighing factors. 48
Table 4.7: MCA. 48
Table 5.1: Spring characteristics of item D24610.[19] 54
Table 5.2: Chemical composition of werkstoffnummer 1.4310/AISI 302 (percentage by mass). 54
Table 5.3: Parameters. 55
Table 5.4: Spring free length values. 61
Table 5.5: Diameter values. 61
Table 5.6: Block top angles and the corresponding block geometry. 67
Table 5.7: Calculation results. 71
Table 5.8: Spring selection parameters. 75
Table 5.9: Pipe flow velocities. 91
Table 5.10: Pipeline allowable volumetric flow. 91
Table 5.11: Load cases and load combinations. 107
Table 5.12: Load cases and load combinations. 119
Table 5.13: Measurements of torque and WOB. 119
Table 5.14: Considered load case. 121
Table 5.15: Considered load case. 132
Table 5.16: Considered load case. 135
Table 5.17: Distribution of torque and WOB. 135
Table 5.18: Parameter values. 144
Table 6.1: Comparison Hydraulic Reamer 600 and renewed design. 152
Table 6.2: Casing properties. 153
Table 6.3: Annulus ID and OD along casing joint, and pump rate. 153
Table 6.4: Results. 154
Table 6.5: Example parameters. 154
Table 6.6: parameters. 156
Table D.1: Reaction force check. 184
Table E.1: New design parameters. 186
Table J.1: Parameters. 194

Appendix A

A.1: Technical drawing Z600H

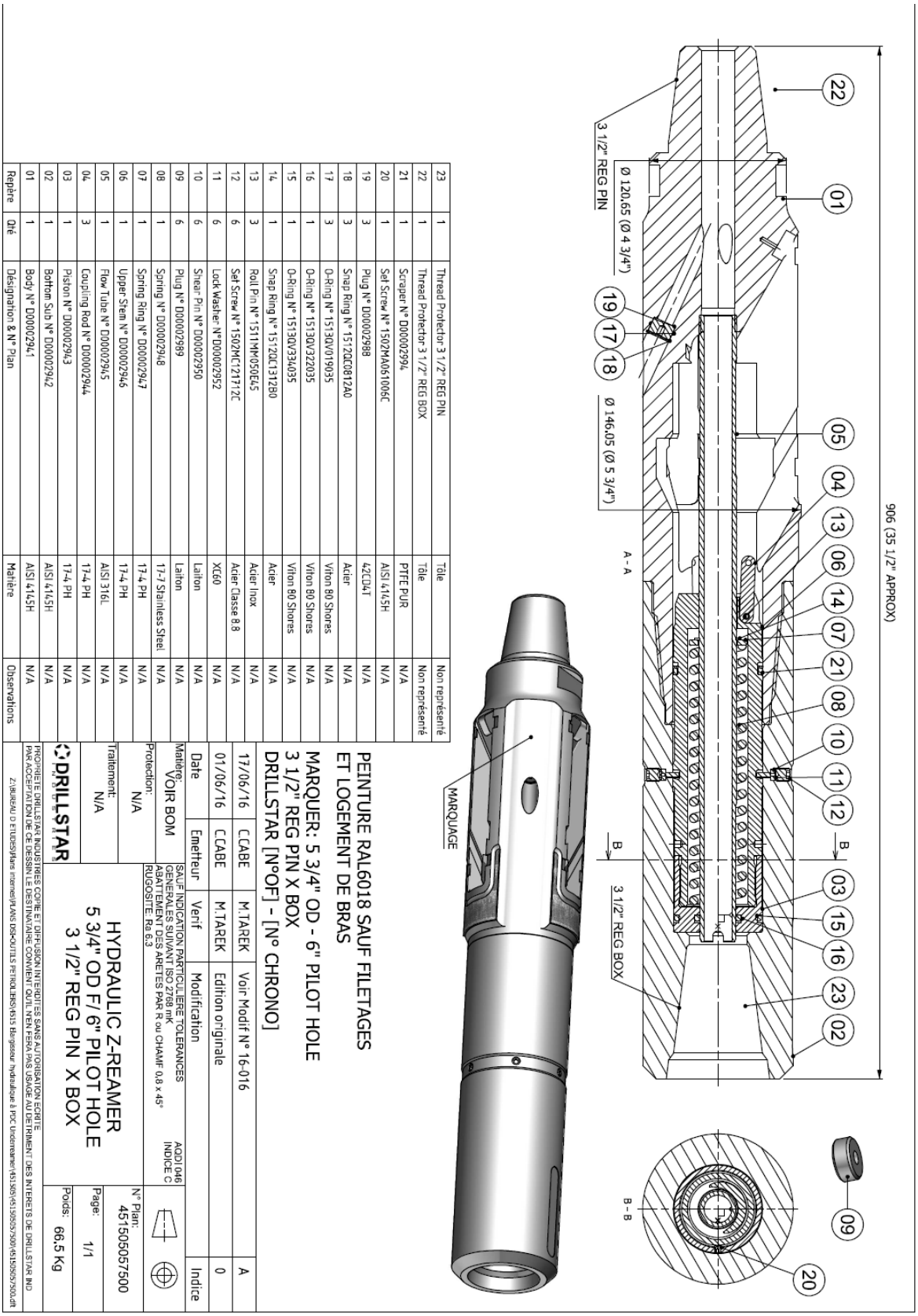

Repère	Qté	Désignation & N° Plan	Matière	Observations
23	1	Thread Protector 3 1/2" REG PIN	Tôle	Non représenté
22	1	Thread Protector 3 1/2" REG BOX	Tôle	Non représenté
21	1	Scraper N° D00002994	PTFE PUR	N/A
20	1	Set Screw N° 1502MA061006C	AISI 4145H	N/A
19	3	Plug N° D00002988	42CD4T	N/A
18	3	Snap Ring N° 15120C0812A0	Acier	N/A
17	3	O-Ring N° 1513QV019035	Viton 80 Shores	N/A
16	1	O-Ring N° 1513QV322035	Viton 80 Shores	N/A
15	1	O-Ring N° 1513QV334035	Viton 80 Shores	N/A
14	1	Snap Ring N° 15120C131280	Acier	N/A
13	3	Roll Pin N° 1511MM050E45	Acier Inox	N/A
12	6	Set Screw N° 1502MC121712C	Acier Classe 8.8	N/A
11	6	Lock Washer N°D00002952	XC60	N/A
10	6	Shear Pin N° D00002950	Laiton	N/A
09	6	Plug N° D00002989	Laiton	N/A
08	1	Spring N° D00002948	17-7 Stainless Steel	N/A
07	1	Spring Ring N° D00002947	17-4 PH	N/A
06	1	Upper Stem N° D00002946	17-4 PH	N/A
05	1	Flow Tube N° D00002945	AISI 316L	N/A
04	3	Coupling Rod N° D00002944	17-4 PH	N/A
03	1	Piston N° D00002943	17-4 PH	N/A
02	1	Bottom Sub N° D00002942	AISI 4145H	N/A
01	1	Body N° D00002941	AISI 4145H	N/A

A.2: Z-reamer information

DRILLING / MILLING / FISHING

DRILLSTAR

Z-REAMER

Zero offset, Zero rathole, Full steerability

Designed with simplicity and reliability in mind, the Drillstar Z-Reamer is a compact block-type underreamer featuring advanced reaming capabilities.

Combining the advantages of a modern underreamer with the short size of a bicenter bit, the Drillstar Z-Reamer opens up new reaming applications. It is now possible to perform directional reaming-while-drilling using PDMs rather than a RSS BHA, even in the smaller borehole sizes and without compromising on steerability.

It is available with either hydraulic or mechanical (WOB) activation. Pilot Bit can be integrated on the lower Body for an even shorter overall length.

One size up

The Z-reamer is the first block-type underreamer capable of enlarging up to one bit size up (or about 50% of pilot size) even in the smaller diameters. This unique feature enables the tool to be run in casing-while-drilling applications with even the smaller casing diameters.

Reduced rathole length

As the reaming blades are now located immediately above the bit, long ratholes are no longer required, saving rig time and reducing drilling risks.

Improved stability and drilling performances

Unlike a bicenter bit, the Z-reamer is a fully centered tool, reducing drilling vibrations and improving stability. And unlike other underreamers, the reaming blades are always in the same formation as the bit. No more guessing whether WOB is set on the bit or on the reamer.

Field maintainable

The Z-reamer is a sturdy tool, tested to perform in harsh drilling environments while remaining simple enough to be maintained in the field with few spare parts and hand tools, reducing turnaround time between runs and improving reliability.

Z600H with 8 ½" single row passive gauge blades

DRILLING

Z-REAMER

Fail-safe design

The Z-reamer does not rely on any specific component to be able to retract. No latch, no pin, no ball: the reaming blades are kept open while drilling by WOB and hydraulics, and retract while pulling out through the casing shoe. Only a light pull is required in normal operations, but you still keep the possibility of applying more pull to retract the blades in case of damage.

Optimized for your well

Bit and reaming blades design can be optimized for your desired well trajectory, taking into account formation and BHA parameters (UCS, PDM limitations, etc.). A full steerability simulation can be run and recommendations made for BHA components and drilling parameters.

Standard dimensions

Type	Pilot Bit size	Max Body OD	Max enlarged hole size	Max flow (GPM)	Standard connection
Z378H	3 7/8"	3 13/16"	5 1/2"	150	2 3/8" REG
Z450H	4 1/2"	4 3/8"	6 3/8"	250	2 7/8" REG
Z600H	5 7/8" - 6"	5 3/4"	8 1/2"	450	3 1/2" REG
Z850H	8 1/2"	8 1/4"	12 1/4"	900	4 1/2" REG
Z1225H	12 1/4"	11 3/4"	17 1/2"	1800	6 5/8" REG
Z1750H	17 1/2"	16"	23"	1800	7 5/8" REG

DRILLSTAR

Tel : +33 5 59 130 100
sales@drillstar.fr
www.drillstar.fr

© Drillstar Industries - 8/09/2015

Go back to page 2

Appendix B: AISI 4145 modified properties

TATA STEEL

TATA

AISI 4145 modified

AISI 4145 modified is a low alloy chromium molybdenum (CrMo) steel similar to 4140 but with amended analysis which contributes towards its increased hardenability at larger diameters.

It is typically used for down-hole drilling tools such as drill collars, stabilisers and whipstock.

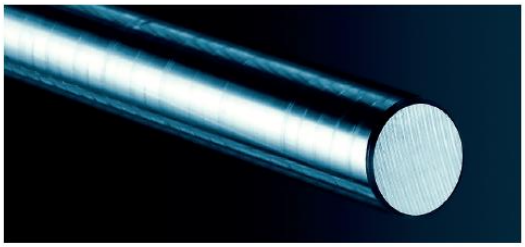

Scope

The specification defines the requirements for AISI 4145 modified hot rolled CrMo bars hardened and tempered to meet either 110ksi, 120ksi or 125ksi minimum yield strength.

Steel Manufacture

Steel is manufactured via Electric Arc Furnace, followed by ladle refining and vacuum degassing and is either cast into bottom-poured wide end up ingots, or continuously cast.

General Delivery Conditions

Applicable bar diameters: 1 – 12".
Surface conditions: Black/Peeled/Smooth Turned.
Straightness: 1mm in 500mm, $^{1}/_{8}$" in 5'.
Enhanced straightness may be available on request.

Chemical Analysis

C	Si	Mn	P	S	Cr	Mo	Ni	Al
0.43	0.15	0.95			0.90	0.25		0.015
0.49	0.35	1.15	0.015	0.020	1.20	0.35	0.25	0.030

Heat Treatment

Furnaces surveyed and calibrated per AMS 2750.

- Austenitised and liquid quenched
- Tempered to meet selected strength variant
- Supplied either stress free or stress relieved
- Note at larger sizes a normalising process may be required.

Mechanical Properties

	110ksi Variant 1-12" (mid radial)			120ksi Variant 1-12" (mid radial)			125ksi Variant 1-12" (mid radial)	
	Minimum	Maximum		Minimum	Maximum		Minimum	Maximum
0.2% Proof Stress (ksi)	110			120			125	
UTS (ksi)	140			140			140	
% Elongation	14			14			14	
% Reduction of Area	40			40			40	
Hardness HRC	30	36		30	36		30	36
Hardness HBW	285	341		285	341		285	341
	Average	Min. Single		Average	Min. Single		Average	Min. Single
CVN @ 23°C (J)	54	54		54			60	
CVN @ -32°C (J)	27	20	CVN @ -20°C (J)	42	30	CVN @ -20°C (J)	27	20

Tensile per ASTM A370, Charpy per ASTM E23, HRC per ASTM E18, HBW per ASTM E10

Structure
Grain size will be ASTM 6 or finer.

Reduction Ratio
Reduction ratio will meet 4:1 as a minimum.

API 6A
Each bar length will be 100% ultrasonically tested per ASTM A388, with acceptance criteria in accordance with API 6A PSL 3 & 4.

Note: Above a rolled size 10.5" the central 20% of the bar will be excluded from ultrasonic testing.

API 7-1
Ultrasonic and surface inspection for any orders <=11" (280mm) diameter can be carried out as follows to demonstrate capability of meeting.

The test certificate will be endorsed with the following statement: 'Ultra Sonic Testing Satisfactory, Confirming Capability To API 7-1'.

Surface inspection is performed on Tata Steels' Thermomatic Inspection Line instead of shear wave ultrasonic inspection.

Machining Tolerances
For 'Machining Quality Bar' to ASTM A29 tolerances the minimum machining allowance should be as follows:

Ordered Surface Condition	Minimum Stock Removal
Peeled/Smooth Turned	1% per side
Black	1.6% per side

Certification
A material test report will be provided, documenting the following: Chemical analysis; Heat treatment processing parameters; Mechanical properties; Surface hardness; Grain size; Reduction ratio; NDE test method/criteria.

Technical Support
Tata Steel has a comprehensive technical support team, available to advise on the selection and use of our oil & gas product range to ensure maximum benefit to you. Technical Account Managers provide specialist advice and help with day-to-day problem solving. Plant based metallurgists and the full resources of Tata Steel Research and Development Laboratories are available to assist with longer-term developments.

For further information, enquiries or any technical guidance on our range of oil & gas steels please contact the Commercial Department at the address below.

www.tatasteel.com

Tata Steel
Speciality Steels
Stocksbridge, Sheffield S36 2JA
United Kingdom
T: +44 (0) 114 2882361 F: +44 (0) 114 2885033
E: enquiries.tss@tatasteel.com W: www.tatasteel.com/oilandgas

English language TSS/4145modDS/05/2015/UK

While care has been taken to ensure that the information contained in this publication is accurate, neither Tata Steel Europe Limited, nor its subsidiaries, accept responsibility or liability for errors or for information which is found to be misleading.

Copyright 2015
Tata Steel Europe Limited

Go back to page 35

Appendix C: API casing specifications

OILProduction.net | API CASING TABLE SPECIFICATION

Size		Weight	ID		Drift		Capacity
Inches	mm	lbs/ft	Inches	mm	Inches	mm	bbl/100ft
4 1/2	114.30	9.50	4.090	103.89	3.965	100.71	1.63
		10.50	4.052	102.92	3.927	99.75	1.59
		11.60	4.000	101.60	3.875	98.43	1.55
		12.60	3.958	100.53	3.833	97.36	1.52
		13.50	3.920	99.57	3.795	96.39	1.49
		15.10	3.826	97.18	3.701	94.01	1.42
		16.60	3.754	95.35	3.629	92.18	1.37
		16.90	3.740	95.00	3.615	91.82	1.36
		17.70	3.696	93.88	3.571	90.70	1.33
		18.80	3.640	92.46	3.515	89.28	1.29
		21.60	3.500	88.90	3.375	85.73	1.19
		24.60	3.380	85.85	3.255	82.68	1.11
		26.50	3.240	82.30	3.115	79.12	1.02
5	127.00	11.50	4.560	115.82	4.435	112.65	2.02
		13.00	4.494	114.15	4.369	110.97	1.96
		15.00	4.408	111.96	4.283	108.79	1.89
		18.00	4.276	108.61	4.151	105.44	1.78
		20.30	4.184	106.27	4.059	103.10	1.70
		20.80	4.156	105.56	4.031	102.39	1.68
		21.40	4.126	104.80	4.001	101.63	1.65
		23.20	4.044	102.72	3.919	99.54	1.59
		24.20	4.000	101.60	3.875	98.43	1.55
		26.70	3.876	98.45	3.751	95.28	1.46
		32.00	3.620	91.95	3.495	88.77	1.27
5 1/2	139.70	13.00	5.044	128.12	4.919	124.94	2.47
		14.00	5.012	127.30	4.887	124.13	2.44
		15.50	4.950	125.73	4.825	122.56	2.38
		17.00	4.892	124.26	4.767	121.08	2.32
		20.00	4.778	121.36	4.653	118.19	2.22
		23.00	4.670	118.62	4.545	115.44	2.12
		26.00	4.548	115.52	4.423	112.34	2.01
		28.40	4.440	112.78	4.315	109.60	1.91
		29.70	4.376	111.15	4.251	107.98	1.86
		32.30	4.276	108.61	4.151	105.44	1.78
		36.40	4.090	103.89	3.965	100.71	1.62
		39.30	4.044	102.72	3.919	79.54	1.59
6	152.40	15.00	5.542	140.77	5.399	137.13	2.98
		18.00	5.424	137.77	5.299	134.59	2.86
		20.00	5.352	135.94	5.227	132.77	2.78
		23.00	5.240	133.10	5.115	129.92	2.67
		26.00	5.132	130.35	5.007	127.18	2.56
6 5/8	168.28	17.00	6.135	155.83	6.010	152.65	3.66
		20.00	6.049	153.64	5.924	150.47	3.55
		24.00	5.921	150.39	5.796	147.22	3.41
		28.00	5.791	147.09	5.666	143.92	3.26
		32.00	5.675	144.15	5.550	140.97	3.13
		35.00	5.575	141.61	5.450	138.43	3.02
		43.20	5.375	136.53	5.250	133.35	2.81
		69.63	4.375	111.13	4.250	107.95	1.86
7	177.80	17.00	6.538	166.07	6.413	162.89	4.15
		20.00	6.456	163.98	6.331	160.81	4.05
		23.00	6.366	161.70	6.241	158.52	3.94
		26.00	6.276	159.41	6.151	156.24	3.83
		29.00	6.184	157.07	6.059	153.90	3.71
		32.00	6.094	154.79	5.969	151.61	3.61
		35.00	6.004	152.50	5.879	149.33	3.50
		38.00	5.920	150.37	5.795	147.19	3.40
		41.00	5.820	147.83	5.695	144.65	3.29
		42.70	5.750	146.05	5.625	142.88	3.21
		44.00	5.720	145.29	5.595	142.11	3.18
		45.40	5.660	143.76	5.535	140.59	3.11
		49.50	5.540	140.72	5.415	137.54	2.98
		56.10	5.376	136.55	5.251	133.38	2.81
		58.00	5.240	133.10	5.115	129.92	2.67
		66.50	5.040	128.02	4.915	124.84	2.47
7 5/8	193.68	20.00	7.125	180.98	7.000	177.80	4.93
		24.00	7.025	178.44	6.900	175.26	4.79
		26.40	6.969	177.01	6.844	173.84	4.72
		29.70	6.875	174.63	6.750	171.45	4.59
		33.70	6.765	171.83	6.640	168.66	4.45
		39.00	6.625	168.28	6.500	165.10	4.26
		42.80	6.501	165.13	6.376	161.95	4.11
		45.30	6.435	163.45	6.310	160.27	4.02
		47.10	6.375	161.93	6.250	158.75	3.95
		51.20	6.249	158.72	6.125	155.58	3.80
		52.80	6.201	157.81	6.000	152.40	3.74
		55.75	6.201	157.51	6.176	156.87	3.74

Size		Weight	ID		Drift		Capacity
Inches	mm	lb/ft	Inches	mm	Inches	mm	bbl/100ft
7 3/4	196.85	46.10	6.560	166.62	6.500	165.10	4.18
8 5/8	219.08	24.00	8.097	205.66	7.972	202.49	6.37
		28.00	8.017	203.63	7.892	200.46	6.24
		32.00	7.921	201.19	7.796	198.02	6.09
		36.00	7.825	198.76	7.700	195.58	5.95
		40.00	7.725	196.22	7.6	193.04	5.8
		44.00	7.625	193.68	7.500	190.50	5.65
		49.00	7.511	190.78	7.386	187.60	5.48
		52.00	7.435	188.85	7.310	185.67	5.37
8 3/4	222.25	49.70	7.636	193.95	7.500	190.50	5.66
9 5/8	244.48	29.30	9.063	230.20	8.907	226.24	7.98
		32.30	9.001	228.63	8.845	224.66	7.87
		36.00	8.921	226.59	8.765	222.63	7.73
		38.00	8.885	225.68	8.76	222.50	7.67
		40.00	8.835	224.41	8.679	220.45	7.58
		43.50	8.755	222.38	8.599	218.41	7.45
		47.00	8.681	220.50	8.525	216.54	7.32
		53.50	8.535	216.79	8.379	212.83	7.08
		58.40	8.435	214.25	8.279	210.29	6.91
		59.40	8.407	213.54	8.251	209.58	6.87
		61.10	8.375	212.73	8.219	208.76	6.81
		64.90	8.281	210.34	8.125	206.38	6.66
		70.30	8.157	207.19	8.001	203.23	6.46
		71.80	8.125	206.38	7.969	202.41	6.41
9 3/4	247.65	59.20	8.560	217.42	8.500	215.90	7.12
9 7/8	250.83	62.80	8.625	219.08	8.500	215.90	7.23
10 3/4	273.05	32.75	10.192	258.88	10.036	254.91	10.09
		35.75	10.136	257.45	10.011	254.28	9.98
		40.50	10.050	255.27	9.894	251.31	9.81
		45.50	9.950	252.73	9.794	248.77	9.62
		51.00	9.850	250.19	9.694	246.23	9.42
		55.50	9.760	247.90	9.604	243.94	9.25
		60.70	9.660	245.36	9.504	241.40	9.06
		65.70	9.560	242.82	9.404	238.86	8.88
		71.10	9.450	240.03	9.294	236.07	8.67
		73.20	9.406	238.91	9.250	234.95	8.59
		76.00	9.350	237.49	9.194	233.53	8.49
		79.20	9.282	235.76	9.126	231.80	8.37
		81.00	9.250	234.95	9.094	230.99	8.31
11 3/4	298.45	38.00	11.150	283.21	10.994	279.25	12.08
		42.00	11.084	281.53	10.928	277.57	11.93
		47.00	11.000	279.40	10.844	275.44	11.75
		54.00	10.880	276.35	10.724	272.39	11.50
		60.00	10.772	273.61	10.616	269.65	11.27
		65.00	10.682	271.32	10.526	267.36	11.08
		66.70	10.656	270.66	10.500	266.70	11.03
		71.00	10.586	268.88	10.430	264.92	10.89
		73.60	10.532	267.51	10.376	263.55	10.78
		75.00	10.514	267.06	10.358	263.09	10.74
		76.00	10.500	266.70	10.344	262.74	10.71
		79.00	10.438	265.13	10.282	261.16	10.58
		80.50	10.406	264.31	10.25	260.35	10.52
		83.00	10.368	263.35	10.212	259.38	10.44
		87.20	10.282	261.16	10.126	257.20	10.27
		95.00	10.124	257.15	9.968	253.19	9.96
11 7/8	301.63	71.80	10.711	272.06	10.625	269.88	11.14
13 3/8	339.73	48.00	12.715	322.96	12.559	319.00	15.71
		54.50	12.615	320.42	12.459	316.46	15.46
		61.00	12.515	317.88	12.359	313.92	15.21
		68.00	12.415	315.34	12.259	311.38	14.97
		72.00	12.347	313.61	12.191	309.65	14.81
		77.00	12.275	311.79	12.119	307.82	14.64
		80.70	12.215	310.26	12.059	306.30	14.49
		83.00	12.175	309.25	12.019	305.28	14.40
		85.00	12.159	308.84	12.003	304.88	14.36
		86.00	12.125	307.98	11.969	304.01	14.28
		91.00	12.055	306.20	11.899	302.23	14.12
		92.00	12.031	305.59	11.875	301.63	14.06
		96.00	11.975	304.17	11.819	300.20	13.93
		98.00	11.937	303.20	11.781	299.24	13.84
		100.30	11.907	302.44	11.751	298.48	13.77
		102.00	11.889	301.98	11.733	298.02	13.73
13 1/2	342.90	81.40	12.340	313.44	12.250	311.15	14.79
13 5/8	346.08	88.20	12.375	314.33	12.250	311.15	14.88

www.oilproduction.net by M.Hirschfeldt

Go back to page 22

Appendix D: Reaction force analysis

A reaction force analysis can be used to check if the FEA model is solved correctly. The applied loads have to be in equilibrium with the reaction forces of the nodes where the supports are located. Constraint problems related to redundancy may cause high reaction forces for some supports. This is unwanted since the results from the FEA may be used to verify manual calculations.

If boundary conditions are sharing the same node, the reaction forces corresponding to that node are calculated twice. This could also cause problems because, for each support, the nodes are selected and the reaction forces are retrieved after which they are added.

Sometimes reaction forces are calculated for directions in which the structure is not constrained. In this case, the error is also be caused by surfaces sharing their topology. The reaction forces are then passed on through common nodes.

To validate a FEA, the following post processing checks should be performed:

- *Does the shape of the deformed structure agree with the boundary conditions that are applied?*
- *Are the reaction forces of the supports in equilibrium with the applied loads?*

To do a nodal force analysis, the nodal forces should be written to the results file in *Ansys*. At *analysis settings* under *output controls*, the nodal forces option can be enabled. Next, the supports can be dragged onto the *solutions* sub-tree. This creates a reaction force probe for these specific contacts. Force reactions are now visible under solutions. By rerunning the simulation, the reaction forces for all directions of the support are determined. The data that results from the rerun is tabulated in the bottom-right corner. This data can be put in an excel file. The reaction forces for all directions are summed and then compared to the applied forces in these directions. The results for a simple simulation are shown in table D.1.

Table D.1: Reaction force check.

Reaction force check				
Link-piston assembly: retraction				
Input	**Dimension**	**X-direction**	**Y-direction**	**Z-direction**
Piston force	[N]	0	-1114	0
Summation	[N]	**0**	**-1114**	**0**
FEA output	**Dimension**	**X-direction**	**Y-direction**	**Z-direction**
Frictionless Support	[N]	-70,467	0	-122,05
Fixed Support	[N]	-964,78	1114	557,01
Frictionless Support 2	[N]	952,12	0	-578,93
Frictionless Support 3	[N]	0,072986	0	0,12642
Frictionless Support 5	[N]	83,061	0	143,87
Summation	[N]	**0,006986**	**1114**	**0,02642**
Difference	[N]	0	0	0
Deviation	[%]	**-**	**0,0**	**-**

It can be seen that the equilibrium for this simulation is satisfied and no problems with constraints are found. This means that the model set-up is defined properly.

Beside from identifying constraint problems related to the *location of application* and *compatibility* with other constraints, reaction forces may also give an indication of the physical correctness of the simulation.

With the reaction force check above, it can be shown that no free body motions are being produced during solving. However, the *kind of constraint* or *constraint behaviour* itself may give rise to stress and displacement related errors. A common mistake is applying a fixed constraint to restrict deflections in directions that are not constrained in reality.

Go back to page 118

Appendix E: Weight on Bit approximation

The maximum WOB the UR needs to convey can be determined by considering the case where only the UR cutting blocks are in contact with the borehole. It has been assumed that the WOB is limited by the dimensions of the tongue-groove connection. When the WOB is applied on top, a reaction force will be present at the bottom of the cutter-block. This reaction force is directed perpendicular to the grooves. This means that when no other external forces are present on the blocks, these grooves will bear the entire load and the block does not slide. The groove connections of both designs are compared determine the amount of force needed to get the same stress as in the original design.

Table E.1: New design parameters.

New design	
Average tongue area	120.25 mm²
Amount of tongues	4
Total area	481 mm²

The force on the bottom of the block can be determined as follows:

$$\frac{WoB \cdot g}{\cos\beta} = F_{bottom} \qquad [E.1]$$

Then the average compressive stress on the grooves can be determined by:

$$\frac{\sigma_{yield}}{FoS} = \frac{F_{bottom}}{A} \qquad [E.2]$$

For the new design, the allowable WOB can now be determined as follows:

$$WoB = \frac{\sigma_{yield} \cdot A \cdot \cos\beta}{FoS \cdot g} \qquad [E.3]$$

For the calculation, a factor of safety of 2.5 will be applied here because the situation down hole is uncertain in terms of the contact area and application points of the forces.

By filling in the numbers, the following result is obtained:

$$WoB = \frac{758 \cdot 10^6 \cdot 0.000481 \cdot \cos 45}{2.5 \cdot 9.81} \approx \mathbf{10500}\ [kg]$$

This is the case where the UR only contacts the borehole. In case the UR and bit contact the borehole, the WOB could be increased. However, this value is chosen as the **maximum value** for all load cases because it is in most cases unknown whether the bit, the UR or both the bit and UR are in contact with the formation rock.

Appendix F: ECI: specifications, features and applications

The following information is retrieved from the websites of WEP and HWT. For convenience the information was merged into lists that describe some of the specifications, features, applications and benefits (1), (2):

"GENERAL SPECIFICATIONS

Functional and operational advantages

- *ECI reduces effects of hole problems like stability, lost circulation, hole cleaning.*
- *ECI reduces rig time and increases personnel safety (no pipe tripping for BHA changes, casing or cementing).*
- *ECI is fully retrievable: BHA components can be retrieved through casing on cable or by reverse circulation.*
- *Composite casing shoe tracks allow logging through casing: M/LWD tools remain within casing and both rathole and bit/reamer stick out can be kept at minimum distance to improve stabilization and to optimize drilling performance.*
- *More Productive Time:*
    - *Casing in place when TD is reached*
    - *Minimum of mud losses*
    - *Better hole quality for better cementations and logging results*
- *Safer and lower environmental impact:*
    - *No tripping*
    - *Efficient dynamic kills*
    - *Less handling*
    - *Less pump power required*
    - *No drill pipe*
    - *Less chance on swab kicks and no stripping to bottom during a kick*
- *Efficient drilling:*
    - *Less vibrations due to higher pipe stiffness*
    - *High rotational stiffness for higher ROP's*
    - *Better hole cleaning*
    - *Smaller hole sizes*
    - *Lower mud weights for higher ROP's*

SPECIAL FEATURES

- *Lock Down Device to connect BHA to casing.*
- *ECI BHA is fully retrievable.*
- *Reamer for hole opening.*
- *Composite Casing shoetrack section allows logging.*
- *Flexible set up allows freedom of choice for third party BHA equipment (bits, mud motors, logging tools).*
- *Drilling directional wells, e.g. for cluster drilling*
- *Small stick-out to minimize rathole and the risk of getting stuck BHA*
- *Better stabilized BHA and drill section*
- *Shorter and lighter BHA*
- *Fully mechanical RSS*
- *Automated directional drilling*
- *Providing extra down hole power by using mud motors*
- *Robust (steel) bits and reamers*
- *Measurements While Drilling and Logging While Drilling possible*
- *Compact BHA's allowing pressure or cable retrieval*

APPLICATIONS

- *ECI is available for 9 5/8" and 7" liners and casing.*
- *ECI simplifies the drilling process, reduces well costs, and improves operational safety.*
- *ECI can be used as a general mitigation to reduce*
- *NPT caused by drilling problems: open hole time is minimised while drilling through troublesome formations.*
- *Logging through casing.*
- *Performance drilling with casing.*
- *Directional drilling with casing."*

(1) http://wellengineering.nl/wp-content/uploads/2012/01/ECI_final.pdf
(2) http://huismanwelltechnology.com/applications/eci-application-xx/

Go back to page 4

Appendix G: Assembly overview

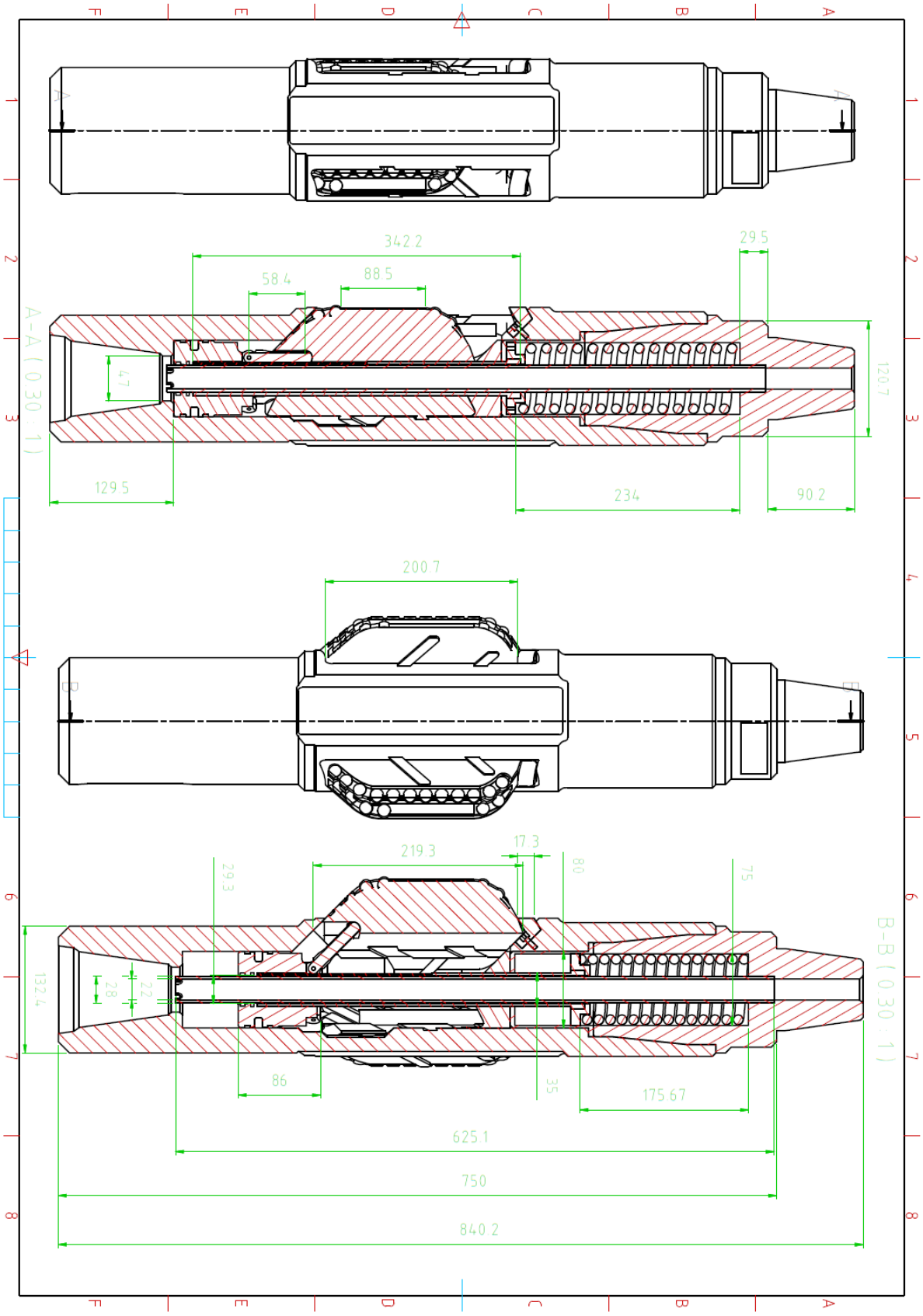

Go back to page 151

Appendix H

H.1: Nominal torque, peak WoB

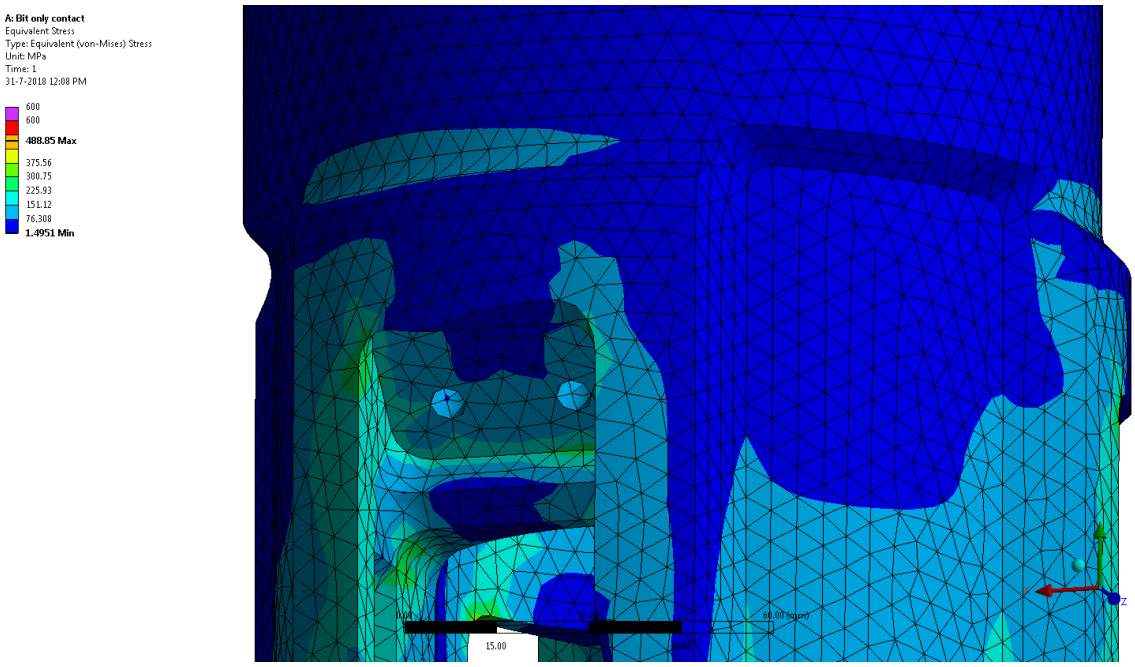

Figure H.1: UR loaded with nominal torque and peak WoB.

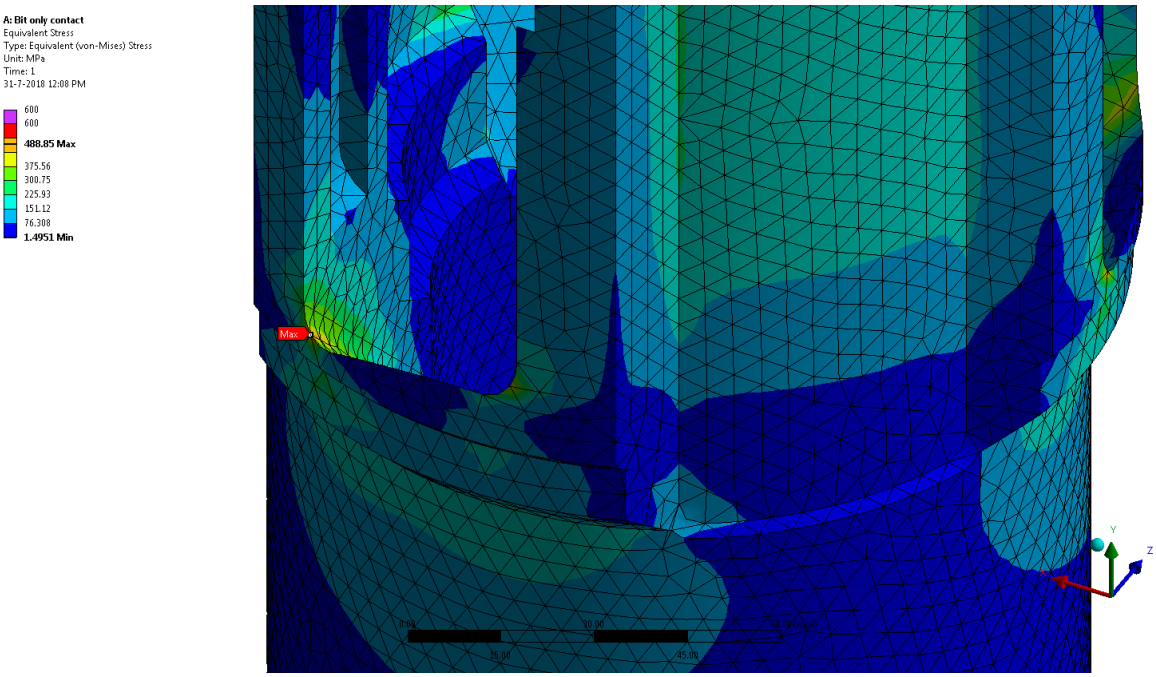

Figure H.2: UR loaded with nominal torque and peak WoB.

H.2: Maximum torque, peak WoB

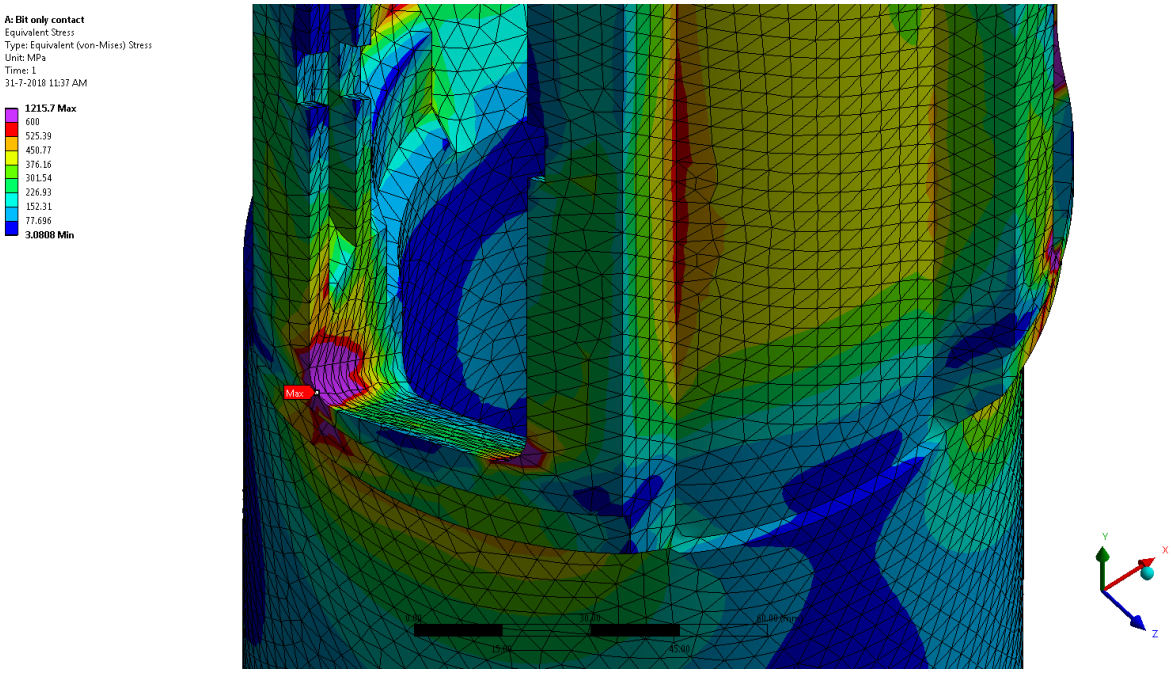

Figure H.3: UR loaded with maximum torque and peak WoB.

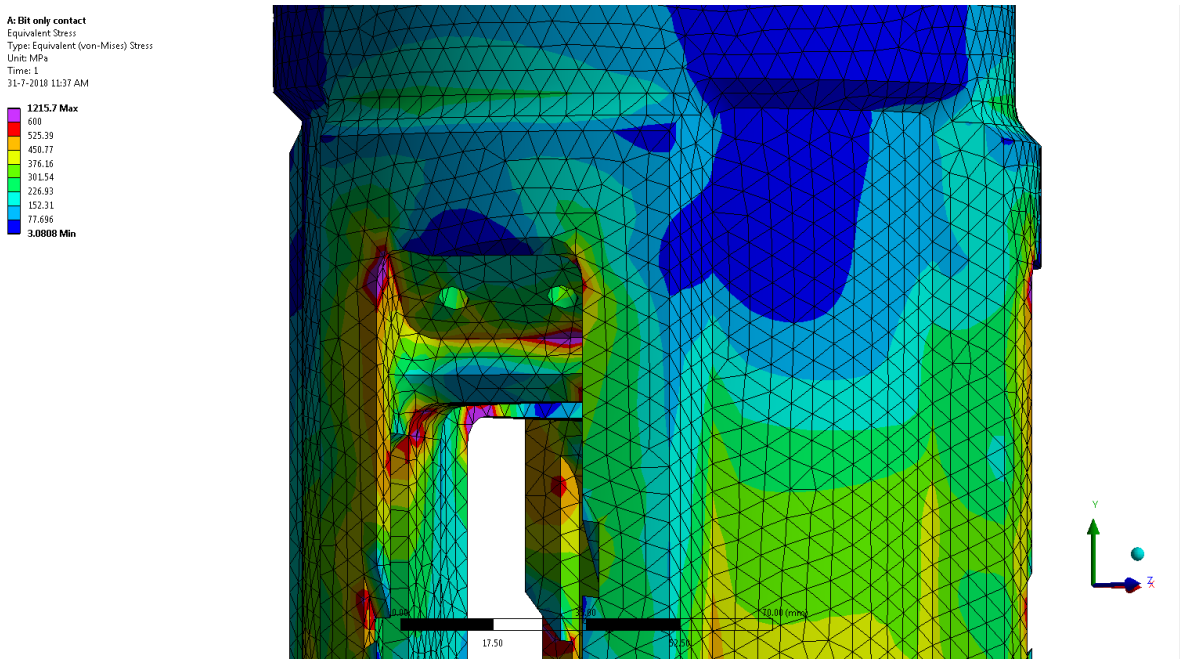

Figure H.4: UR loaded with maximum torque and peak WoB.

H.3: Limiting load case

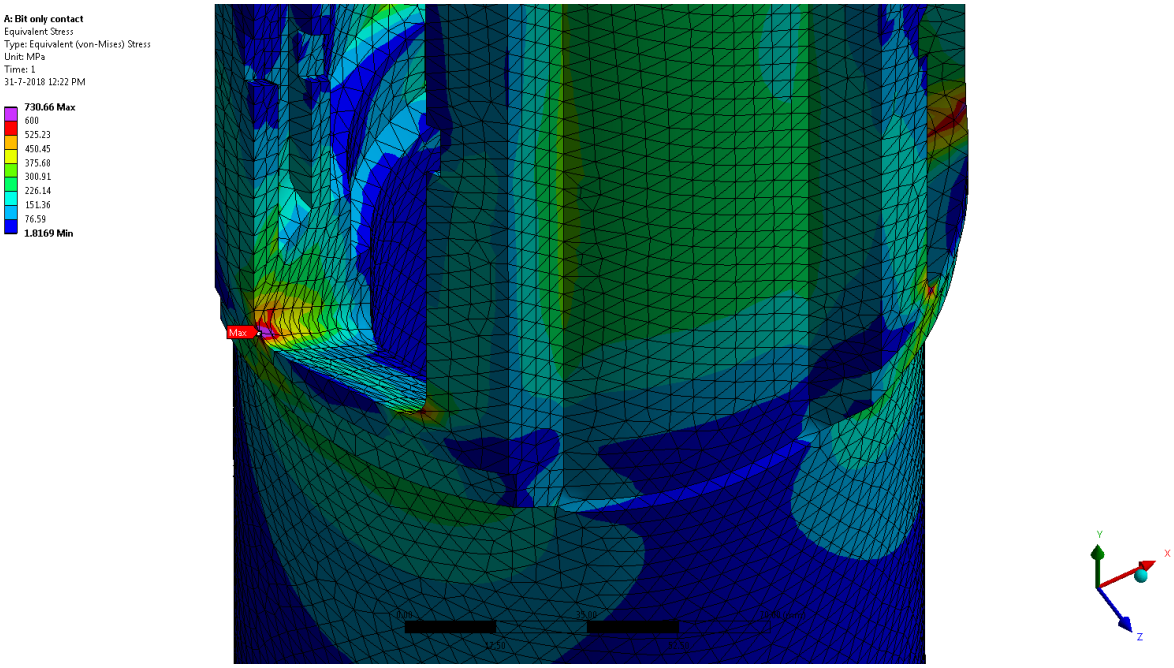

Figure H.5: UR subjected to the limiting torque and WoB load.

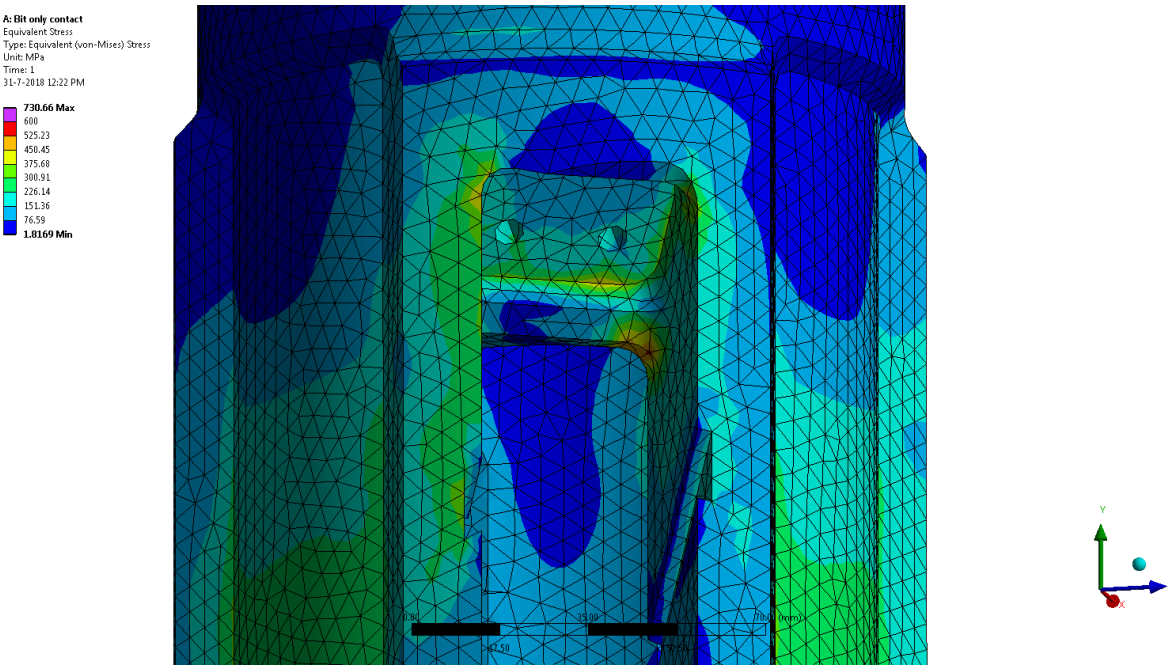

Figure H.6: UR subjected to the limiting torque and WoB load.

Go back to page 133

Appendix I: Armstopper limiting load case

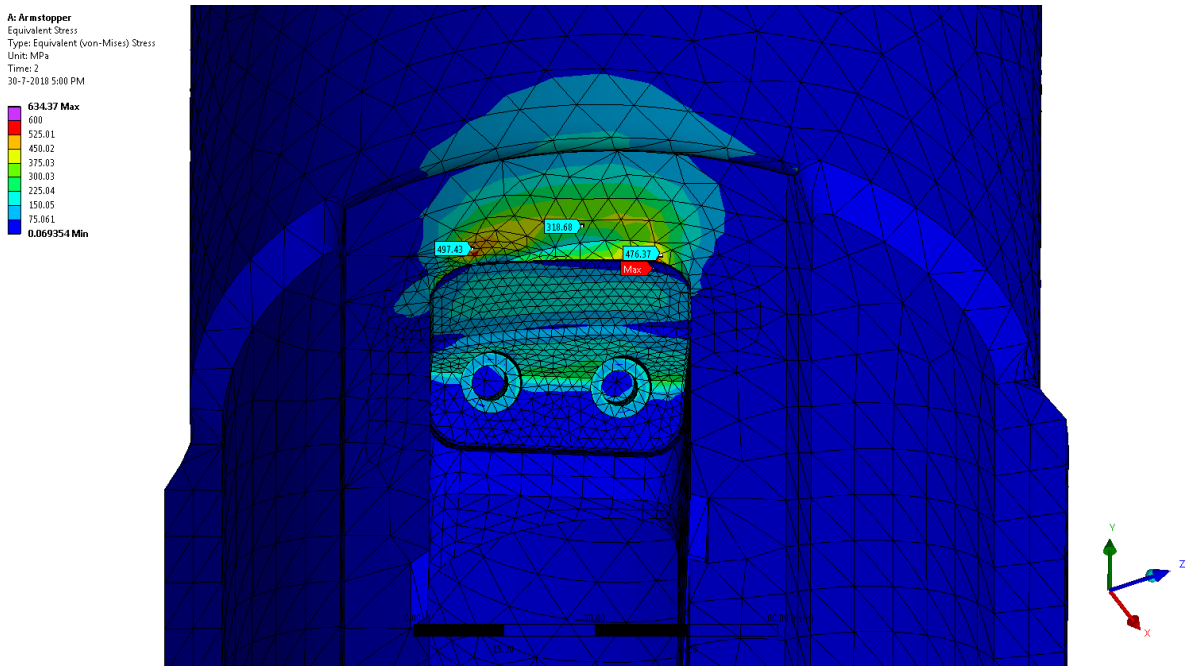

Figure I.1: Armstopper subjected to the limiting piston load.

Go back to page 141

Appendix J: Specific energy, cutting power and soil type derivation

Parameters and equations

Table J.1: Parameters.

Parameter	Unit	Description
ROP	[meter/hour]	Drilling penetration rate (meter/hour)
RPM	[1/minute]	Revolutions per minute of the casing string (rounds/minute)
$A_{1,cutters}$	[m²]	Surface area of the cutted surface
v_{down}	[m/s]	Drilling penetration rate (meter/second)
t_{layer}	[m]	Thickness of the layer cut (meters/round)
$D_{pilot\ hole}$	[m]	Pilot hole or drill bit diameter
D_{UR}	[m]	(Maximum) diameter of the underreamer
w	[m]	Width of the cutting blade
v_c	[m/s]	(Tangential) cutting velocity of the blade
E_{sp}	[MPa] or [MJ/m³]	Specific cutting energy
P_c	[W] or [J/s]	Cutting power required
Q_v	[m³/s]	Volumetric production
T	[N·m]	Torque generated at the underreamer
E	[J]	Energy for rock breakage
V	[m³]	Volume of formation removed
F_h	[N]	Horizontal cutting force
r_{cutter}	[m]	Average radius of cutted section
ω	[1/s]	Angular velocity (radians per second)
n	[-]	Number of cutter blocks (n=3 for the underreamer)
WoB	[kg]	Weight on Bit
F_v	[N]	Vertical cutting force
g	[m/s²]	Acceleration of gravity

The layer thickness per round can be calculated with:

$$\frac{ROP/3600}{RPM/60} = \frac{ROP}{RPM \cdot 60} = t_{layer} \qquad [J.1]$$

The volumetric production can be calculated with:

$$Q_v = A_{1,cutters} \cdot v_{down} \qquad [J.2]$$

$$v_{down} = ROP/3600 \qquad [J.3]$$

$$A_{1,cutters} = \frac{\pi}{4} \cdot \left(D_{UR}^2 - D_{pilot\ hole}^2\right) \qquad [J.4]$$

Alternatively, the volumetric production can be calculated with:

$$Q_v = t_{layer} \cdot w \cdot \frac{2 \cdot \pi \cdot r_{cutter} \cdot RPM}{60} \qquad [J.5]$$

$$w = \left(\frac{D_{UR} - D_{pilot\ hole}}{2}\right) \qquad [J.6]$$

$$r_{cutter} = \frac{D_{pilot\ hole}}{2} + \frac{1}{2} \cdot \left(\frac{D_{UR} - D_{pilot\ hole}}{2}\right) \quad [J.7]$$

The specific cutting energy can be calculated with (Miedema, 2016):

$$E_{sp} = \frac{P_c}{Q_c} = \frac{F_h \cdot v_c}{t_{layer} \cdot w \cdot v_c} = \frac{F_h}{t_{layer} \cdot w} \quad [J.8]$$

The downward velocity is neglected here because it is very small compared to tangential velocity:

$$v_c = \frac{2 \cdot \pi \cdot r_{cutter} \cdot RPM}{60} = 0.99\ m/s \quad [J.9]$$

$$v_{down} = ROP/3600 = 2.77 \cdot 10^{-3}\ m/s \quad [J.10]$$

$$\rightarrow v_c \gg v_{down}$$

Since $F_h \cdot v_c$ equals torque times omega generated by the formation, one may rewrite this relation:

$$F_h \cdot v_c = F_h \cdot r_{cutter} \cdot \omega = T \cdot \omega \quad [J.11]$$

$$\rightarrow E_{sp} = \frac{E}{V} = \frac{P_c}{Q_c} = \frac{T \cdot \omega}{t_{layer} \cdot w \cdot v_c} = \frac{T \cdot \frac{2 \cdot \pi \cdot RPM}{60}}{t_{layer} \cdot w \cdot \frac{2 \cdot \pi \cdot r_{cutter} \cdot RPM}{60}} = \frac{T}{t_{layer} \cdot w \cdot r_{cutter}} \quad [J.12]$$

Huisman data

ROP = 10 [m/hr], RPM = 100 [-], D_{UR} = 228.6 mm (9 in.), $D_{pilot\ hole}$ = 149.23 mm (5 7/8 in.), T = 8000 N·m (nominal torque), (Total power top drive ≈ 600 kW)

Results

Layer thickness:

$$\frac{ROP/3600}{RPM/60} = \frac{ROP}{RPM \cdot 60} = t_{layer} \rightarrow \frac{10}{100 \cdot 60} = \mathbf{1.67 \cdot 10^{-3}\ m} \quad [J.13]$$

Volumetric production:

$$Q_v = A_{1,cutters} \cdot v_{down} = \frac{\pi}{4} \cdot \left(D_{UR}^2 - D_{pilot\ hole}^2\right) \cdot ROP/3600 \quad [J.14]$$

$$\rightarrow \frac{\pi}{4} \cdot (0.2286^2 - 0.14923^2) \cdot 10/3600 = \mathbf{6.54 \cdot 10^{-5}\ m^3/s} \quad [J.15]$$

Alternatively:

$$Q_v = t_{layer} \cdot w \cdot \frac{2 \cdot \pi \cdot r_{cutter} \cdot RPM}{60} \quad [J.16]$$

$$Q_v = \frac{ROP}{RPM \cdot 60} \cdot \left(\frac{D_{UR} - D_{pilot\ hole}}{2}\right) \cdot \frac{2 \cdot \pi \cdot \left(\frac{D_{pilot\ hole}}{2} + \frac{1}{2} \cdot \left(\frac{D_{UR} - D_{pilot\ hole}}{2}\right)\right) \cdot RPM}{60} \quad [J.17]$$

$$\rightarrow \frac{10}{100 \cdot 60} \cdot \left(\frac{0.2286 - 0.14923}{2}\right) \cdot \frac{2 \cdot \pi \cdot \left(\frac{0.14923}{2} + \frac{1}{2} \cdot \left(\frac{0.2286 - 0.14923}{2}\right)\right) \cdot 100}{60} \qquad [J.18]$$

$$= \mathbf{6.54 \cdot 10^{-5}\ m^3/s}$$

It can be seen that both calculations give exactly the same result!

Specific energy:

$$E_{sp} = \frac{E}{V} = \frac{P_c}{Q_c} = \frac{T \cdot \omega}{t_{layer} \cdot w \cdot v_c} = \frac{T \cdot \frac{2 \cdot \pi \cdot RPM}{60}}{t_{layer} \cdot w \cdot \frac{2 \cdot \pi \cdot r_{cutter} \cdot RPM}{60}} = \frac{T}{t_{layer} \cdot w \cdot r_{cutter}} \qquad [J.19]$$

$$w = \left(\frac{D_{UR} - D_{pilot\ hole}}{2}\right) \qquad [J.20]$$

$$r_{cutter} = \frac{D_{pilot\ hole}}{2} + \frac{1}{2} \cdot \left(\frac{D_{UR} - D_{pilot\ hole}}{2}\right) \qquad [J.21]$$

$$\rightarrow \frac{8000}{1.67 \cdot 10^{-3} \cdot \left(\frac{0.2286 - 0.14923}{2}\right) \cdot \left(\frac{0.14923}{2} + \frac{1}{2} \cdot \left(\frac{0.2286 - 0.14923}{2}\right)\right)} = \mathbf{1280\ MJ/m^3} \qquad [J.22]$$

Cutting power required by the underreamer:

$$P_c = E_{sp} \cdot Q_v \rightarrow 1280 \cdot 10^3 \cdot 6.54 \cdot 10^{-5} = \mathbf{84\ kW} \qquad [J.23]$$

This answer seems very reasonable. The remainder of the top drive power is consumed by wall friction and string accelerations.

Derivation of soil type

Because the horizontal and vertical cutting forces can be derived from the torque and WoB load, the type of soil being drilled can also be determined. The (average) horizontal cutting force per cutter block can be calculated when the torque is known:

$$T = n \cdot F_h \cdot r_{cutter} \qquad [J.24]$$

$$\rightarrow F_h = \frac{T}{n \cdot r_{cutter}} = \frac{8000}{3 \cdot \left(\frac{0.14923}{2} + \frac{1}{2} \cdot \left(\frac{0.2286 - 0.14923}{2}\right)\right)} = \mathbf{28231\ N} \qquad [J.25]$$

The (average) vertical cutting force per cutter block can be derived from the WoB:

$$\frac{WoB \cdot g}{n} = F_v \qquad [J.26]$$

$$\rightarrow F_v = \frac{5000 \cdot 9.81}{3} = \mathbf{16350\ N} \qquad [J.27]$$

According to (Miedema, 2016), the cutting forces in horizontal and vertical direction can be described by:

$$F_h = \lambda_{HF} \cdot c \cdot h_i \cdot w \qquad [J.28]$$

$$F_v = \lambda_{VF} \cdot c \cdot h_i \cdot w \qquad [J.29]$$

Here:

$$w = \left(\frac{D_{UR} - D_{pilot\ hole}}{2}\right) \qquad [J.30]$$

$$h_i = t_{layer} = \frac{ROP/3600}{RPM/60} = \frac{ROP}{RPM \cdot 60} \qquad [J.31]$$

$$c = \frac{UCS}{2} \cdot \left(\frac{1 - \sin\varphi}{\cos\varphi}\right) \qquad [J.32]$$

The internal angle of friction is assumed to be 30°. Now, the UCS value can be calculated as follows:

$$UCS = \frac{2 \cdot F_h}{\lambda_{HF} \cdot h_i \cdot w \cdot \left(\frac{1 - \sin\varphi}{\cos\varphi}\right)} \qquad [J.33]$$

$$\rightarrow UCS = \frac{2 \cdot 28231}{30 \cdot 1.67 \cdot 10^{-3} \cdot \left(\frac{0.2286 - 0.14923}{2}\right) \cdot \left(\frac{1 - \sin 30}{\cos 30}\right)} \approx 49.2\ MPa \qquad [J.34]$$

This number corresponds to the average UCS value of **shale**. This seems to coincide with the data from test boreholes.

Back cover image source: http://getwallpapers.com/wallpaper/full/c/6/5/551278.jpg